AFRL-AFOSR-UK-TR-2023-0011

Anode Materials for High Power Microwave Devices

O'Neill, William
THE CHANCELLOR, MASTER AND SCHOLARS OF THE UNIVERISTY OF CAMBRIDGE
THE OLD SCHOOLS
CAMBRIDGE, , CB2 1TN
GB

10/18/2022
Final Technical Report

Air Force Research Laboratory
Air Force Office of Scientific Research
European Office of Aerospace Research and Development
Unit 4515 Box 14, APO AE 09421

REPORT DOCUMENTATION PAGE

PLEASE DO NOT RETURN YOUR FORM TO THE ABOVE ORGANIZATION.

1. REPORT DATE	2. REPORT TYPE	3. DATES COVERED	
20221018	Final	START DATE 20170703	END DATE 20190702

4. TITLE AND SUBTITLE
Anode Materials for High Power Microwave Devices

5a. CONTRACT NUMBER	5b. GRANT NUMBER	5c. PROGRAM ELEMENT NUMBER
	FA9550-17-1-0317	61102F
5d. PROJECT NUMBER	**5e. TASK NUMBER**	**5f. WORK UNIT NUMBER**

6. AUTHOR(S)
William O'Neill

7. PERFORMING ORGANIZATION NAME(S) AND ADDRESS(ES)
THE CHANCELLOR, MASTER AND SCHOLARS OF THE UNIVERISTY OF CAMBRIDGE
THE OLD SCHOOLS
CAMBRIDGE CB2 1TN
GB

8. PERFORMING ORGANIZATION REPORT NUMBER

9. SPONSORING/MONITORING AGENCY NAME(S) AND ADDRESS(ES)	10. SPONSOR/MONITOR'S ACRONYM(S)	11. SPONSOR/MONITOR'S REPORT NUMBER(S)
EOARD UNIT 4515 APO AE 09421-4515	AFRL/AFOSR IOE	AFRL-AFOSR-UK-TR-2023-0011

12. DISTRIBUTION/AVAILABILITY STATEMENT
A Distribution Unlimited: PB Public Release

13. SUPPLEMENTARY NOTES

14. ABSTRACT
This project focuses on solving the problems of outgassing and SEE of the anode materials in HPM devices by manufacturing low outgassing and secondary electron emission substrates using laser processing from materials which would most benefit anode applications, thereby, increasing the efficiency of high power microwave devices.

15. SUBJECT TERMS

16. SECURITY CLASSIFICATION OF:			17. LIMITATION OF ABSTRACT	18. NUMBER OF PAGES
a. REPORT U	b. ABSTRACT U	c. THIS PAGE U	SAR	183

19a. NAME OF RESPONSIBLE PERSON	19b. PHONE NUMBER *(Include area code)*
JASON FOLEY	555-555-5555

Anode Materials for High Power Microwave Devices

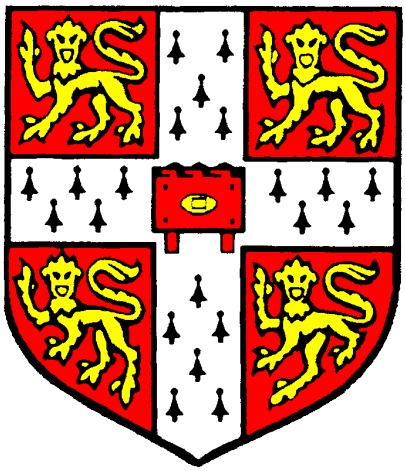

Daniel Piotr Gortat

Pembroke College

University of Cambridge

This dissertation is submitted for the degree of

Doctor of Philosophy

June 2019

Declaration

This dissertation is the result of my own work and includes nothing which is the outcome of work done in collaboration except as declared in the Preface and specified in the text. It is not substantially the same as any that I have submitted, or, is being concurrently submitted for a degree or diploma or other qualification at the University of Cambridge or any other University or similar institution except as declared in the Preface and specified in the text. I further state that no substantial part of my dissertation has already been submitted, or, is being concurrently submitted for any such degree, diploma or other qualification at the University of Cambridge or any other University or similar institution except as declared in the Preface and specified in the text. It does not exceed the prescribed 65,000 words and 150 figures of the Engineering Degree Committee.

Daniel Gortat

14 June 2019

Abstract

The research is undertaken in order to increase the operational efficiency of high power microwave (HPM) devices by developing novel anodes with minimal outgassing and secondary electron emission properties, anodes which do not erode during usage nor limit the lowest achievable pressure in an HPM device. To accomplish this, two methods have been identified: laser surface melting for outgassing reduction and laser surface structing for secondary electron emission reduction.

Localised laser surface melting allows controlled grain nucleation, grain size increase and shaping, to create a hydrogen atom diffusion barrier between the surface layer and the bulk of the treated metal with an added benefit of evacuating the hydrogen atoms from the laser surface melt layer. The tests showed that anodes of 304 stainless steel processed by a continuous wave Yb fibre laser with a wavelength of 1.064 μm and subjected to 50 keV electron bombardment showed a reduction in outgassing by approximately a factor of 4 compared to that from untreated stainless steel. This is attributed to a reduction in the number of grain boundaries which serve as trapping sites for hydrogen in stainless steel through which, when heated, rate of hydrogen atom diffusion to the surface of the anode is reduced where it recombines with another hydrogen atom into a hydrogen gas molecule for outgassing. The current manufacturing method for HPM anodes is baking or vacuum annealing. Laser treated anodes do not require post-processing to preserve the benefits of the treatment and are excellent candidates for use in high power microwave devices.

For secondary electron emission reduction, laser surface structing via pulsed laser irradiation was implemented to create secondary electron traps in the areas of the anode which are directly exposed to the electron beam. Pulsed laser irradiation is a high precision surface structuring tool which allowed to design two types of traps: laser-induced periodic surface structures and high aspect-ratio holes. Both increase the surface roughness of the anode increasing the number of sites for the secondary electron absorption. Laser-induced periodic surface structuring stopped the secondary electron emission (secondary electron yield = $\frac{\text{secondary electrons}}{primary\ electrons} < 1$) with the highest secondary electron yield measured to be 0.84 for treated 316 SS, which is lower that C-based materials. Maximum secondary electron emission reduction with high-aspect ratio holes achieved was 0.98 on 304 SS with 0.52 % porosity, percentage of holes per surface area. Increasing the porosity reduces the secondary election yield further.

The work conducted led to a novel one-step manufacturing technique for treatment of metals for vacuum applications. Commercial applications include but are not limited to: laser surface melting of steel chambers for ultra/extreme high vacuum systems (particle accelerators, etc.), analytical techniques (XPS, SIMS, SEM, FIB, etc.). Additionally, a single crystal grain refinement and a security marking techniques have been established for polycrystalline metals. Single crystals were achieved after three

consecutive passes with constant laser parameters throughout the length of the laser raster at 19.17 kJ/cm^2 average energy density by a continuous wave non-polarised fibre laser with a wavelength of 1.064 μm at 300 K, 0.1 % oxygen environment. The depth of localised grain nucleation was measured to be ~20 μm for a single pass, making hidden messages in the bulk of the material possible after mechanically removing the immediate surface melt. The patterns are undetectable by conventional optical microscopy but can be viewed with differential interference contrast microscopy or grain imaging tools (FIB, EBSD), this way establishing a metal security marking technique. Several areas have been outlined for future investigations of the benefits of laser surface melting: reduction of hydrogen embrittlement for mechanical failures in metals for increased strength of structural metals, electrical conductivity increase, substrates for chemical vapour deposition growth of graphene and single crystal grain refinement in high thermal conductivity metals, e.g. copper.

Laser drilling high aspect-ratio holes has been chosen for secondary electron emission reduction of metal anodes in HPMs due to the evidence of laser-induced periodic surface structuring method nucleating the surface grains and disrupting the laser surface melt treatment. The method is being added to the patent on reduced hydrogen outgassing and secondary electron emission HPM anode manufacture. The identified direction for further work includes: conical and reverse conical boreholes for reducing secondary election emission during an angular e-beam impact on the anode and microstructural transformation after laser drilling.

Acknowledgements

I would like to take this opportunity to thank the people without whom this journey would not have been possible.

First, I would like to thank my supervisor, Dr Martin Sparkes, for his creative advice, encouragement, and thorough analysis of my writings whose great input and guidance made this thesis possible. My second thanks is to Prof William O'Neill, my thesis advisor, for his insights into laser-material interaction, support and prompt response to my queries.

I would like to express my appreciation to the US Air Force team, Dr Steven Fairchild, Dr Tyson Back, Gregg Gruen, Dr Marc Cahay, Dr David Turner, Dr John Boeckl and Dr Nathaniel Lockwood who arranged the trip to the USA and provided laboratory facilities to conduct hydrogen outgassing measurements via Anode Materials Characterisation System. I would like to thank Prof Terry Murray for the Monte Carlo electron beam trajectory simulations and schematics of the Anode Materials Characterisation System.

I would also like to thank Dr John Bulmer, a CNT expert, materials guru and a good friend; Dr David Ingram for the Elastic Recoil Detection measurements; Dr David Hasko who kindly allowed me to use his equipment for the electrical conductivity measurements and his personal time to explain to me how microwaves work; Dr Peter Blake for sample manufacture at the National Graphene Institute; Dr Richard Langford and Eric Tapley for their training and expertise in using the FIB/SEM microscopes which were essential to my sample analysis; Franco Ussi who, despite being pulled apart by other students, always found time to advise me on my laser system setups; Chris Summerfield who manufactured the vacuum chamber; Jason Ten for his immeasurable expertise in ultrafast lasers; Sophie Fuller who was able to handle enormous amount of administrative work for equipment usage and purchase.

I would like thank Dr Andrew Cockburn, Dr Andrew Payne, Dr Francisco Orozco, Dr Nicky Sloane who gave me a warm welcome to the research group; Alexandre Diaz and Diego Punin, my cohort peers with whom I started this journey, for their friendship and support.

My final acknowledgement goes to Talia Shmool, who has encouraged me every step of the way throughout my time in Cambridge. Thank you for all your love and support. To you I dedicate this thesis.

I would also like to thank my family members and those that I have forgotten to mention here.

Contents

List of Figures.

List of Tables.

Nomenclature.

AGG	Abnormal Grain Growth
AMCS	Anode Materials Characterisation System
AES	Auger Electron Spectroscopy
CPD	Critical Point Dryer
CVD	Chemical Vapour Deposition
CW	Continuous Wave
EBSD	Electron Backscatter Diffraction
ED	Energy Density
FWHM	Full Width at Half Maximum
GB	Grain Boundaries
GBE	Grain Boundary Engineering
HAZ	Heat Affected Zone
HPM	High Power Microwave
HOPG	Highly Ordered Pyrolitic Graphite
LSM	Laser Surface Melting
LSMZ	Laser Surface Melted Zone
LIPSS	Laser-Induced Periodic Surface Structures
MVED	Microwave Vacuum Electronic Device
NC-CM	Nanostructure-Covered Conical Microstructure
OFHC	Oxygen-Free High-Conductivity
PLM	Pulsed Laser Melting
RBS	Rutherford Backscattering Spectrometry
SEE	Secondary Electron Emission
SEY	Secondary Electron Yield
SS	Stainless Steel
USAF	United States Air Force

Chapter 1

Introduction.

High power microwaves (HPM) are devices which generate electromagnetic radiation spanning the frequency range of approximately 1 GHz to 100 GHz [1]. Their applications vary from radar and communication systems to heating and current drive of plasmas in tokamaks and active denial technology for non-lethal crowd control [1]–[4].

This project focuses on the directed energy source application, exemplified today by such devices as the Magnetically Insulated Line Oscillator (MILO, 1.2 GHz at 2 GW) [1], among other reasons, due to the increasing interest in effecting electrical equipment at significant distances. It is triggered by the heavy reliance on electronic components in today's weaponry. Short bursts of high power microwave energy are lethal to electronics while having no effect on humans operating the equipment, making HPM weapons useful in a wide variety of missions, where avoiding civilian casualties is a major concern [5].

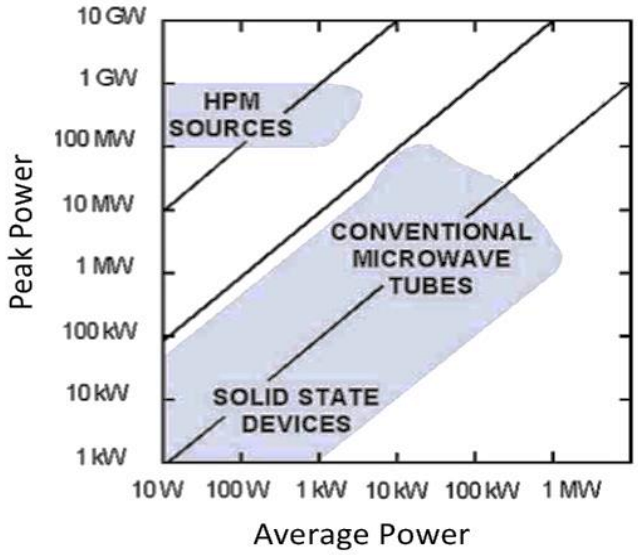

Figure 1. Power domains for microwave production. Average power entails long pulse duration, high repetition rate sources, peak power – short pulse duration, low repetition rate sources [6].

HPM devices operate in different physical regimes to conventional microwave vacuum electronic devices (MVEDs). Figure 1 illustrates this distinction, in which the device peak and average powers of standard MVEDs and HPM are compared. The fact that HPMs operate at much higher power densities than conventional MVED devices implies that they pose a unique set of technological challenges, studied in this work.

Currently, primary areas of HPM investigation are [6]:

- High current density robust cathodes.
- Novel anodes (also referred to as collectors).

Cathodes, along with the anodes are not surprisingly among the most important portions of an HPM device, as they directly affect its efficiency [3]. Recent advancements have been towards new materials for cathodes [7] and anodes [8] to lower the HPM's vacuum levels of operation. While the investigations of cathodes appear to have reached a high level of success the anode still remains underdeveloped [6].

Existing HPM anodes erode during usage [9]. The challenges lie with their significant contribution to outgassing, predominantly of hydrogen atoms and plasma formations caused by the near surface ionisation of the outgassed neutral atoms by the desorbed electrons or secondary electrons due to anode's secondary electron emission (SEE). Both of these are thermally driven phenomena generated by the electron beam (e-beam) impacting the anode's surface during HPM operation, Figure 2. All these effects reduce the vacuum in an HPM device, undermining its performance. Additionally, plasma formations can cause short circuiting, limiting the duration of microwave or radio frequency output [10].

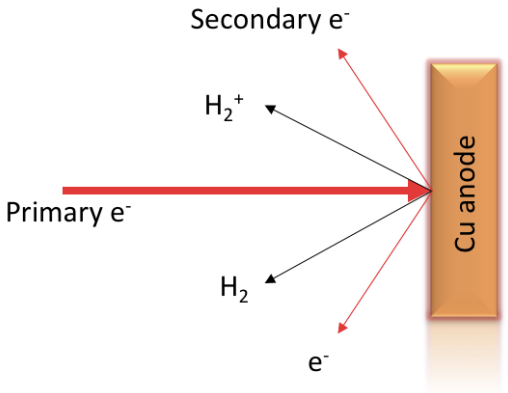

Figure 2. Electron beam impact on the surface of a copper anode.

Scope of PhD Work.

This project focuses on solving the problems of outgassing and SEE of the anode materials in HPM devices by manufacturing low outgassing and secondary electron emission substrates using laser processing from materials which would most benefit anode applications, thereby, increasing the efficiency of high power microwave devices.

Chapter 2

Literature Review and Research Questions.

In order to evaluate microwave power electronics, it is necessary to identify the anode regions and their vulnerable points. The anode regions are defined as those parts of its surface area upon which electrons impact after they have passed through the microwave interaction region of the device [6], Figure 3.

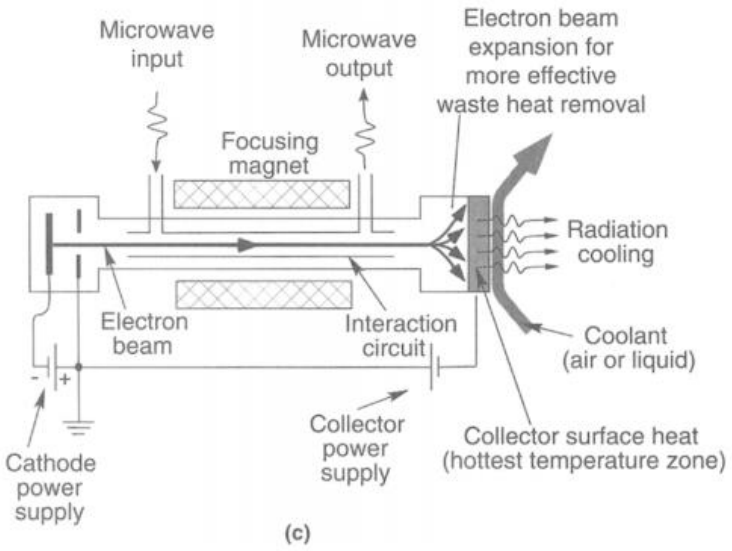

Figure 3. Typical vacuum microwave power electronic device: two–cavity klystron amplifier [6].

An example of an HPM source is a klystron amplifier, shown in Figure 3, traveling-wave tube (TWT), virtual cathode oscillator (vircator) or a magnetron [6]. The working principle is that of a vacuum tube, where the interaction of a stream of electrons with a magnetic field generates microwaves. Electrons are produced by a negatively charged, heated component (cathode) and accelerated by a positively charged component (anode) to produce a high velocity electron stream. The conversion of the kinetic energy of the electron current to coherent electromagnetic radiation experiences no energy or efficiency loss and no internal heat generation, due to the electron stream moving without collision through the evacuated region [6] - key to generating high power microwaves. However, energetic electrons incident on a conducting surface cause extensive heating, especially on anode surfaces which are constantly bombarded with electrons resulting in a pressure rise inside any microwave power electronics [6]. In HPM devices this is intensified, compared to that in lower power conventional microwave vacuum electronic devices (MVEDs) [6], leading to the problems outlined in the introduction of the report, further discussed in section 2.2.

2.1. HPM Anodes.

HPM anodes are made of high conductor materials to create a positive electrode and include stainless steel (SS), copper-tungsten (CuW), tantalum (Ta), nickel (Ni), molybdenum (Mo), and oxygen-free high-conductivity copper (OFHC Cu) [11]. The design of the anode varies from wire [9], [11] and mesh grids [9], [12] to solids [13], [14]. The anode in this work is a solid plate ~300 x 200 x 60 mm.

Hydrogen is not the only gas that is known to outgas from metal anodes under HPM e-beam bombardment [11]. Desorption gasses observed from Cu anodes include H_2, CO, and CO_2 [15]. CO and CO_2 desorption is, likewise, thermally driven. H_2 desorption yield is many magnitudes higher than CO and CO_2 desorption yields [15]. That is why, primarily, the project will be focusing on H_2 outgassing reduction in metal anodes.

2.2. Mechanisms of Anode's Outgassing.

High energy and high current HPM e-beam causes extensive heating of the anode surface leading to its thermal desorption or outgassing, predominantly of the hydrogen atoms stored in bulk materials due to their exposure to humid air [3], [6], [16]. This leads, in turn, to two effects:

1. Pressure rise.

The pressure rise in the HPM device causes it to lose vacuum and consequently reduces the electron emission, e.g. vircator pressure change after a single e-beam shot with Ta anode; 2×10^{-6} to 5×10^{-5} Torr [11].

2. Plasma formation.

Plasma formation occurs due to the primary electron impact on the surface of the anode, causing the secondary electron emission. SEE is the liberation of electrons from the material due to bombardment by a beam of charged particles [17]. The desorbed electrons ionise the outgassed neutral atoms near the anode surface, creating plasma. The resulting plasma can cause changes in the electrical impedance of the HPM device, and possibly lead to an impedance collapse or pulse-shortening [10].

All of these phenomena centre on anode material desorption mechanisms that must be controlled or eliminated in order to improve the performance of an HPM device.

In conventional MVEDs, the problem of outgassing has been solved with well-accepted and proven techniques, such as modifying the anode's geometry or creating depressed collectors in the system (distributing the beam over a larger area reduces thermal desorption and averaging the collector's voltage, relative to the ground potential of the device, forms a "depressed collector" [6]). Depressed collectors partially convert the kinetic energy of the e-beam into electrical energy rather than allowing

it to transform into thermal energy [18]. Neither of those techniques can be applied to HPM devices. Modifying the collector's geometry is not a practical solution as the overall size of the HPM device is already large. Depressed collectors can be also ruled out as in HPM devices they would require as much power as was needed to form the e-beam in the first place. Thus, a material solution, either its complete substitute or property change, appears most beneficial.

2.3. Outgassing.

Outgassing in this work refers to two processes [16], [19]

1. Diffusion of gas molecules through the bulk material.
2. Desorption of gas molecules from the surface of the material.

Metals with low hydrogen outgassing rates, such as austenitic stainless steel, are the most common materials for vacuum applications, due to low hydrogen outgassing properties [16]. To further reduce outgassing in these metals, several treatments have been proven effective: baking [19]–[23], vacuum baking [8], [11], [21], [22], [24], [25], polishing [21], [25] and surface treatments to create oxide or other protective surface films (e.g. titanium nitride or boron nitride [26]).

In HPM devices, the anode material will be exposed to high temperatures and intense electron bombardment. Thus, the anode substrate must sustain reduced outgassing predominantly at high temperatures.

2.3.1. Diffusion.

Hydrogen is present within many metals, where it exists as atomic hydrogen at defects such as grain boundaries [27]. In the first outgassing process, the diffusion rate is regulated by the size of the grain boundaries (GB). GBs are preferential sites for diffusion and also trapping of hydrogen [28]. Trapping occurs when the binding energy of a GB is larger than the activation energy of hydrogen diffusion [27]. Increasing the temperature will release hydrogen and increase the outgassing rate of the sample. This is because the GB's binding energy is temperature-dependant, it decreases with temperature rise [29]. Thus, in polycrystals at high temperatures, the hydrogen diffusion along the grain boundaries is mainly due to high energy boundaries ("Random", $\Sigma > 29$), where Σ is the reciprocal of the fraction of lattice points in the boundaries that coincide between the two adjoining grains [30] and is commonly calculated from the Brandon ($\theta \leq 15\,\Sigma^{-1/2}$) or Palumbo-Aust criteria ($\theta \leq 15\,\Sigma^{-5/6}$) [31]–[35], section 3.1.6.3. Special boundaries or low energy boundaries (between Σ 1 and Σ 29) will contain less hydrogen atoms due to their low binding energy levels and consequently reduce the overall sample's diffusion [31]–[36]. This condition approaches single crystal characteristics; the larger the grains, the less GBs are present, the lower is the coefficient of hydrogen permeability [37]. Single crystal metals cannot be used for the anode

in this work due to its dimensions, section 2.1. Therefore, special boundaries can be created in the material and used to reduce its diffusion.

A common way of generating special boundaries in metals is annealing [38]–[40]. Table 1 shows an example of a pure copper specimen annealing results in terms of the percentage of special grain boundaries achieved according to temperature and annealing time [39], the specimen is cold rolled and annealed four times.

Table 1. Special boundary fraction after annealing [39].

Temperature (°C)	Time (h)	Initial GB	2nd Annealing	4th Annealing
RT	0	0.35	0.62	0.64
700	2	0.54	0.60	0.68
	12	0.57	0.66	0.70
	36	0.65	AGG	0.69
	108	0.64	0.64	0.70
800	6	0.66	0.71	0.71
	18	0.68	AGG	0.70
900	8	AGG*	AGG	0.74

** AGG – abnormal grain growth*

It is noted that the prolonged exposure increases the percentage of the special boundaries, but can also result in abnormal grain growth (AGG), also termed as secondary recrystallisation. AGG is the growth of new grains at the expense of their neighbours, occurring at temperatures, above the recrystallisation temperature, which lowers the hardness of the bulk material [41]. To avoid AGG during annealing, the temperatures are kept below 800 °C [42].

2.3.2. Desorption.

In the second outgassing process, the outgassing is not regulated by the diffusion rate but by the rate at which the hydrogen atoms recombine into molecules at the surface of the material [27]. Smoothing out a surface will allow less segregation spaces for hydrogen atoms. The smaller the number of freely-movable hydrogen surface atoms, the less probable the recombination is [19]. A decrease in surface roughness has been shown to reduce substrate's outgassing [43]–[45], Figure 4.

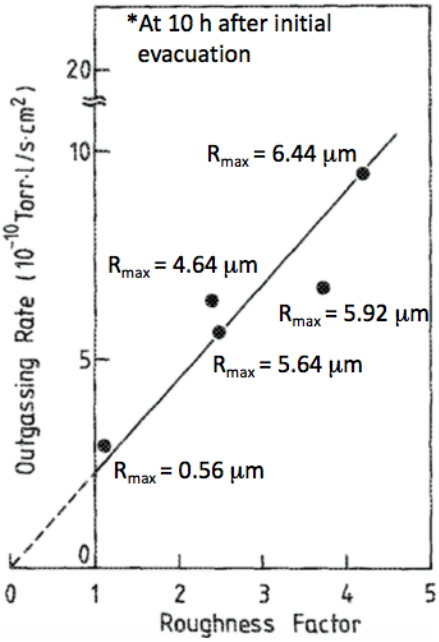

Figure 4. Outgassing rate from aluminium-alloy (A6063) as a function of surface roughness. Roughness Factor attributed to the ratio of the actual surface area to the geometrical area (modified diagram from).

However, reduced surface roughness leads to an increase in the SEE of the material, which is undesirable for the anode [46], discussed in section 2.4.1. It should be noted that at high electron dose (such as in HPM devices) only in pure metals surface roughness is the criteria that leads to changes in SEE. For other materials and alloys it is the carbon build-up [17], [47].

To have the hydrogen atoms ejected from a surface, they must first be absorbed. If adsorption can be reduced the subsequent desorption drops as well. Again, the number of adsorption sites depends on the material and its surface roughness [48], but it can also depend on the history of its environments, prompting HPM engineers to demand increased cleanness and advanced processing conditions of the anode substrates (e.g. vacuum processing).

2.4. Secondary Electron Emission.

Secondary electron emission is suppressed if the ratio of the number of secondary electrons leaving the anode's surface to the number of its incident primaries is lower than 1 or secondary electron yield (SEY) of the sample is < 1 [49]. This avoids the electron multiplication - an uncontrollable generation of free electrons in HPM devices [49].

Grain boundaries can act as natural scattering centres which attenuate the internally generated secondary electrons, caused by the e-beam bombardment, reducing the SEY of the sample. This phenomenon was studied by J. Y. W Seto in polycrystalline silicon films [50]. GBs can trap electrons due to their energy charge difference to the rest of the lattice [51]. Thus, polycrystalline metals have lower SEY than single crystal ones [52].

In the current work elimination of grain boundaries is beneficial, thus, an artificial generation of "electron trapping" sites is the solution to reduce the specimen's SEY.

2.4.1. Secondary Electron Yield and Surface Roughness Dependence.

Increased surface roughness reduces the secondary electron yield [46], [53]–[56]. This is due to the way the secondary electrons are trapped within the irregularities of the surface, demonstrated in Figure 5. For maximum SEY reduction, the surface of the sample must have enough grooves to sustain the diffraction of the secondary electrons until the energy of higher generation SE (2^{nd} and 3^{rd}) becomes too low to knock out more secondaries.

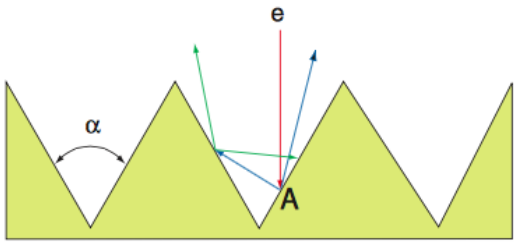

Figure 5. Triangular grooves on the surface. An initial electron (red) hits the surface at point A produces secondary electrons (blue), these are absorbed or can generate further secondary electrons (green) [57].

Three types of groove geometries have been predominantly explored in literature: triangular, rectangular and sawtooth [57]–[60]. Of these, angular grooves showed the most effective SEY reduction. Magnetic fields can be used to aid the grooves in further SEY reduction by changing orbits of secondary electrons, directing their collision [61]. In reality this does not always enhance the SEE suppression, for example, if the sawtooth surface in Figure 6 has $\alpha > 70$ °, its SEY reduction becomes independent of the magnetic field (> 0.2 Tesla produced no effect on the SEY reduction [57], [59]).

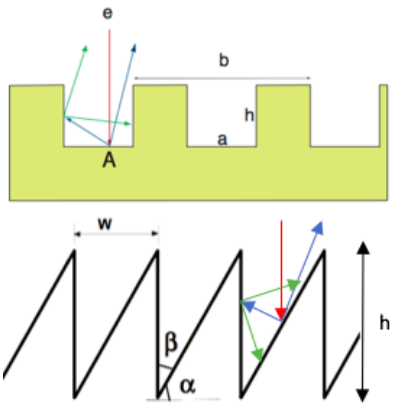

Figure 6. Top image: rectangular grooving [52], Bottom image: sawtooth grooving .

Thus, for maximising material's SEY reduction, an increased number of grooves must be generated on its surface. Other factors which can affect the grooves' SEE suppression include the e-beam incidence angle, its energy and the scale of the generated surface features. These have been studied by K. Ohya [62]. Gaussian-distribution nanogrooves of constant width of 25 nm and variable depth from 0 to 4 μm have been bombarded at normal incidence (e-beam angle to the surface 90 °) with variable energy [62]. Figure 7 shows a 2D map of the "bowl-structured" surface. The bombardment points are randomly chosen within the ranges of x ($0 \leq x \leq 4W$) and y ($0 \leq y \leq 4W$). Secondary electrons emitted from the surface are divided into zones A, B, C, D, E and F at intervals of 30 ° for calculation of angular distribution.

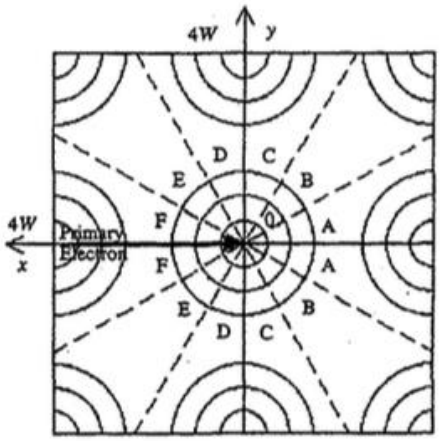

Figure 7. Model of a "bowl structure" for surface roughness [62].

The results showed that for shallow grooves the SEY becomes larger than for the flat surface at all e-beam energies due to the increased surface area. On the other hand, for deep grooves the SEY becomes smaller due to SE being trapped successfully within the neighbouring part of the groove.

It is proposed to seed the surface of HPM anodes with tall nanostructures, e.g. spikes, or deep "holes" to maximise its SEY reduction.

2.4.2. Secondary Electron Emission of Carbon-Based Materials.

Carbon-based materials have the lowest SEY in HPM devices [17], [44], [63] compared to metals. A patent exists for carbon nanotube (CNT) coated cylindrical anodes for low and high vacuum applications with reduced plasma formations and outgassing (plasma formations > 475 keV) [64]. These anodes permit "microwave and radio frequency vacuum electronics to be run with higher efficiency due to lower pumping requirements" [64]. The drawback of such C-coated anodes is that a direct e-beam bombardment will destroy them [65], additionally, they still require a substrate for deposition. Hence, the substrate material must be prepared accordingly (e. g. baked, polished) before CNT coating is applied to create an efficient anode for HPM devices. Graphene, another C-based material, could be a substrate-less C-based anode in HPM devices due to its high electrical conductivity, thermal stability, low outgassing and SEE. Substrates are not desired in graphene-based anodes as the interaction of the e-beam with it in HPM conditions can result in doping the graphene film with unwanted elements [66], [67] changing its properties. With a complete removal of the substrate the prolonged e-beam exposure of graphene degrades its properties: lattice disorder and conductivity reduction [68], [69], degrading the material into amorphous carbon. Thus, to ease the harmful effects of the electron stream, an electron-absorbing substrate with minimal doping properties could be a solution. However, this means that the shielding substrate now has the same SEE problem. It is interesting to note here that because of graphene's ultrathin thickness, it is more sensitive to low energy electrons than high energy electrons [70], as high energy electrons can pass straight through the film. This means, e-beam current regulates

the degradation of graphene sheets - at high electron voltage the higher the current, the more damaging is the electron beam. The voltage threshold for C atom ejection from the lattice is 86 keV [65].

The electron irradiation results in defect formation in both mono and bilayer graphene with I_D/I_G ratios higher in monolayer graphene due to its higher defectivity [71].

Multilayer graphene can be used to increase the anode's electrical conductivity but would this also increase its overall SEY? The SEE of multilayer graphene depends on the crystal orientation of its stacked layers. If all layers are in the Bernal configuration (AB), without twists or rotations, multilayer graphene SEE, most likely, will be the same as for a single layer. 70 % of all chemical vapour deposition (CVD) synthesised multilayer graphene is stacked in the Bernal configuration, while the rest rotated with a relative angle ranging from 4 ° to 30 ° [72]. It would be interesting to investigate by what factor the SEE is increased due to additionally introduced degrees of freedom through variations in interlayer rotation angle, Figure 8, and whether there is an optimal configuration, however, this is out of scope of the current study.

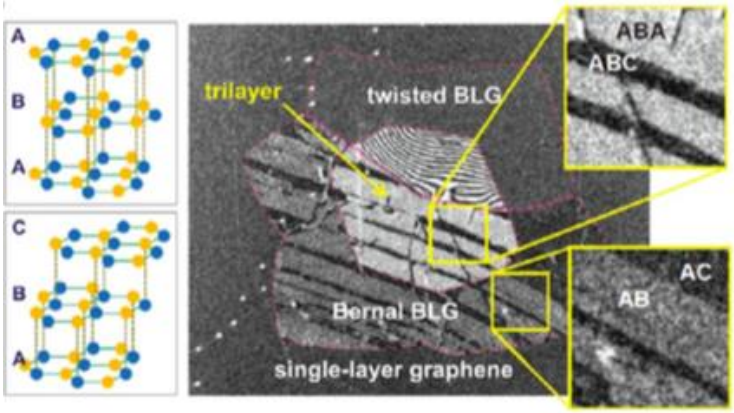

Figure 8. DF-TEM image of a CVD grown bilayer graphene (BLG), a three-layer system showing AB to AC twinning in Bernal stacked bilayer and alternating ABA/ABC regions in oriented trilayer [73].

Another C-based material, Pyrolitic Graphite, a vapour deposited form of carbon [74] or its annealed version, Highly Ordered Pyrolitic Graphite (HOPG), shows promise for HPM anode applications due to its low mass, high thermal conductivity and ultra-high vacuum properties [74]–[76]. It does not require a substrate, is readily available and it even can be structured with an ultrafast laser for periodic surface structures for further SEY reduction. However, in its pure form it exhibits insufficient electrical conductivity for HPM anode applications due to its anisotropic nature [77]. This can be solved by doping it with alkali metals [77], [78]. Electron beam and femtosecond laser irradiations [79], [80] can be used as doping techniques. Further, to reduce the outgassing of the obtained doped HOPG anode, laser annealing in sub-melt regime could be used [81] as a technique to avoid the loss of implanted dopants, however, due to the damage threshold of 130 keV [82] it is also rejected.

Summarising the discoveries in this section, CNT and graphene coatings of anodes will not be investigated further as such are deemed to be ineffective for HPM application here.

2.5. Project Targets.

This section formulates the initial research questions and proposes solutions based on the literature review of the problems discussed.

2.5.1. Research Questions.

1. **Is it possible to use laser processing to reduce the outgassing of HPM anodes?**

   Reduction of hydrogen outgassing in metals:
   - Diffusion.
   - Desorption.

2. **Can laser processing achieve < 1 secondary electron yield of HPM anodes?**

   Reduction of the metal anode's SEE via surface structuring.

2.5.2. Solutions.

2.5.2.1. Diffusion Reduction.

It was found out that it is the fraction increase of the special grain boundaries that reduces the diffusion rate of polycrystalline materials, section 2.3.1. Moreover, a processing technique that optimises the generation of low Σ value special GBs will prove most efficient. Laser surface melting (LSM) experiments in [83] showed that it is possible to enhance the percentage of low Σ value special GBs in metals. Figure 9 shows the cross-section morphology of the 304 SS sample after being processed with LSM, where the depth of the treated area is shown.

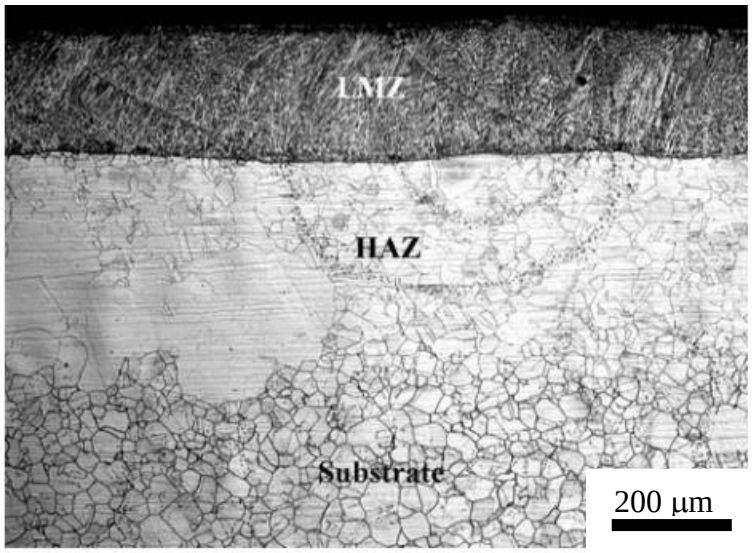

Figure 9. Macrograph of the molten pool from the longitudinal cross-section [83].

The generated grain boundary results of LSM with a 2 kW continuous wave (CW) Nd: YAG laser of the sample in Figure 9 are recorded in Table 2. It is noted that laser melted zone (LMZ) has the greatest percentage of Σ 1 boundary, a perfect crystal (no boundary [27]).

Table 2. The fraction (%) of the special boundaries after laser surface melting. Measured with orientation image microscopy (OIM) [83].

Position	Σ 1	Σ 3	Σ 9	Σ 27	Total Σ (1 – 29)
LMZ	46.0	32.7	3.3	0.4	84.1
HAZ	12.1	55.3	4.0	0.8	74.9
Substrate	12.0	34.8	4.0	0.4	57.6

It can be observed that the heat affected zone (HAZ) benefits from an increase of 17 % in special GBs which means the underlayers of the substrate are improved as well during LSM. Thus, the larger the penetration depth, the more effective the LSM technique is. Thermal annealing of the 304 SS sample in Figure 9 further enhanced the density of special GBs. But the maximum density it could reach in the laser effected region under optimal processing conditions was 88.6% (1220 K and 28 h) [83], not far from the LSM generated 84.1 %, thus showing the benefit of the LSM technique. Laser surface melting is proposed as an effective method of reducing hydrogen diffusion in metal substrates.

2.5.2.2. Laser Selection for Increased Penetration of the Laser Radiation into the Material.

Continuous wave lasers are ideal for increased laser penetration depth due to their increased dwell time on the material [83]. The average thermal penetration depth of a CW laser is between 10 μm – 80 μm compared to pulsed laser radiation which is smaller than 5 μm [84]. CW is a continuous remelting process rather than localised one, Figure 10.

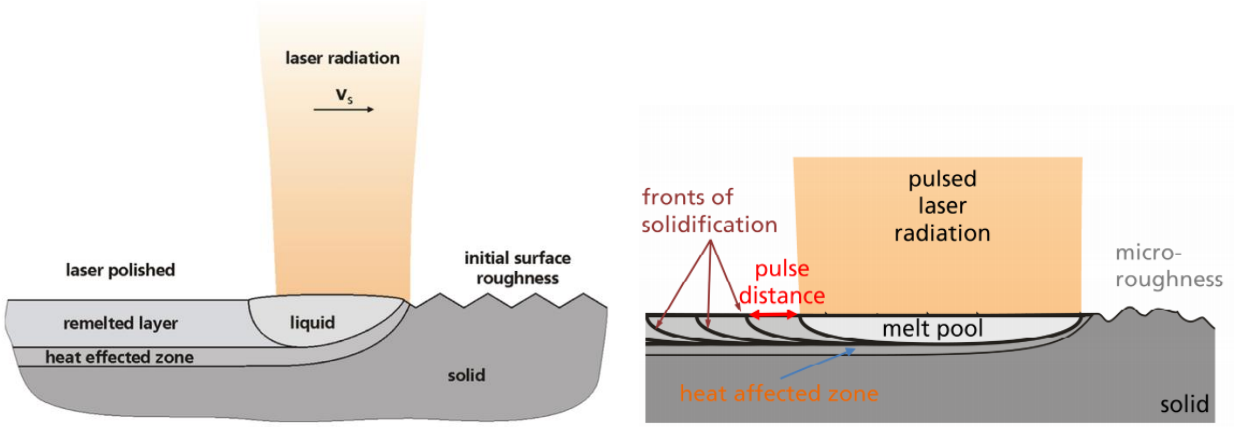

Figure 10. Laser radiation, a) continuous, b) pulsed [84].

In CW mode, the laser beam is moved over the surface with a defined scanning velocity, giving a continuous melt zone, the material is molten on one side of the melt pool and resolidified on exit. In pulsed laser melting (PLM) each pulse creates a new melt pool, which resolidifies separately from the next [84], [85]. This allows a tighter parameter control of the effects of the laser radiation, making PLM a suitable approach for reducing the surface roughness of the processed material [84].

Two surface melting regimes are available:

1. $T_{mp} \leq T < T_{vp}$
2. $T > T_{vp}$

In the first regime the temperature of material's surface is between its melting point (T_{mp}) and evaporating point (T_{vp}). Hence, melting occurs and morphology changes as a result of flow and resolidification [86]. When temperature exceeds the evaporation point, as seen in the second regime, surface peaks are evaporated and the bulk's temperature exceeds the melting point, causing flow and resolidification. In this case, the surface morphology changes with the melting depth of the bulk [86].

The choice of the regime depends on the height of the surface features. For either mechanism average laser energy density (ED) governs the process. Average laser ED represents the energy radiated per surface unit [87] and depends on four process parameters — energy distribution (FWHM of beam profile), beam power P (Watts), spot diameter D (cm) and radiation time V_f (cm per second). In CW mode the radiation time is directly controlled by the scan speed of the laser [87]:

$$ED_{Av} = \frac{P}{V_f D}\ (J/cm^2); \tag{1}$$

For PLM, average laser ED is known as laser fluence and is confined to a laser spot:

$$F = \frac{E}{A}\ (J/cm^2); \tag{2}$$

where, A is the area of the laser spot and E is the energy per pulse and is defined by:

$$E = \frac{P}{R}\ (J); \tag{3}$$

where R is the repletion rate of the laser (Hertz).

2.5.2.3. Recrystalisation with Laser Irradiation.

Recrystalisation or nucleation of the grains is the mechanism behind grain boundary engineering. For recrystalising the sample with laser radiation optimal laser ED must be identified. In this context, optimal means the average laser ED equivalent to the critical point in the temperature transformation curve during the heating process for that particular material, Figure 11. Beyond this point resolidification occurs much faster without passing through the recalescence point. Hence, the treated material ends up with homogenous or no change in its crystal structure after the LSM process.

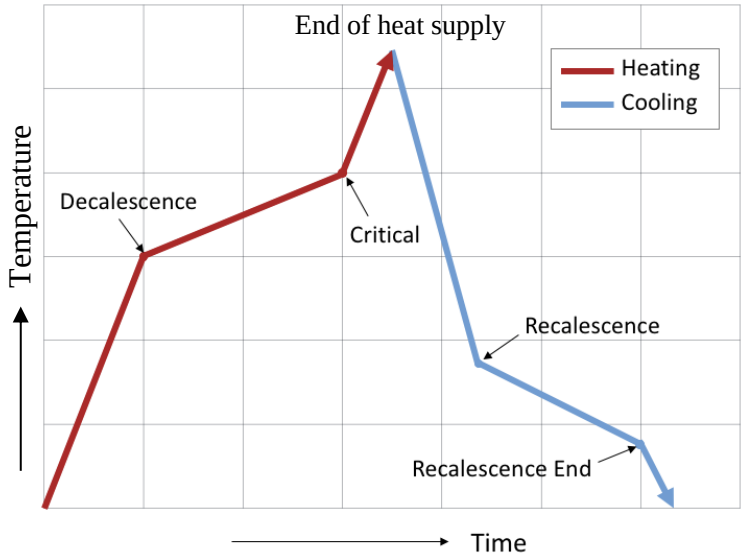

Figure 11. Transformation temperature curve [88].

- *Decalescence* – material experiences a sudden reduction in the rate of its bulk temperature increase. This reduction is due to the change in the internal crystal structure of the material [88].
- *Critical* - material fully melts resulting in no solid form to be left as a seed for recrystallisation causing elimination of spontaneous crystallised formation [88].
- *Recalescence* - a sudden spontaneous increase in the temperature of cooling resulting from an exothermic change in crystal structure. This is the critical state in the cooling process whereby the formation of crystal structure takes place [88].
- *Recalescence End* – a reduction in the cooling temperature caused by the completion of the crystal transformation.

Several researchers have investigated the effects of the heat transfer coefficient, the melt thickness and the nucleation temperature on the recrystalisation phenomenon [89]–[91]. The results show that lower

nucleation temperature and thinner melt lead to a longer recalescence time, maximising the grains laterally. Consequently, in materials with larger heat transfer coefficients this results in a weaker recalescence effect. For example, when nucleating Cu, high laser ED is needed to balance rapid dissipation of the thermal energy by its bulk.

2.5.2.4. Electrical and Thermal Conductivity Dependence on Grain Size.

Recrystallisation or grain growth is known to increase the electrical [92], [93] and thermal [94] conductivity of metals, qualities vital to the HPM anode's performance. In vircators, the anode is typically several cm in diameter, thus the heat conduction from the centre is slow and the erosion is accelerated [95]. HPM magnetrons require higher voltages and currents during operation which require high electrical conductivity electrode materials for anodes (e.g. copper, silver, platinum), comparing to standard magnetrons [96]. The LSM treatment can also be used to improve polycrystalline metal anode's conductivity.

2.5.2.5. Desorption Reduction.

For reduction of the hydrogen desorption, electropolishing has been the method of choice [21], [22], [97] for reducing the surface roughness of anode materials, it additionally creates an oxide layer which further reduces hydrogen outgassing. However, electropolishing may also introduce hydrogen and other contaminants into the surface of specimens in significant quantities during its application [97]. Electropolished components require a further bake to thoroughly outgas the surface [43]. LSM may provide a more beneficial polishing method, as it introduces less contaminants into the surface and can also create an oxide layer [98], [99].

For surface roughness reduction with lasers PLM can be applied. At high repetition rates (~7.2 MHz) with low pulse energies (~1.05 to 2.08 μJ) [100] it significantly reduces already mirror-like surfaces without any post processing, compared to electropolishing due to the technique being contactless.

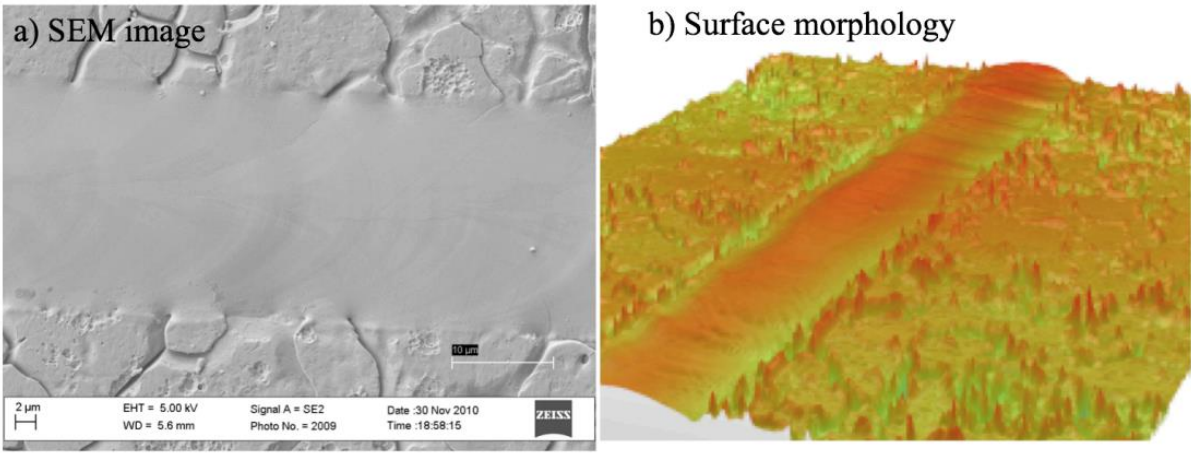

Figure 12. (a) Scanning electron microscope (SEM) and (b) interferometer images of laser irradiated 304 SS, showing treated and untreated areas and the laser line width [100].

Figure 12 shows an electron microscope image and an interferometer reading of the treated 304 SS sample with picosecond pulsed laser, wavelength 1.064 µm and pulse energy 2.08 µJ. The surface roughness R_a was reduced from ~140 nm to ~70 nm. The smoothing occurred at pulse energies between 1 µJ and 2.08 µJ. Pulse energies greater than 2.08 µJ induced residual features (ripples) into the surface morphology. These features are a geometrical effect of beam diameter on the solidification topography of the processed surface, Figure 13.

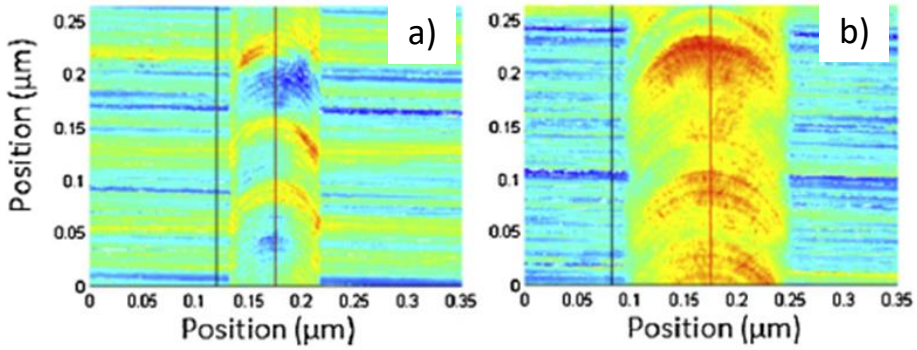

Figure 13. Laser wavelength 1.07 µm, S7 tool steel, R_a = 400 nm, a) 85 µm and b) 150 µm diameter melt pools [101].

A line scan with the 85 µm diameter melt pool, showed a significant roughness reduction (R_a = 74 ± 6 nm) with small residual features (ripples) on S7 tool steel, Figure 13(a). A 150 µm diameter line scan showed less roughness reduction (R_a = 89 ± 9 nm) due to the elevation of the centre of the laser path across the entire measurement length compared to the original surface, Figure 13(b).

The mechanism causing this effect is called the Marangoni flow. "Marangoni flow is a result of surface tension being a function of temperature and temperature gradients existing in the melt pool" [102]. Tool steel has a positive temperature gradient of surface tension, hence the melt pools created during PLM experience the highest temperatures at their centre and resolidify last. Thus, larger pool diameters prove to effectively distribute the roughness content of the whole surface more equally but, at the same time,

can produce more localised residual features due to prolonged solidification time. Monitoring the pulse energies, just like in the example of 304 SS picosecond pulsed laser melting [100] in Figure 12, should balance the distribution of the surface roughness content in the melt pools.

2.5.2.6. Secondary Electron Emission Reduction.

For maximising the SEY reduction of anodes, their surface can be densely structured to create sufficient traps for SE. Such high precision manufacturing tasks have been undertaken successfully on metals, polymers and semiconductors by the ultrafast laser systems in the form of laser-induced periodic surface structures (LIPSS) [103]–[106] and laser drilling arrays of microholes [55], [107], but never tested for their performance in reducing SEY in HPM devices. Both methods will produce deep SE traps, however, the benefit of the LIPSS method in this case can be its minimal influence on the grain structure of the treated sample.

Laser drilling is an ablation process [107] and it remains to be seen how strongly micro laser drilling will affect the microstructure and, consequently, hydrogen outgassing of the LSM treated sample, but due to low laser powers [108]; Figure 14 shows a range of laser fluence for structuring molybdenum, steel and titanium, LIPSS generation is unlikely to nucleate the grains. However, this is a direct opposite of surface requirements in vacuum tube industry (surface smoothing to reduce the outgassing of metals [109]). Consequently, it is important to conduct a study on the outgassing rates of samples, treated with either method for reduced secondary electron emission.

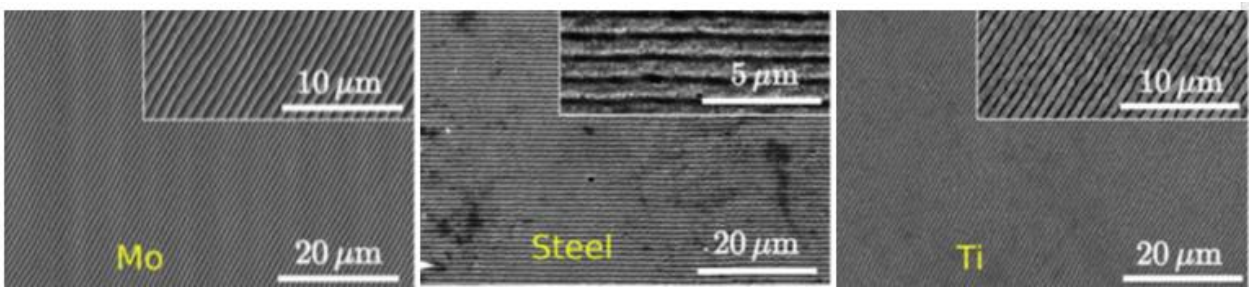

Figure 14. SEM images of LIPSS formed on molybdenum (effective pulse number N ~ 3.7, fluence F = 0.69 J/cm^2), steel (N ~ 2.1, F = 0.45 J/cm^2) and titanium (N ~ 2.1, F = 0.59 J/cm^2) [108].

2.5.2.7. Laser-Induced Periodic Surface Structures.

LIPSS are parallel oscillations perpendicular to the laser electric field [110]. The oscillation spacing Λ is approximately equal to the laser wavelength λ, however, for oblique incidence and P polarisation the oscillations become irregular and occur with some Λ given by:

$$\Lambda = \frac{\lambda}{1 \pm sin\theta}; \quad (4)$$

where θ is the incidence angle measured normal to the surface. The reason for this has not yet been determined as the formation mechanisms themselves [110]–[112]. Two types of mechanisms are largely accepted [111]:

- Inhomogeneous energy deposition just beneath the laser ablated surface - surface roughness confined to a region of height much less than the laser wavelength is responsible for the symmetry breaking [112]. The laser ED is relatively close to its ablation threshold, just before the onset of plasma formation [113].
- Capillary waves formed in the melted layer - a thin melted zone exists below the surface; oscillation spacing is formed by the high pressure plasma which produces a pressure-driven fluid motion of the molten material outwards from the centre of the laser formed crater [114].

Today tight control and better understanding of the physics of creating LIPSS allows a diverse design of surface structures with the oscillation spacing. Figure 15 shows generation of larger periodic surface structures which are called nanostructure-covered conical microstructures (NC-CMs).

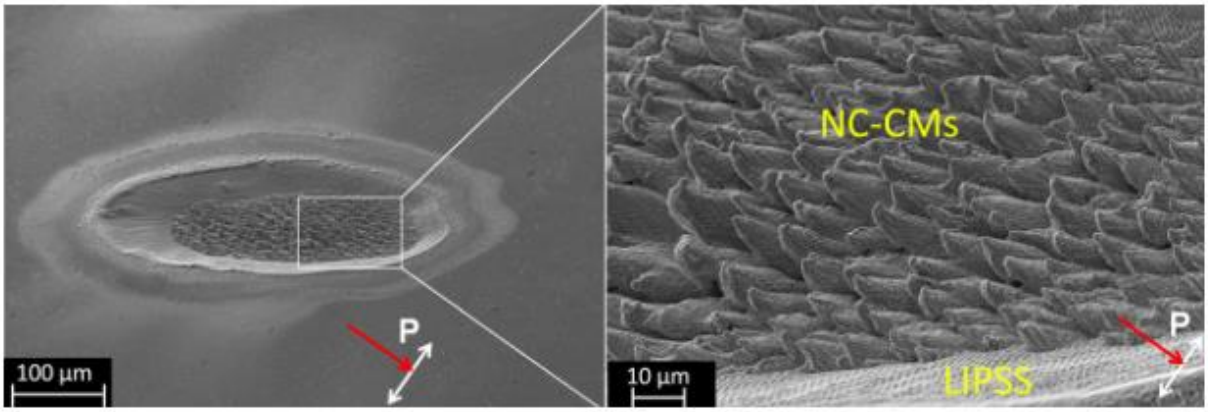

Figure 15. SEM images of LIPSS on nickel produced following 1000-pulse irradiation at an incident angle of 45 ° with P polarisation at a fluence of 0.37 J/cm^2 [106].

Higher laser fluence (at the centre of the laser spot) created larger periodic surface structures, the angle of which can be controlled via polarisation of the incident beam, Figure 15. The features are covered with a significant number of nanostructures, also at a controlled angle, Figure 16.

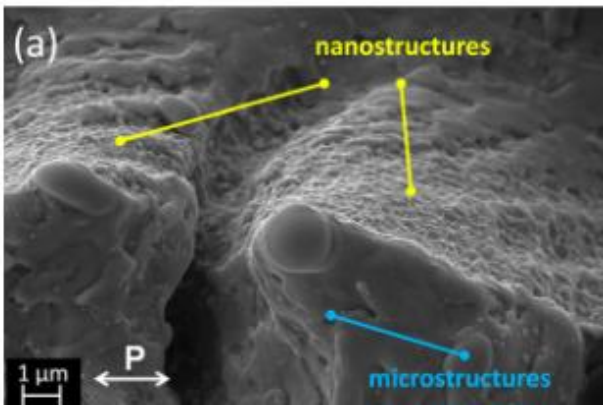

Figure 16. SEM images of NC-CMs on Ni produced at an incident angle of 45 ° with polarisations P at a fluence of 0.37 J/cm^2. The NC-CMs are viewed from the direction of the incident laser beam [106].

As discussed in section 2.4.1, angular grooving is the most effective type of patterning for trapping secondary electrons ejected from the surface at normal incidence of the e-beam. The design with nanoparticles, seeding all the surface grooves as seen here, is attractive to enhance the SE trapping effect even further. Different types of groove design can be tested for optimal SEY reduction.

2.5.2.8. Laser Drilling of Microhole Arrays.

An analytical formula has been derived to suppress the multipactor effect on the surface of metals with an array of high aspect ratio holes [115], [116]. The theoretical aspect ratio of a micro hole in metals for < 1 SEY is $A_R = 2$, where A_R is:

$$A_R = \frac{H}{D}, \tag{5}$$

where H is the height and D is the diameter a hole with packing density of $P \geq 0.7$. P is the surface porosity and is defined as the area ratio of micro-holes relative to the whole surface, namely, the micro-hole area per unit surface area:

$$P = \frac{\pi R^2}{D^2}, \tag{6}$$

where R is the hole radius and D is the distance between two adjacent holes. Therefore, the goal is to manufacture a clean entrance borehole with a minimum of 1:2 aspect ratio and packing density of ≥ 0.7.

2.5.2.9. Polarisation Criteria and Drilling Strategy in High-Aspect Ratio Hole Laser Drilling.

Linearly polarised laser beam has different absorptivities depending on the direction (S or P) [117]. Laser drilling with such beams results in linear elongation and distortion of the borehole entrance [117], [118]. To avoid these effects circular polarisation is used. Using circular polarised beams produces clear borehole entrances and exits [119]. To further improve the ripple formation inside and roundness of the

holes a workpiece rotation can be applied. The sample is then rotated with the borehole axis coinciding with the rotation axis [118], [120].

Helical drilling [121] is employed most commonly in industry for borehole laser drilling with circular polarised beam without workpiece rotation [117]. In the current experiment laser drilling will be done via dwelling the laser beam on the spot and rotating the workpiece with circular polarised beam, which in industry are called single-shot and trepanning laser drilling, respectively [120].

2.6. Conclusion.

2.6.1. Targets and Research Questions.

The research will focus on laser treatments of metals for HPM anode application. The research questions in section 2.5 are adjusted according to the findings of the Literature Review Chapter:

First Objective: Hydrogen outgassing reduction of metal anodes.

1. By what factor does LSM reduce the hydrogen outgassing of metal samples under HPM conditions?
2. Does LSM generate any abnormal grain growth?
3. How would additional PLM treatment affect the LSM treated microstructure of metals?
4. Can LSM compete with thermal annealing in its efficiency for hydrogen outgassing reduction of metals?

CW LSM technique will be investigated for fraction reduction of GBs in metals with PLM for reduction of surface adsorption/desorption sites of H atoms. The outcome of the research is laser-based hydrogen outgassing reduction technique for metals. LSM can also be used to improve metal's thermal and electrical conductivity. It is proposed to measure the electrical resistivity of the LSM treated metal samples.

Second Objective: Secondary electron emission reduction of metal anodes with pulsed laser irradiation.

1. What design of LIPSS/micro holes would maximise the SEE reduction?
2. How LIPSS/laser drilling for SE trapping micro holes would affect the microstructure of the sample, consequently its diffusion?
3. What types of groove design reduce the SEY most effectively: laser drilled micro hole array or LIPSS?

Pulsed laser irradiation is proposed for investigation for generating secondary electron traps on the surface of treated samples in the form of laser-periodic surface structures and high aspect ratio micro holes.

Chapter 3.

Methodology.

This Chapter describes the appropriate instruments, methods and a plan of work used in the study. The Chapter is divided into types of the experiments conducted with appropriate equipment and methods described. The experiments are divided into:

1. Laser surface melting.
2. Single-shot laser drilling.
3. Trepanning laser drilling and laser-induced periodic surface structuring.

3.1. Laser Surface Melting.

3.1.1. Materials.

Four types of metals were used:

- 304 SS, 3 mm and 0.6 mm thickness.
- 316 SS, 1 mm thickness.
- Polycrystalline Ni, 2 mm [122].
- Polycrystalline Ti, 2 mm thickness.
- C101 Cu, 3 mm thickness.
- OFHC Cu, 3 mm and 0.91 mm thickness.

The thickness of samples had to be < 3 mm to fit in the holder of Anode Materials Characterisation System (AMCS), section 3.1.6.7.

SS was chosen due to its low coefficient of hydrogen outgassing [123] for testing the limits of LSM technique for reduction of hydrogen outgassing in metals. The 3 mm 304 SS was chosen for increased bulk H_2 content for the analysis. The 0.6 mm 304 SS was chosen for its smaller grain size compared to 3 mm 304 SS. Two grades of SS, 304 and 316 were chosen to vary the H_2 content and microstructures for validating the LSM effects. Ni and Ti were chosen to verify the LSM-caused microstructural transformations. OFHC Cu was chosen due to its wide use in HMP devices and C101 to vary the grain size of Cu samples.

3.1.2. Laser Systems.

For low power LSM experiments, SPI G3 Yb non-polarised fibre laser, wavelength 1.064 μm, an output beam $M^2 < 2$ and maximum output power of 20 W in CW mode [124] was selected, as it is the closest

available system to the grain engineering experiments in [83], section 2.5.2.1. For copper treatments, a linearly polarised CW Coherent Verdi G20 solid-state laser, wavelength 532 nm, an output beam $M^2 < 1.1$, maximum output power of 20 W and raw beam dimeter of 2.25 mm was used. An SPI SP200C CW non-polarised fibre laser, 200 W, 1075 nm, M2 < 1.2 was used for high power CW laser surface melting. The lens for both systems wavelength of 1.064 was a JENOPTICTM fused silica collimating lens, with focal length (FL) of 125 mm. For wavelength of 532 nm, a Comar lens, 25 OP 05, FL 25 mm, was used.

3.1.3. Sample Cutting and Cleaning Techniques for Laser Processing.

A Struers™ Secotom-10 precision cut-off machine is used to cut the samples, Table 3.

Table 3. Chosen parameters for cutting with Struers™ Secotom-10.

Material	Thickness (mm)	Feed rate (mm/s)	Spindle (rpm)	Disc Type (HV)
304 SS	3 & 0.6	0.2	2200	HV > 500
316 SS	1	0.2	2200	HV > 500
Ni and Ti	2	0.35	2200	HV < 500
C101 Cu	3	0.25	2200	HV < 500
OFHC Cu	3	0.25	2200	HV < 500

Ethanol was used to clean/remove contaminants from the sample's surface prior to laser processing, in accordance with [83]. The saw was used to section 304SS for laser penetration depth measurements in section 4.1.3.

3.1.4. Power Measurements.

Figure 17 shows the power measurements for SPI G3, SPI SP200C and Coherent Verdi G20 CW fibre lasers performed with Coherent™ 100XL sensor (max beam power 100 W, max power density 6 kW/cm^2) and Fieldmaster GS power meter. For SPI SP200C laser, the results were interpolated to estimate the maximum output power. The measurements showed a linear reduction ($R^2 = 0.99$) in the beam power for both laser systems past the Nutfield 2–axis scan head and 125 mm focal length lens. Maximum output power for SPI G3 was 17 W and 159 W for SPI SP200C.

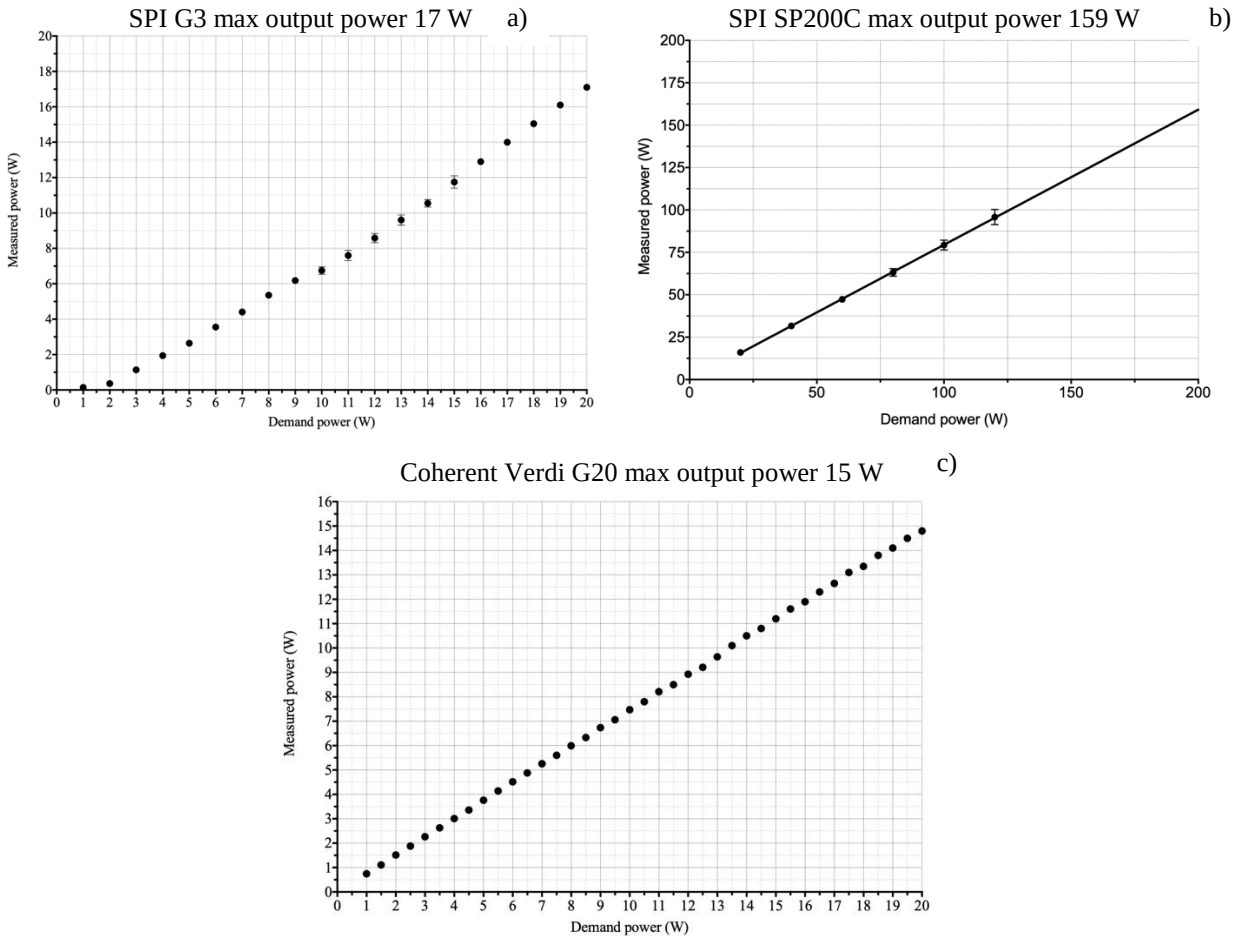

Figure 17. Power measurements for a) SPI G3, b) SPI SP200C and c) Coherent Verdi G20 CW fibre lasers.

3.1.5. Laser Setup. Temperature and Oxygen Measurements.

Figure 18 shows the LSM experimental setup. An isolator is present to prevent back reflection into the laser. The beam expander telescope (BET) produces an input beam of 4.3 mm in diameter, directed by the XY-axis scan head, Nutfield XLR8. The isolator, BET and scan head is a mobile assembly on the Z-axis. The nitrogen supply was a nitrogen tank with a pressure gauge to monitor the output N_2 pressure. The sample stage is static with a transparent plastic cap to maintain the 0.1 – 0.2 % oxidation levels.

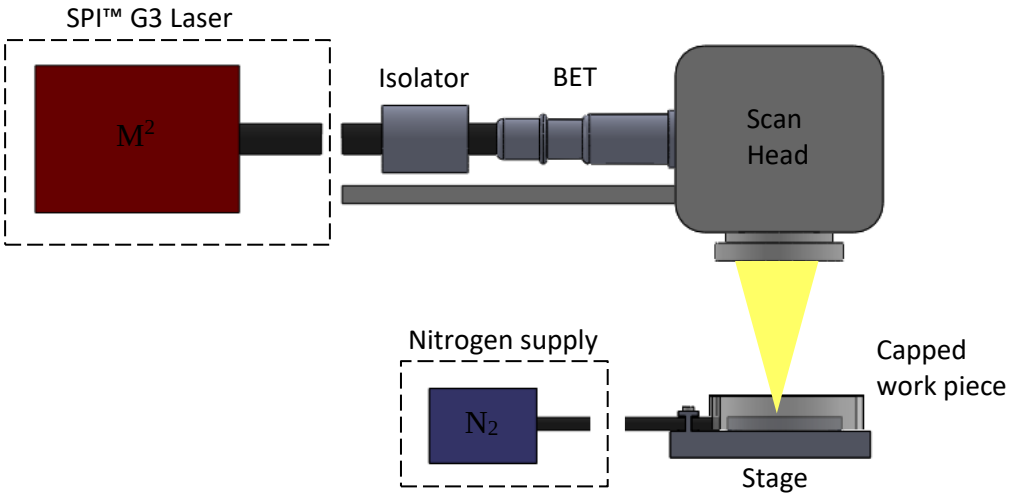

Figure 18. Laser processing workstation showing the SPI™ G3 Yb fibre laser, Isolator, beam expander telescope (BET), nitrogen supply and sample stage.

300 K was chosen as the optimal processing temperature, according to the previous laser melting [70] experiments [83]. A continuous flow of nitrogen at 0.84 l/min was supplied into the capped stage to minimise the sample's oxidation during LSM. Greisenger™ oxygen meter was used to track the oxygen levels to 0.1 – 0.2 %.

A vacuum chamber has been designed to laser process Ni samples at high average ED with SPI SP200C CW laser, maintaining 0.1 – 0.2 % oxidation levels. The CAD drawings are available in Appendix A. The laser power reduction through the AR coated glass, UQG optics WAS-153, is 10 %. Cu processing was conducted in a stainless steel vacuum chamber (CAD drawings in Appendix A) at a 14.37 degree angle with respect to normal, Figure 19, to prevent unwanted feedback from processed samples to Coherent Verdi G20 laser as the system did not have an isolator. The laser power reduction through the AR coated glass, UQG optics WAS-503, was 10 %.

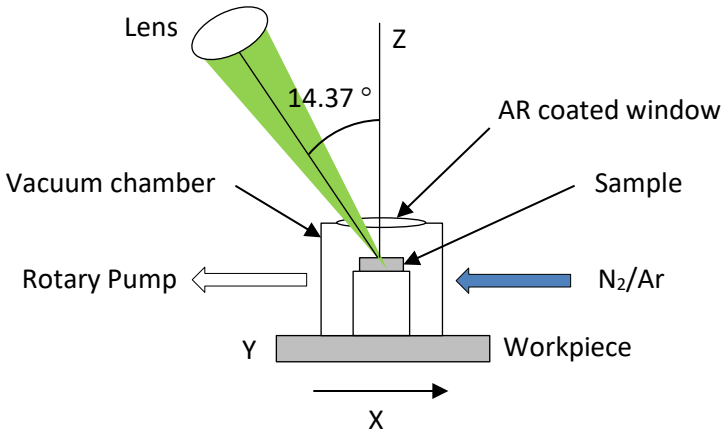

Figure 19. Schematics of the lens and vacuum chamber setup for Cu processing.

3.1.5.1. Titanium Coating of Copper in Ion Beam Sputterer.

For processing Cu with SP200C CW laser, the samples were titanium coated with an RF magnetron sputtering system, CCR Technology GmbH, base pressure of $\sim 10^{-6}$ mbar. The Ti target was a 100 mm disk, 99.9 % purity. The Ti layer deposited thickness was 100 nm.

3.1.6. Analysing Techniques.

3.1.6.1. Microscopy and Measuring Techniques.

Feature measurements of the samples were performed on the optical images acquired with Olympus BX51 optical microscope with JENOPTIC™ ProgRes $C10^{+}$ CCD camera. Differential interference contrast (DIC) microscopy was performed on Olympus™ BX51M. Higher resolution features were imaged using FEI/Philips™ XL30 FEG ESEM and below 50 µm with FEI Helios NanoLab™ 650 DualBeam™ scanning electron microscopes (SEM).

A Veeco™ NT3300 white light interferometer was used for surface roughness measurements. The samples were measured at room temperature repeatedly along the laser tracks. Phase shifting interferometry (PSI) regime was used for $R_a < 160$ nm and vertical shifting interferometry (VSI) for $R_a > 160$ nm. Modulation threshold was set accordingly: smooth samples 10 %, rough < 4 %.

For measuring the electrical conductivity, the microwave source Agilent Technologies, E8257D, 250-50 GHz, was used. The sweeping frequency range was chosen according to the circuit length, 1 m, and was 2.25 - 3 GHz with a constant amplitude of 10 dBm. Effectively, the microwaves were reflected from the sample into the power meter, KEITHLEY 236 Source Measure Unit, 100 nA, 10 V, which converted the signal into voltage. Figure 20 shows the circuit setup. The microwave probe had the inner diameter of ~ 1 mm and outer diameter of ~ 2 mm, establishing a sampling area of ~ 0.79 mm^2. Figure 20(b) illustrates the direction of the microwave signal and all the modules used in the circuit.

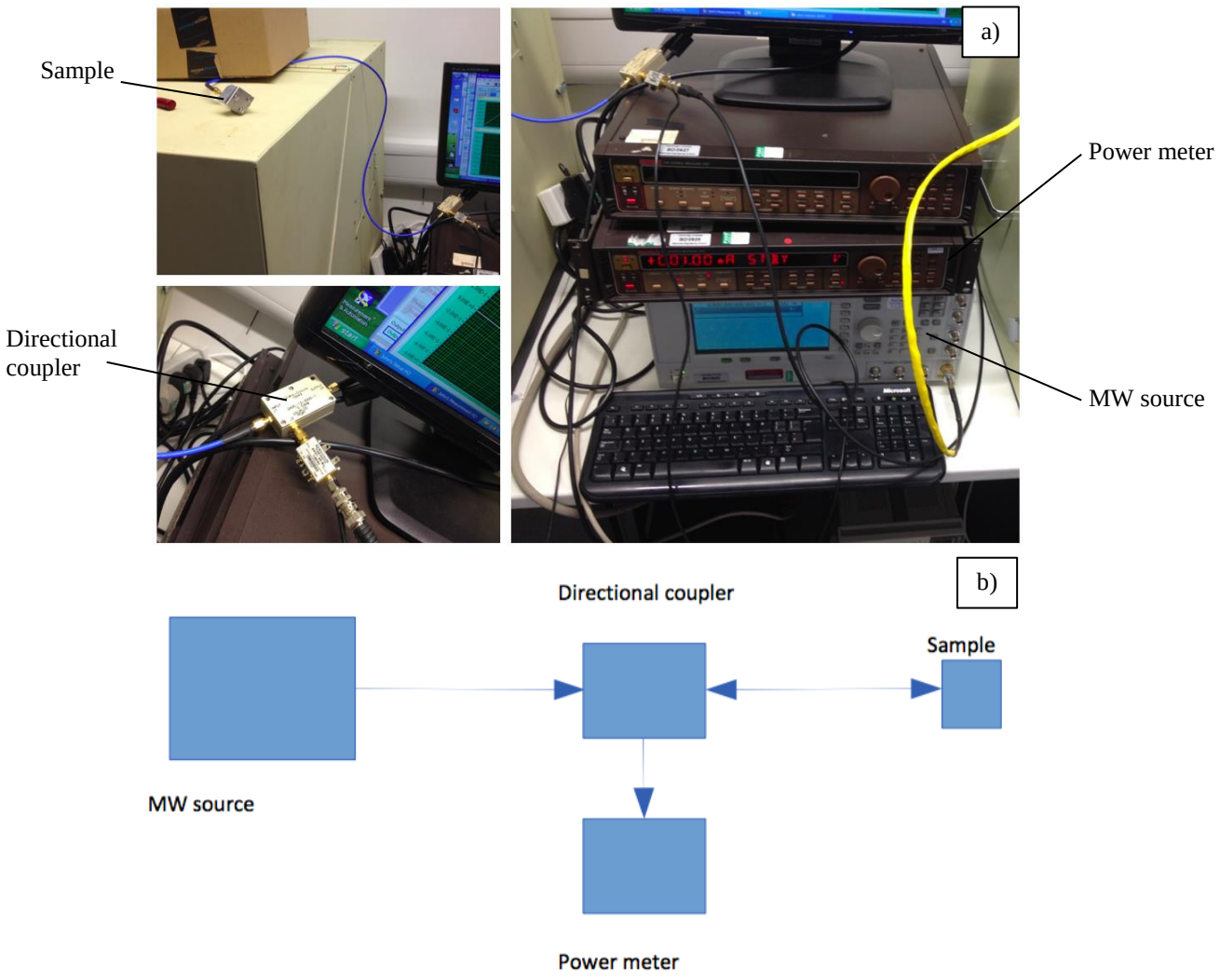

Figure 20. a) Photos of the MW circuit equipment, b) schematic of the circuit.

3.1.6.2. Microstructure Characterisation.

For fast microstructural imaging FEI Quanta 3D focused ion beam (FIB) and for < 100 µm features FEI Helios NanoLab™ 650 DualBeam™ FIB were used. FIB is a rapid grain imaging technique without any external surface preparation (~5 minutes to image 500 x 500 µm area). The grain orientation contrast is caused by the depth of penetration of the channelled incident ions, which varies with the relative angle between the ion beam and the lattice plane and the interplanar spacing of the lattice [125].

For characterising the grains and grain boundaries, an SEM with a capability of orientation image microscopy (OIM) was used to quantify the grains and analyse the percentage of special grain boundaries generated in the sample. FEI/Philips™ XL30 FEG ESEM and FEI Helios NanoLab™ 650 DualBeam™ with Electron Backscatter Diffraction (EBSD) analysis capability were selected as the microstructure characterisation tools.

3.1.6.3. Electron Backscatter Diffraction.

EBSD is a measurement and characterisation technique of grain structures for quantitative metallography [126]. Individual GBs are identified by a misorientation angle, misorientation axis and the orientation of the GB plane [30]. For certain angles and axes of misorientation two grains can hold a number of common lattice sites [35]. The ratio of the number of common lattice sites (CSL) to the lattice sites of a single grain of that boundary in its plane is denoted as Σ [127]. The Σ value is computed for each misorientation angle-axis pair and spans values from Σ 1 – 49 [127]. The Σ 1 grain boundary is a single grain with no boundary condition, therefore for the EBSD system this means a selection of all pixels on the solid grains in the acquired image. This is disruptive for the rest of Σ value boundaries and thus is not included in the current analysis. Two criteria exist to classify the special GBs:

- Brandon ($\theta \leq 15\ \Sigma^{-1/2}$),
- Palumbo-Aust ($\theta \leq 15\ \Sigma^{-5/6}$),

where θ is the maximum deviation angle from the computed misorientation angle of the GB [128], [129]. Brandon is applied for classifying special GBs in materials with intergranular degradation (i.e., corrosion, cracking, cavitation) and more restrictive Palumbo-Aust used for the rest [130]. Palumbo-Aust is chosen as the main criterion in this work due to the lack of degradation in the tested materials.

Visual representation of the grains is generated by the EBSD software in a form of the Euler maps through Miller indices [131]. A combined 3 angle Euler map or orientation map normal to the detector will be used for a 3-dimensional representation of the samples' crystal lattices in this work.

To minimise the errors during measurement, the sampling area is required to facilitate a large amount of grains. This way, all of the errors will be minimised to the largest clusters (a connected path of boundaries, which can span many grains) [132].

All the measurements were performed according to EBSD ASTM standard E 2627 [133], Table 4.

Table 4. Parameters specified by E 2627 [133].

Points per grain	> 100
Cleanup	< 10 % of points modified
Total number of grains	> 500

3.1.6.4. Sample Preparation for Electron Backscatter Diffraction.

EBSD is a surface technique with the diffraction pattern signal coming from the top few nanometres of the surface layer. The diffraction pattern or electron backscatter pattern (EBSP) comes from individual grains, thus allowing characterisations of each grain in the crystal structure of the material [134]. EBSP consists of symmetrically arranged bands or Kikuchi bands – diffraction patterns produced by

backscattered electrons from a crystalline sample [135]. Therefore, the sample surface must be crystalline for identifying successfully the Kikuchi bands. This means that the sample's surface must be free of any plastic deformation. Any damage to the crystal lattice in the surface layer will worsen the EBSP or prevent it altogether. As well as that, the surface must be clean and free from external particles, due to imaging at a high tilt angle (70 °) - external particles can cause shadowing and obstruct the EBSP acquisition.

EBSD sample surfaces acquired must have the mean angle deviation (MAD) value of < 0.4 for reliable EBSD measurement (measured with the EBSD software). Then, it can be concluded that the specimen preparation is adequate.

Several methods are applied to sample preparation for EBSD. The following methods are chosen in this work for SS and Ni specimens:

Mechanical polishing with ATM Saphir™ 550 - to remove the internal stresses caused by the mechanical cutting, section 3.1.3.

1. Mounting:
   Metal samples are hot mounted (< 473 K) in acrylic resin with iron filler for mechanical grinding [136] and later imaging with an SEM.
2. Mechanical polishing:
   Polishing is performed on a planocloths with self-lubricating diamond suspensions 9, 3, 1 μm in descending order. Each cycle lasts till the scratches of the previous particle size disappear.
   Polishing with colloidal silica 0.04 μm solution on a chemcloth is applied to reduce the size of the scratches further and expose the crystalline structure of the specimen.
3. Vibratory polishing.
   This ensures the removal of the plastic deformation layer and the oxide layer on the surface, exposing the microstructure. The specimens are submerged in colloidal silica 0.04 μm and vibrated on a chemcloth till < 0.4 MAD is achieved.
4. Ultrasound cleaning.
   The specimens are cleaned from the colloidal silica in acetone via ultrasonic bath.

Once the samples are prepared they start to deteriorate in the ambient air. An oxide layer forms on the surface that undermines EBSP identification. To prevent this, the samples were stored in the SEM chamber.

3.1.6.5. Etching.

Chemical etching is used to see the laser penetration depth into the material and estimate the area and step size for EBSD scanning, hence, parameter selection of the microstructural characterisation for the EBSD. Chemical composition of the etchants is recorded in Table 5.

Table 5. Etchant composition [137].

For 304 & 316 SS	For Ni
10 g $FeCl_3$	20 g $CuSO_4$
30 ml HCl	50 mL H_2SO_4
120 water	100 HCI
	100 water

3.1.6.6. Sample Preparation for Etching.

Chemical etching requires a similar preparation to EBSD to obtain the crystalline structure of the surface. The etched surface should be free of any damages (e.g. scratches), as those will etch deeper into the material and distort its microstructure. The preparation from section 3.1.6.4 is repeated omitting step 3.

3.1.6.7. Sample Analysis at US Air Force Research Laboratory and Ohio State University.

The laser processed SS specimens were tested at US Air Force research laboratory with Auger Electron Spectroscopy (AES) for chemical composition and electron beam bombardment for outgassing and secondary electron emission.

The electron beam bombardment was done in Anode Materials Characterisation System (AMCS), Figure 21. The electron gun operates in CW and pulsed modes. Residual Gas Analyser (RGA), a mass spectrometer, is built into the chamber and is used for characterisation of the outgassed elements from the anode. Outgassing characterisation was carried out by bombarding the samples at normal incidence with the focused output of a 50 keV electron beam to simulate the HPM anode operational conditions with a spot size of 1.6 mm in diameter (determined by measuring the size of a hole formed in a thin Ni foil under the conditions identical to those used for the present work) with 60 s duration current pulse, and recording the time evolution during the pulse of the H_2 signal with a residual gas analyser situated 45 degrees from the surface normal. The electron current density at the sample surface was approximately 16.4 mA/cm^2, and the base pressure was 5 x 10^{-10} Torr. E-beam trajectory simulations were conducted via Monte Carlo simulations.

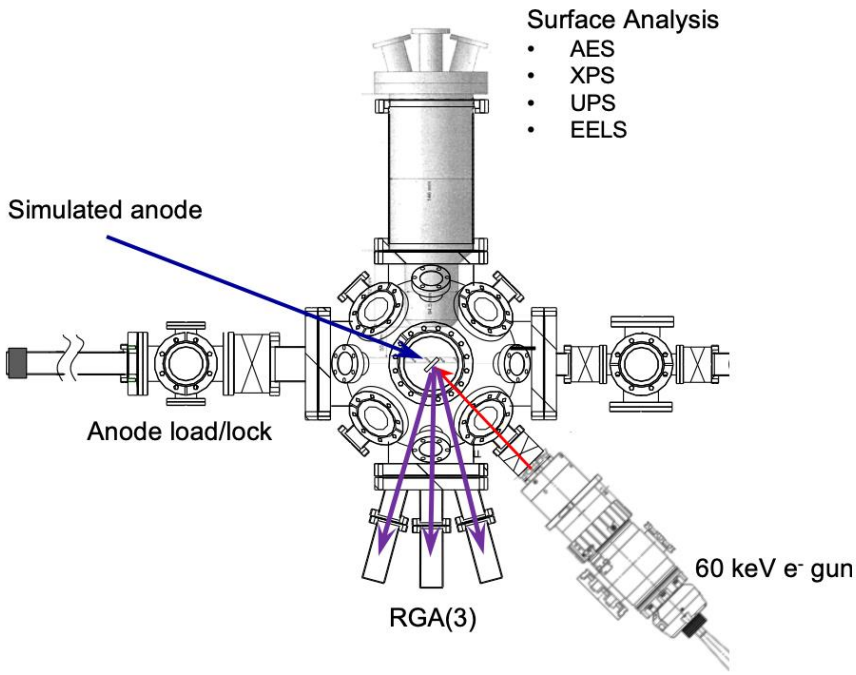

Figure 21. Anode Materials Characterisation System schematic.

Elastic Recoil Detection (ERD) analysis at Ohio State University was used to map the hydrogen concentration profile in the surface layer of the untreated and treated SS. ERD is typically used to determine the composition of materials by measuring the backscattering (energy distribution and yield at a given angle) of high energy (MeV) ions (i.e., He2+) striking the surface of the sample. The backscattering cross section for each element is known, therefore it is possible to measure the compositional depth profile from the RBS spectrum. The measurable depth is 1 – 4 μm max. The measurements were done at 75 degrees incidence to the sample, 15 degrees to the beam. The spot size was 1 mm wide 2 mm high. The beam energy was 3.05 MeV, < 1 μm surface depth.

3.2. Single-Shot Laser Drilling.

3.2.1. Materials.

Single-shot laser drilling was conducted on 304 SS, 3 mm thick. 304SS was selected as it can be delivered as a finished product – H_2 outgassing and SEE reduced HPM anode. Before laser processing to avoid tilts and highlight the drilling results, the sample was mechanically polished to R_a of 14.81 nm according to section 3.1.6.4, excluding step 3.

3.2.2. Laser System.

The single-shot laser drilling was conducted according to [138], [139], [140] with COHERENT™ Talisker Ultra linearly polarised fibre laser, 1064 nm, < 15 ps pulse duration, $M^2 < 1.3$ and maximum output power of 16 W. The objective used was LMH-20X-1064 with 10 mm focal length. All laser drilling experiments were conducted in focus with the spot size of 8.8 μm in diameter in ambient air at 300 K in accordance with [141]. A $\lambda/4$ wave plate for 1030 nm was used to achieve circular polarisation in accordance with section 2.5.2.9. No lens shielding gas and debris-cleaning agent for the sample's surface was used. The dwell time was < 3 seconds to minimise the drilling time.

The laser was focused via XYZ workpiece motion achieved using a 5-axis Aerotech A3200 Npaq stage, pattern programming via G-code (available in Appendix B).

3.2.3. Microscopy and Measuring Techniques.

Feature measurements of the samples were performed on the optical images acquired with Olympus BX51 optical microscope and FEI/Philips™ XL30 FEG ESEM for < 50 μm resolution features.

A Veeco™ NT3300 white light interferometer was used for hole depth and surface roughness measurements. Vertical shifting interferometry was used with 0.1 % modulation threshold for depth profiling.

3.3. Trepanning Laser Drilling and Laser-Induced Periodic Surface Structuring.

3.3.1. Materials.

304 SS, 3 mm, surface Ra of 14.81 nm was used for trepanning laser drilling and 304 SS, 0.6 mm, Ra of ~260 nm, for LIPSS generation. After drilling the samples were cleaned in ultrasonic bath in acetone for 30 minutes to remove the drilling debris.

3.3.2. Laser System.

The trepanning laser drilling experiments have been conducted with Amplitude Systèmes Satsuma linearly polarised fibre laser, 1030 nm, > 300 fs pulse duration, $M^2 < 1.1$ and maximum output power of 5 W, raw beam diameter of 4.4 mm with 12.7 mm FL lens, effective spot diameter 4.1 μm. The experiments were conducted in ambient air at 300 K with a $\lambda/4$ wave plate for 1030 nm for circular

polarisation. N_2 was used as the lens shielding gas only during manufacturing of the SEE reduction samples for testing in AMCS. The laser was focused on the substrate via 3-axis Aerotech A3200 Npaq stage. The number of pulses was controlled with a pulse synchronized output of the laser. The laser setup is illustrated in Figure 22.

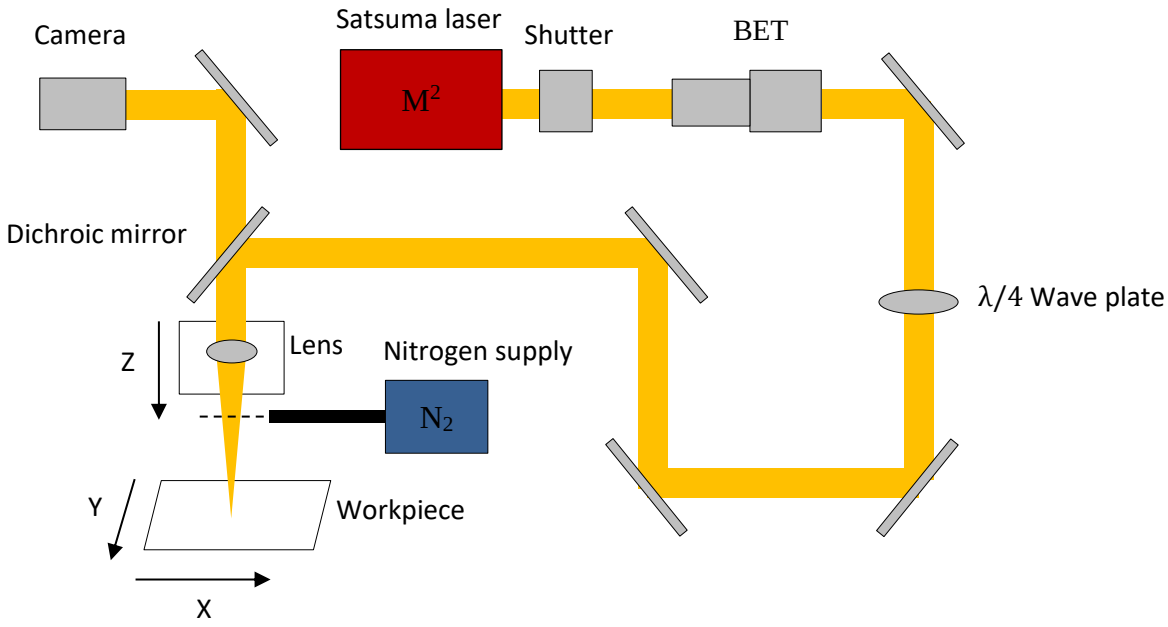

Figure 22. Schematic of the experimental setup showing the Satsuma ultrafast laser, mechanical shutter, beam expander telescope (BET), $\lambda/4$ wave plate, dichroic mirror for inline beam monitoring, camera, focusing lens, 3-axis motion stage and nitrogen supply.

The pulse duration and laser power were measured using an APE PulseCheck autocorrelator and Coherent LM-3 power meter, respectively.

For LIPSS, Satsuma femtosecond laser system with 12.7 mm FL lens, 4.1 µm spot diameter, Figure 22, was once again utilised due to similarity to the system in [106], section 2.5.2.7. LIPSS experiments were conducted in ambient air at 300 K, in accordance with [87].

The G-code for the XYZ motion pattern programming for hole drilling and LIPSS patterning is available in Appendix C.

3.3.3. Microscopy and Measuring Techniques.

Hole measurement was performed with FEI Helios NanoLab™ 650 DualBeam™ SEM.
LIPSS measurements were done with FEI/Philips™ XL30 FEG ESEM.
A Veeco™ NT3300 white light interferometer was used for surface roughness measurements.

For measuring high aspect ratio holes, FIB sectioning and SEM cross-sectional measurement was applied. Mechanical sectioning of the laser drilled holes was also used. The cross-sectioned samples were polished according to section 3.1.6.4, step 1 and 2, and the images were taken with Olympus BX51 optical microscope.

AMCS was used to measure the SEE of the laser drilled and LIPSS samples. Electron backscattering detector (BSD) is used to measure the SEY of the anode and image its position in the AMCS chamber. For SEE testing, 1 - 5 keV e-beam was used as the maximum material SEY occurs at 100 - 400 eV [53], [54], [142]. The e-beam spot size was kept constant at 1.6 mm in diameter, as for the outgassing testing in section 3.1.6.7.

Auger electron spectroscopy was used to determine the chemical composition of the surface layer of samples.

Chapter 4

Results and Discussion.

This Chapter describes the results obtained from the CW and pulsed laser irradiation tests in order to verify the efficiency of the LSM method for outgassing improvement in SS and laser surface structuring tests for SEY reduction of metals. The discoveries branched-off into separate in-depth grain engineering studies.

The Chapter is divided into three parts:

1. LSM treatment of 304SS for hydrogen outgassing reduction.
2. Photonic metallurgy. Grain engineering and its theory.
3. Laser surface structuring of metals for SEY reduction.

Part 1. LSM Treatment of 304SS for Hydrogen Outgassing Reduction.

The section explains the motivation behind the chosen experimental plan, records results and draws conclusions to answer the first objective of the work. It consists of:

- Single pass and line overlap optimisation – for large area sample generation.
- Hydrogen outgassing testing – rationale behind sample selection for the study and hydrogen outgassing measurements.
    - Surface and laser penetration depth study.
    - Microstructural analysis.
    - AMCS testing, higher laser ED sample generation.
    - Elastic recoil detection analysis.
    - Continuous e-beam AMCS testing.
    - Post-e-beam microstructural study.
    - AMCS e-beam Monte Carlo simulations.

4.1. Experimental Plan and Motivation.

The initial parameters were chosen according to [83], where using Equation 1, the maximum and minimum *ED* for CW laser with wavelength of 1.064 μm, were:

$$ED_{min} = \frac{(6000 * 721)/1000}{(3 * 50 * 60)} = 0.5\ (kJ/cm^2)$$

$$ED_{max} = \frac{(6000 * 1415)/1000}{(3 * 5 * 60)} = 9.43\ (kJ/cm^2)$$

Where the lowest power, 721 W, and highest scanning speed, 50 mm/s, produced the lowest *ED* and the highest power, 1415 W, and lowest scanning speed, 5 mm/s, produced the highest *ED* in the experiment in [83]. A range of processing parameters was tested, *EDs* between 0.04 - 21.57 kJ/cm^2 to increase the parameter sweep (see Appendix D for optical microscope images).

The SPI™ G3 laser was the closest laser choice available to [83] in terms of its specifications. Therefore, due to high probability of successful diffusion reduction of the material via grain boundary engineering, the parameters from [83] are optimised for desorption reduction capability, reduction of sample's roughness, while preparing the specimens for the AMCS testing. First, single pass optimisation is used to identify the laser energy densities with maximum roughness reduction. Next, optimal line overlap is determined to pattern an area of 12 x 12 mm (requested sample size for AMCS's sample holder).

4.1.1. Single Pass Optimisation.

The goal of the single-pass optimisation experiment is to determine the scan speed-power relationship of the laser to produce single line melts with the lowest roughness. The line width is recorded for the line overlap for large area processing. The tests were done in-focus with a minimum beam diameter calculated to be:

$$d_{\min} = \frac{4M^2 f\lambda}{\pi D} = 0.0394\ (mm);\ d_{\min} = 39.4\ (\mu m) \quad (7)$$

The formula is used from [143]. The laser processing parameters are recorded in Table 6.

Table 6. Laser processing parameters for single pass optimisation.

Scanning velocity (mm/s)	2 - 1000
Output power (W)	17
N_2 Shielding gas (l/min)	0.84

Figure 23 demonstrates the relationship between surface roughness/laser energy density and line width. For reference, conventional fabrication processes (milling, turning and grinding) create surfaces with Ra > 0.4 μm [144]. R_a of 75 nm is possible with CW laser polishing on 304SS [145].

Twenty-three lines were generated with *ED* ranging from 0.04 to 21.57 to kJ/cm^2. The different *ED* values were achieved by varying the scan speed of the laser keeping the power constant, making the endothermic reaction responsible for the line width increase. The table recording the scan speed vs ED is available in Appendix D.

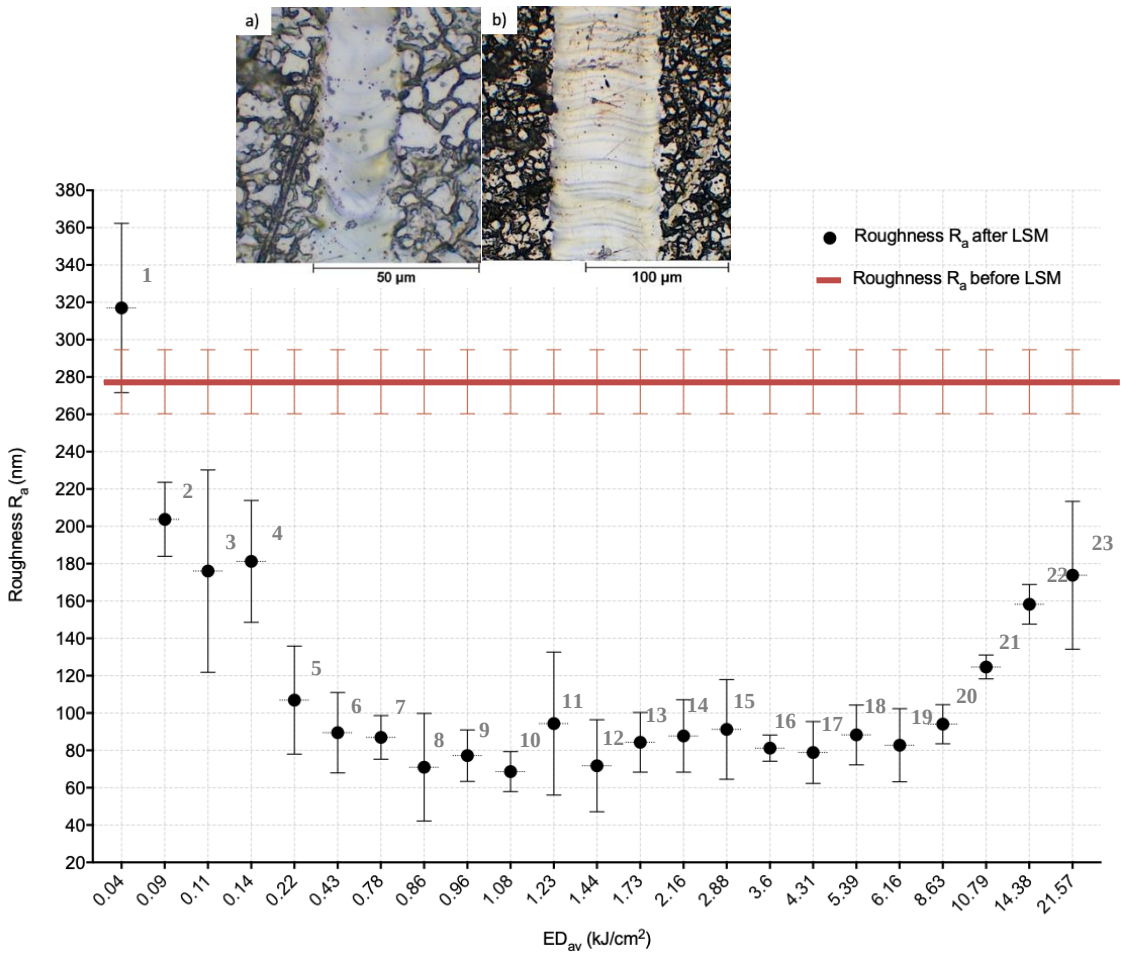

Line No.	Line width (µm)
1	24.25
2	32.91
3	35.31
4	38.61
5	42.32
6	51.22
7	52.48
8	53.77
9	54.07
10	54.56
11	54.93
12	55.58
13	55.99
14	57.21
15	57.94
16	61.38
17	62.39
18	63.51
19	64.41
20	66.50
21	70.05
22	71.78
23	76.30

Figure 23. 304SS roughness reduction vs. average laser energy with SPI™ G3 laser surface melting. a) Optical microscope image of the 304SS surface laser treated with line 1 and b) line 23 parameters.

The roughness increase at high *ED* is caused by the formation of ripples, Marangoni flow, Figure 23(b), and at low *ED* by insufficient melt, Figure 23(a). The maximum roughness reduction was recorded in lines 6 to 20, which corresponds to the experimental results in [83], *ED* between ~0.5 and 9.43 kJ/cm^2, thus satisfying the first optimisation condition. Knowing the relationship between the scan speed and laser power in terms of surface roughness and width for each line, large area patterning for sample generation for the AMCS testing can begin.

4.1.2. Line Overlap Optimisation.

Table 7 records the laser energy densities selected for the overlap experiments on the basis of maximum roughness reduction recorded between lines 6 to 20, *EDs* ~0.43 to 8.63 kJ/cm^2, in single pass optimisation trials, section 4.1.1. The laser ED parameter range limits were expanded to maximise the laser penetration into the material hence diffusion reduction via grain boundary engineering. 304SS was processed by bidirectionally raster scanning the laser beam across the surface in a uniform pattern to minimise the manufacturing time.

Table 7. Laser processing parameters for overlap test.

ED (kJ/cm^2)	Reasoning
13.54	Out of the [83] parameter range
7.55	Within [83] parameter range
5.80	Large roughness reduction/line width
3.60	Large roughness reduction/line width
3.04	Large roughness reduction/line width
2.03	Large roughness reduction/line width
0.40	Lower limit of [83] parameter range
0.30	Out of the [83] parameter range

Figure 24 shows the roughness measurements with different line overlaps. The line overlaps range from 80 – 55 - 30 % to maximise roughness reduction in the experiment. The energy densities of 7.55 and 0.40 kJ/cm^2 are the closest to the reference parameters in [83] and, therefore, maintain the 30 % overlap, Table 8.

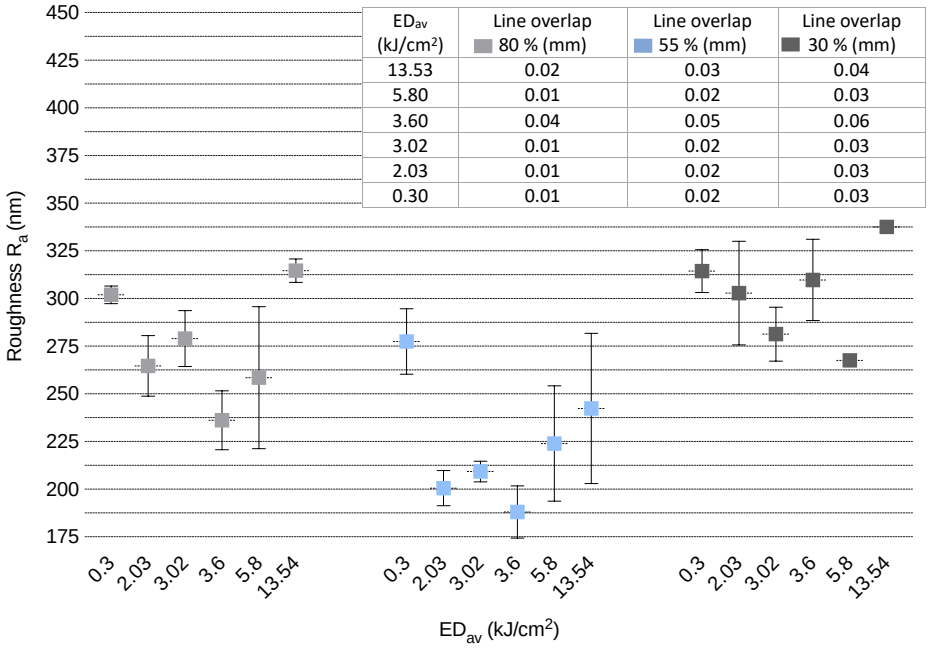

Figure 24. 304SS line overlap vs. roughness measurements.

From Figure 24 it is evident that *Line overlap 55 %* showed the lowest surface roughness and samples produced with this line overlap are optimised for desorption reduction capability in this work. Thus, the following samples have been manufactured for hydrogen outgassing testing via AMCS, Table 8.

Table 8. Laser processing parameters for AMCS specimens. Scan speed values available in Appendix D, Table 45.

Sample	ED (kJ/cm^2)	Line spacing (mm)
1	13.54	0.03
2	7.55	0.03
3	5.80	0.02
4	3.60	0.05
5	3.02[a]	0.02
6	2.03	0.02
7	0.40	0.027
8	0.30	0.02
9	3.60[b]	0.05

a - offset of 0.26 mm was intentional, larger roughness reduction was observed for the ED value.
b - double pass.

The surface roughness is recorded in Figure 25. Samples 2, 4, 5, 6 and 9 (double pass) show the most reduction in the surface roughness.

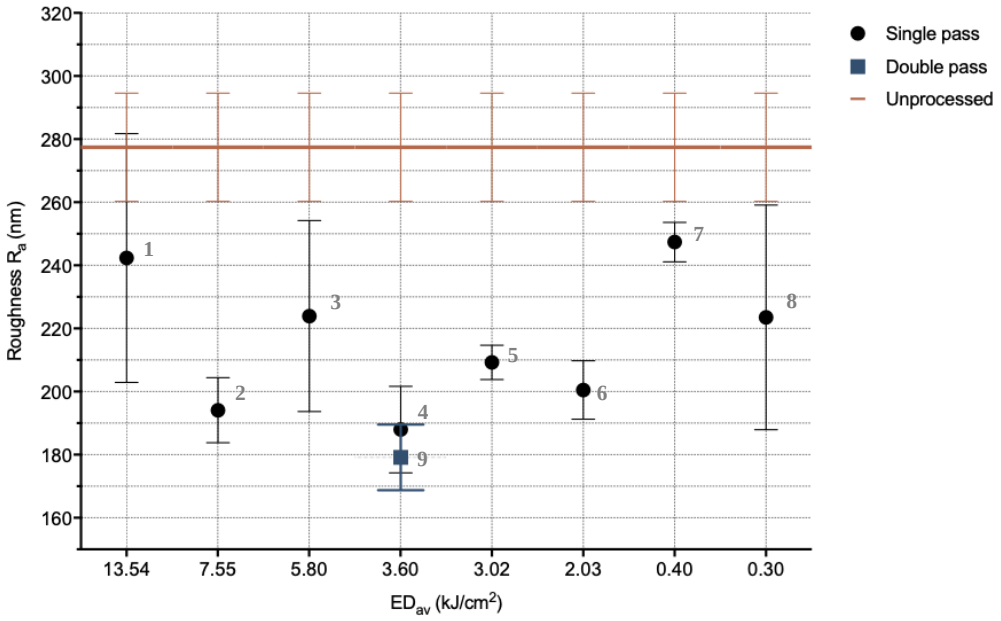

Figure 25. Surface roughness of the 304SS specimens generated for AMCS testing.

Sample 1, ED_{av} 13.54 kJ/cm^2, was selected for a detailed study for hydrogen outgassing reduction due to the largest laser penetration, diffusion reduction, of the material, hence reduction of H_2 outgassing. A paper titled "Laser surface melting of stainless steel anodes for reduced hydrogen outgassing" was based on this sample and published in March, 2017 [146].

4.1.3. Sample 1, Energy Density 13.54 kJ/cm^2, Surface and Laser Penetration Depth Characterisation.

The laser parameters of *Sample 1* from section 4.1.2 are recorded in Table 9.

Table 9. Laser Parameters.

Scanning velocity (mm/s)	2.25
Output power (W)	12
Line spacing (mm)	0.03
Spot size d (μm)	39.4
Oxidation in the irradiated area (%)	0.1- 0.2

Shown in Figure 26(b) is a chemically etched, according to section 3.1.6.5, longitudinal cross-section view of the treated sample, where the treated region is comprised of an LSM zone (LSMZ) and heat-affected zone (HAZ). The depth of the LSMZ is approximately 9.7 μm, HAZ 4.0 μm, Figure 26(a) shows an SEM image of the surface of the sample; treated and untreated areas are visible.

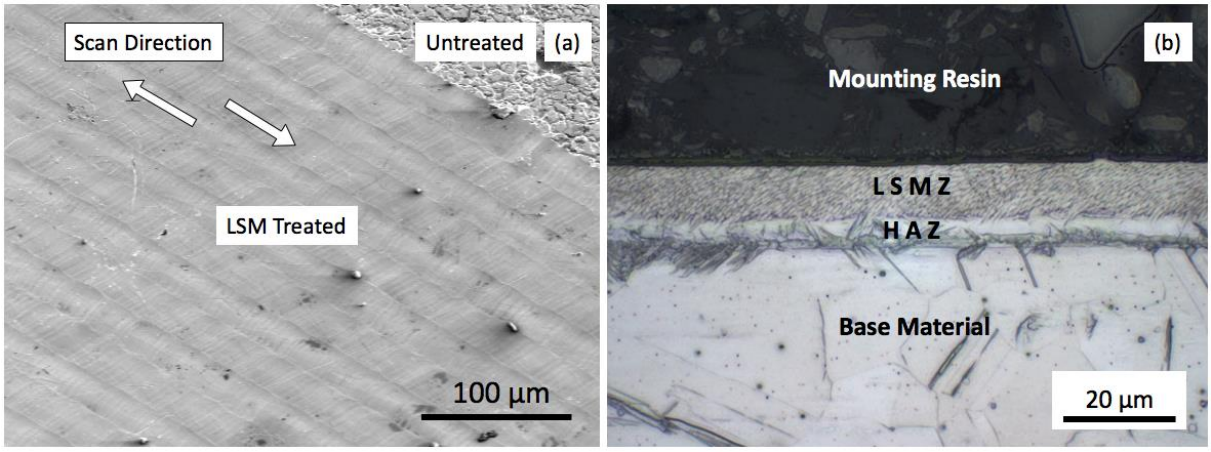

Figure 26. (a) SEM image of the raster scanned 304 SS sample with average ED 13.54 kJ/cm^2, image tilted at 45 degrees to the electron beam column, the arrows show the direction of the laser raster, (b) optical micrograph of the section view.

The individual laser tracks can be seen as can the ripples within each track that are orientated in the direction of the laser beam scan (a phenomenon in CW laser melting commonly observed at high average ED values [147]). There are also small, bump-like formations present within the treated area, which represent the SS surface morphology features that were incompletely melted by LSM and most likely result from the specific choice of scan parameters, as these occur exclusively near the overlap between adjacent laser scan lines. This can be minimised by changing the laser spot size, degree of overlap between adjacent scan lines or by subsequent laser passes over the sample.

4.1.4. Microstructural Analysis. Sample 1, Energy Density 13.54 kJ/cm^2.

FIB was applied for imaging the microstructure of the *Sample 1*, according to reasons listed in section 3.1.6.2. The sample was prior mechanically polished in colloidal silica solution 0.04 µm, according to section 3.1.6.4, to expose the grains and effectively speed up the ion beam imaging, parameters of which are recorded in Table 10:

Table 10. FIB imaging parameters.

Voltage	30 kV
Current	1 nA
Dwell time	0.1 ms

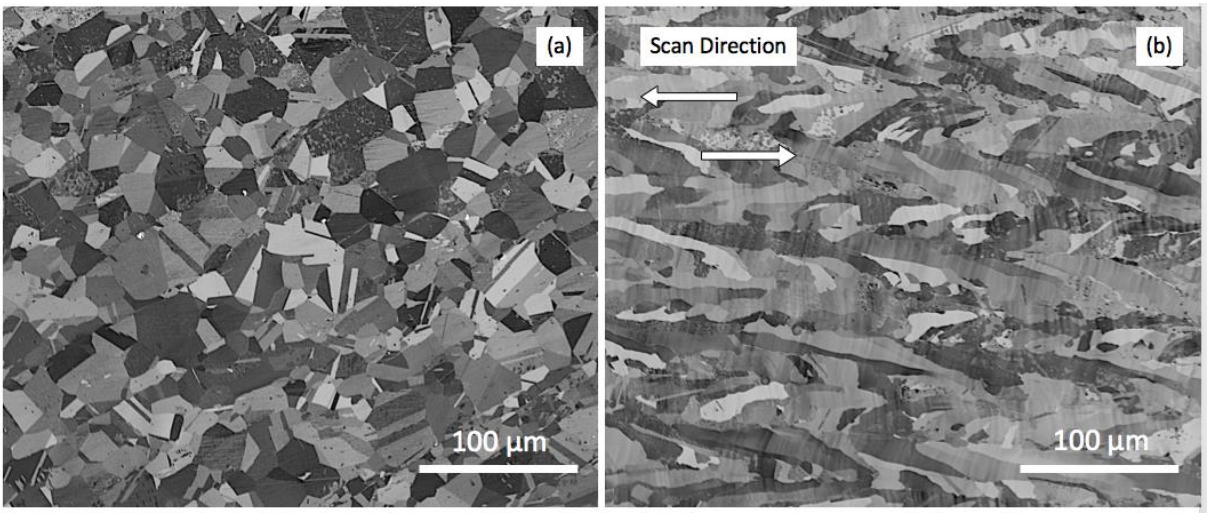

Figure 27. FIB image showing the microstructure of the (a) untreated and (b) 13.54 kJ/cm^2 treated 304 SS samples, surface view. Arrows show the direction of the laser raster.

Shown in Figure 27(a) and Figure 27 (b) are FIB images of the untreated and treated samples, respectively, demonstrating the microstructural changes induced by the laser radiation. It can be observed that the grains in the laser treated area are elongated in the direction of the laser scan and have increased in size, Figure 27(b).

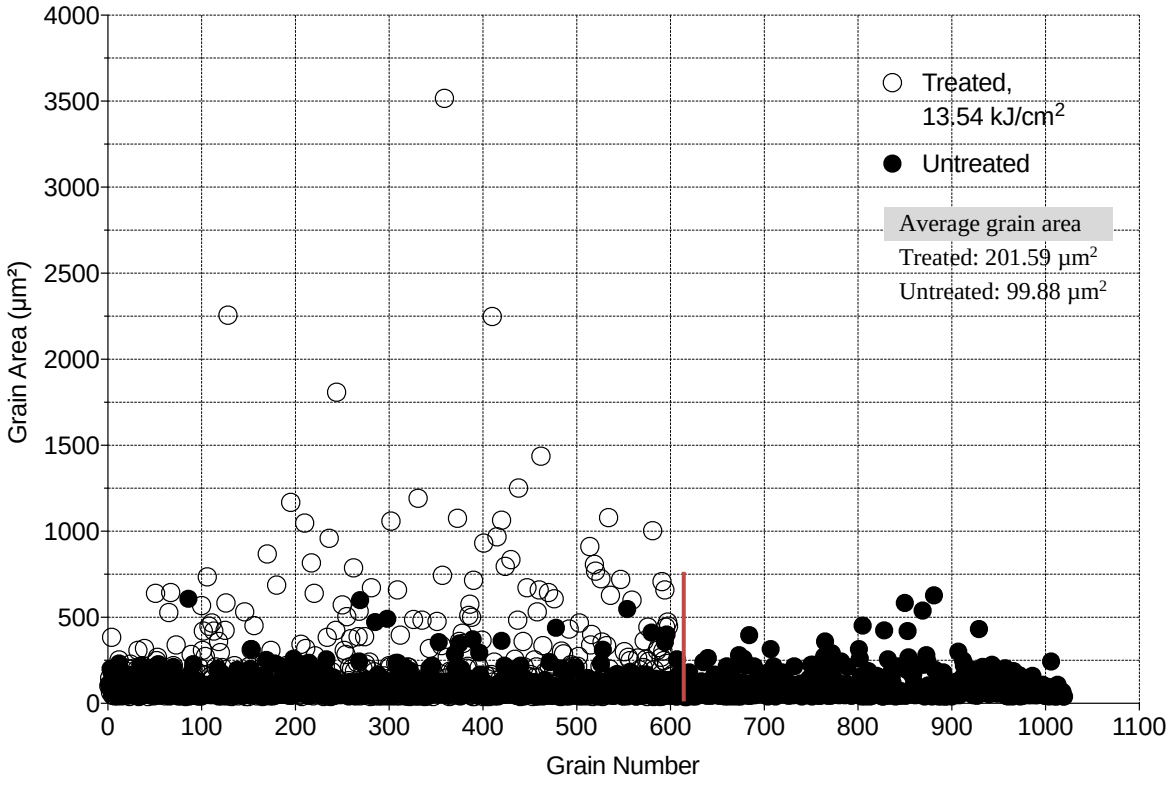

Figure 28. EBSD scan of 0.12 mm^2 area, mean MAD 0.20-0.28. Each point represents a single grain with its measured area.

The total number of grains was reduced from 1020 to 617 per 0.12 mm^2 surface area with some grains growing to 3500 µm^2 indicating AGG effect, Figure 28. The AGG is attributed to the laser scanning strategy. Grain nucleation is not dependent on original grain size but, rather, regulated by the laser

power, spot size, speed and line spacing, investigated further in section 4.2. The treatment led to a reduction in the number of Special and Random grain boundaries with an ~18 % reduction in Σ 3, GB majority, Figure 29.

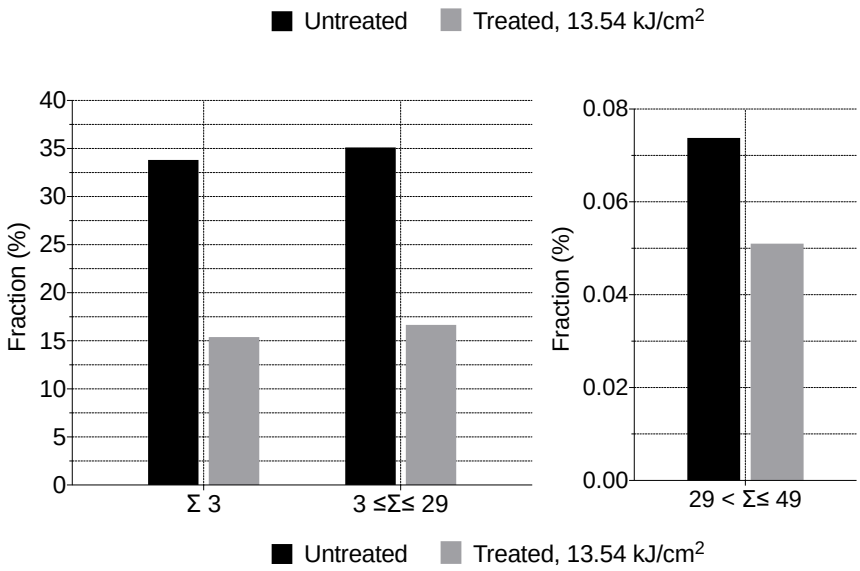

Figure 29. Special grain boundary classification for 304 SS, 13.54 kJ/cm^2.

Figure 30 shows the hydrogen outgassing results of the LSM treated vs the Untreated sample.

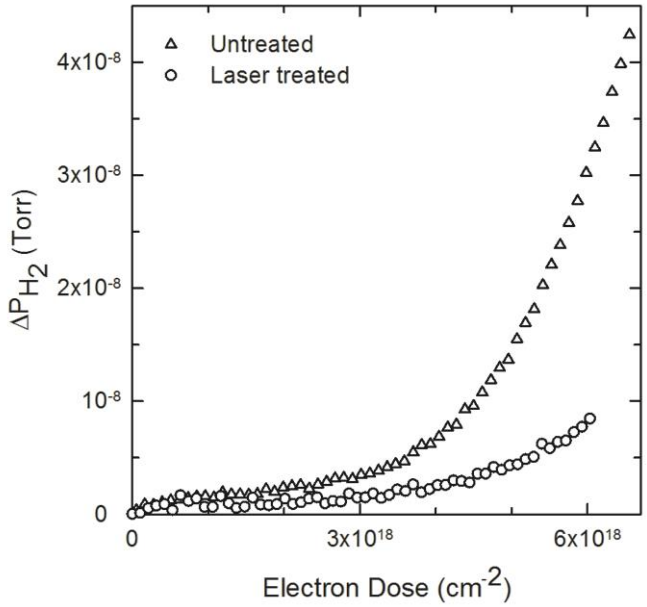

Figure 30. Outgassing results showing the change in H_2 partial pressure with electron dose during 60 second electron irradiation.

The results are presented as the change in H atom partial pressure (above baseline) with electron dose. Both curves exhibit an increase in H_2 signal with electron dose. Note that the H_2 signal for the untreated sample does not immediately rise with the electron dose but instead shows an incubation period (extending from a dose of 0 to ~ 3 x 10^{18} cm^{-2}) in which the H_2 signal first increases gradually after which there is a more rapid increase. The incubation period most likely is comprised of slow atomic H diffusion to the metal surface in which the majority of incident electron flux goes toward heating the

sample and enhancing H atom diffusion to the surface. Only after the induction period is there sufficient atomic H at the surface which recombines and proceeds to desorb more effectively and a larger desorbed H_2 signal is detected – desorption of nascent, molecular hydrogen H_2 into the gas phase [148]. The data from the LSM treated sample exhibits a smaller initial slope, suggesting a lower rate of diffusion of atomic H to the surface because of the decreased number of grain boundaries.

In summary, the data indicates that H_2 outgassing from the LSM treated sample was approximately a factor four less than that from the untreated SS sample for the conditions employed here. The hydrogen reduction is attributed to the reduction of the number of the GBs in the laser treated layer. To reduce the diffusion further via grain nucleation entails extending the surface cooling time [88], as discussed in section 2.5.2.3, therefore, higher laser energy densities were explored.

4.1.5. Surface Cooling Time and Higher Laser Energy Density Dependence.

To nucleate the grains further, the surface cooling time is extended, thus prompting higher initial surface temperatures. The 3 mm thick 304 SS, grain size 99.88 μm^2, was changed to 0.6 mm 304 SS with a smaller average grain size, 73.35 μm^2. The specimen was processed by raster scanning the CW laser beam across the surface in a uniform pattern, identical to *Sample 1* but with increased laser power, Table 11.

Table 11. Laser parameters for treatment of 304SS, 0.6 mm.

Scanning velocity (mm/s)	2.25
Output power (W)	17
Spot size diameter (μm)	39.4
Line spacing (mm)	0.03
Oxidation (%)	0.1-0.2

Figure 31(a) shows the FIB image of the sample's microstructure and Figure 31(b) is a longitudinal cross-section view of the SS sample, treated with ED_{av} of 19.17 kJ/cm^2.

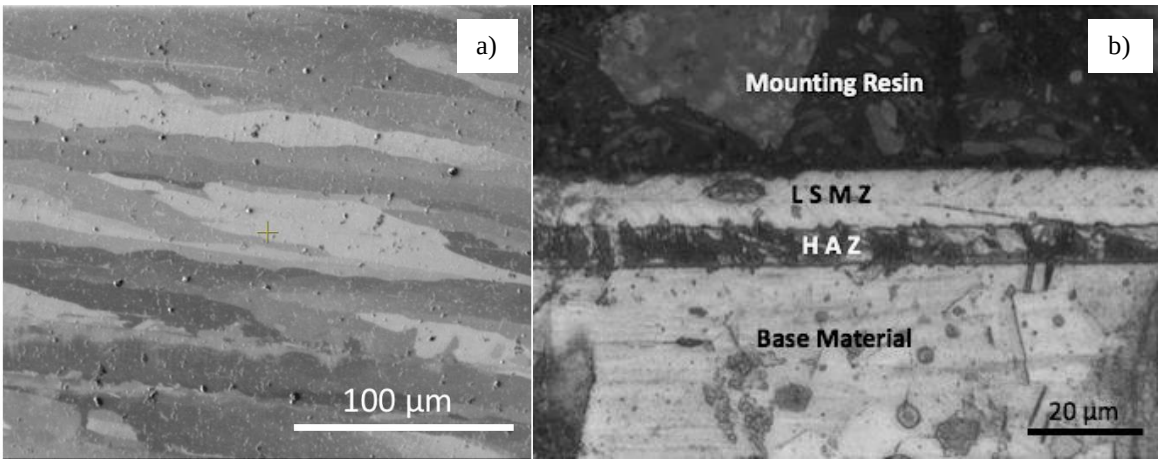

Figure 31. (a) FIB image of the laser treated microstructure and (b) optical image of the section view of the raster scanned 304 SS sample, 0.6 mm, 19.17 kJ/cm^2 laser energy density.

The depth of the LSMZ increased to ~11 µm from ~9.7 µm in section 4.1.3. From the FIB image, the grains appear larger and much more elongated comparing to those treated previously with ED_{av} of 13.54 kJ/cm^2. Once again EBSD scan is utilised to quantify the grain size and percentage of the grain boundaries obtained in the treated sample, Figure 32.

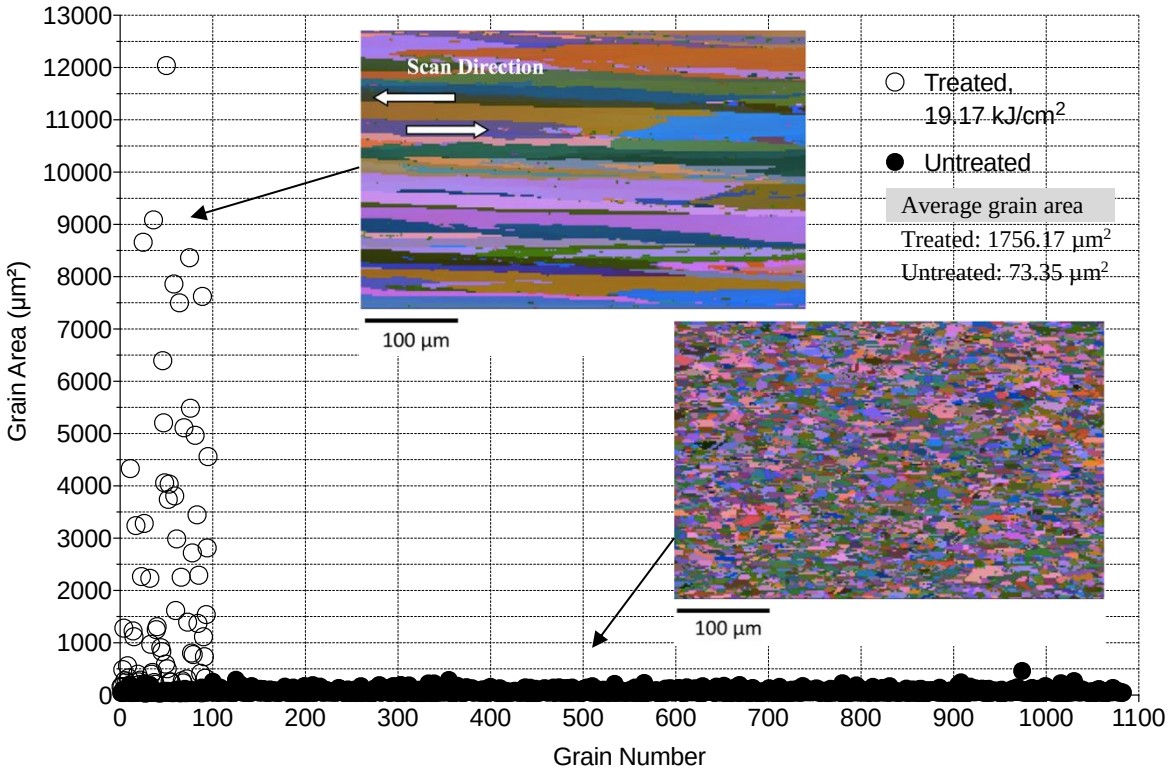

Figure 32. EBSD scan of 0.17 mm^2 area, mean MAD 0.3. Each point represents a single grain with its measured area with 3 angle Euler maps indicating the treated and untreated grains.

The number of grains was reduced from 1083 to 96 per 0.17 mm^2 surface area with some grains reaching 12040 µm^2 in size, a more prominent AGG effect. Higher *ED* lead to a further reduction in the number of Special and Random grain boundaries with an ~21 % reduction in Σ 3, Figure 33.

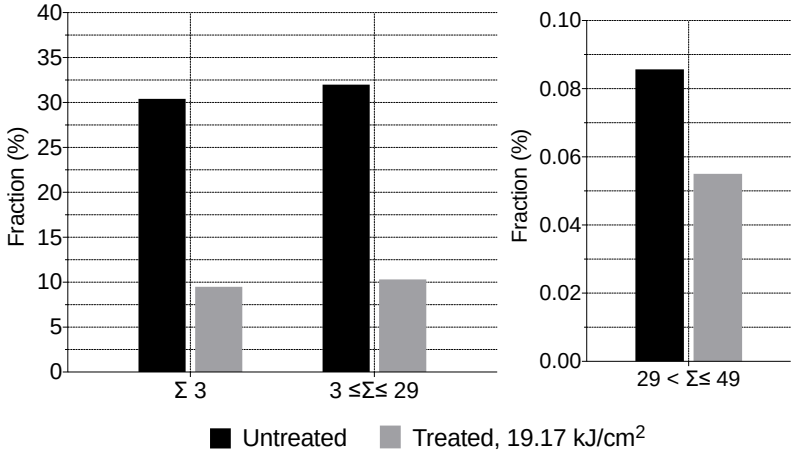

Figure 33. Special grain boundary classification for 304 SS, 19.17 kJ/cm^2.

In summary, higher average laser EDs help extend the surface cooling temperature, generating much larger grains in the SS microstructure. The drawback is an increase in the AGG effect, in the current case with a 244 % maximum increase in grain size for 19.17 kJ/cm^2 compared to 13.54 kJ/cm^2 (3500 μm^2 to 12040 μm^2), attributed to the scanning strategy namely line overlap. The total grain boundary count was reduced by 21.72 % with 19.17 kJ/cm^2 per 0.17 mm^2 comparing to 18.47 % with 13.54 kJ/cm^2 per 0.12 mm^2. The effects of 304SS treated with increased laser energy densities are tested for hydrogen outgassing reduction in section 4.1.7.

4.1.6. Hydrogen Depth Concentration Profile Mapping.

Elastic recoil detection (ERD) analysis was performed on the untreated and 19.17 kJ/cm^2 treated 304 SS, 0.6 mm. The sample was specially prepared for the ERD analysis by placing the N_2 nozzle for uneven oxidation distribution on the surface of the sample. The lack of N_2 produced excessive hydroxide and hydrocarbons on the surface due to oxygen ignition and burning of the steel's surface. Thus, two areas of the 19.17 kJ/cm^2 treated 304SS were analysed: carbon-contaminated and carbon-free (see Appendix E for an example of the low N_2 effects on the 304 SS sample treatment, Figure 142).

Figure 34 shows the results of the ERD analysis. Channel 20 to 60 represent the underlying surface region and channel 75 is the surface of the sample. Untreated showed H atom present in near surface region, denoted as H (bulk). The ERD measurement did not detect any H atoms in either carbon-contaminated nor carbon-free LSMZ of the treated sample.

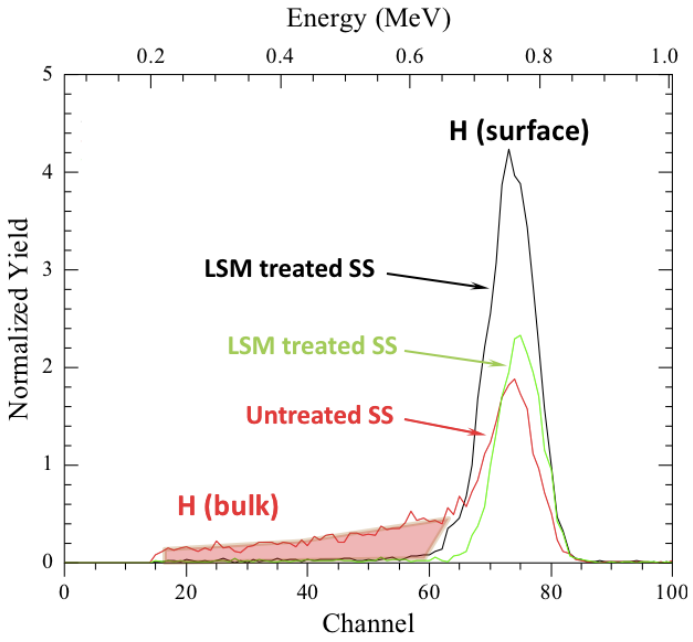

Figure 34. ERD surface layer measurements of untreated and treated 304SS, 19.17 kJ/cm^2. The black line represents the carbon-contaminated area of the treated sample and the green one is carbon-free.

The peak at channel 75 is seen for all materials since all materials tend to have water vapor and hydrocarbons on their surface. Surface H was present in both untreated and treated samples. Both carbon-contaminated and carbon-free areas showed higher H atom yield to that of the untreated sample with the carbon-free area being ~50 % less than the carbon-contaminated one. It seems the LSM treatment still produces increased levels of hydroxide and hydrocarbons even in the carbon-free area of the sample. This can be attributed to either not sufficiently low O_2 levels in the irradiated area or the oxidation layer still present on the surface of the sample after cleaning for laser processing described in section 3.1.3. It is also possible that some of the H atoms evacuated from the bulk segregated on the surface of the sample from adjacent irradiation paths due to raster scanning, adding another argument for the benefits of a larger beam size for LSM. For the purposes of microstructural transformation this effect is negligible. It is, however, acknowledged that LSM might not be a post-processing free technique if the surface H atom concentration is too high for the user's application and would require surface cleaning, e.g. ultrasonic bath.

In summary, the ERD results confirm that a total evacuation of H atoms in the laser treated layer occurs during LSM treatment. The lower the oxygen content during LSM processing the less surface H atoms it generates. Reduced content of surface H atoms after LSM was not observed.

4.1.7. Continuous Electron Beam Hydrogen Outgassing Testing.

Hydrogen outgassing testing was changed to continuous e-beam mode to minimise errors in the data analysis extraction (integration of data points with a single current rather than each pulse with its own

current for e-beam). Pulsed e-beam testing was originally used due to HPM devices normally operating in pulsed mode.

The goal of the experiment was to measure the H_2 reduction in steels treated with higher average laser ED, according to section 4.1.5. For continuous e-beam experiment three samples have been tested:

- Untreated 316 SS.
- Treated with 19.17 kJ/cm^2.
- Treated with 1.72 kJ/cm^2.

304 SS, 0.6 mm, was too thin for the testing. 316 SS was chosen for the experiment to allow better clamping of the samples in the chamber for the outgassing testing. The sample dimensions were 10 x 10 x 1 mm. This proved to be inconvenient for the analysis as thinner samples have less H content for detection. In ~100 seconds all of hydrogen was outgassed from the samples, Figure 35.

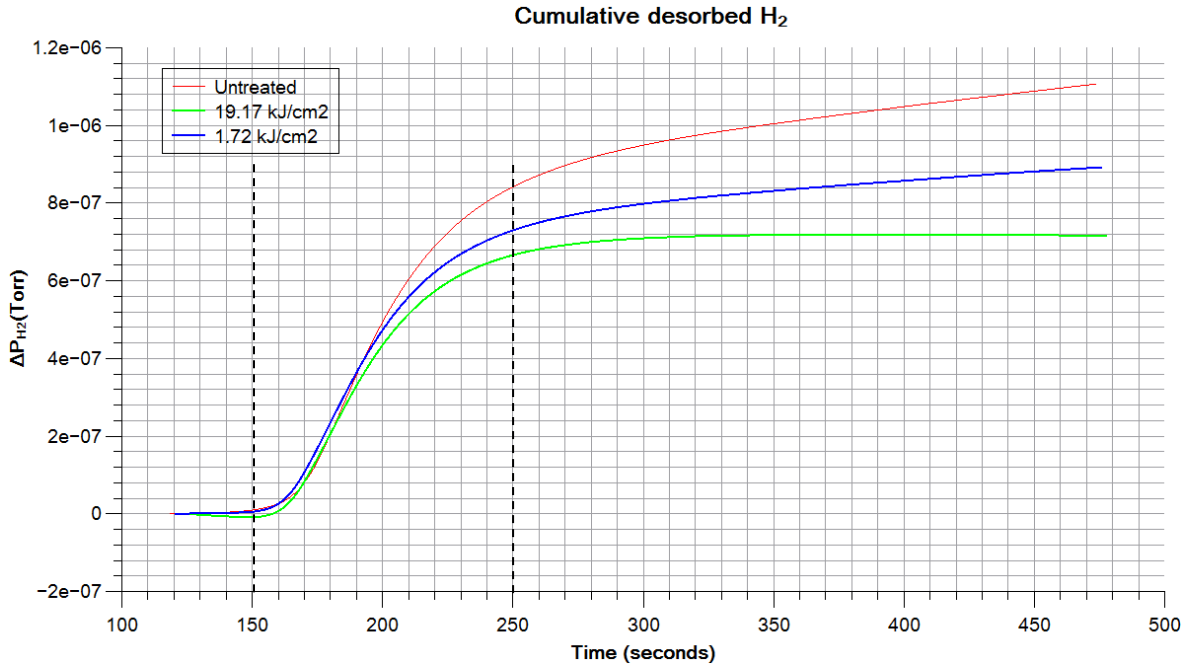

Figure 35. Hydrogen outgassing data for 316 SS.

Figure 35 shows the total hydrogen desorbed from the samples under 50 keV continuous e-beam bombardment over a period of 360 seconds. The H outgassing from the untreated 316 SS peaks at ~1.1 x 10^{-6} Torr, whereas for 19.17 kJ/cm^2 it is at ~7 x 10^{-7} Torr, which is 4 times lower. For 1.72 kJ/cm^2 it peaks at ~8.5 x 10^{-7} Torr, proving that higher average EDs is the right direction for H reduction treatment in steels.

4.1.8. Post-Electron Beam Bombardment Microstructure.

During e-beam bombardment samples heat up and glow bright red, slightly orange colour, Figure 36.

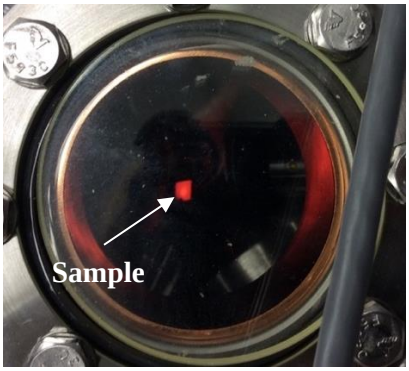

Figure 36. Image of the 316 SS sample through the window of the AMCS chamber, 19.17 kJ/cm^2, during e-beam bombardment with 50 keV.

According to thermal radiation scale for metals, the temperature of the sample is around 730 C °, thus no further nucleation occurs (< 1400 °C, the melting temperature of SS). The testing chamber does not have a pyrometer to track the sample's temperature. Therefore, to verify the claim, the outgassed samples were inspected with FIB for microstructural changes caused by the electron beam bombardment.

The FIB images show no changes in the post-electron beam microstructure, Figure 37. Therefore, it can be concluded that the temperature of the sample during e-beam bombardment is indeed < 1400 °C.

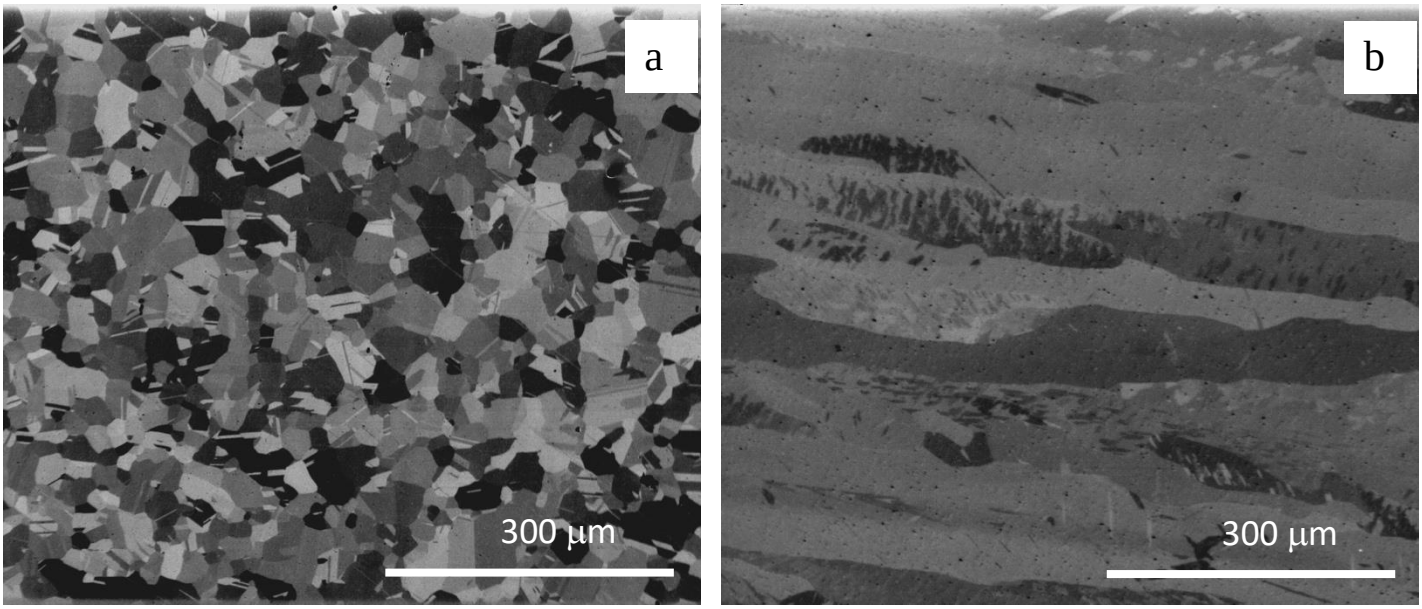

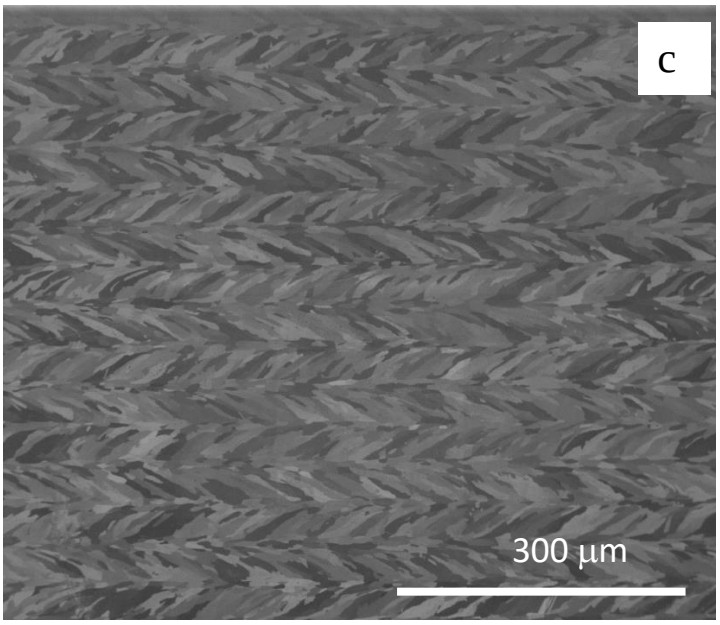

Figure 37. FIB images of 50keV outgassed 316SS with (a) untreated, (b) 19.17 kJ/cm^2, (c) 1.72 kJ/cm^2.

4.1.9. Monte Carlo Trajectory Simulation.

The 50 keV e-beam penetration depth was simulated to be 6 µm, Figure 38, which means most heating/diffusion in the outgassed sample in section 4.1.3 occurred within the LSMZ, 9.7 µm thick. From the ERD measurements in section 4.1.6 there is no H content in the LSMZ, therefore, for LSM hydrogen outgassing reduction of metals it is beneficial to increase the LSMZ so higher keV will not bypass the LSMZ and the maximum heating/diffusion can take place in H depleted area, Figure 38.

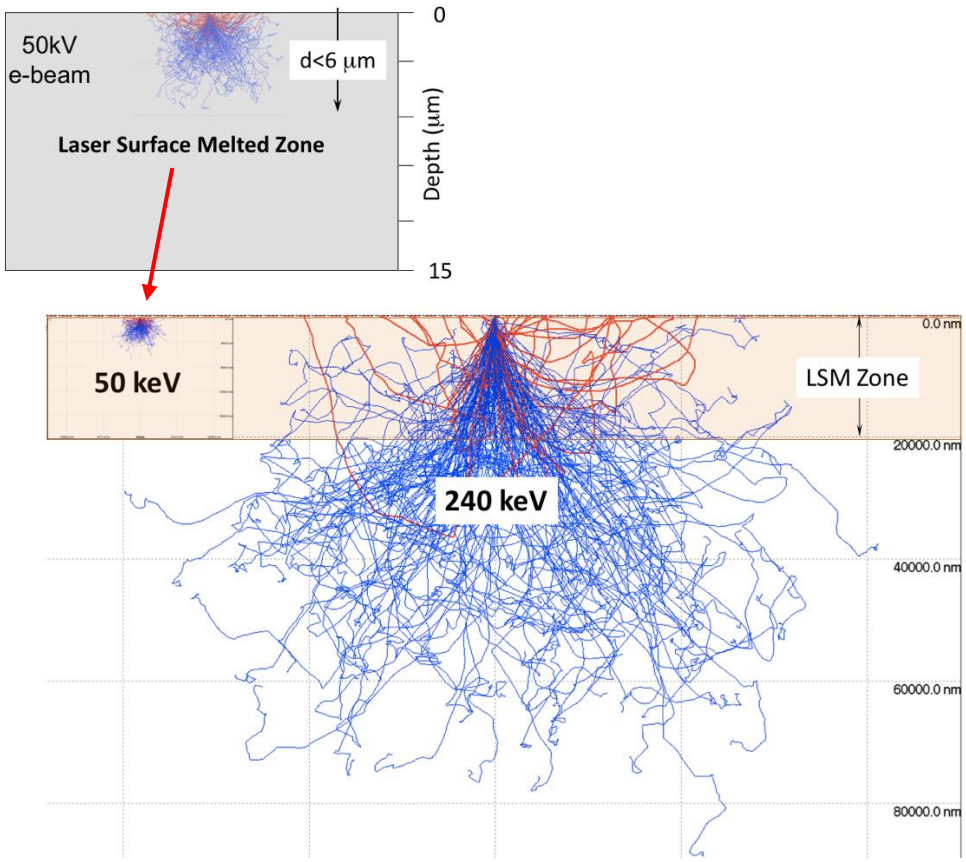

Figure 38. Image of the 50 keV e-beam compared to 240 keV e-beam penetration depth.

Part 2. Photonic Metallurgy. Grain Engineering and its Theory.

A repeatable grain transformation has been observed in all laser treated samples throughout hydrogen outgassing reduction study. This section looks in-depth at the mechanisms behind the grain elongation transformations in 304 SS and other metals. It consists of:

- Grain elongation mechanisms.
- Security marking technique.
- Single crystal generation and gran engineering theory demonstrated in Ni, SS, Ti and Cu.
- LSM treatment of Metal Substrates for CVD Graphene Growth.
- Electrical Conductivity Dependence on Grain Size.

4.2. Motivation. Grain Elongation Study Using EBSD.

The combined 3 angle Euler map acquired with EBSD scan, shows that the FIB images of the treated and untreated SS surfaces from Figure 27 indeed show that the grains are pulled in the direction of the laser scan, Figure 39.

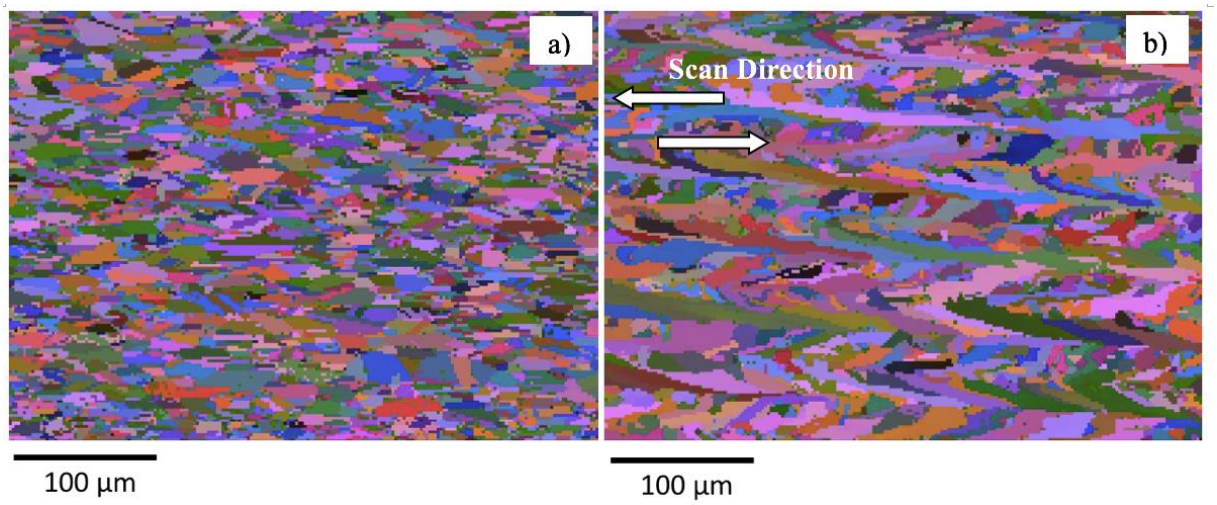

Figure 39. Euler combined 3 angle map of (a) untreated and (b) LSM treated 304 SS sample with ED of 13.54 kJ/cm^2 from Figure 27.

This observation prompted further experiments in localised grain nucleation. By controlling the direction and area of laser irradiation it is possible to directly draw with grains in the microstructure of steels, Figure 40. After scanning the surface of 304 SS with CW laser radiation, the grains formed patterns corresponding to the melt on the surface, Figure 42.

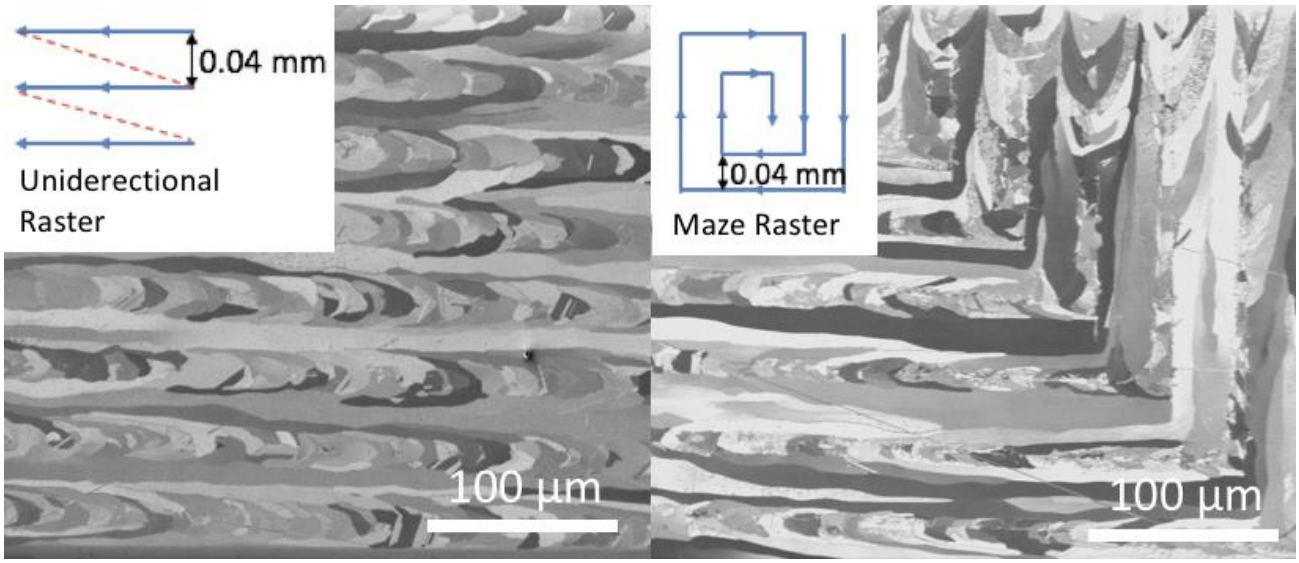

Figure 40. FIB images of LSM treated 304 SS with 13.54 kJ/cm^2 using different scanning strategies.

This way, using LSM technique, letters and numbers were laser melted in the microstructure of the steel samples, Figure 42-Figure 43. The following pattern was laser melted in the surface of 304 SS, Figure 41. The laser parameters are recorded in Table 12.

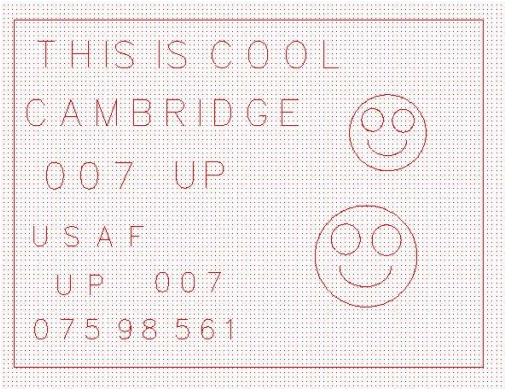

Figure 41. The red lines represent the scan strategy.

Table 12. Laser Parameters for direct grain writing in metal microstructures.

Scanning velocity (mm/s)	2.25
Output power (W)	17
Spot size d (μm)	39.4
Oxidation (%)	0.1-0.2

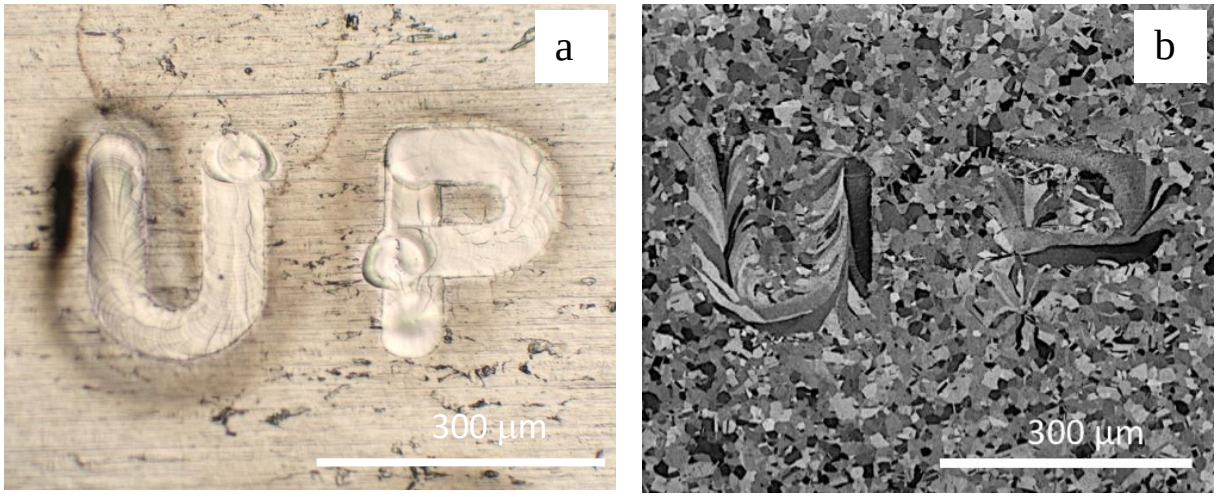

Figure 42. 304 SS irradiated with ED of 19.17 kJ/cm^2, spot size 39.4 μm, (a) optical image showing the surface melt pool forming letters UP and (b) FIB image showing the microstructure underneath.

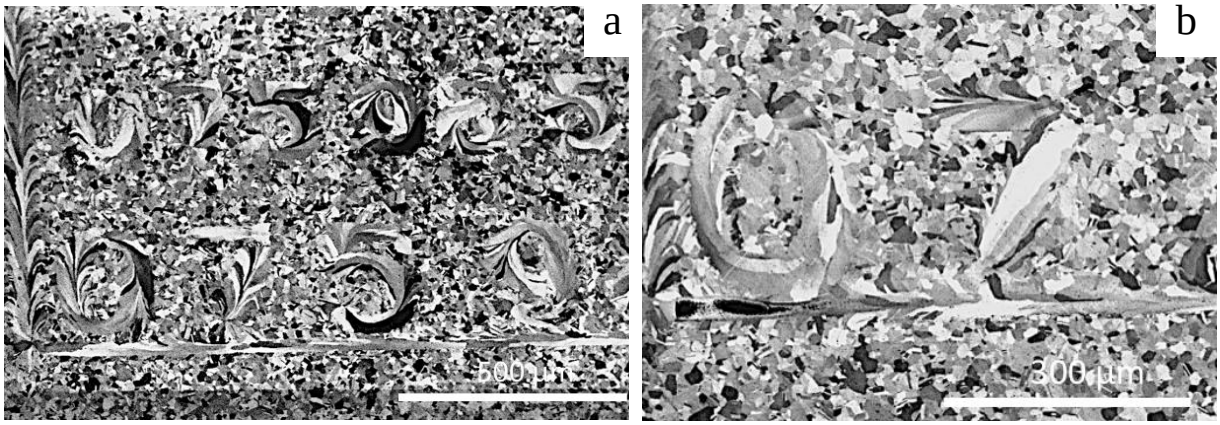

Figure 43. FIB images showing 304 SS irradiated with ED of 19.17 kJ/cm^2, spot size 39.4 μm, (a) numbers 0 7 5 9, (b) magnification of digits 0 and 7.

Letters and numbers can be easily recognised and do correspond to the surface melt patterns. The same experiment has been conducted on Titanium and 316 SS to verify that the process is not unique to 304 SS, Figure 44 - Figure 45.

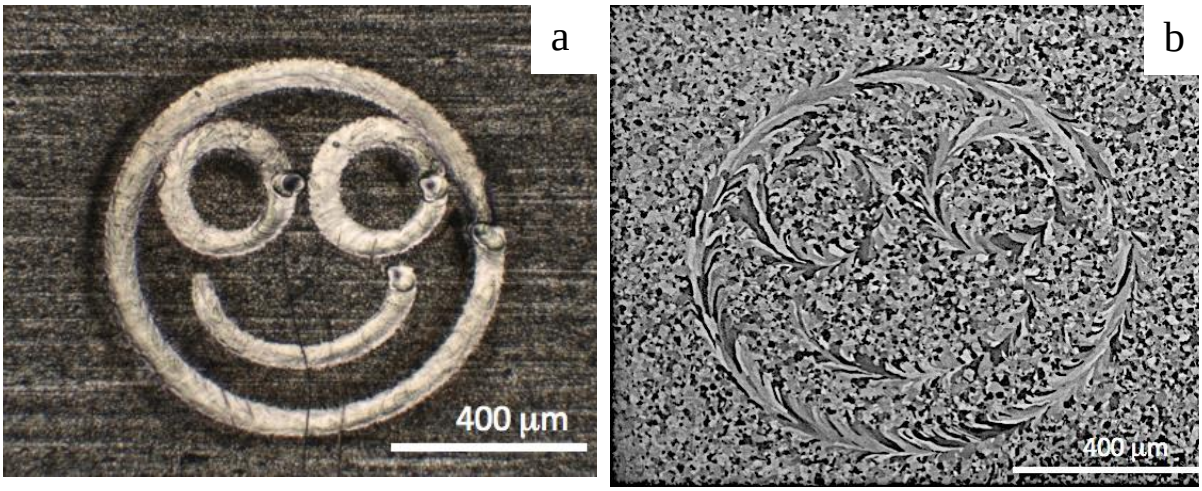

Figure 44. 316 SS irradiated with ED 19.17 kJ/cm^2, spot size 39.4 µm, (a) optical (b) FIB images.

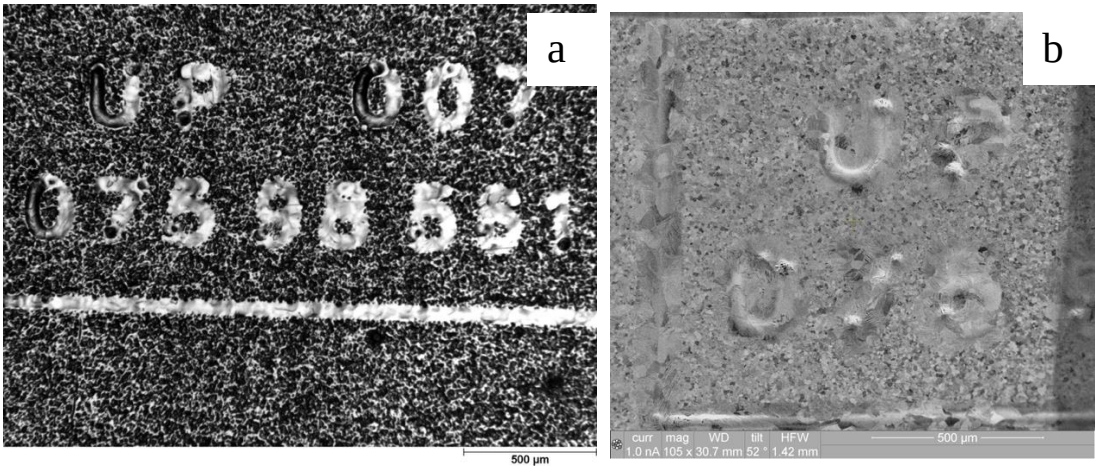

Figure 45. Ti irradiated with 19.17 kJ/cm^2 average laser ED, (a) optical image showing surface melt pools forming letters & numbers, (b) FIB image showing the microstructure underneath. Additional Ti experiments are available in Appendix.

The surface morphology is independent of the microstructure. The depth of localised grain transformation in steel samples counts ~20 µm, Figure 46, thus, the surface melt can be machined away, leaving the hidden messages in the bulk of the material.

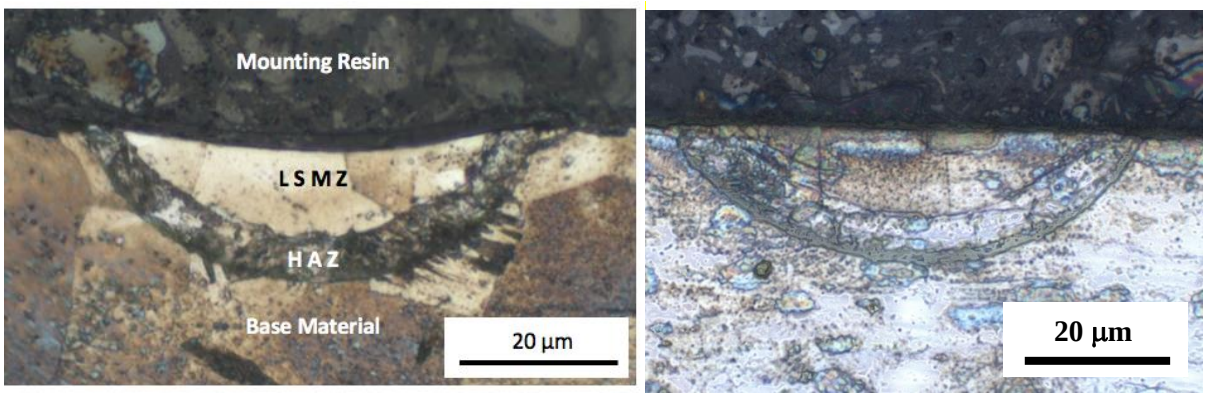

Figure 46. Optical image of the section view of single pass scanned 304 SS, left, and 316SS, right, with average ED 19.17 kJ/cm^2.

The 316 SS irradiated samples have been mechanically polished with 1 µm diamond particle solution to the surface roughness of Ra 12.06 $\pm$ 0.73 nm. Optical microscopy shows little evidence of any visible

melt pools, Figure 47(a). The patterns are visible with differential interference contrast (DIC) microscopy due to fine height difference between the untreated and treated areas in sample's microstructure, Figure 47(b).

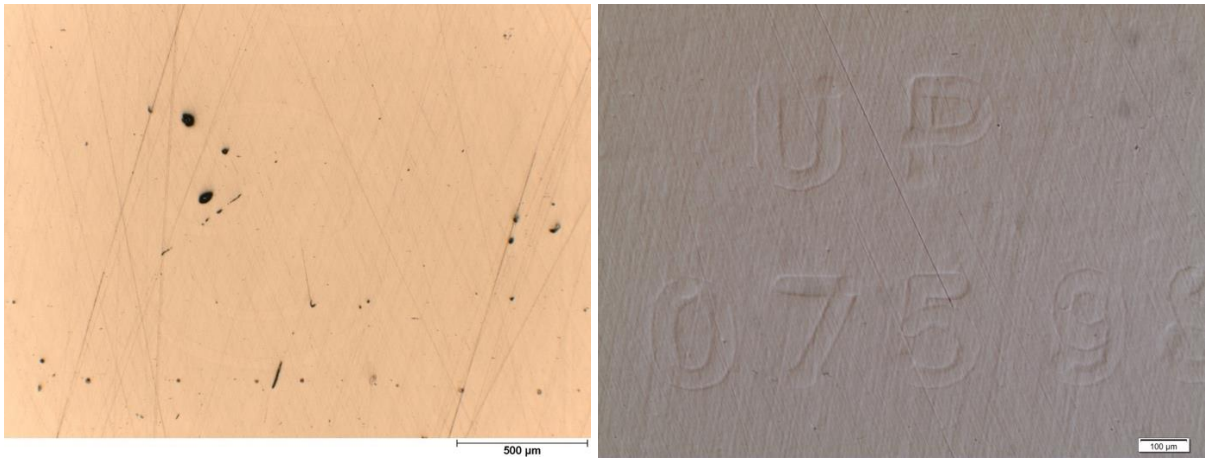

Figure 47. a) Image showing the surface of 316 SS after irradiation with optical microscope, BX51 Olympus, focused area is the Smiley face. b) Optical image with Nomarski microscope showing 316 SS surface after the mechanical polish, letters & numbers.

White light interferometry showed the maximum Rt value of the melt to be ~40 nm, Figure 48.

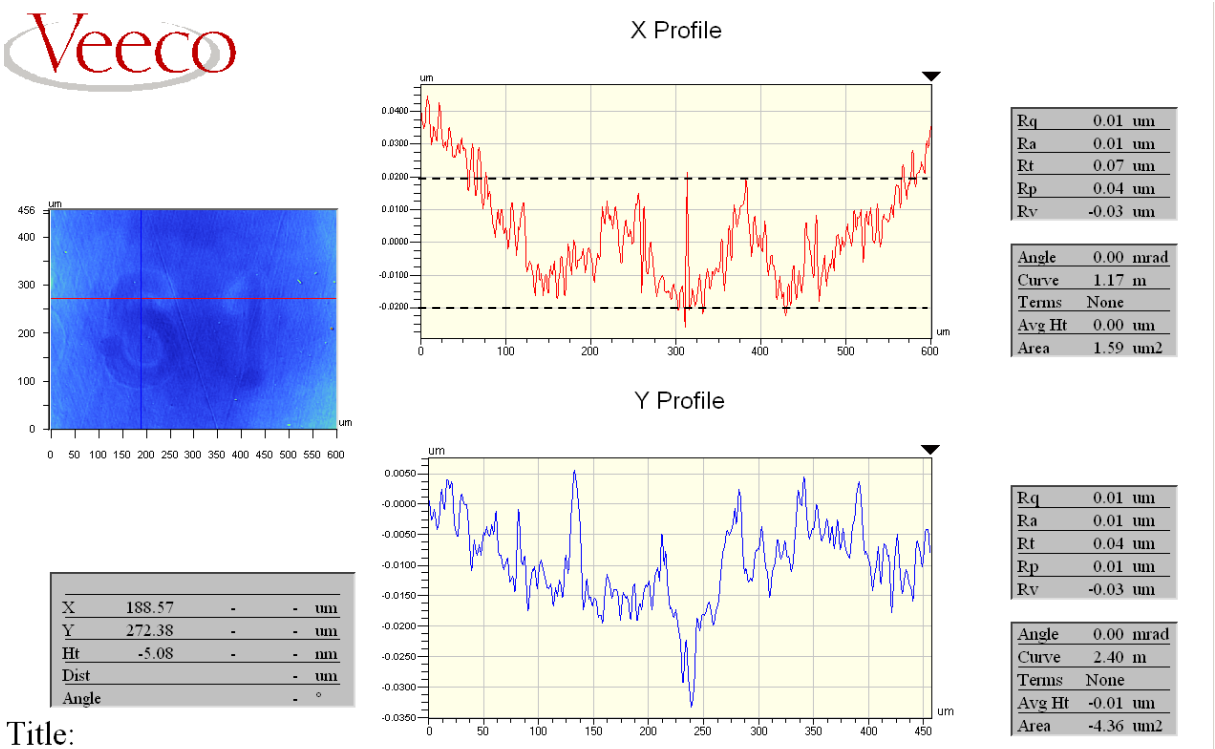

Figure 48. Interferometer image showing the 2D profile of the 316 SS surface after the mechanical polish. Maximum peak to valley difference ~40 nm.

Further mechanical polishing does not erase the surface melt patterning. It is recognised that due to the microstructural change, the sample will always experience a morphology difference between the treated and untreated surface areas on microscale.

4.3. Security Marking Test with Direct Grain Writing with Laser Radiation.

A QR code and a bar code were laser melted into the surface of 316 SS, Figure 49.

Figure 49. The black lines represent the scanning path of the laser.

The processing parameters are recoded in Table 13.

Table 13. QR and bar code laser melting parameters.

Scanning velocity (mm/s)	100
Output power (W)	17
Spot size d (μm)	39.4
Oxidation (%)	0.1-0.2

Figure 50 shows optical images in bright and dark fields of the surface of the 316 SS where the QR and the bar code were laser engraved. No pattern is visible.

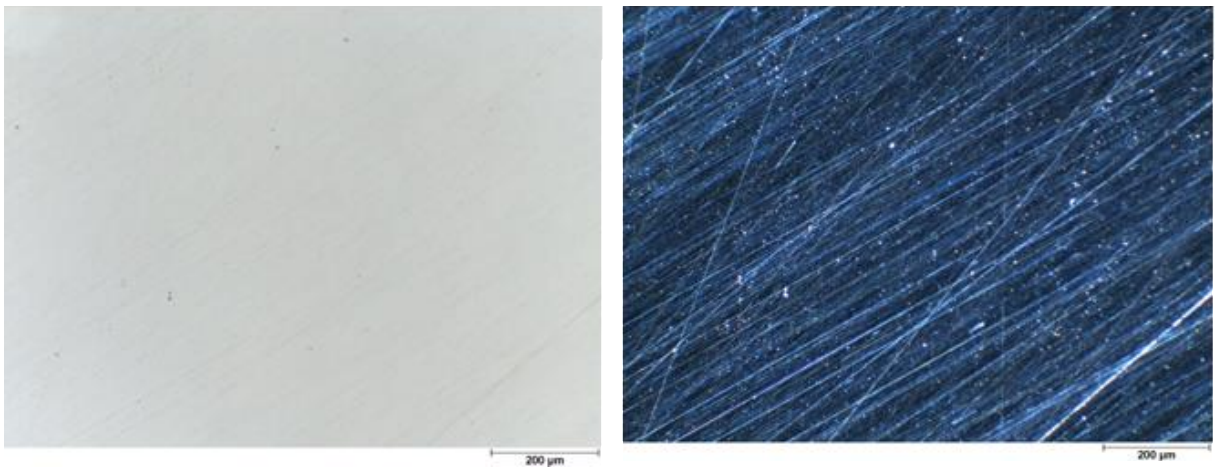

Figure 50. Optical images of laser processed 316 SS and polished in 1 µm diamond suspension. Left, bright and, right, dark field.

Viewed with DIC microscope the same surface shows the hidden pattern underneath, Figure 51.

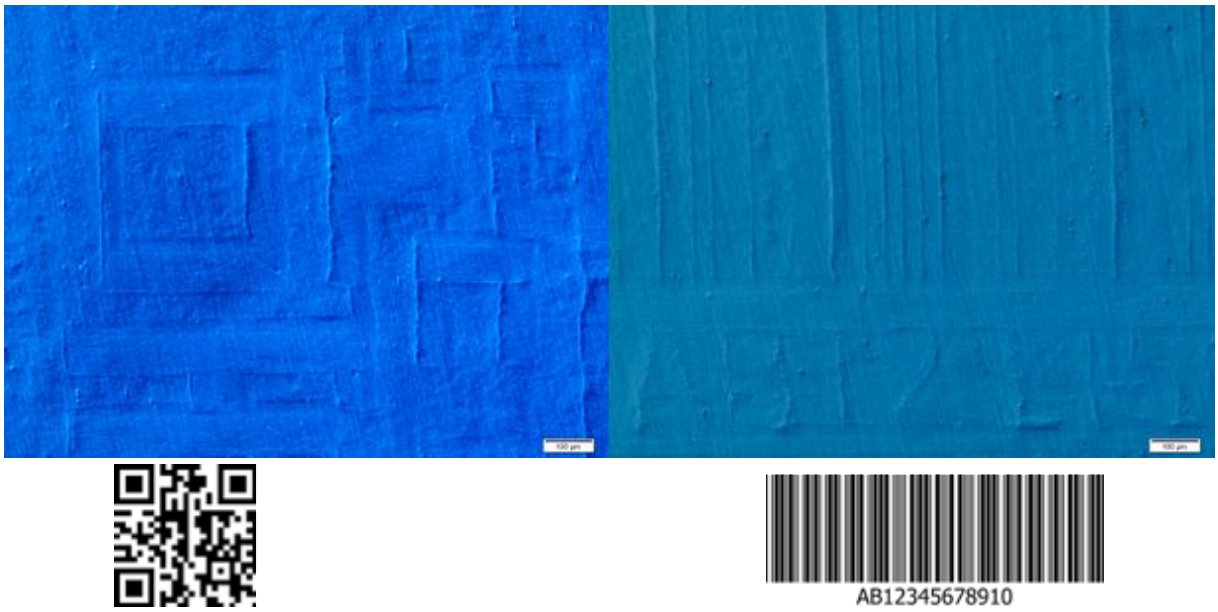

Figure 51. DIC optical microscope images of the 316 SS surface laser patterned with QR, left, and bar code, right.

Thus, with only three tools, a metal security marking method can be implemented, Table 14.

Table 14. Processing equipment for metal security marking.

Processing equipment	Time
• Laser, SPI™ G3 20 W	< 10 sec
• Grinder, ATM Saphir™ 550	< 3 min
• DIC microscope, Olympus™ BX51M	

4.4. LSM of 304 SS for Single Crystal Generation.

Multiple laser passes generate single crystals within the irradiated area. The laser pass in Figure 52 shows the surface structure and the underlying microstructure of 304 SS before and after laser irradiation. Upon second laser pass in the same area, keeping laser parameters constant, the grains in the middle of the pass are enlarged and have an ordered structure, Figure 53. With the third laser pass the grains become long single crystals, Figure 54.

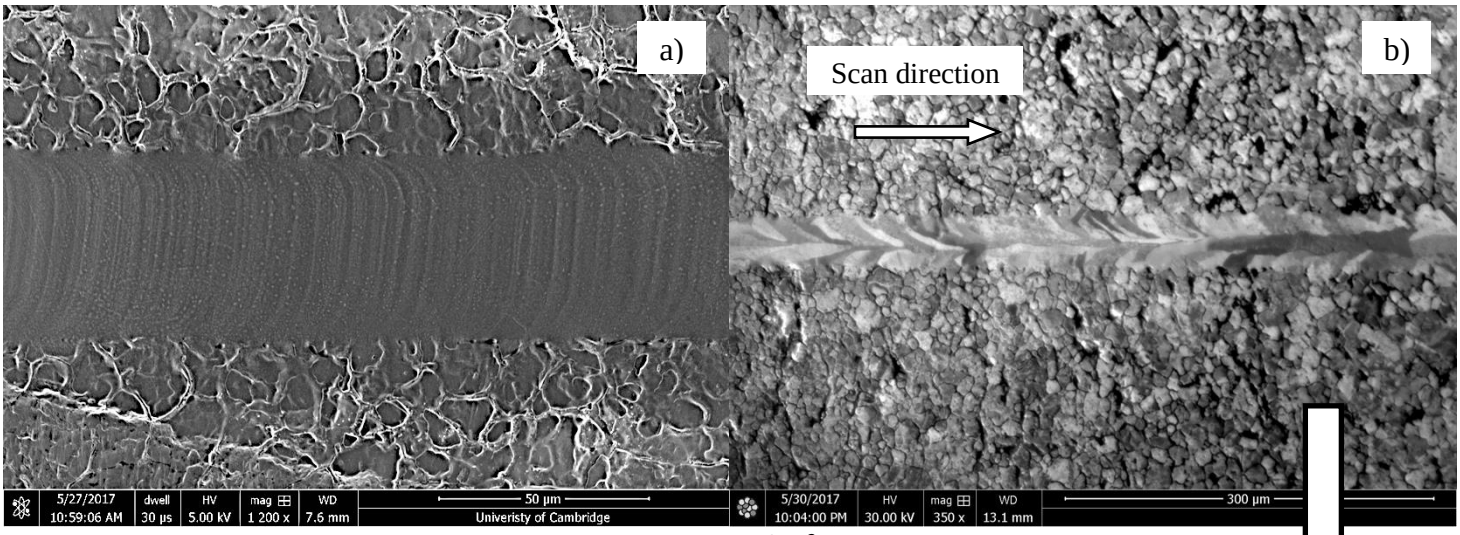

Figure 52. a) SEM and b) FIB images of 304SS irradiated with 19.17 kJ/cm² laser intensity, single pass.

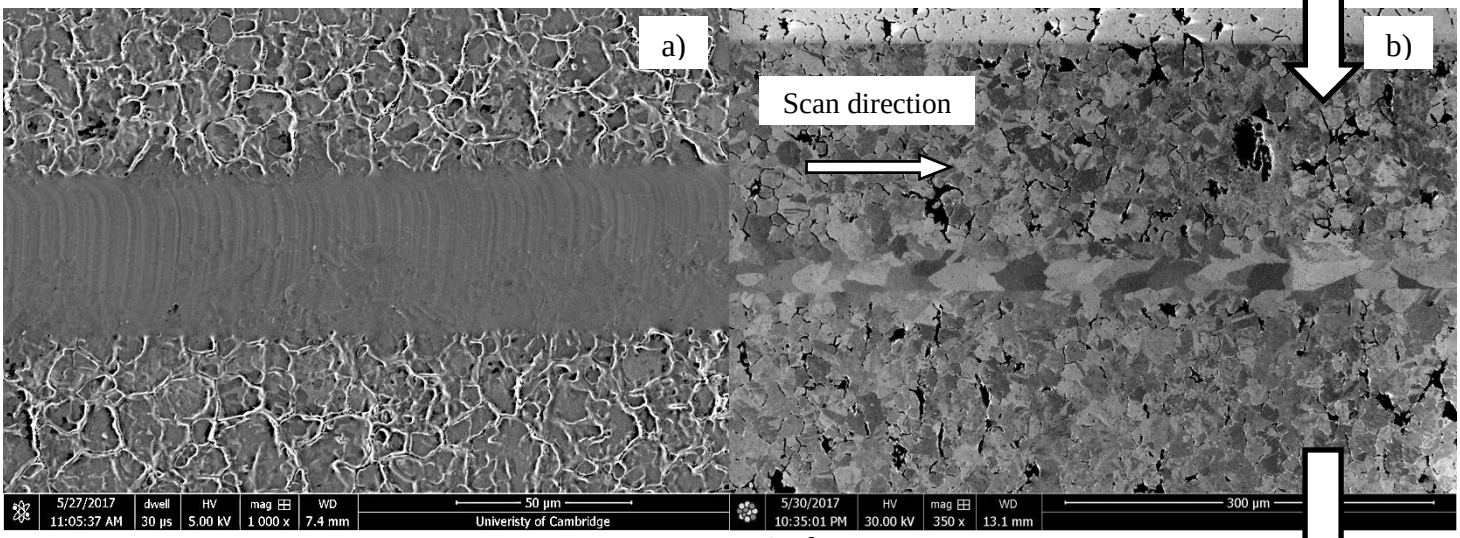

Figure 53. a) SEM and b) FIB images of 304SS irradiated with 19.17 kJ/cm² laser intensity, double pass.

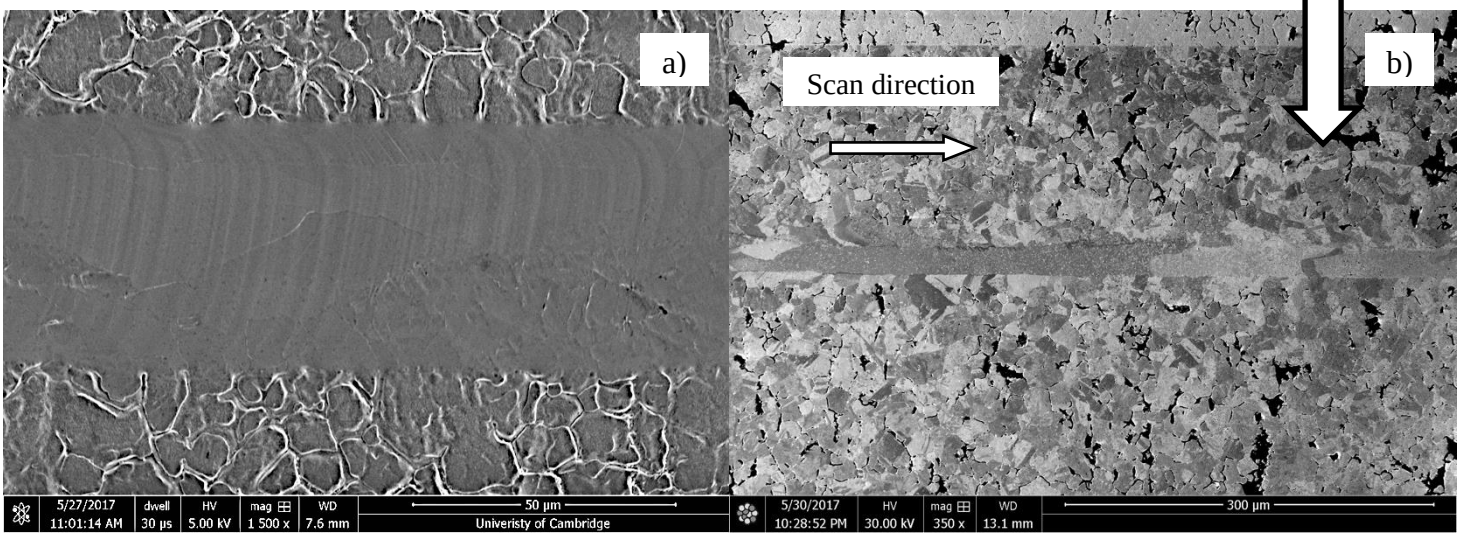

Figure 54. a) SEM and b) FIB images of 304SS irradiated with 19.17 kJ/cm² laser intensity, triple pass.

A clear progression of the centre grain enlargement with increased passes is observed when the laser parameters are kept constant. The surface experiences a ripple effect due to the surface tension [84]. The surface roughness decreased from the first pass to the third, Table 15. Increased number of laser passes

also increased the lines in width, Table 15.

Table 15. Surface roughness measurements and laser pass width for the 304SS samples for single crystal growth.

Number of laser passes	R_a (µm)	R_t (µm)	Width (µm)
1	0.21	1.69	46.84
2	0.19	0.88	54.51
3	0.16	0.85	59.16
Untreated	0.21	1.33	-

In conclusion, a clear progression of the centre grain enlargement with increased passes is observed when the laser parameters are kept constant at 19.17 kJ/cm^2 average ED. Single crystal circuits within the surface microstructures of metals are possible with this method. Images of a single crystal circuit grid in the microstructure of 304 SS is available in Appendix F.

Another experiment with single crystal generation but different laser scanning strategy was performed. 304 SS was raster scanned once (bidirectional raster) with two laser intensities, 19.17 and 13.54 kJ/cm^2, alternating only the line spacing.

The experiment yielded single crystals in each laser pass min 400 µm in length for the highest ED and largest line spacing, Figure 55 (a). Each subsequent test with reduced line spacing yielded less single crystals for both 19.17 and 13.54 kJ/cm^2 EDs but more grain pulling instead. This effect is attributed to the laser spot (~40 µm in diameter) overlap which explains the line spacing 0.04 mm to be adequate for single grain generation in Figure 55(a). The grain pulling and fewer single crystals in Figure 55(b) is attributed to the lower ED value producing less laser surface melt. Figure 56(a) still produces single crystals whereas in Figure 56(b) these are rare. The single crystal generation here, however, contradicts the finding in the previous section – three passes were needed to nucleate single crystals in one area with the same laser parameters. It is suspected that the irradiation area had a steady temperature increase throughout adjacent laser track generation, whereas the previous sample had only 3 short laser passes one after the other, creating a preheating effect.

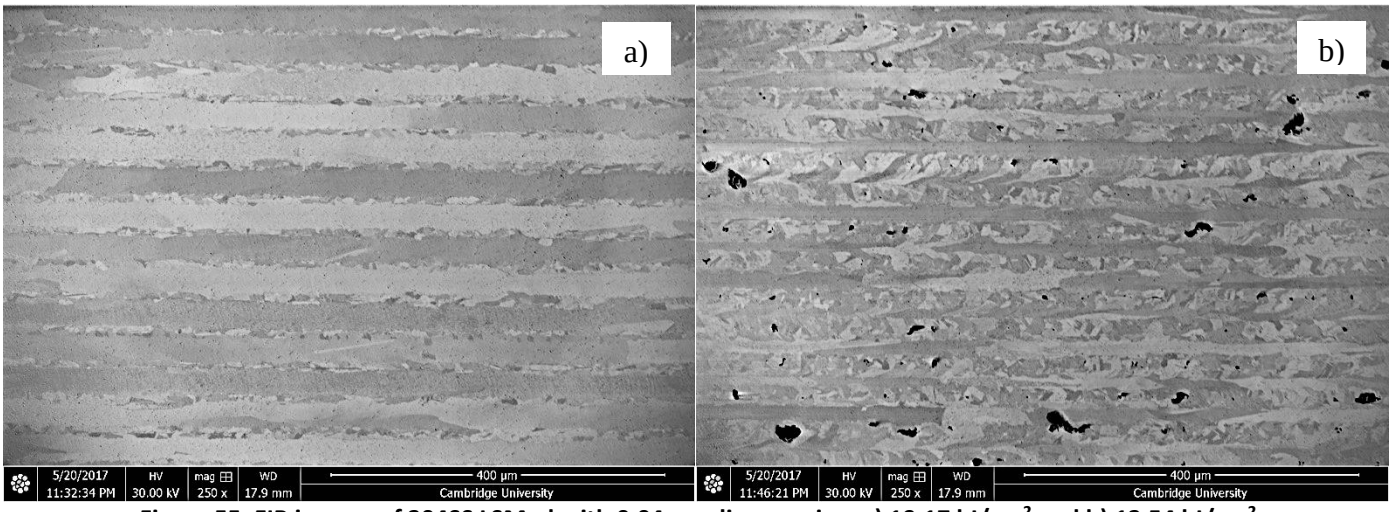

Figure 55. FIB images of 304SS LSMed with 0.04 mm line spacing, a) 19.17 kJ/cm^2 and b) 13.54 kJ/cm^2.

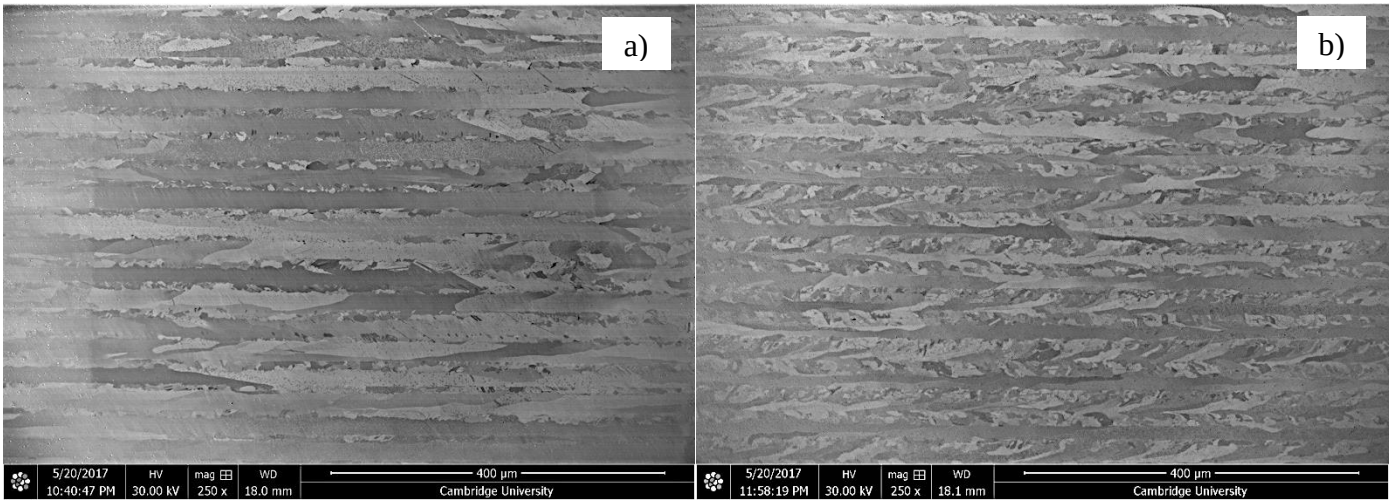

Figure 56. FIB images of 304SS LSMed with 0.03 mm line spacing, a) 19.17 kJ/cm² and b) 13.54 kJ/cm².

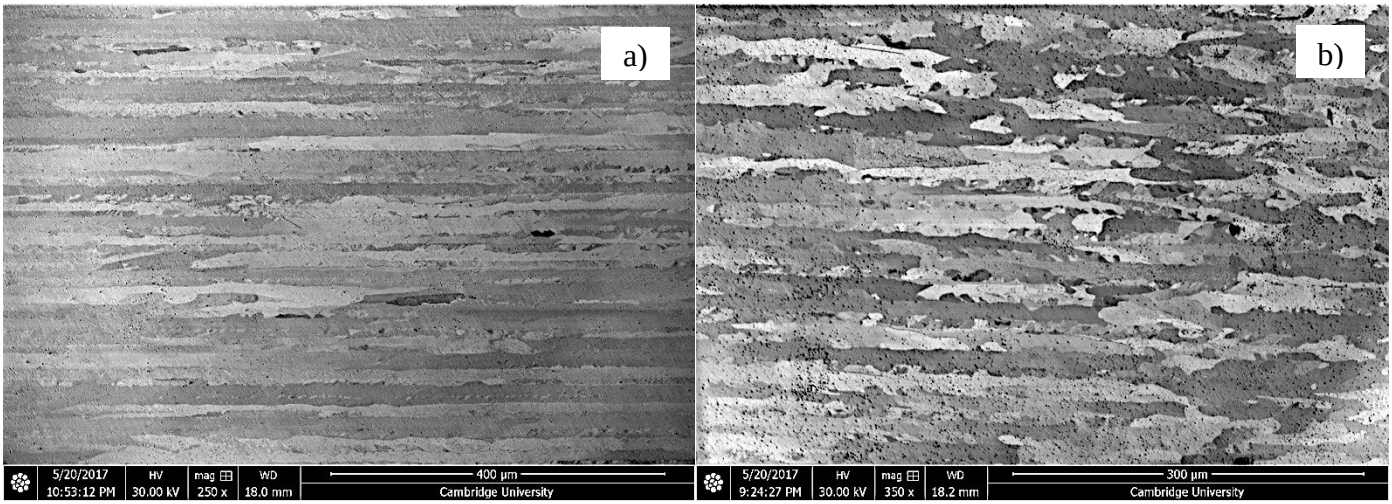

Figure 57. FIB images of 304SS LSMed with 0.02 mm line spacing, a) 19.17 kJ/cm² and b) 13.54 kJ/cm².

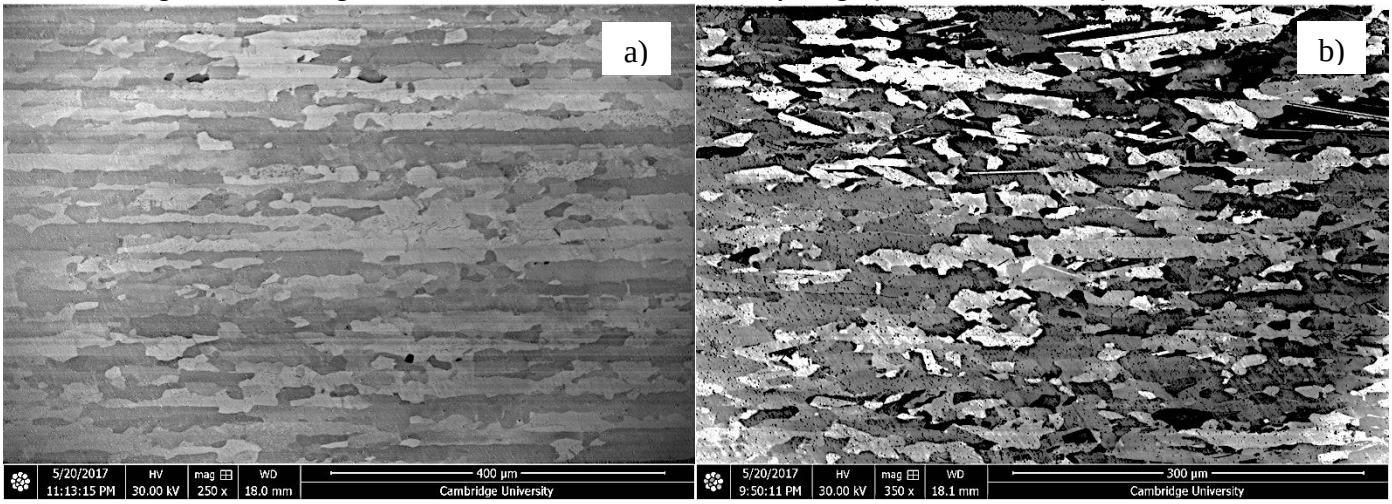

Figure 58. FIB images of 304SS LSMed with 0.01 mm line spacing, a) 19.17 kJ/cm² and b) 13.54 kJ/cm².

In conclusion, the tests conducted present two scanning strategies for single crystal generation in steels – multiple passes and bidirectional raster scanning. Single crystal generation with CW LSM is explored further in section 4.5 with increased laser energy density. The exact mechanism for single crystal generation remains to be clarified. Preheating is not investigated as the surface melt solidifies before the

next pass. It is also possible that the grain size of the original microstructure is responsible for the single crystal generation with the selected laser parameters. The effects of the laser spot size on direct grain writing are explored in section 4.6.

4.5. Tests with SPI SP200C CW laser for CW LSM Towards Increased Single Crystal Growth.

SPI SP200C CW laser allows increased spot size processing of samples with the same average laser ED to confirm the findings in section 4.4. Three sets of experiments have been undertaken on 304 SS:

1. Multiple pass LSM with laser intensity of 13.57 kJ/cm^2 increasing only the spot size:
    - 1st pass - 40.6 µm.
    - 2nd pass - 81.2 µm.
    - 3rd pass - 121.8 µm.
2. Multiple pass LSM with laser intensity of 13.57 kJ/cm^2 with 81.2 µm spot size.
3. Verification of the multiple pass experiment in section 4.4 with a different laser system; LSM with laser intensity of 19.15 kJ/cm^2 with a spot size of 40.6 µm.

Multiple pass LSM with laser intensity of 13.57 kJ/cm^2 increasing only the spot size.

A faster single crystal generation was achieved by doubling the beam spot size from 40.6 to 81.2 µm keeping the laser intensity constant at 13.57 kJ/cm^2, Figure 59. The image clearly shows several single crystals generated in the centre of the laser pass.

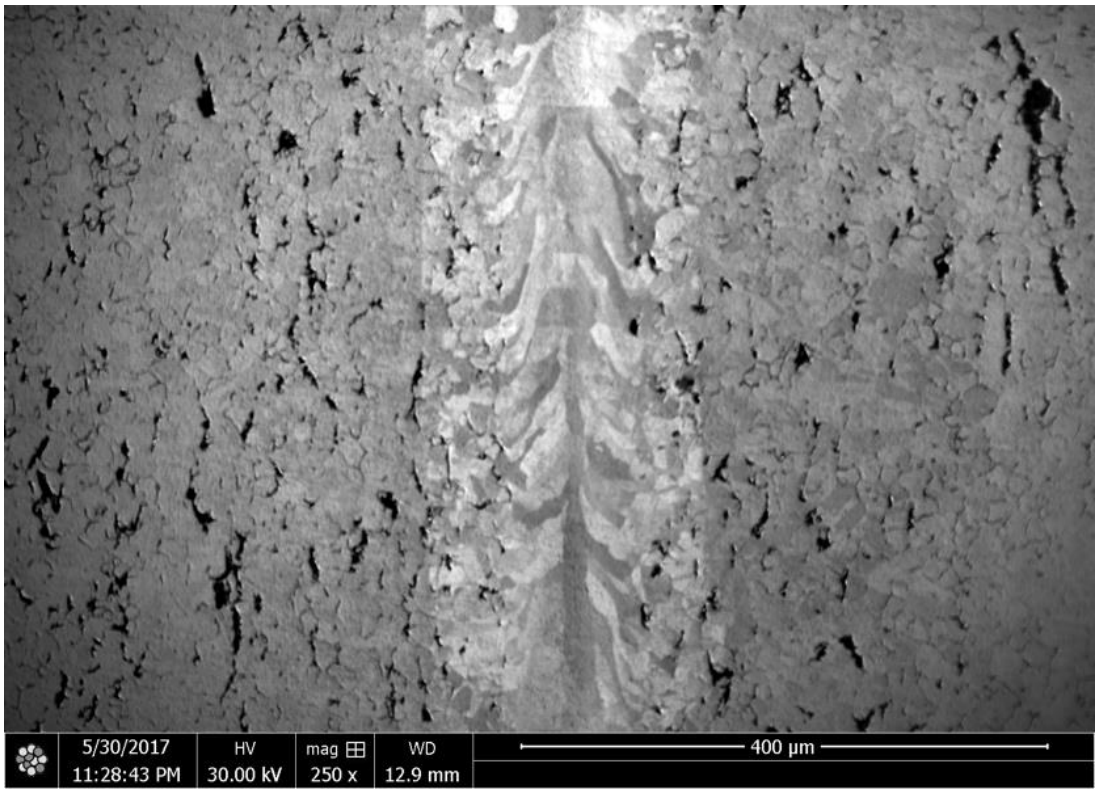

Figure 59. FIB image of 304 SS LSMed with 13.57 kJ/cm^2. First pass with 40.6 µm spot size in focus, second pass in offset by 2.03 mm.

In terms of surface topography, the laser passes produced trenches ~2 µm deep, Figure 60. The trench is widened upon the second pass with the doubled spot size, Figure 63.

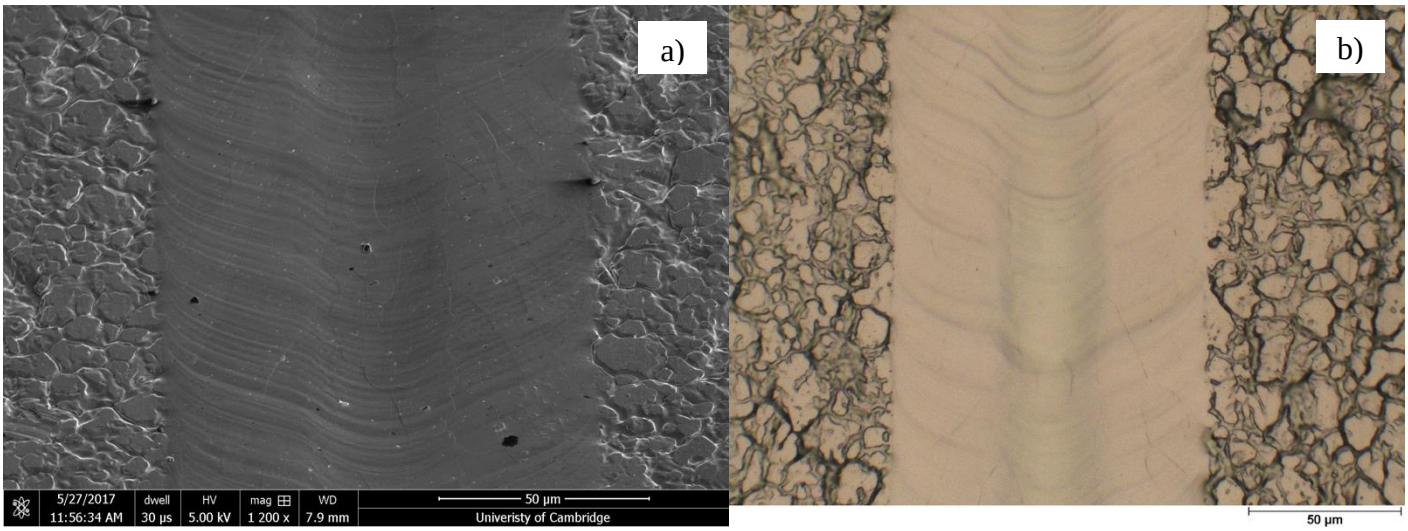

Figure 60. a) SEM and b) FIB images of 304 SS irradiated with 13.57 kJ/cm^2, single pass with 40.6 µm spot size.

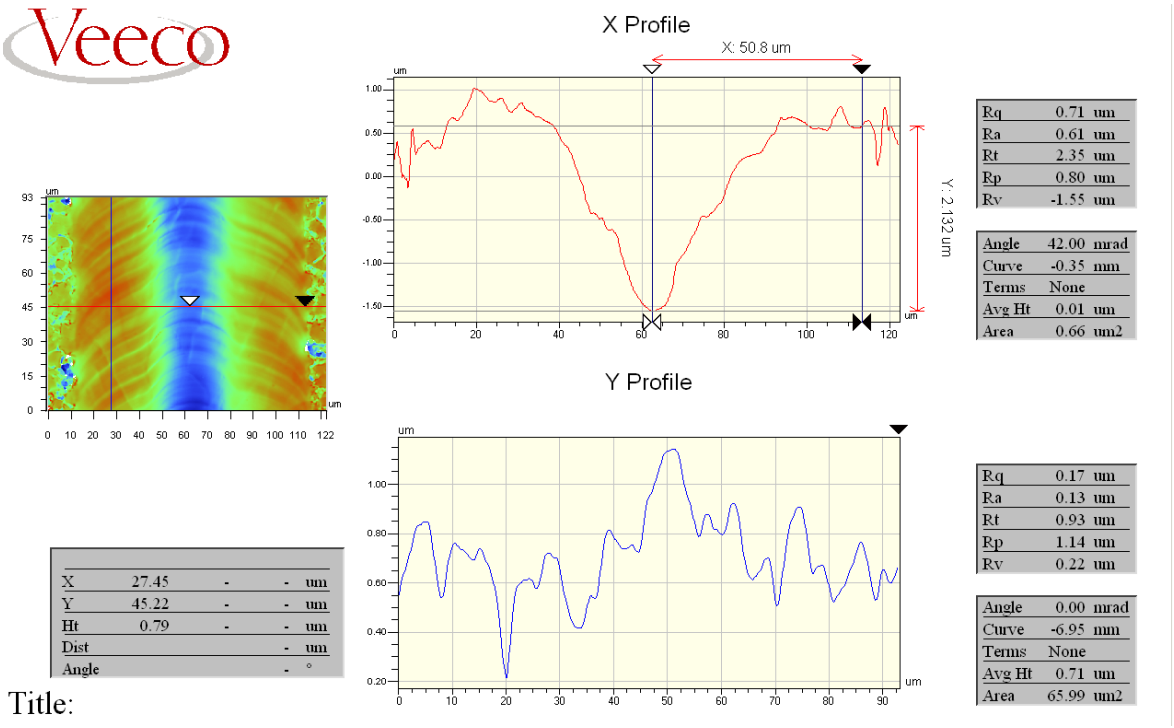

Figure 61. White light interferometer measurements of 304 SS irradiated with 13.57 kJ/cm^2, single pass with 40.6 µm spot size.

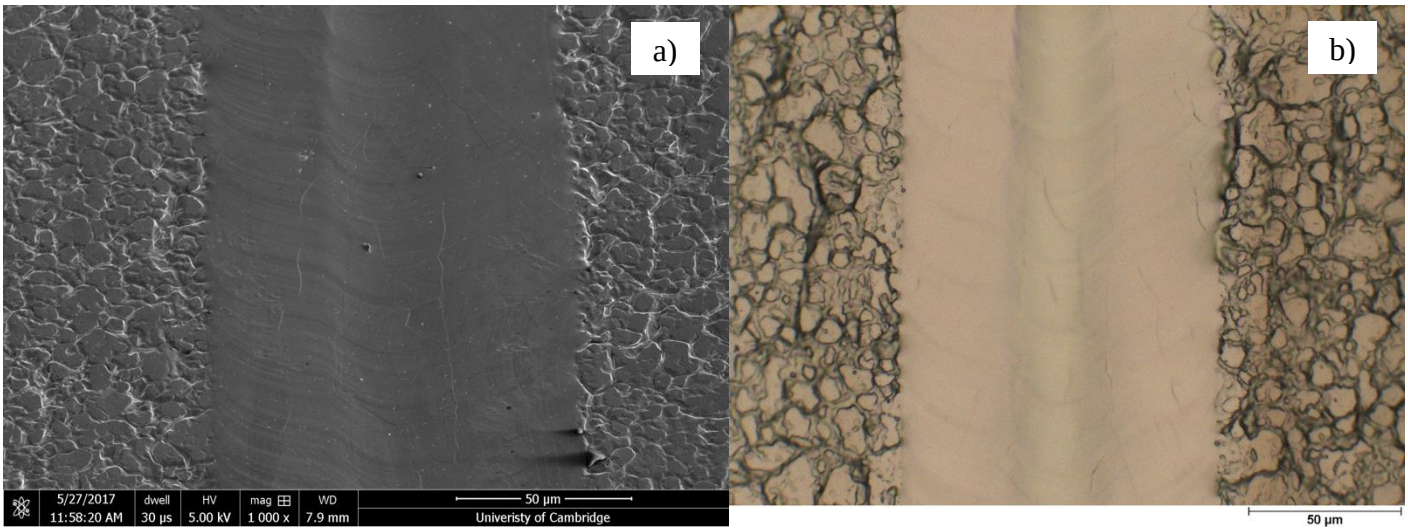

Figure 62. a) SEM and b) FIB images of 304 SS irradiated with 13.57 kJ/cm^2, double pass with 40.6 and 81.2 µm spot sizes, respectively.

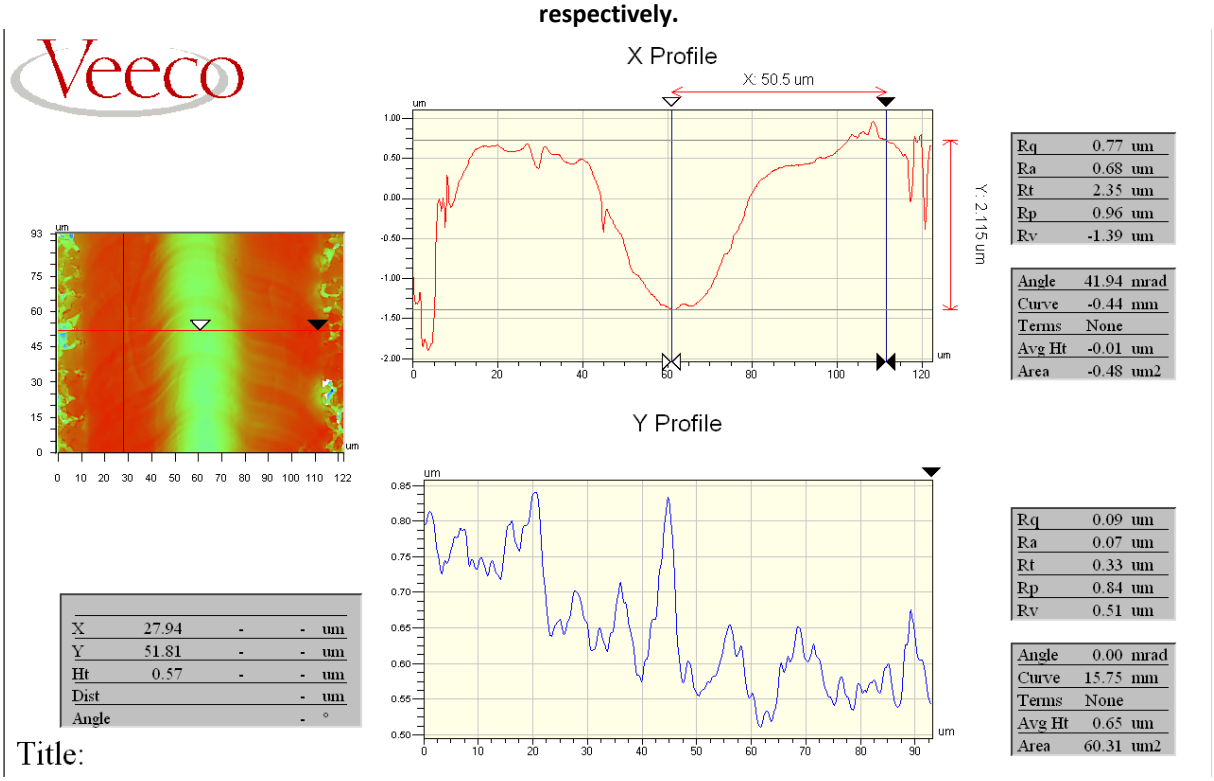

Figure 63. Interferometer measurements of 304 SS irradiated with 13.57 kJ/cm^2, double pass with 40.6 and 81.2 µm spot sizes, respectively.

The single crystal generated in Figure 59 did not grow to the expected 81.2 µm width of the spot size used. On the third pass with a spot size of ~121.8 µm the single crystal in the centre of the laser pass finally widened in the centre of the laser pass, Figure 64.

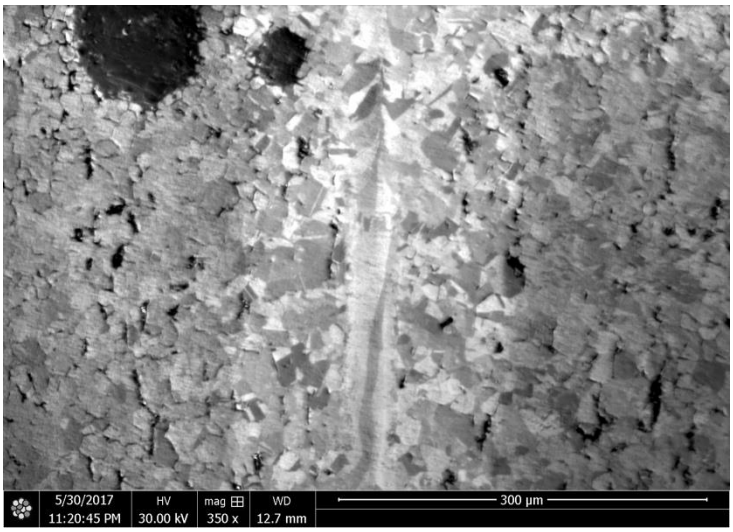

Figure 64. FIB image of 304 SS LSMed with 13.57 kJ/cm^2 single pass with 121.8 µm spot size.

It is suspected that changing the laser distrubution from gaussean to top hat, a more uniform energy distrubution, would refine the grains in the whole of the spot size thus icreasing the area of single crystal generation.

Multiple pass LSM with laser intensity of 13.57 kJ/cm^2 with 81.2 µm spot size.

Next, Figure 65 shows 304 SS irradiated with 81.2 µm spot size in diameter for both passes. Upon the second pass with the same laser parameters the centre grains are enlarged with the width of the spot size, as expected from the experiments in section 4.4, Figure 53.

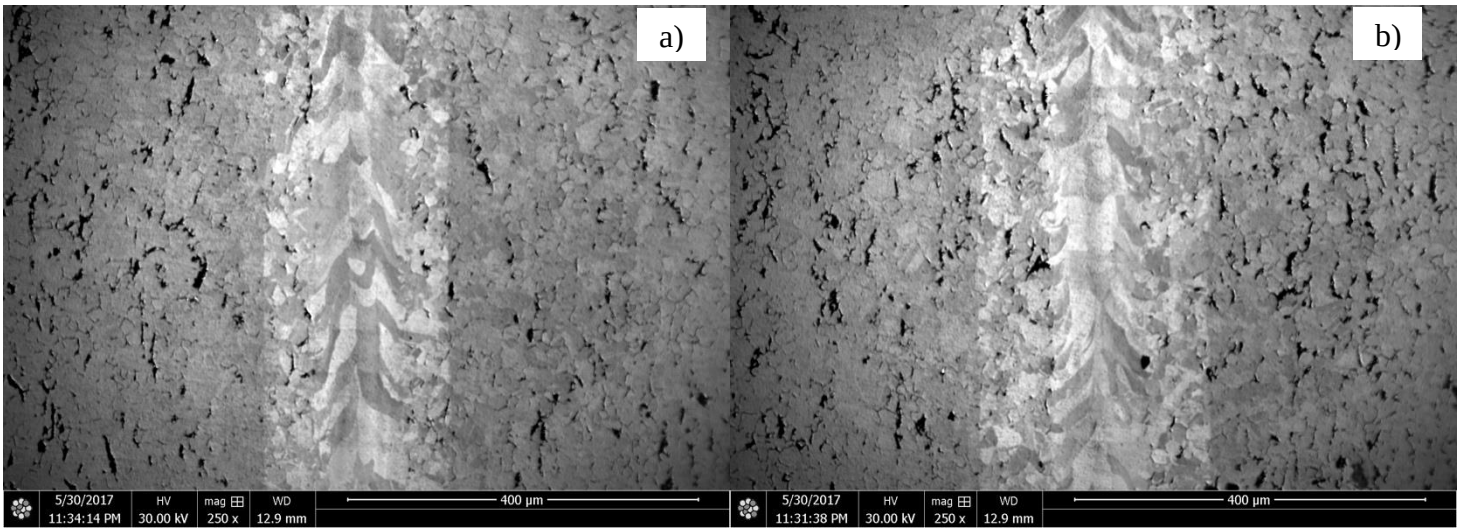

Figure 65. FIB images of 304 SS LSMed with a) 13.57 kJ/cm^2 single pass and b) 13.54 kJ/cm^2 double pass.

Multiple pass LSM with laser intensity of 19.15 kJ/cm^2 with a spot size of 40.6 µm.

Multiple passes with SPI SP200C CW laser yielded more pronounced single crystals and less surface ripples. Figure 77 shows 304SS microstructure after a single laser pass with 19.15 kJ/cm^2 in focus. The surface morphology does not ehibit any ripple structure, Figure 77 (a), contary to the result in Figure 52 (a) with almost the same laser intensity.

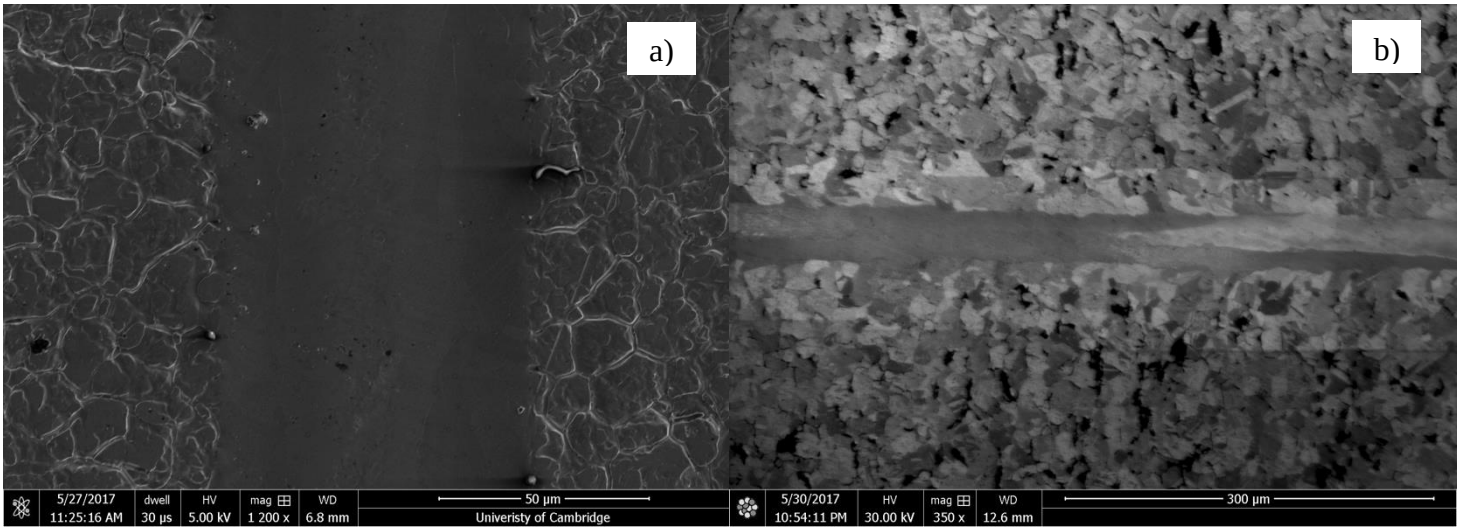

Figure 66. a) SEM and b) FIB images of 304 SS irradiated with 19.15 kJ/cm^2 laser intensity, single pass with 40.6 µm spot size.

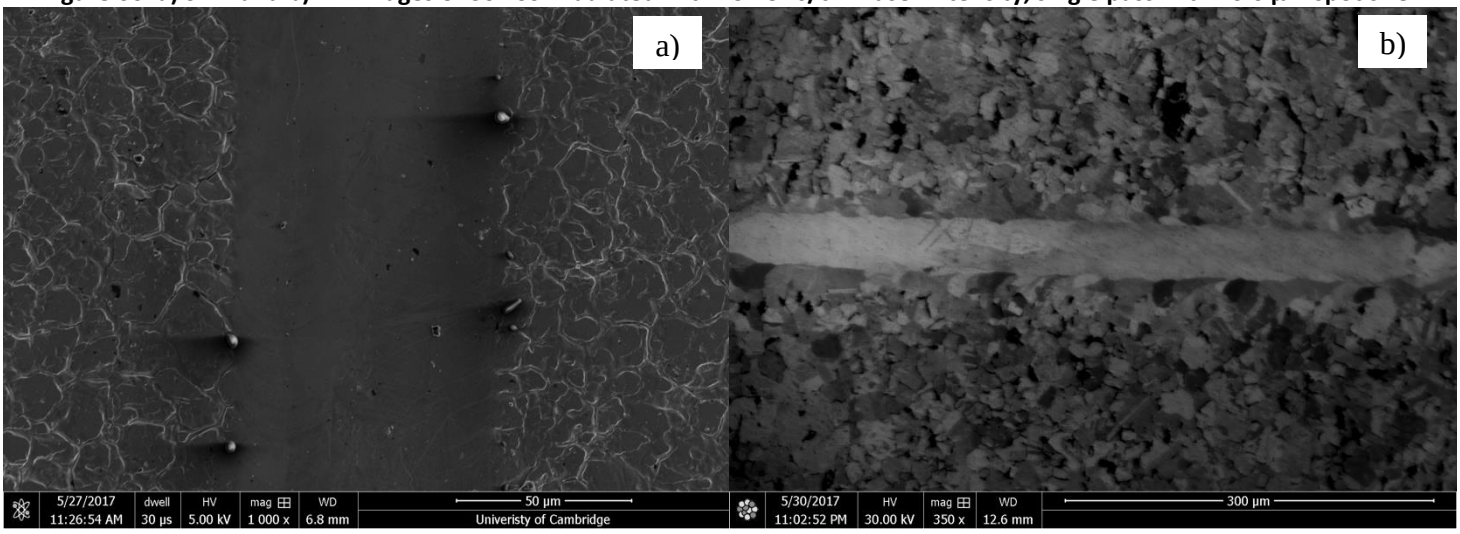

Figure 67. a) SEM and b) FIB images of 304 SS irradiated with 19.15 kJ/cm^2 laser intensity, double pass with 40.6 µm spot size.

Figure 67 shows a longer and wider single crystal grain generated with douple laser pass with 19.15 kJ/cm^2. Again, no surface ripples are observed.

Additional tests with laser ED of 19.15 kJ/cm^2 and increased spot size of 81.2 µm were conducted but proved to be innacurate due to the laser radiation striking the plastic cover cap containing the nitrogen environment, thus rendering the results inaccurate. Due to the damages to the plastic cap the trench was

not fully generated, however, the start of the laser pass came through and generated periodic surface structures, Figure 69.

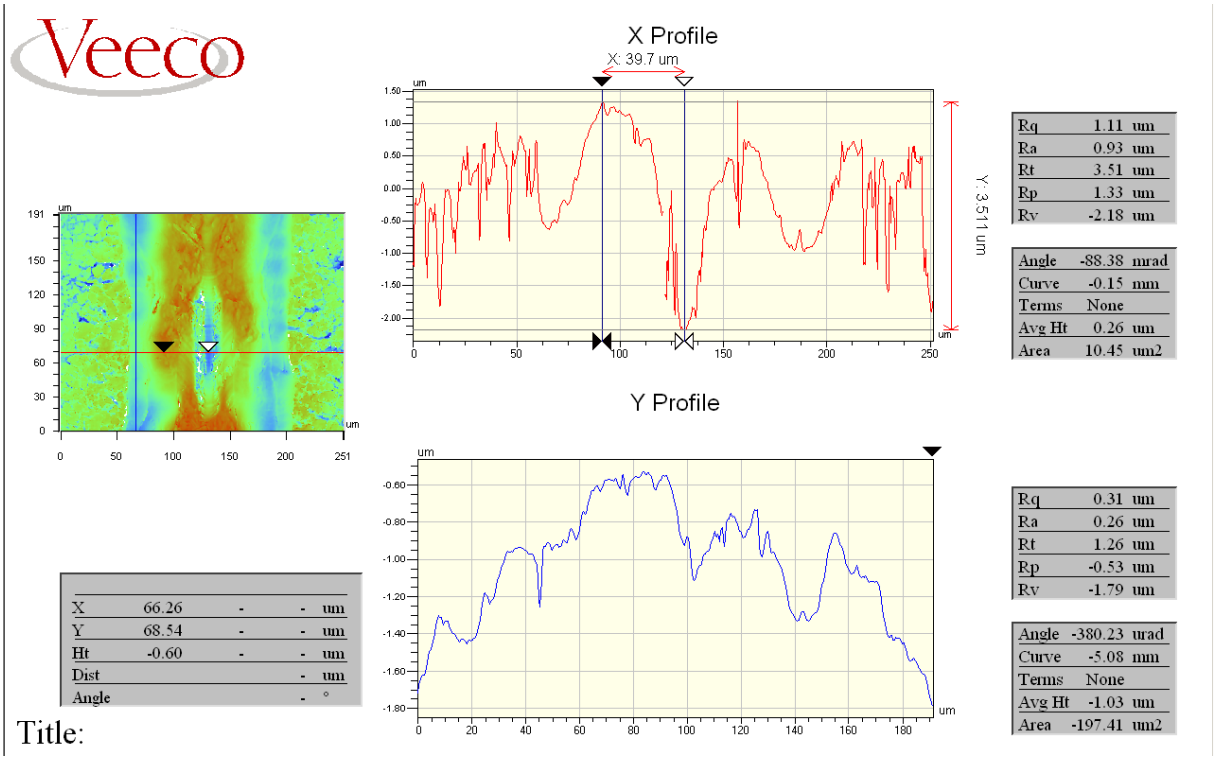

Figure 68. Interferometer measurements of 304 SS irradiated with 19.15 kJ/cm^2, double pass with 81.2 µm spot size.

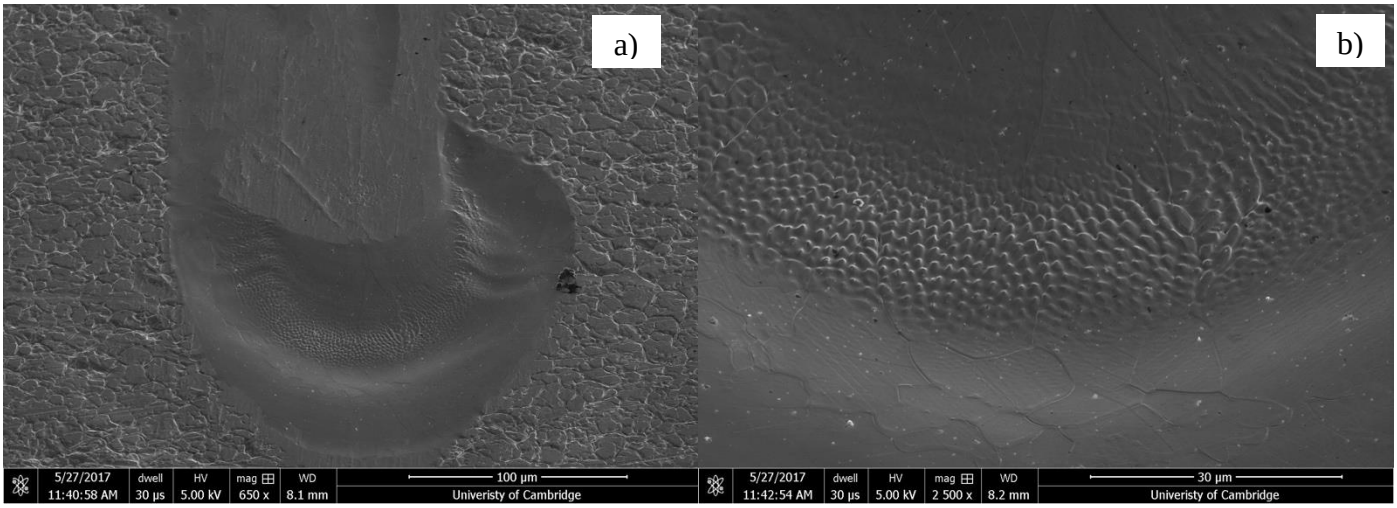

Figure 69. SEM images of 304 SS irradiated with 19.15 kJ/cm^2, single pass with 121.8 µm spot size, a) start of the laser pass, b) magnified image of the periodic surface structures.

Conclusions: doubling up the spot size mid grain transformation is inefficient in generating larger single crystals in the current work. There is a clear progression of centre grain enlargement with constant laser ED and beam spot. SPI SP200C CW laser experiments verified that single crystal generation is possible in the microstructure of 304 SS with multiple laser passes.

4.6. Spot Size Effect in Direct Grain Writing.

So far the direct grain writing effect has been observed in all metals with an average grain size < 99.88 μm^2 in CW LSM with a spot size ~40 μm in dimeter. Would the same effect be observed in samples with grains double the size? This section explores the dependence of the grain size on the direct grain writing with CW LSM.

Nickel has been chosen due to a larger average grain area, 170.94 μm^2, and similar to SS negative temperature gradient [149], [150], [151]. First, single-pass optimisation experiment was carried out to determine the line width of a melt path with the lowest roughness, spanning the average EDs used for CW LSM of 304SS. The tests were done with a minimum beam diameter calculated to be:

$$d_{\min} = \frac{4M^2 f\lambda}{\pi D} = 0.044\ (mm);\ d_{\min} = 44\ (\mu m) \quad (8)$$

The laser processing parameters are recorded in Table 16.

Table 16. Laser processing parameters for Ni single pass optimisation.

Scanning velocity (mm/s)	2 - 1000
Output power (W)	17
Shielding gas (l/min)	0.84

Figure 70 shows the relationship between line width/surface roughness and laser energy density. Twenty-two lines were generated with *ED* ranging from 0.04 to 12.88 kJ/cm^2 (see Appendix A for additional optical microscope images).

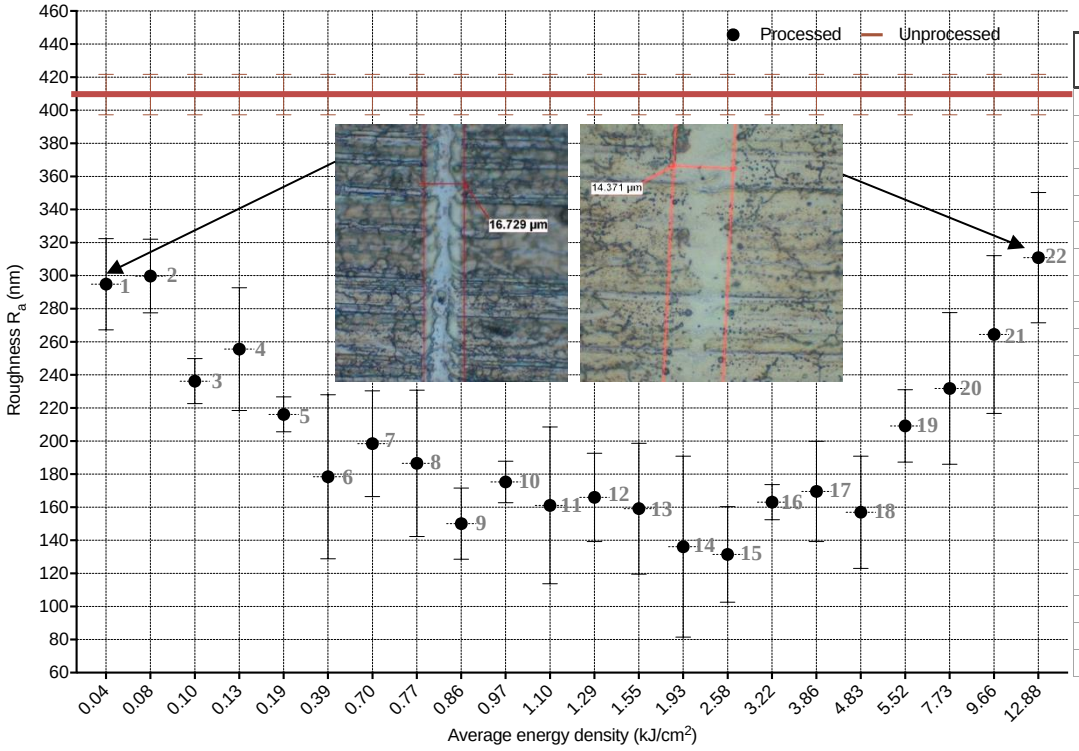

Line No.	Line width (μm)
1	16.73
2	16.62
3	19.28
4	19.83
5	20.20
6	19.66
7	19.63
8	20.46
9	20.67
10	21.19
11	23.56
12	23.00
13	24.43
14	22.33
15	25.85
16	20.88
17	26.36
18	24.77
19	26.68
20	25.45
21	17.70
22	14.37

Figure 70. Nickel roughness reduction results with CW SPI™ G3 fibre laser irradiation.

In the parameter domain used for 304 SS, the maximum roughness reduction was achieved for laser passes 6 to 18, ED of 4.83 to 0.39 kJ/cm^2. The line width did not follow the expected increase at higher EDs but instead measured the widest between 10 to 20. The laser radiation coupling of nickel is out of scope of the research and this phenomenon was not investigated further.

Next, to observe the effects of different average EDs on the grain growth the nickel samples were all raster scanned with the line spacing of 0.01 mm due to the line width being ~20 μm on average. Experimental conditions were replicated according to 304 SS sample in Figure 26. No elongation of the grains was observed, Figure 71.

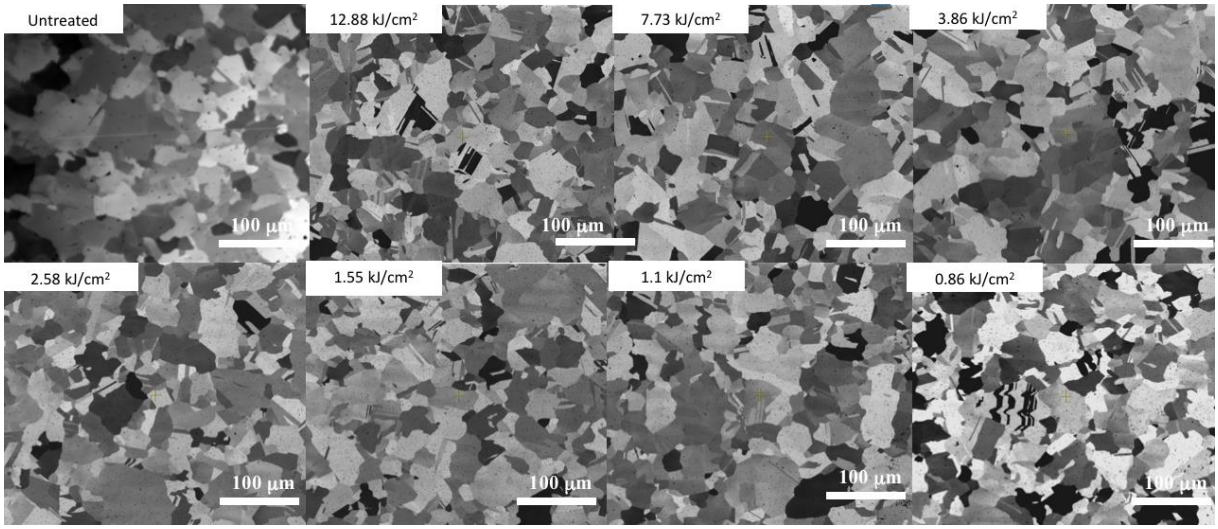

Figure 71. FIB images of LSM treated Ni with various average EDs. Optical images available in Appendix G.

It is suspected that the spot size was too small to capture the entirety of the grain in a melt path. Therefore, the following trials have been conducted with SPI SP200C CW in nitrogen with an increased spot size of 150 μm. The results showed the expected grain shaping. The grain elongation follows the laser scan direction, Figure 72.

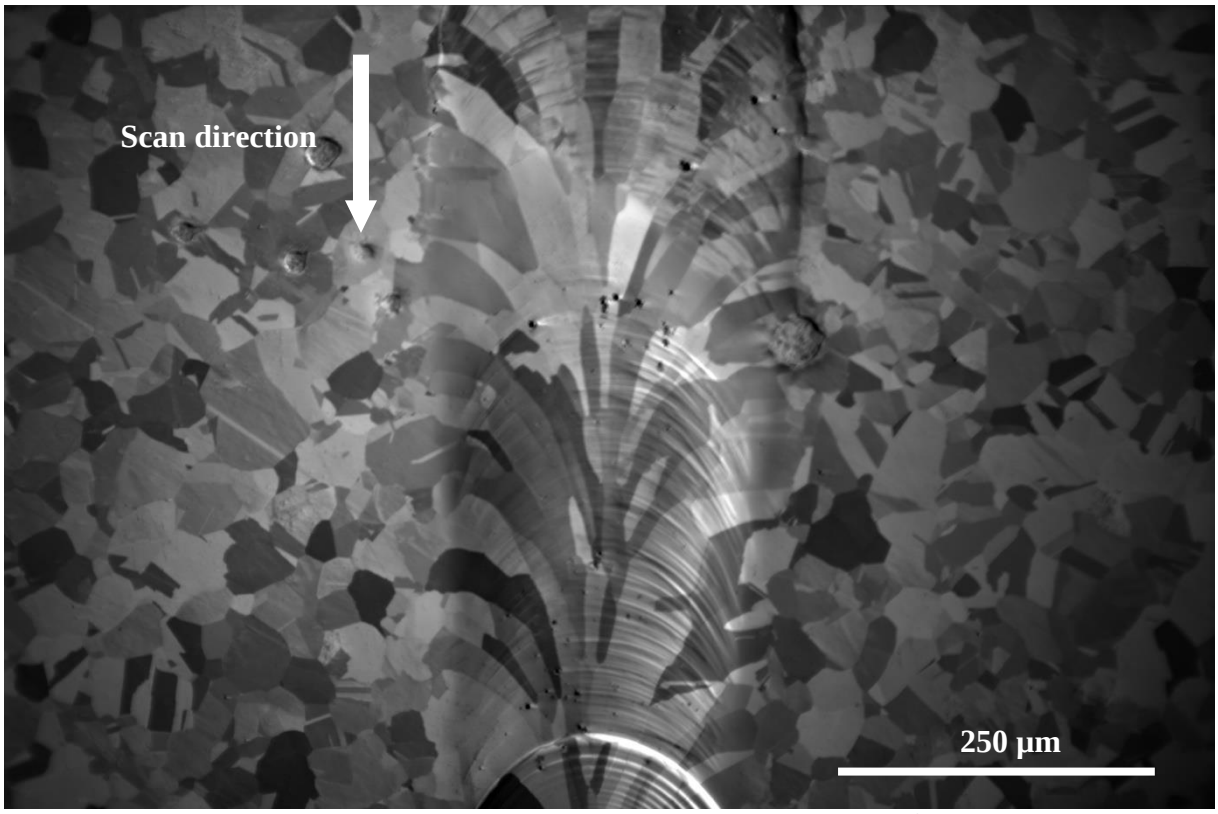

Figure 72. FIB image of nickel processed with 8.09 kJ/cm^2.

Surface quality after laser irradiation can be seen in Figure 72. The surface exhibits ripples away from the laser beam end point. This is attributed to Marangoni or thermocapillary flow [152]. The upwelling of the surface is towards the edges, away from the centre of the laser spot, indicating a negative surface tension gradient. The continuous meltpool created during CW laser melting experienced the highest temperature at its centre. The ripple effect can be minimised by reducing laser power or increasing the laser scan speed.

Figure 73 shows the surface quality of nickel, bi-raster scanned with 8.09 kJ/cm^2 average laser ED, illustrating the ripple effect and microstructural transformation dependence on the laser scan direction. The grains are increased in size and the number of the grain boundaries has been reduced, Table 17.

Table 17. Grain size and grain boundary character distribution per 0.32 mm^2 surface area. Palumbo-Aust criterion [130].

Grain size	**Untreated**	**Treated**
Min grain area [µm^2]	40	90
Max grain area [µm^2]	1316	3447
Average grain area [µm^2]	170.94	268.62
Grain boundary distribution		
Σ 3	35.63	24.02
Σ 9	4.91	3.58
$3 < \sum \leq 29$	41.40	28.09
$29 < \sum \leq 49$	0.037	0.04

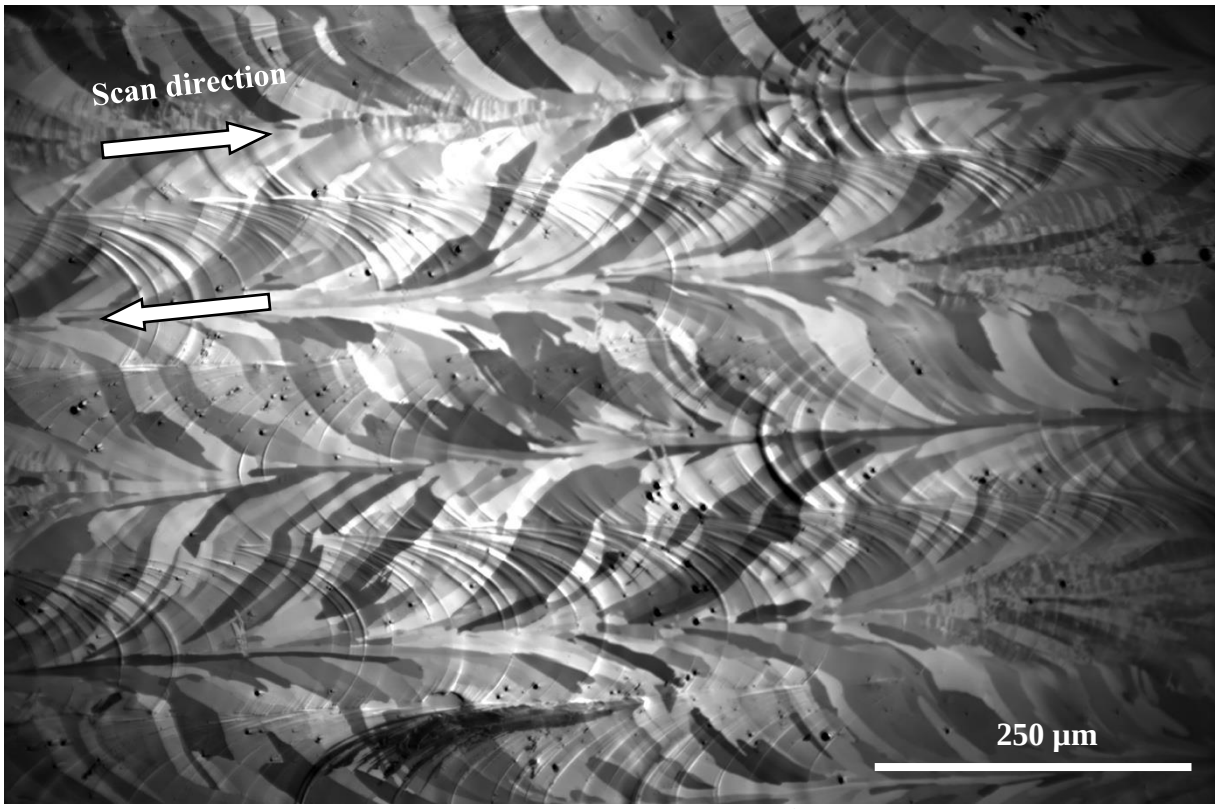

Figure 73. FIB image of nickel processed with 8.09 kJ/cm^2, line spacing 0.15 mm.

In conclusion, the direct grain writing with CW LSM in 304 SS and Ni requires the laser spot size to generate surface melt larger or equal to the grain size.

4.6.1. Copper Laser Surface Melting and its Microstructure Analysis.

Copper, C101 and OHFC, a material with a temperature gradient >>SS and Ni, was tested for the grain shaping and spot-grain size relationship. The average grain size is recorded in Table 18.

Table 18. Grain size comparison of C101 and OHFC copper against 304 SS, 3 mm thickness.

	304SS Untreated, per 0.12 mm^2	C101 Cu, per 0.036 mm^2	OFHC Cu, per 0.049 mm^2
	Area (µm^2)	Area (µm^2)	Area (µm^2)
Average	99.88	18.55	42.53
Min	40.00	3.60	10.00
Max	628.00	259.92	792.00

For Cu treatments with 1064 nm SPI SP200C CW the reflectance of the samples had to be reduced. According to Fresnel equations describing the behaviour of light when moving between media [153], the Cu reflectance can be reduced up to 0.54 % if the light passes through 100 nm thick titanium media, Figure 74.

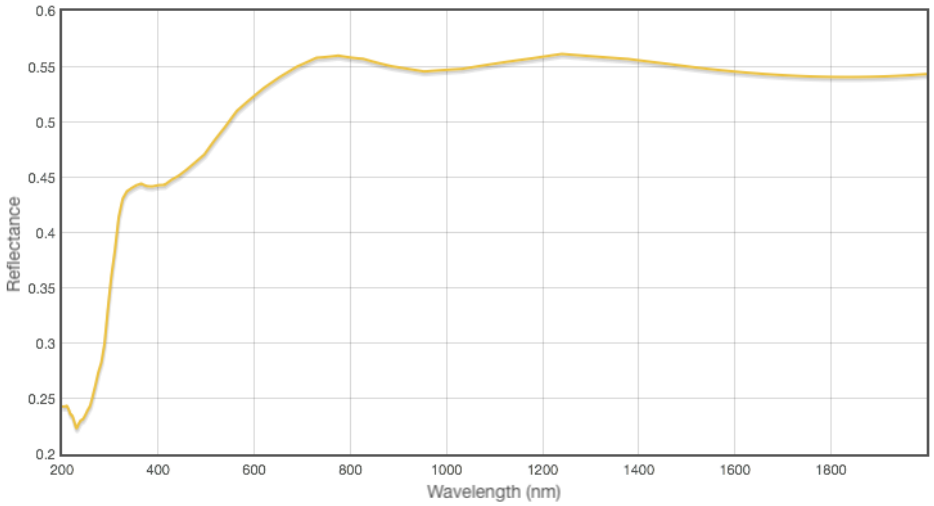

Figure 74. Light reflectance for air – 100 nm thick titanium layer – Cu.

The Cu samples have been sputtered with Titanium, ~100 nm thick, to reduce reflectivity. The maximum laser spot size with enough average laser energy density to melt copper was ~66 μm in diameter. The spot size appears to be smaller than the sample's grain size in the irradiated area, Figure 75, and is suspected to be the reason for no microstructural transformation.

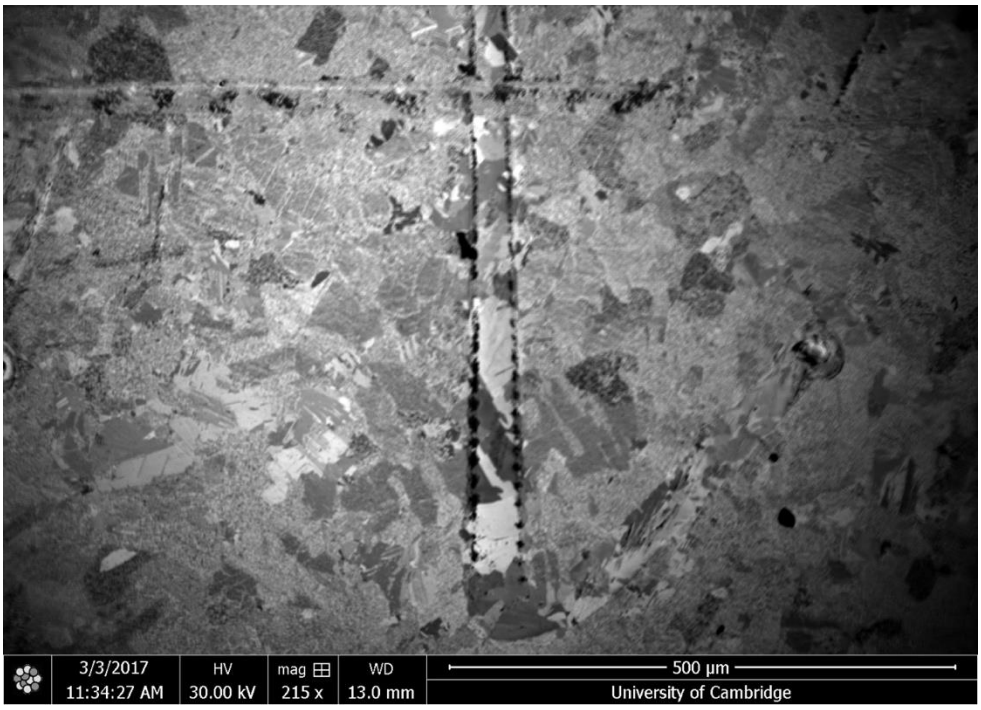

Figure 75. FIB image of Cu C101 coated with 100 nm Ti treated with 18.93 kJ/cm2.

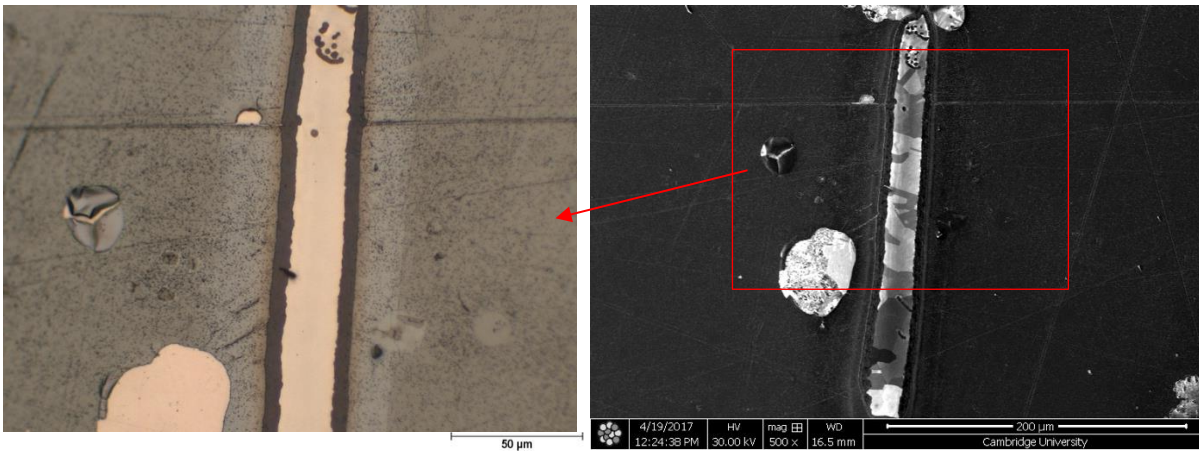

Figure 76. OFHC Cu coated with 100 nm Ti, treated with 50.5 kJ/cm2 a) optical and b) FIB images.

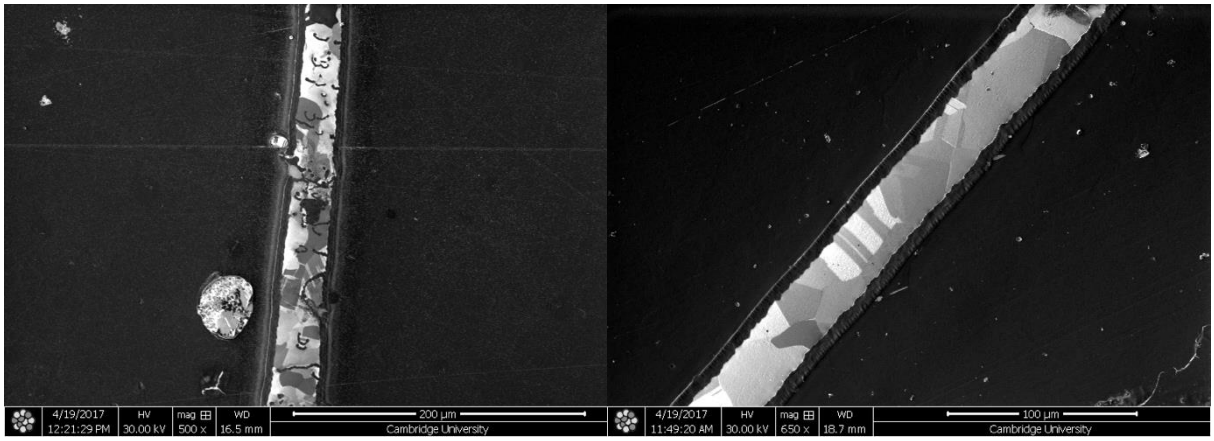

Figure 77. FIB image of a) OHFC Cu treated with 45.45 kJ/cm^2 and b) Cu C101 treated with 64.93 kJ/cm^2.

To verify this discovery additional tests with a 532 nm wavelength laser have been undertaken on the copper samples.

C101, 3 mm thick, has been mechanically polished to R_a of ~13.80 nm. The sample then was processed by scanning the 532 nm wavelength CW laser beam across the surface at 14.37 degree angle to normal. Moving the laser head in the Z axis allowed to generate X distance to establish the approximate angle value to normal, Figure 77(b).

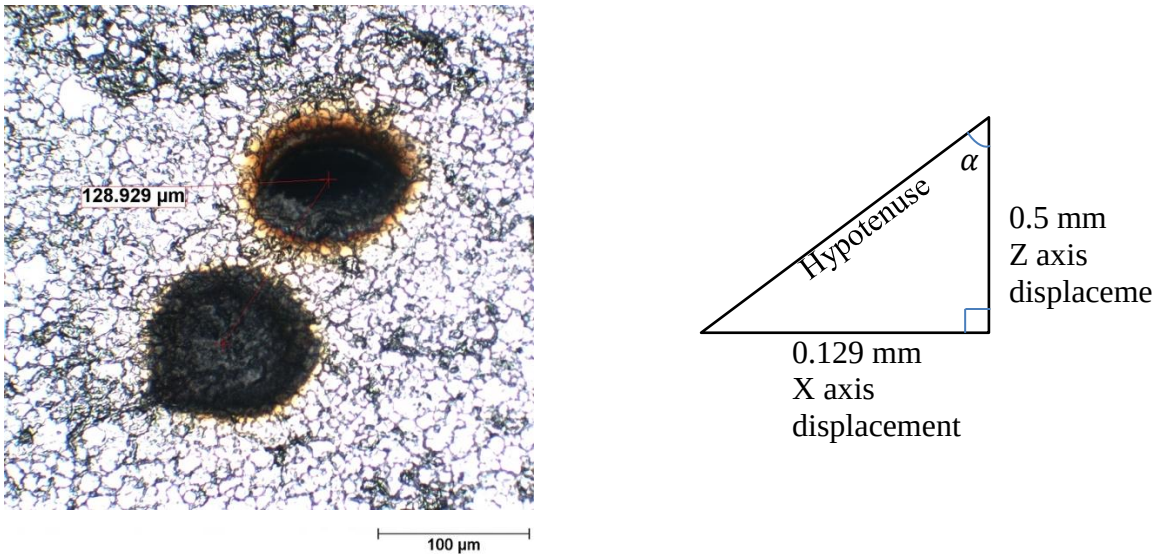

Figure 78. Angle calculation based on optical image of the distance between two laser spots.

Using formula:

$$\sin\alpha = \frac{X\ displacement}{Hypotenuse}$$

The incidence angle to normal is:

$$\sin\alpha = \frac{0.129}{0.52} = 14.37^{\circ}$$

The following set of lines was generated in argon, nitrogen and vacuum environments (O_2 levels of 0.1 %). Each laser parameter was tested twice in the form of two consecutive lines, Figure 79. The power remained constant while the scanning velocity was varied, Table 19.

Table 19. Laser parameters for processing C101 Cu with Verdi G20.

Scanning velocity (mm/s)	0.01-1
Output power (W)	14.8
Spot size diameter (µm)	8.28
Line spacing (mm)	0.04

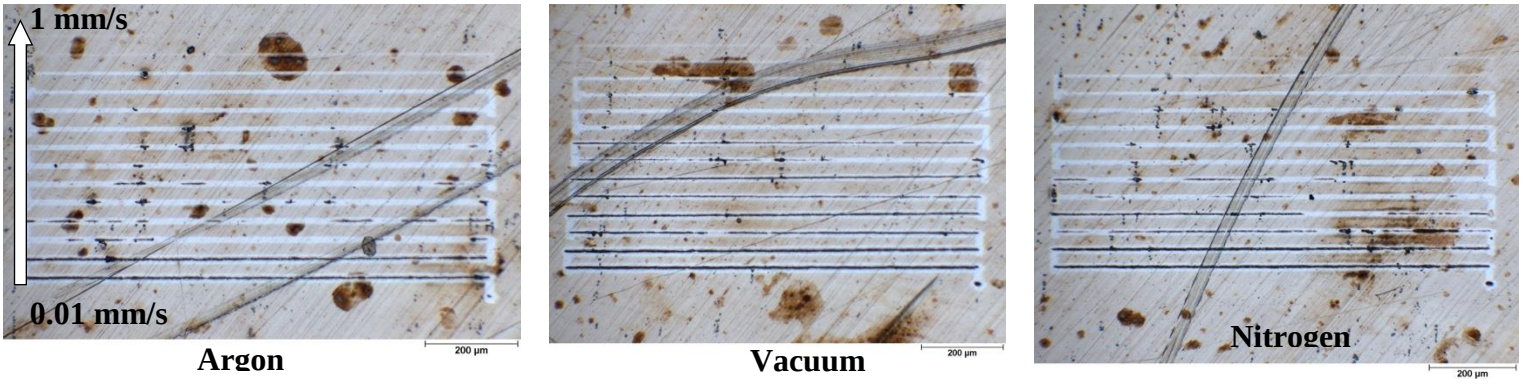

Figure 79. Optical images of the processed C101 Cu sample.

The black lines are the LIPSS formation, Figure 80. It is observed that vacuum environment promotes LIPSS at slower scanning velocities, 0.01 – 0.1 mm/s (laser energy densities, 18.50 – 1.85 MJ/cm^2).

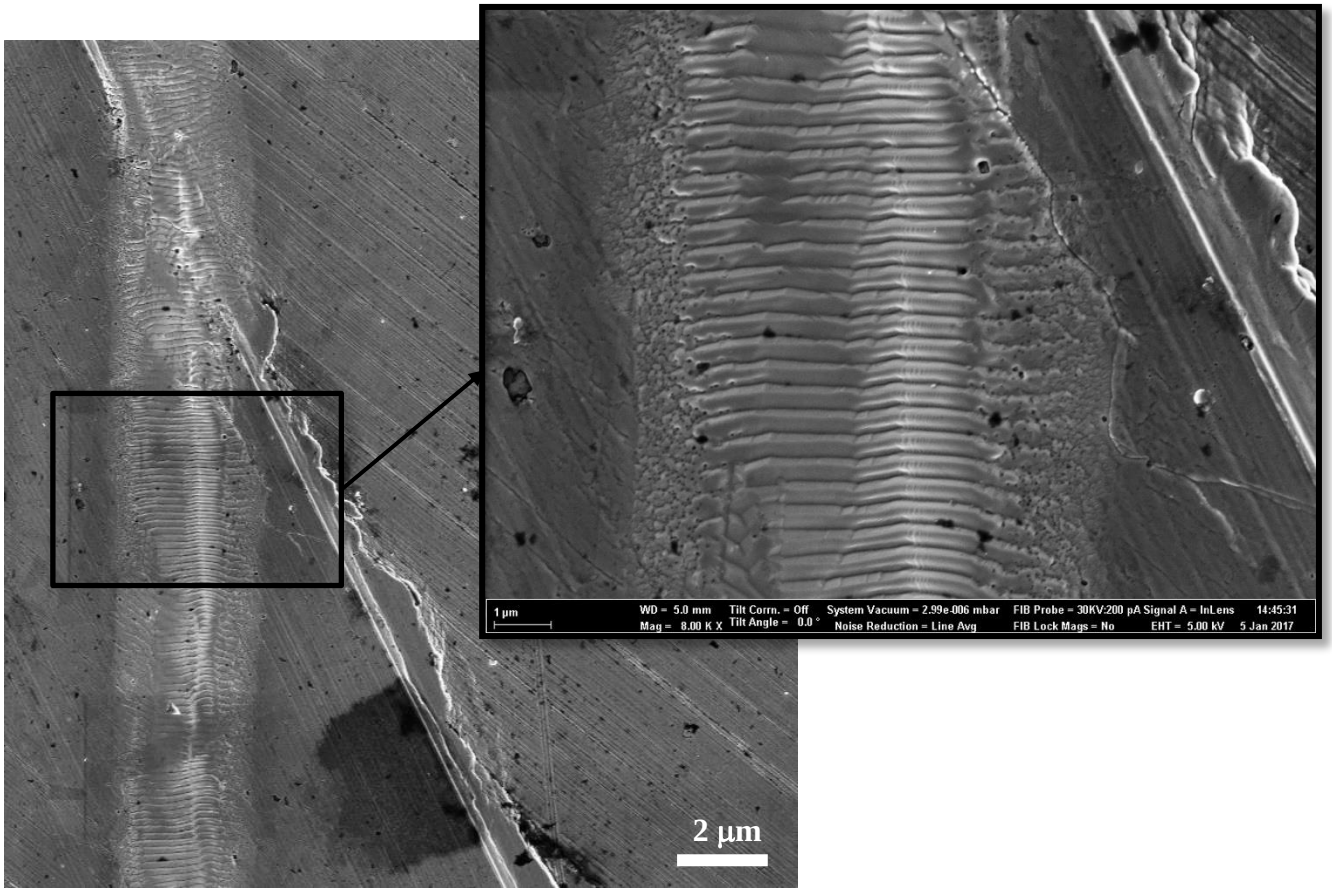

Figure 80. SEM image of line 0.01 mm/s in argon.

For argon environment, scan speeds > 0.05 mm/s have little effect on the surface structure, Figure 81.

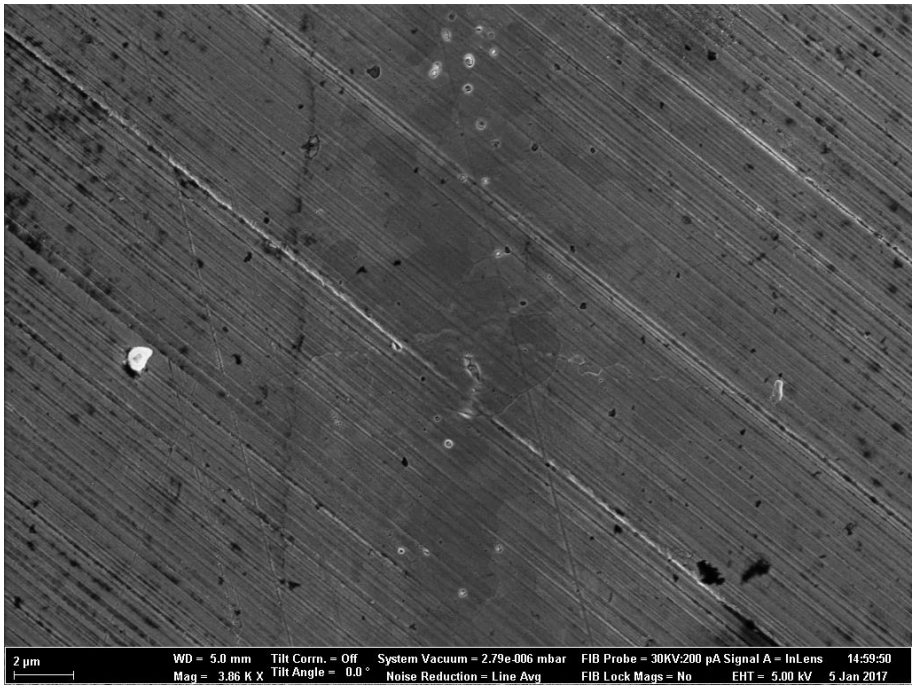

Figure 81. SEM image of line 0.05 mm/s in argon.

More prominent LIPSS are observed for lines generated in vacuum environment, Figure 82.

Figure 82. SEM image of line 0.01 mm/s in vacuum.

The LIPSS persist till 0.1 mm/s scan velocity, Figure 83(a). The surface metamorphosis stops at 0.3 mm/s with what appears to be surface cleaning, Figure 83(b).

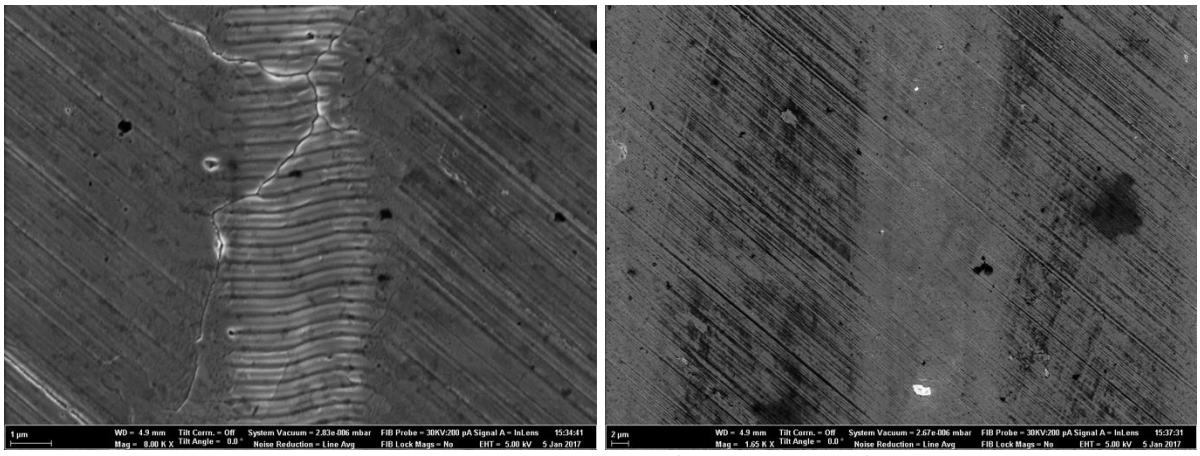

Figure 83. a) SEM image of line a) 0.1 mm/s and b) 0.3 mm/s in vacuum.

For lines generated in nitrogen environment, the LIPSS are observed between 0.01 – 0.05 mm/s, Figure 84 (a, b), with surface cleaning at 0.1 mm/s, Figure 84 (c).

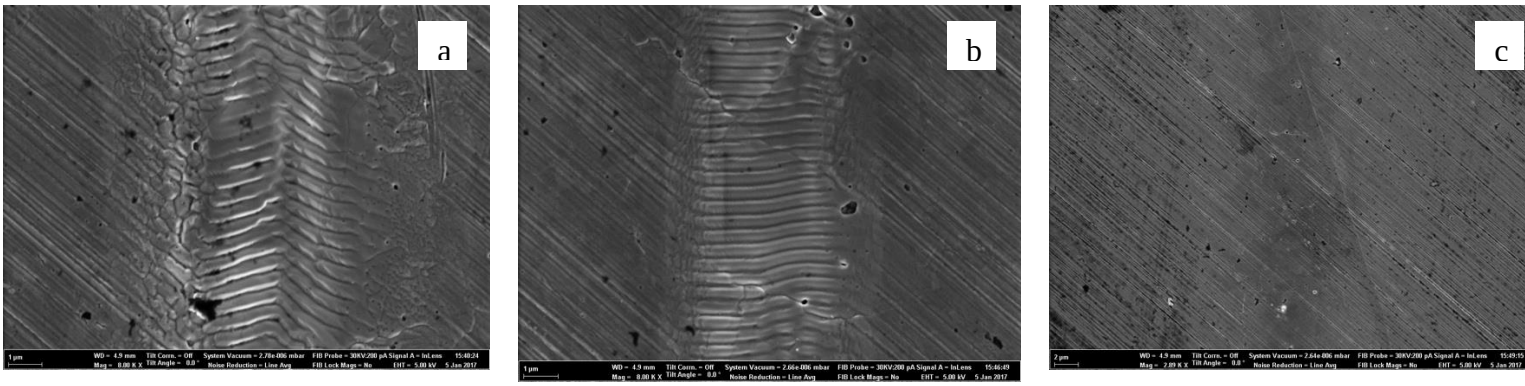

Figure 84. SEM images of lines a) 0.01 mm/s, b) 0.05 mm/s and c) 0.1 mm/s in nitrogen.

It is also observed that the line spacing has a direct effect on LIPSS generation, Figure 85. The samples were raster scanned with constant power and scan velocity, varying only the line spacing, Table 20.

Table 20. Raster scanning laser parameters.

Scanning velocity (mm/s)	0.5
Output power (W)	14.8
Spot size diameter (μm)	8.28
Line spacing (μm)	2 - 14

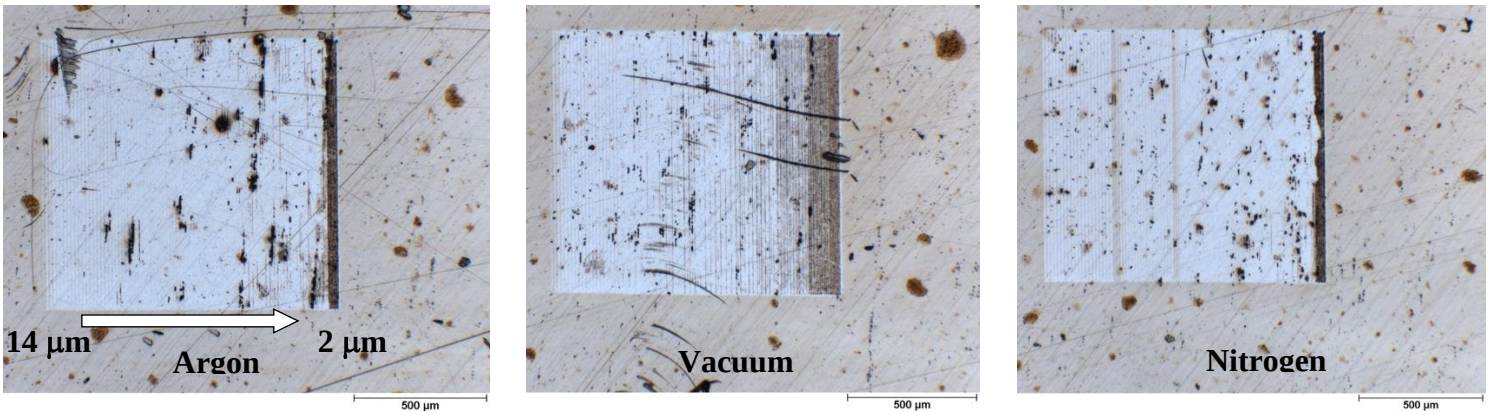

Figure 85. Optical images of raster scanned C101 Cu sample.

Scan velocity of 0.5 mm/s is chosen to minimise any surface metamorphosis. However, with lines now overlapping, LIPSS are formed in all environments with vacuum environment displaying the largest amount again, Figure 85. Figure 86 shows the examination of the LIPSS formed in nitrogen with 2 μm line spacing.

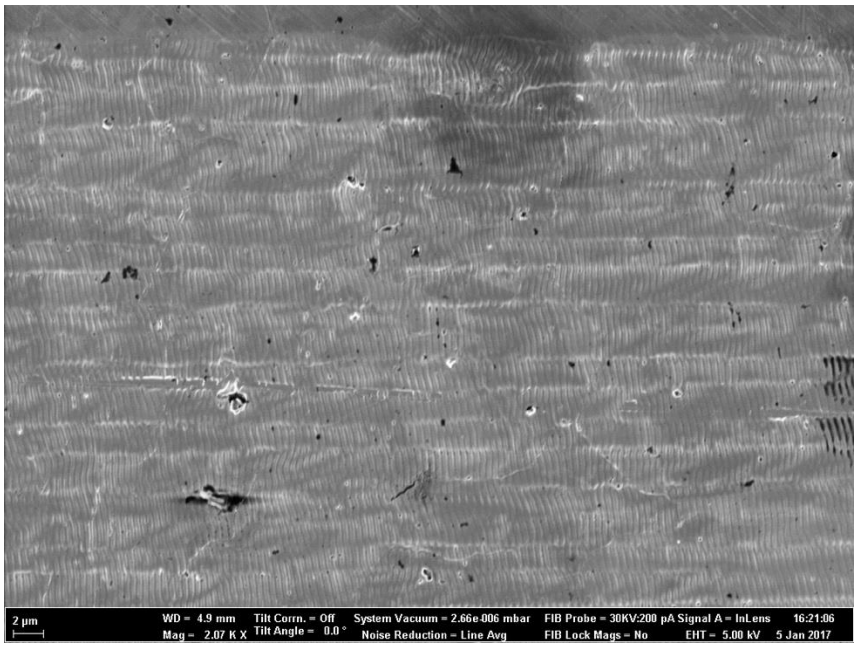

Figure 86. SEM image of LIPSS in nitrogen with 2 µm line spacing.

To summarise, evacuated environment amplifies LIPSS generation. Argon and nitrogen gases exhibit little difference on surface structuring for laser parameters tested. Line overlap plays an important role in LIPSS generation; the larger the overlap the more prominent are the LIPSS.

In further pursuit of the surface melt, increased laser energy density trials were conducted, Table 21. Once again, each laser parameter is tested twice in the form of two consecutive lines, Figure 87. The testing was conducted in argon environment to minimise LIPSS generation, according to the previous findings.

Table 21. C101 Cu processing with increased laser energy density parameters for Verdi G20.

Scanning velocity (mm/s)	0.001 – 0.008
Output power (W)	14.8
Spot size diameter (µm)	8.28
Line spacing (µm)	0.09

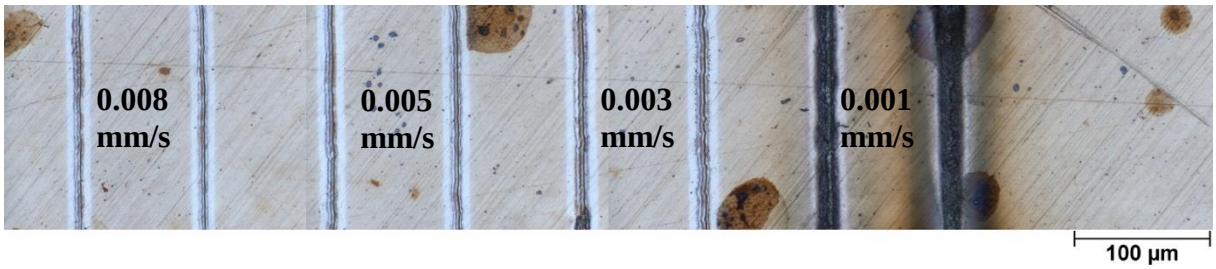

Figure 87. Optical image of the increased laser energy density processing of C101 Cu sample.

Increased scan velocities show LIPSS generation once again, Figure 88. No melt is detected.

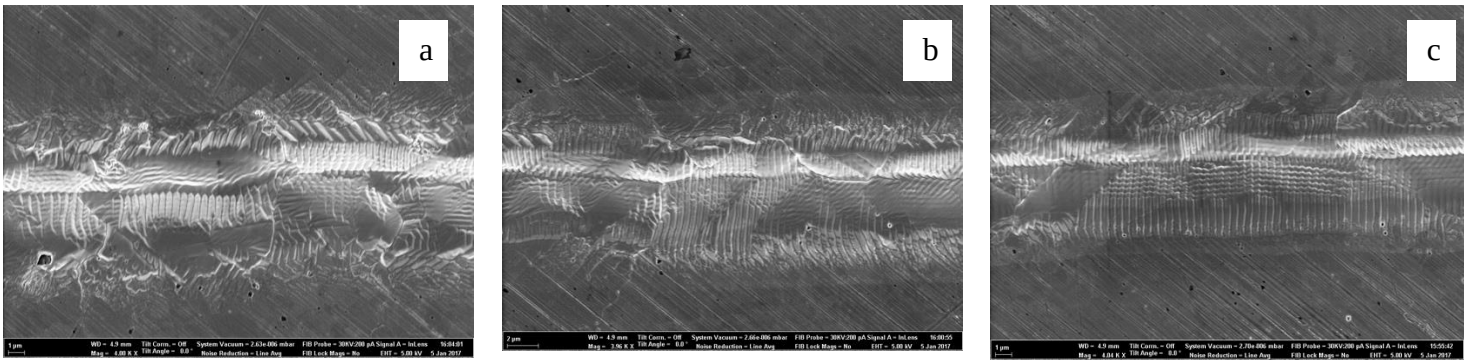

Figure 88. SEM images of lines a) 0.003 mm/s, b) 0.005 mm/s and c) 0.008 mm/s.

The result in Figure 89 appears to show a start of ablation due to increased debris present.

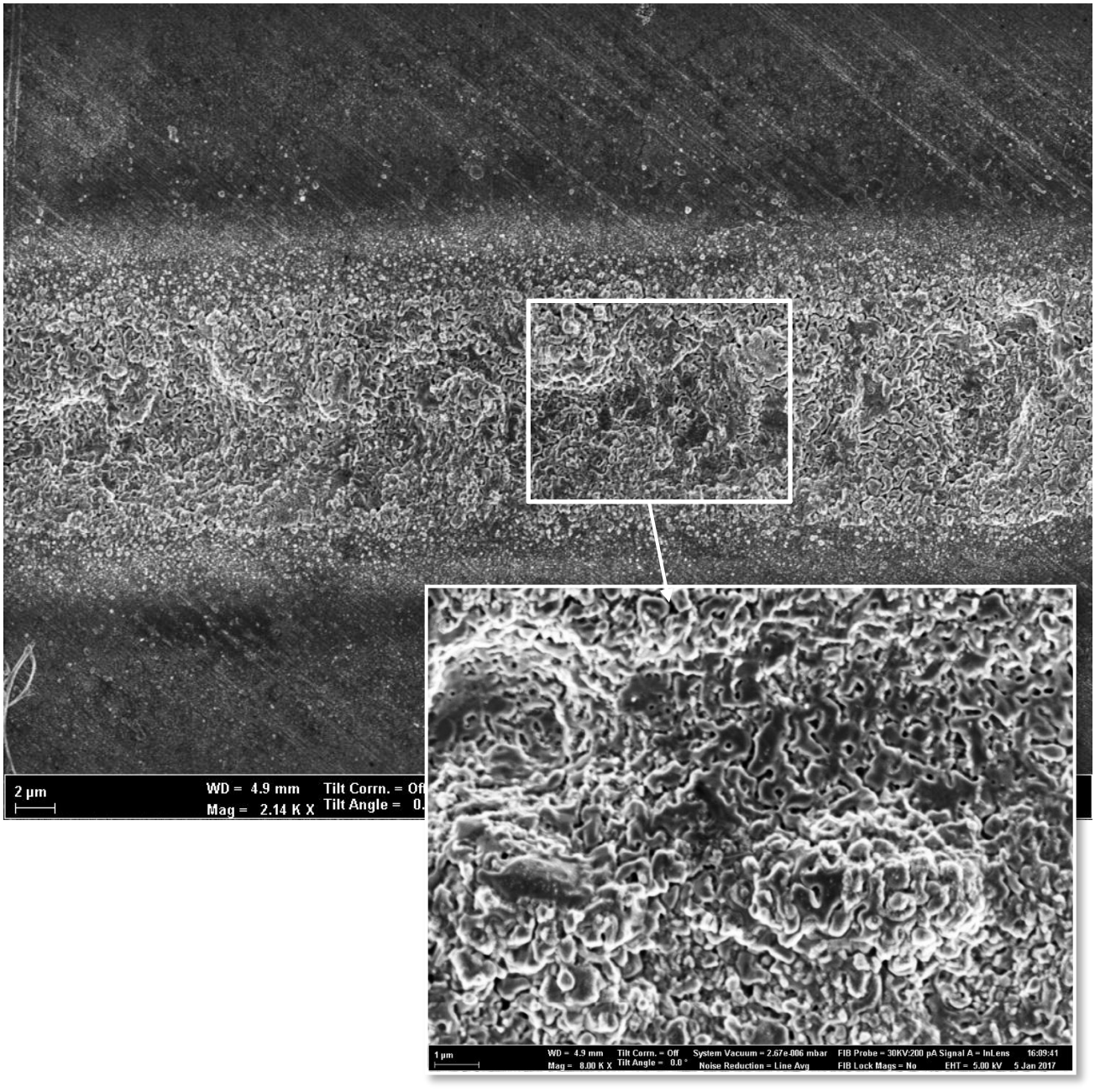

Figure 89. SEM image of line generated with 0.001 mm/s in argon.

In conclusion, the laser energy density of 178 MJ/cm^2, 0.001 mm/s, exhibits the start of ablation. Therefore, it is suspected that surface melting can be achieved in this region of energy density parameter domain (between ablation and LIPSS generation). It is recommended to test < 178 MJ/cm^2 < laser energy densities.

4.5.1.1. Copper LIPSS Microstructural Characterisation.

For microstructural characterisation, two samples of OFHC Cu, 0.91 mm thick, were processed by raster scanning the CW laser beam across the surface with constant laser power and line spacing, varying only scan velocity, Table 22.

Table 22. Laser parameters for OFHC Cu treatment for microstructural characterisation.

Scanning velocity (mm/s)	0.5, 1
Output power (W)	14.8
Spot size diameter (μm)	8.28
Line spacing (μm)	0.004

The 0.5 mm/s scan velocity generated the LIPSS, Figure 90.

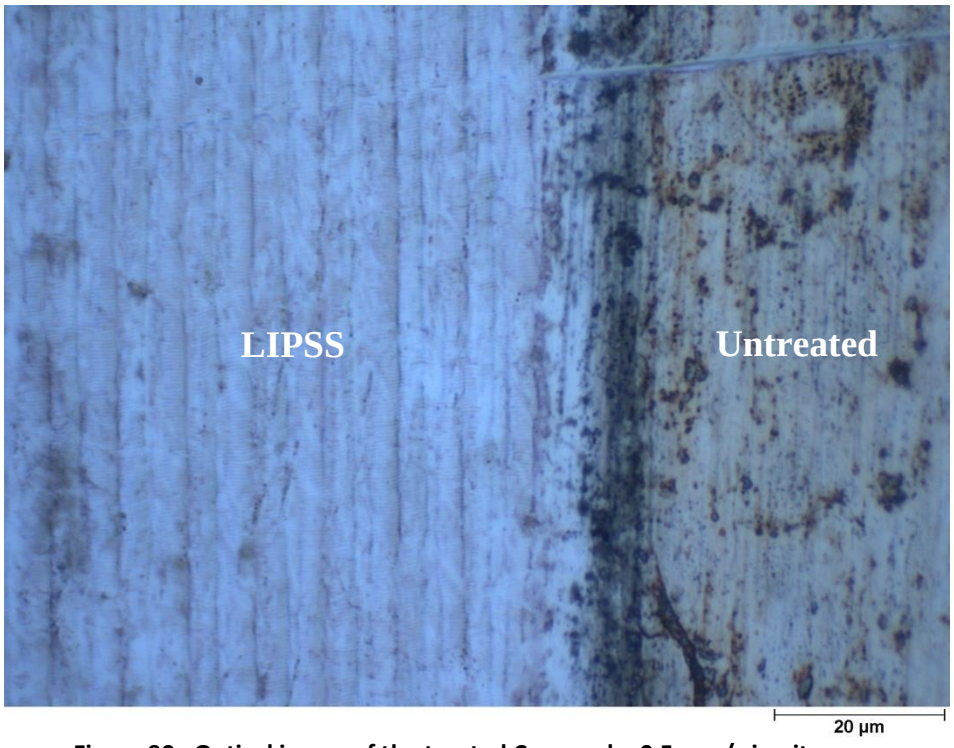

Figure 90. Optical image of the treated Cu sample, 0.5 mm/s in nitrogen.

The surface microstructure has been observed. The grains appear to have increased in size in the laser treated region, Figure 91.

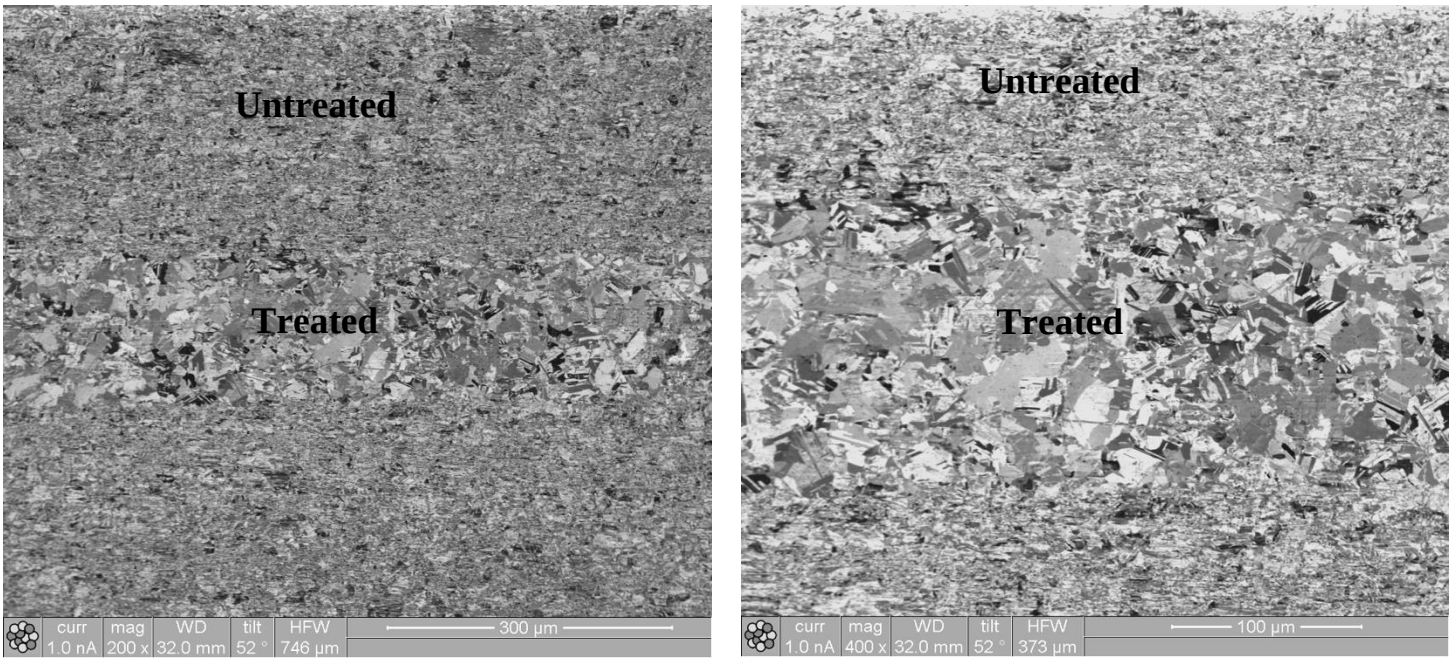

Figure 91. FIB images of the treated Cu sample, 0.5 mm/s in nitrogen.

The same happened for the Cu sample treated with increased scan velocity of 1 mm/s, which demonstrated the surface cleaning effect, Figure 92. Nevertheless, the microstructure exhibits similar grain increase, Figure 93.

Figure 92. Optical image of the treated Cu sample, 1 mm/s in nitrogen.

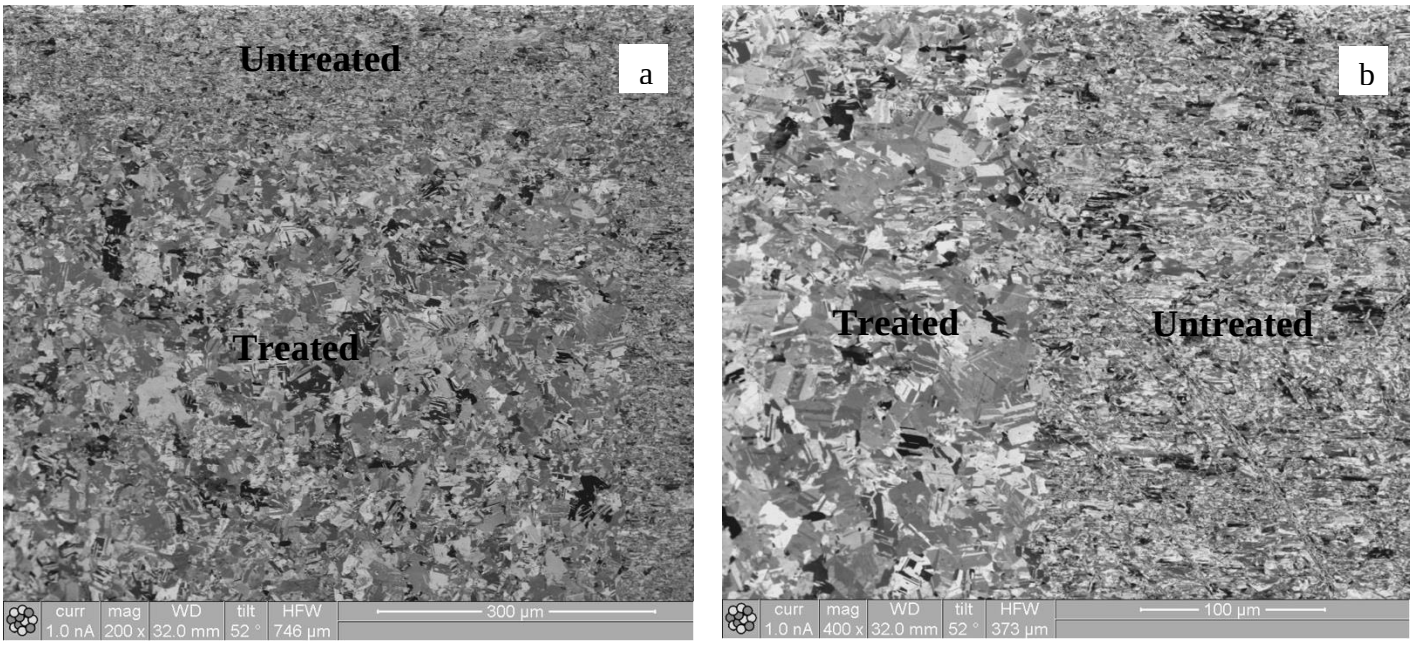

Figure 93. a) FIB image of the treated Cu sample, 1 mm/s in nitrogen.

Both LIPSS and surface cleaning laser parameters induce microstructural transformations in the Cu samples. The grains do not follow the stated spot size theory for grain refinement. This is attributed to copper's increased thermal gradient, Table 29.

Table 23. Thermal conductivity of SS, Ni and Copper [154].

Stainless Steel	45 W/mK
Nickel	90 W/mK
Copper	385 W/mK

The following is forwarded to the Future work Chapter:

- Quantify the grain size increase with EBSD testing in OFHC Cu treated with 0.5 and 1 mm/s.
- Increased laser spot size trials.
- For faster manufacturing of samples, a 532 nm wavelength CW laser system with increased laser power is required.

4.7. Pulsed Laser Radiation Direct Grain Writing.

Direct grain writing is not unique to CW laser melting. This phenomenon has been observed in pulsed laser melting of steel samples for surface roughness reduction. A 304 SS has been treated with picosecond fibre laser with wavelength 1.064 μm [100]. The roughness R_a was reduced from 140 nm to 70 nm. Laser processing parameters are recorded in Table 24.

Table 24. PLM Laser Parameters [100].

Energy per pulse (μJ)	2.08
Spot size (μm)	21
Pulse duration (ps)	100

Repetition rate (MHz)	7.2

The microstructure of the PLM treated samples from [100] have been then analysed using FIB imaging, Figure 94. Additional laser track images are available in Appendix H.

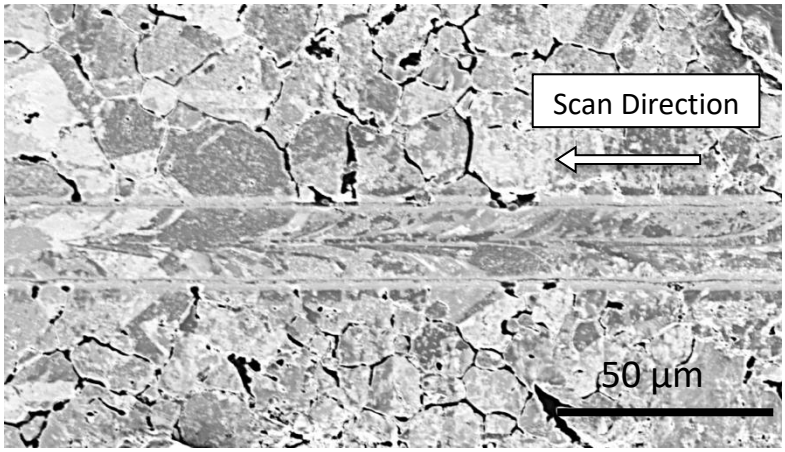

Figure 94. FIB image of the PLM generated laser track on 304 SS sample.

It can be observed that the grains, effected by the laser radiation, become elongated once again in the direction of laser scan, proving the two processes, PLM and CW LSM treatments, are regulated by the same mechanism.

4.8. LSM treatment of Metal Substrates for CVD Graphene Growth.

CVD growth requires high temperatures, therefore metal substrates are likely to outgas. This disrupts the growth of graphene nanostructures, resulting in imperfections in its crystal lattice [155]. To minimise the substrate's diffusion, annealing is applied, causing grain growth in the metal, thus reducing the number of the grain boundaries, through which the outgassing occurs. Studies on single crystal and polycrystalline nickel substrates showed that 1-2 layer graphene grows on top of the flat single-crystal grains and multilayer graphene usually grows at the grain boundary regions [156]. For the application of graphene-based devices, the growth of single layer graphene is of interest, thus obtaining large grains in the substrate is favourable in minimising the non-uniformity of the produced graphene film.

LSM can be used as an alternative method to thermal annealing to minimise the outgassing of CVD substrates and generate single crystal microstructure in them.

- Thickness and Surface Qualities of the CVD Substrates.

  The thickness of the Ni films is directly related with the time it requires to form a graphene layer, Figure 95, as the carbon atoms need time to reach the saturation state (a state in which a chain of carbon atoms is linked together by single bonds). However, the saturation time is not

the main time constraint parameter, before that the C atoms must diffuse into the Ni substrate. The speed of C solubility can be promoted by increasing the processing temperature, Figure 96, the higher the temperature the faster is the diffusion. As a result, the thinner the Ni substrate the less time it takes for C atoms to diffuse and reach the saturation state in it. Additionally, surface of the substrate must be as smooth as possible to avoid irregularities in the graphene nanostructure.

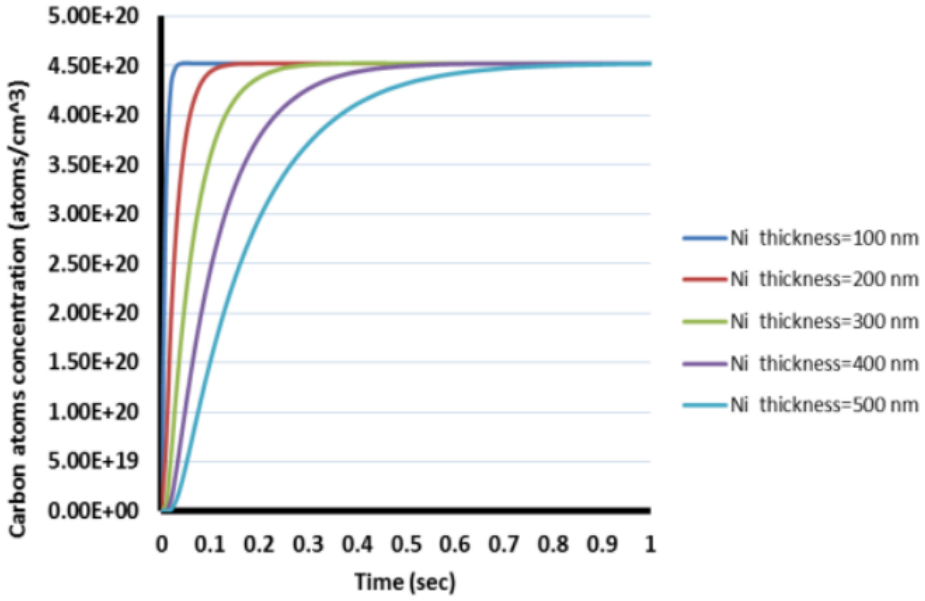

Figure 95. The influence of the Ni film thickness upon carbon atom concentration [157].

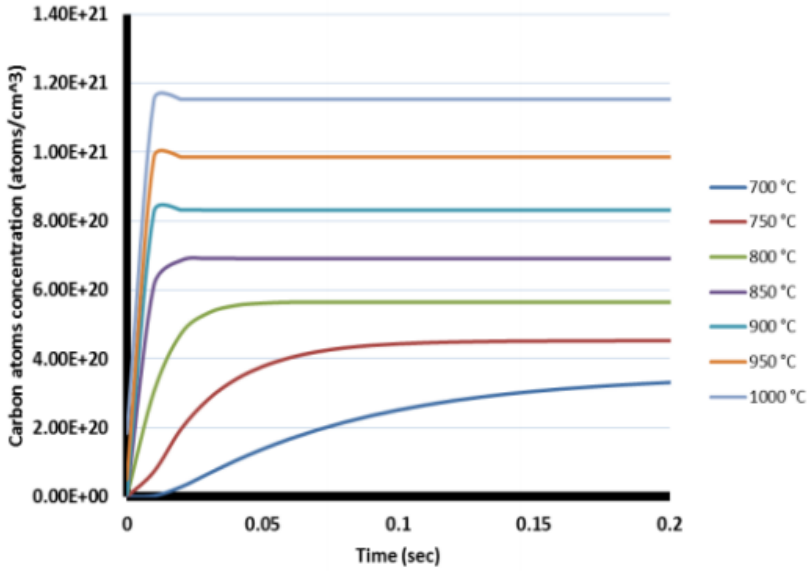

Figure 96. The influence of temperature on carbon atoms diffusion inside the Ni film [157].

Picosecond laser melting can be applied to increase the grain size with a benefit of an ultra-smooth surface finish of the nickel foil [100]. Minimal number of grain boundaries in the graphene sheet, so far, has been possible only with exfoliation. PLM has shown potential in both optimising the grain size and surface roughness in metals. To sum up, the chosen steps in manufacturing Ni substrates will put to the test the benefit of laser treating metals (LSM and PLM techniques) for graphene growth:

- Eliminate the grain boundaries by increasing the grain size with LSM - this method is beneficial for both single layer graphene formation and reduction of hydrogen diffusion of the substrate.
- Laser polish (PLM treat) the Ni substrate to smooth out its surface and reduce the H adsorption/desorption sites.
- Minimise the thickness of the Ni substrates as much as possible.

4.9. Electrical Conductivity Dependence on Grain Size.

As stated previously in the first objective, larger grains increase sample's conductivity [93]. From the theory of metallic conduction, electrons pass freely through perfect crystal lattice. Resistance is due to irregularities in the lattice (heat motion of the atoms, impurities, foreign atoms [158]) or grain boundaries [159]. Conduction also depends on temperature. Graphs of electrical resistivity vs temperature are available for commercially used metals [160]. For copper, however, the electrical conductivity does not vary significantly with the grain size [161], only with temperature. Therefore, the electrical conductivity has been investigated at 300 K as the resistivity of laser treated 304 SS, 3 mm thickness, for different grain sizes.

The linear function used for calculations of the electrical resistivity vs temperature is expressed by:

$$\rho(T) = \rho_0[1 + \alpha(T - T_0)] \tag{9}$$

where ρ_0 is resistivity at ambient temperature T_0, $\rho(T)$ is resistivity at temperature T, α is the temperature coefficient of the electrical resistivity (1/°C).

In the current work, the number of the grain boundaries and the grain shaping will dictate the electrical conductivity at any given temperature. The electrical conductivity of the samples is measured at 300 K before and after laser irradiation. The measuring method is the skin effect – property of the electromagnetic waves to penetrate short distances into the sample:

$$\boldsymbol{\delta = \sqrt{\frac{\rho}{\pi f \mu}}} \tag{10}$$

where f is frequency, ρ the resistivity, μ the magnetic permeability of the material.

μ = permeability ($4\pi * 10^{-7}\ \Omega * s/m$)

δ = skin depth (m)

ρ = resistivity ($\Omega * m$)

f = frequency (Hz)

This method is chosen due to capability of detecting small voltage changes in thin metal sheets, ideal

for controlled measurements of laser surface melt zones < 15 μm deep. Using Equation 10, the microwave penetration for 304 SS is 881.36 - 763.28 nm for 2.25 - 3 GHz. The microwave circuit setup is described in section 3.1.6.1.

The samples were generated with the laser setup illustrated in section 3.1.5. The scanning strategy involved a single bidirectional raster scan with variable line spacing across 4 x 4 mm surface area. Five samples were measured:

- Untreated (original microstructure).
- 1L – 13.54 kJ/cm^2, 0.03 mm line spacing (36 % overlap).
- 1R – 19.17 kJ/cm^2, 0.03 mm line spacing (36 % overlap).
- 2L - 13.54 kJ/cm^2, 0.01 mm line spacing (79 % overlap).
- 2R – 19.17 kJ/cm^2, 0.04 mm line spacing (15 % overlap).

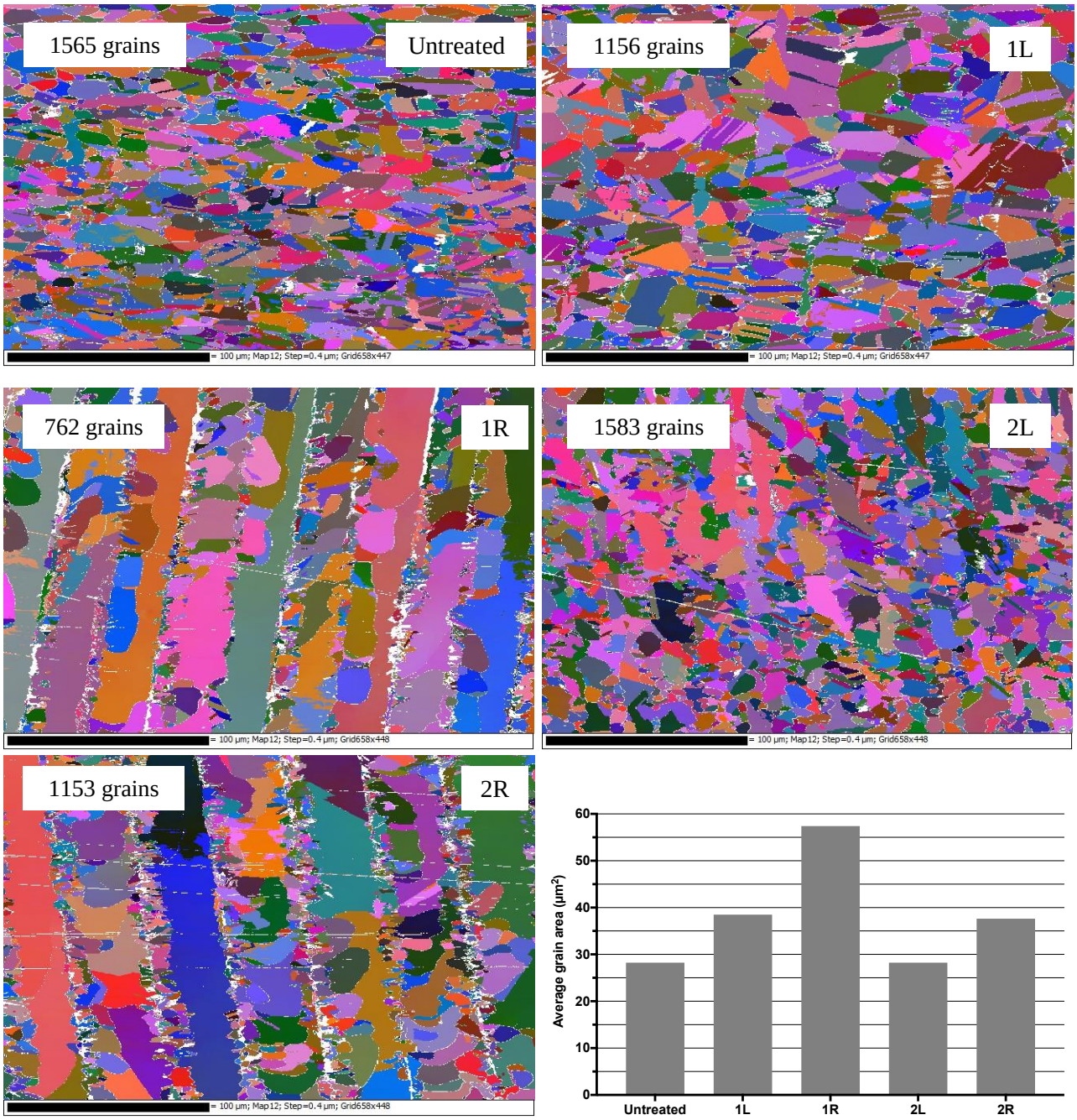

Figure 97. Combined 3 angle Euler maps of 304SS per 0.048 mm2 surface area with a grain area comparison chart.

Figure 97. shows the combined three angle Euler maps where the grain count and grain area for each sample is quantified. Sample 1R showed the lowest grain count and the highest grain area per 0.048 mm^2 surface area. 1L and 2R are almost the same according to their grain count and grain area. So is the Untreated and 2L samples.

The samples were mechanically polished after LSM treatment to minimise the surface roughness error in the microwave measurements. The surface roughness measurements are recorded in Table 25.

Table 25. Surface roughness measurements for the 304SS samples for testing the electrical conductivity dependence on the grain size.

Sample	R_a (µm)	R_t (µm)
Untreated	0.01	0.28
1L	0.03	0.18
1R	0.06	0.26
2L	0.04	0.19
2R	0.04	0.20

The microwave measurements are recorded in Figure 98. As the frequency increases the signal amplitude grows due to the probe becoming more sensitive to the surface roughness. From the voltage results measured it is evident that the 1R sample has the highest microwave reflection and effectively electrical conductivity, which is not surprising as its grains have the highest average area size out of all samples measured. 2L and Untreated showed the lowest voltage signal, indicating the least conductivity.

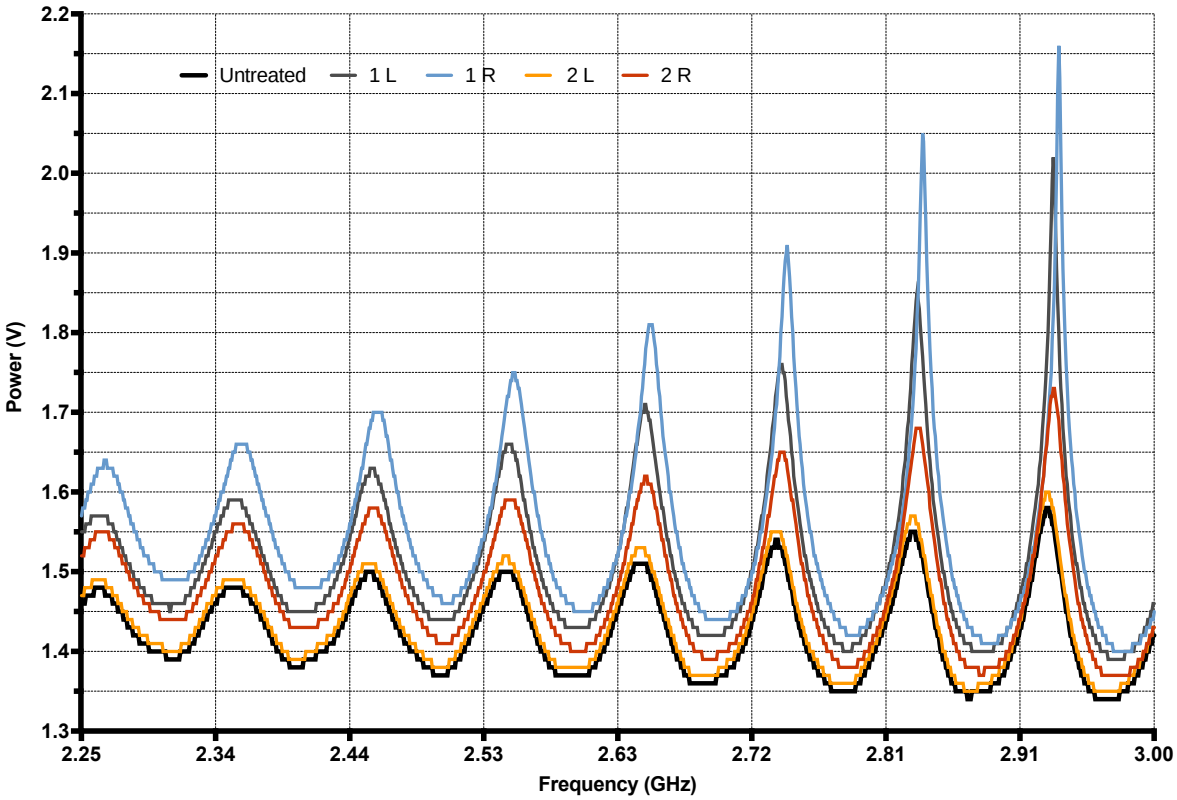

Figure 98. Voltage measurements of the samples in Figure 97.

In conclusion, the measured samples are clearly distinguishable by this method. The LSM treatment can be used as technique for controlled electrical conductivity increase of metals.

The voltage signal needs to be converted to stainless steel's bulk conductivity to indicate how significant the laser surface melting treatment is for electrical conductivity increase in metals. Finding the laser parameters to maximise the grain size favouring single crystal growth is the direction forward.

Part 3. Laser Surface Structuring of Metals for SEY Reduction.

The section answers the second objective of the work. It is divided into two according to the surface structuring method:

Laser drilling of high aspect ratio holes.

Laser-induced periodic surface structuring.

Three strategies have been explored in laser drilling:

- Single-shot laser drilling.
- Trepanning laser drilling and SEY testing.
- Reverse conical boreholes in 304 SS for SEE reduction efficiency comparison.

4.10. Motivation. SEE Reduction Experimentation and Measurements.

Sample 1, LSM treated with ED_{av} 13.54 kJ/cm^2, from section 4.1.3 has been tested for SEE measurements to see whether LSM can be used without SEE reduction treatment.

The SEY results are recorded in Figure 99. The LSM treated sample showed higher SE yield compared to the Untreated 304 SS. This is attributed to the surface roughness reduction recorded in section 4.1.2, Figure 25, between the LSM treated and Untreated 304 SS, R_a 242.34 nm and 277.45 nm, respectively.

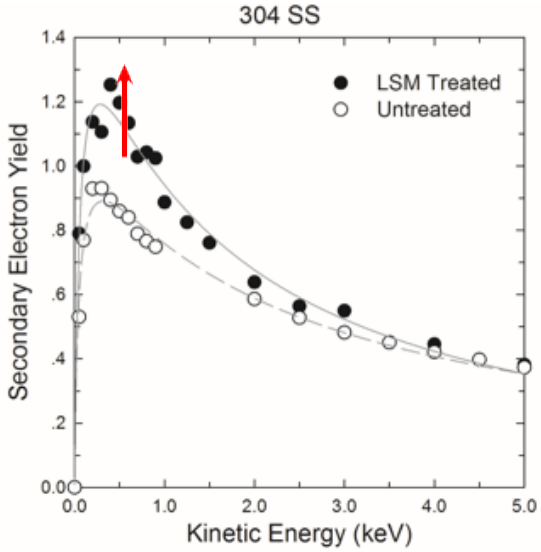

Figure 99. SEY measurement of Sample 1, LSM treated with ED_{av} 13.54 kJ/cm^2 vs Untreated 304 SS.

In conclusion, LSM for H outgassing reduction requires a SEE reduction technique due to surface smoothing as a product of LSM treatment.

4.11. Laser Drilling of High Aspect Ratio Holes for SEE Reduction.

To achieve the second objective, the SEY must be < 1. From section 2.5.2.8, the laser drilled holes must be ≥ 1:2 aspect ratio and packing density of ≥ 0.7. The process is to be scalable, thus, the drilling time for a single hole must be minimised.

4.11.1. Single-Shot Laser Drilling.

Laser power was varied from 3.09 W to 115 mW ranging the frequency from 200 – 0.05 kHz, the peak fluece per pulse was between 1.1 - 2216.7 J/cm^2, which is higher that the ablation threshold for 304 SS; for 10 ps pulse > 1 J/cm^2 [140]. The experiments below 1 J/cm^2 yielded non-circular holes, Figure 100, ~6 μm deep, measured with a white light interferometer.

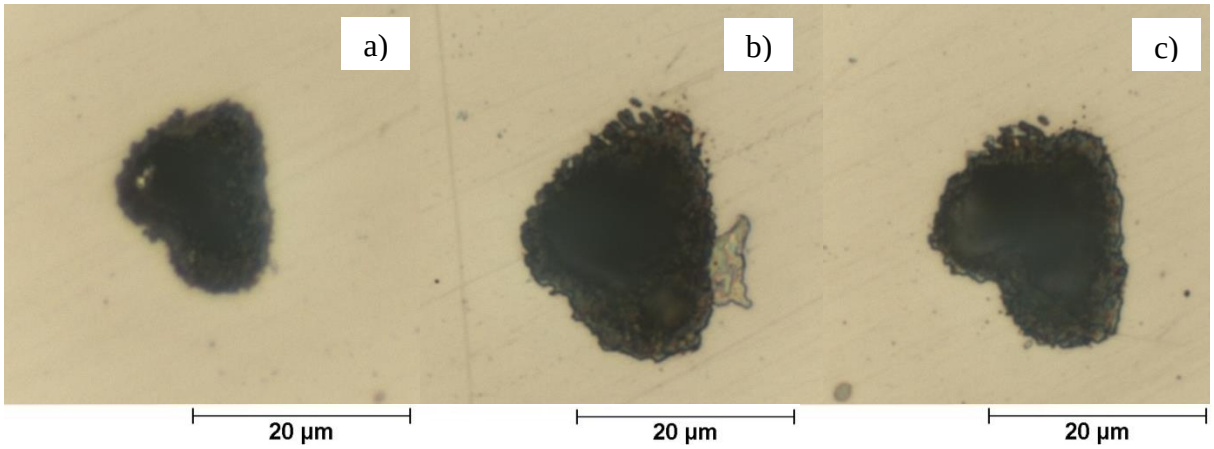

Figure 100. Optical images of 304 SS irradiated with a) 9 mW, 33.3 kHz, 1 second dwell, sample 213, b) 9 mW, 16.6 kHz, 1 s dwell, sample 217, c) 9 mW, 13.3 kHz, 1 s dwell, sample 219.

Three laser parameters between 33.69 - 48.14 J/cm^2 showed promise. The depth characterisation of the holes in Figure 101 - Figure 102 is available in Table 26.

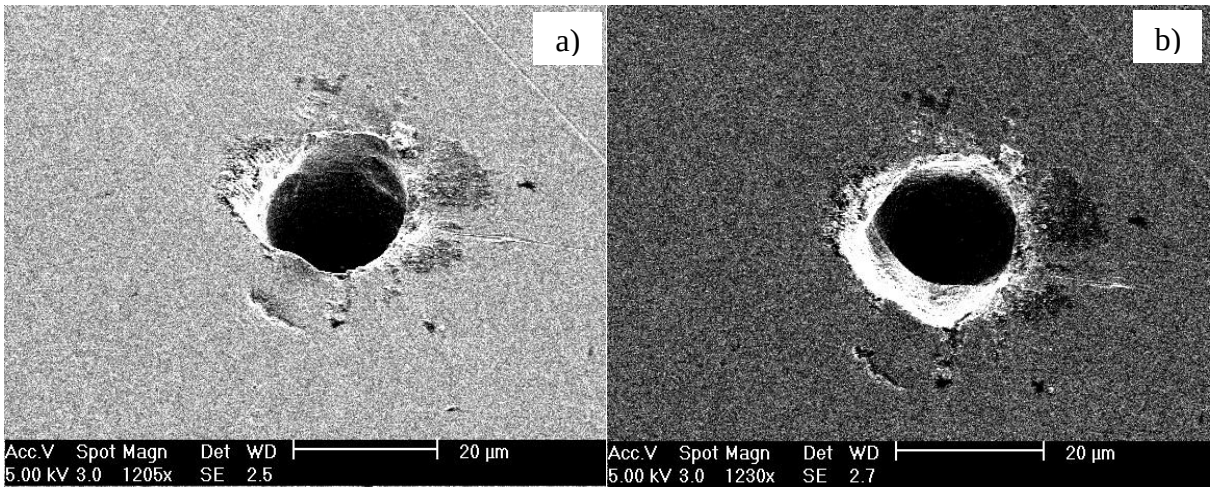

Figure 101. SEM images of 304 SS irradiated with 10 mW, 1 kHz, 1 second dwell time, sample 173, a) 35° tilted to normal, b) 0° to normal, 48.14 J/cm^2 peak fluence per pulse.

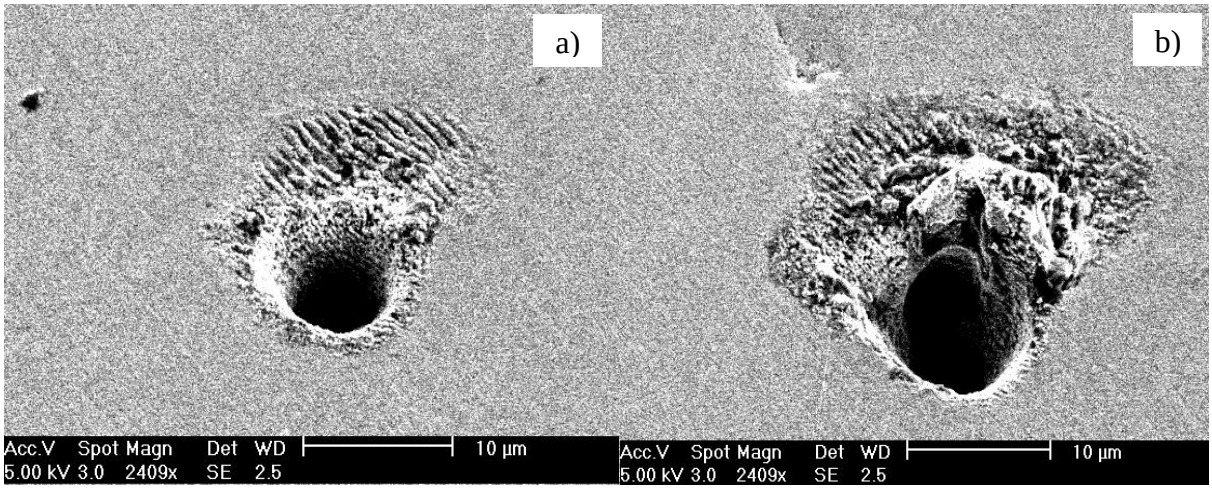

Figure 102. SEM images of 304 SS irradiated with a) 4 mW, 500 Hz, (38.5 J/cm^2), 2 s dwell time, sample 191, b) 7 mW, 1 kHz, (33.69 J/cm^2), 1 second dwell time, sample 192.

Table 26. Hole depth for samples 173, 191 and 192.

Hole No.	Depth (µm)
Sample 173	11
Sample 191	5
Sample 192	11

The holes were measured with the white light interferometer. The depth of all three holes was measured only 1/3 of the way, indicating a non-uniform drilling. The total depth is unknown. The holes in Figure 102 are significantly smaller in diameter compared to sample 173.

The next set of experiments was done with a $\lambda/4$ wave plate for 1064 nm, aligned using reflection from a glass slide at Brewster's angle. The laser parameters from samples 173, 191 and 193 were replicated.

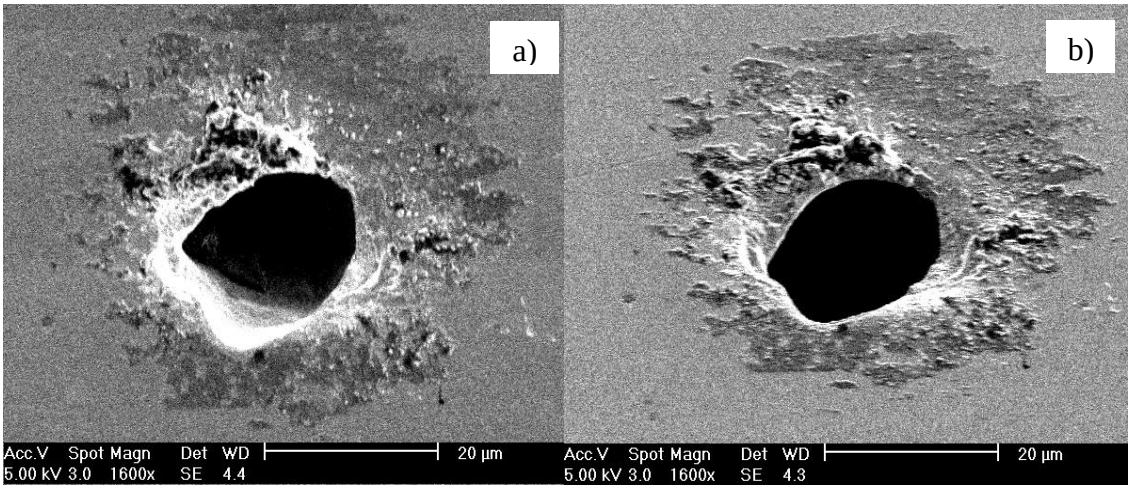

Figure 103. SEM images of 304SS irradiated with 10 mW, 1 kHz, 1 s dwell time, sample 196, a) 0° to normal, b) 30° tilted to normal. 1000 pulses, 18 µJ.

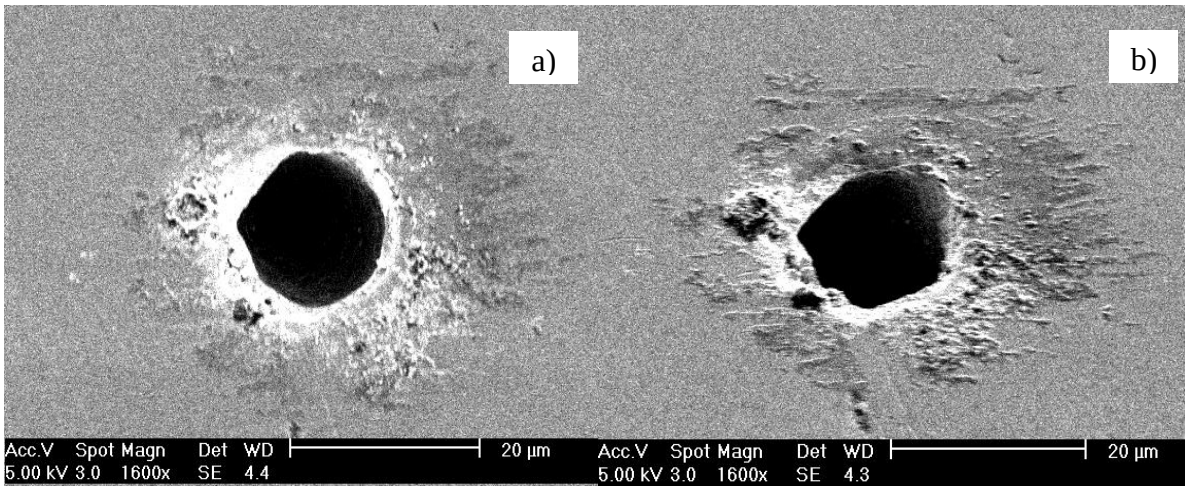

Figure 104. SEM images of 304 SS irradiated with 4 mW, 500 Hz, 2 s dwell time, sample 194, a) 0° to normal, b) 30° tilted to normal. 500 pulses, 14.4 µJ.

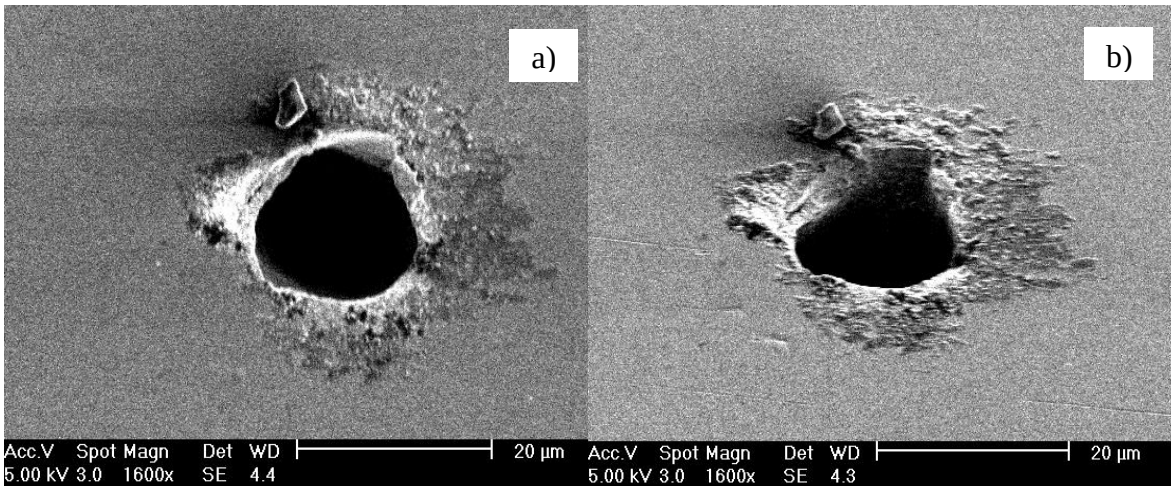

Figure 105. SEM images of 304 SS irradiated with 7 mW, 1 kHz, 1 s dwell time, sample 195, a) 0° to normal, b) 30° tilted to normal. 100 pulses, 13.5 µJ.

The characterisation of the holes in Figure 103 - Figure 105 is available in Table 27.

Table 27. Hole depth for samples 196, 194 and 195.

Hole No.	Depth (µm)
Sample 196	35
Sample 194	30
Sample 195	31

Less entry deformation is observed for holes 194 and 195 but more for 196 compared to its counterpart 173 in Figure 101. As well as that, all holes appear to be less circular than its predecessors. It is noted that the depth was much more uniform with the interferometer being able to measure the total depths.

The hole number 194 satisfies the manufacturing criteria with its diameter of 16 µm and depth of 30 µm; minimum borehole requirement is 1:2 aspect ratio. However, it fails in terms of the surface entry quality. Picosecond laser drilling does not satisfy the objective criteria for the conditions explored here.

4.11.2. Trepanning Laser Drilling.

For trepanning laser drilling the laser was changed to Satsuma femtosecond fibre laser to improve the quality of holes. It is also noted that at fluences higher than the ablation threshold the material removal rate for stainless steel increases as the pulse duration decreases past 10 ps [138].

The laser drilling parameter domains investigated were:

- Power (W).
- Pulse width (fs).
- PRF (kHz).
- Speed (mm/s).
- Number of trepanning circles.

4.11.2.1. Power.

The drilling strategies employed were:

- Trepanning.
- Trepanning/single-shot (trepanning for outlining the hole then a 1 second laser beam dwell for depth increase).

Figure 106 illustrates the way hole diameter increases with the increase in laser power. Fixed drilling parameters are recorded in Table 28. Trepanning/single-shot strategy was used. The inner wall quality remains constant. The same is observed for trepanning laser drilling strategy, Figure 107, fixed drilling parameters in Table 29.

Table 28. Fixed drilling parameters for trepanning/single-shot strategy, hole diameter vs laser power.

Trepanning speed (mm/s)	0.1
Trepanning diameter (µm)	3
No. of trepanning circles	200
PRF (kHz)	1
Pulse width (fs)	700
Spot diameter (µm)	4.1

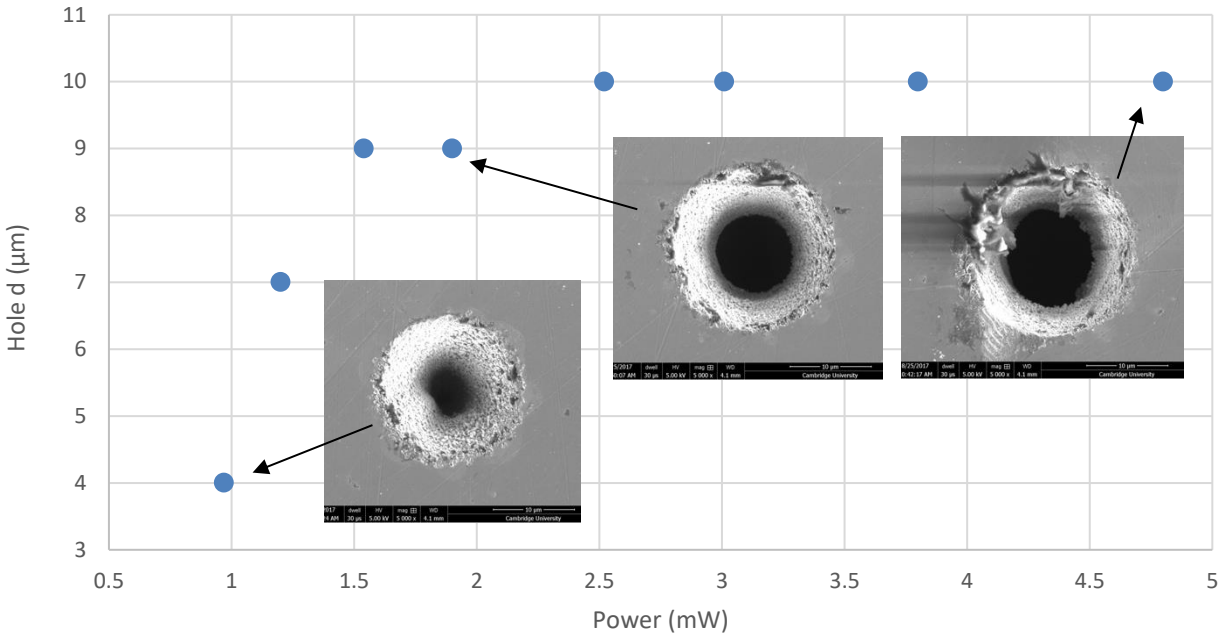

Figure 106. The graph records the hole diameter vs laser power. Selected SEM images illustrate the visual quality of the holes. Complete SEM images are available in Appendix I.

Table 29. Fixed drilling parameters for trepanning laser drilling, hole diameter vs laser power.

Trepanning speed (mm/s)	0.03
Trepanning diameter (µm)	3
No. of trepanning circles	100
PRF (kHz)	1
Pulse width (fs)	700
Spot diameter (µm)	4.1

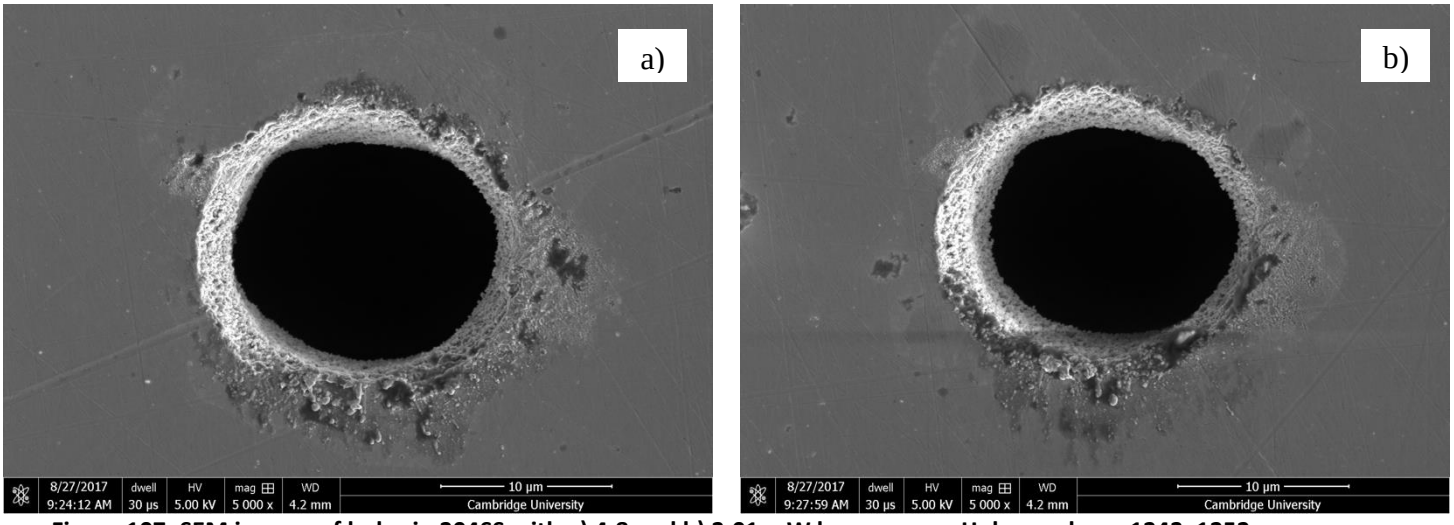

Figure 107. SEM images of holes in 304SS with a) 4.8 and b) 3.01 mW laser power. Hole numbers: 1243, 1252.

The effective diameter of the holes in Figure 107 (a) and (b) measures 16 µm and 14 µm, respectively. The experiment confirms that, no matter the scanning strategy, the hole entrance surface quality and debris count improves with the power decrease, however, the effective diameter of the hole decreases.

4.11.2.2. Pulse Width.

The trepanning diameter is 3 and 6 µm for Figure 108 (a, c, e) and Figure 108 (b, d, f), respectively. Fixed drilling parameters are recorded in Table 30. The debris count increases with longer pulse width. The texture of the inner walls of the holes appears smoother with longer pulse width but this change is little and can be negligible.

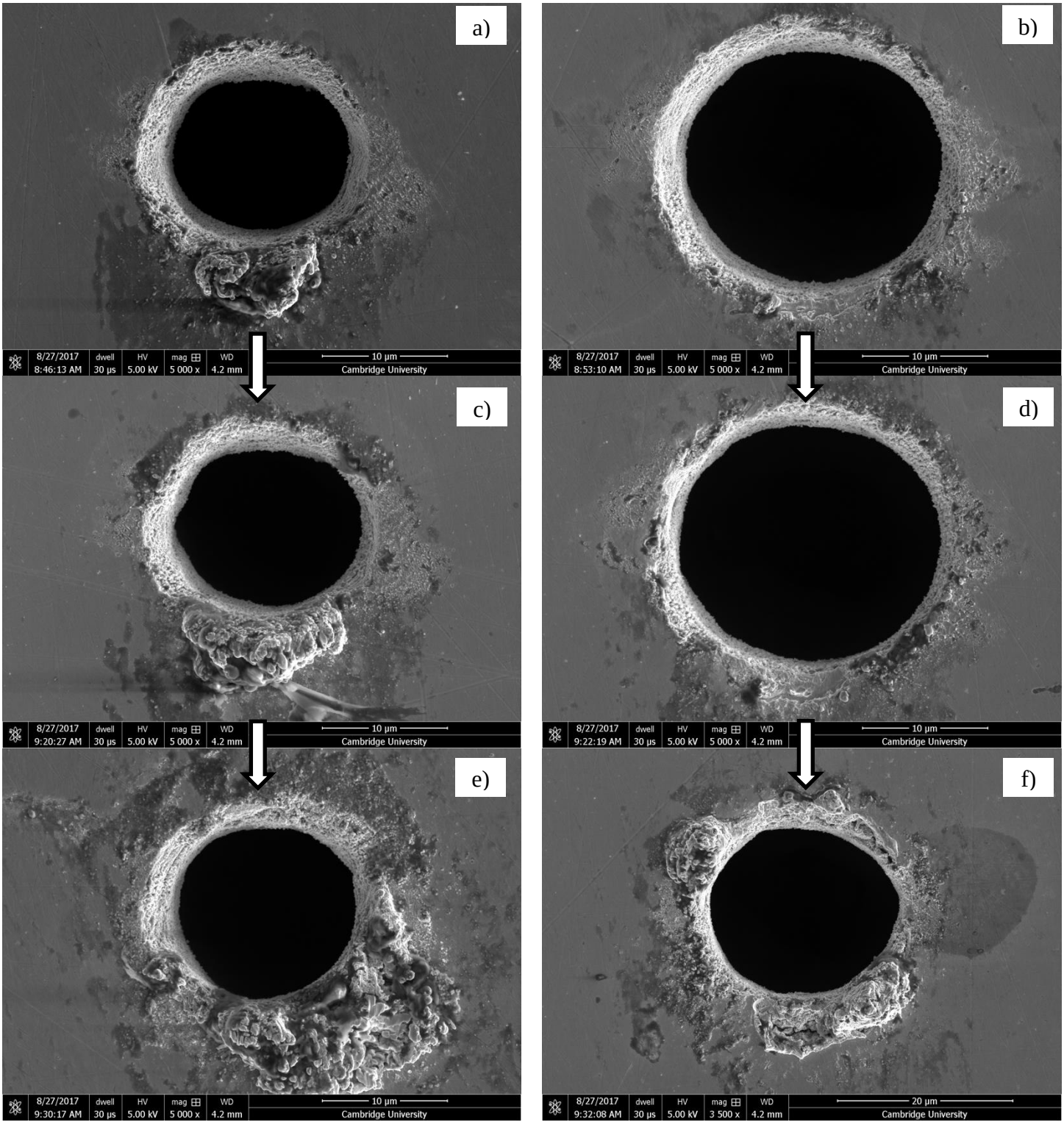

Figure 108. SEM images of hole drilling with trepanning only on 304SS surface, a) 700 fs, b) 700 fs, c) 1 ps, d) 1 ps, e) 5 ps, f) 5 ps. *Hole numbers: 1216,1219-1240,1241-1255,1256.*

Table 30. Fixed drilling parameters for trepanning laser drilling, hole quality vs pulse width.

Power (mW)	4.8
Trepanning speed (mm/s)	0.09
No. of trepanning circles	200
PRF (kHz)	1
Spot diameter (µm)	4.1

4.11.2.3. Pulse Repetition Frequency.

Figure 109 shows the SEM images of holes drilled with trepanning/single-shot strategy. The dwell time was 1 second. Fixed drilling parameters are recorded in Table 31.

Table 31. Fixed drilling parameters for trepanning/single-shot laser drilling, hole quality vs PRF.

Trepanning diameter (µm)	1
Trepanning speed (mm/s)	0.09
No. of trepanning circles	200
Pulse width (fs)	700
Spot diameter (µm)	4.1

High and low limits of laser power are used, 4.8 and 0.97 mW. PRF is set to 100, 250 and 500 kHz for Figure 109 (a, b), Figure 109 (c, d) and Figure 109 (e, f), respectively.

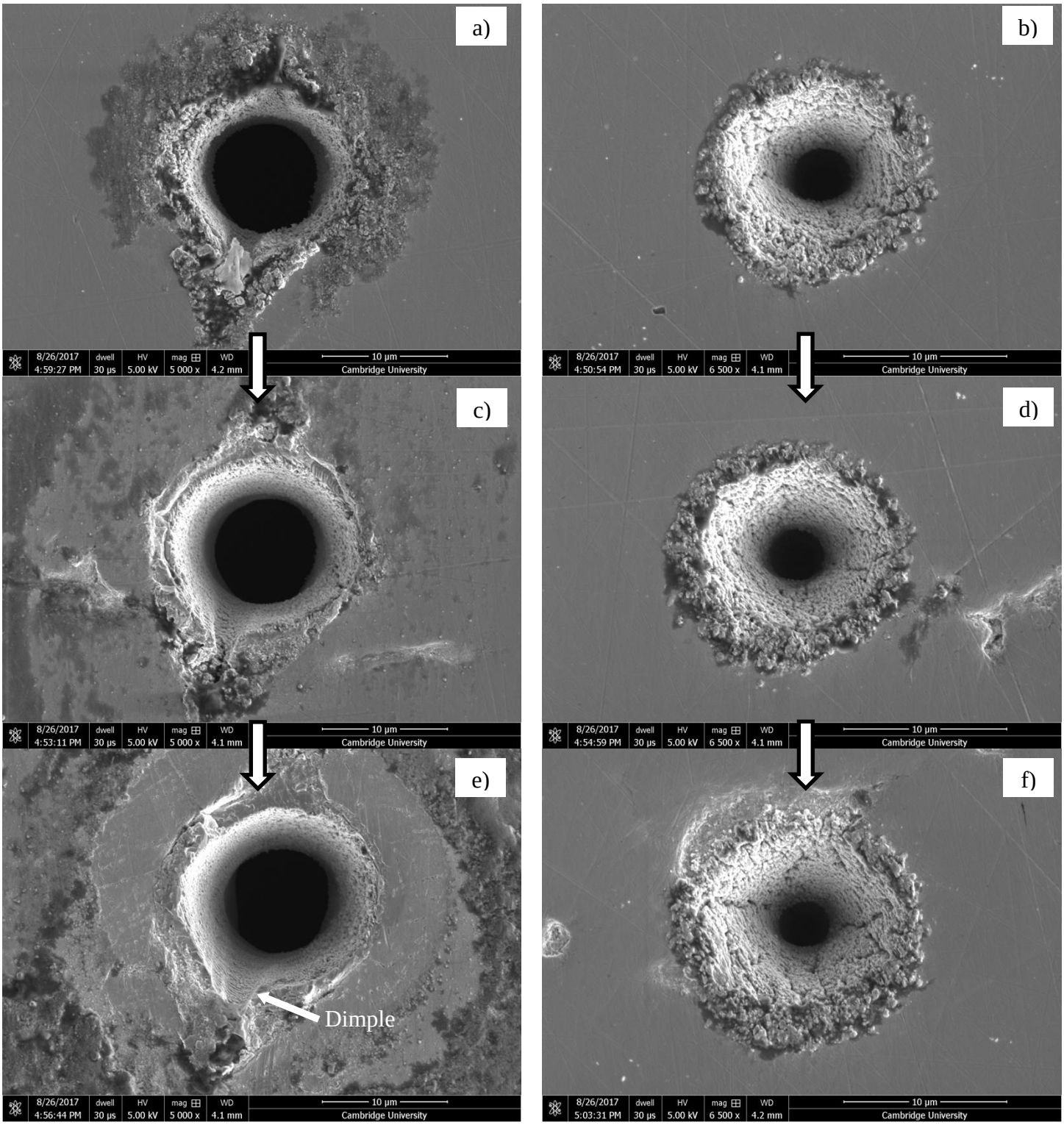

Figure 109. SEM images of hole drilling on 304SS surface, a) 4.8 mW, 100 kHz, b) 0.97 mW, 100 kHz, c) 4.8 mW, 250 kHz, d) 0.97 mW, 250 kHz, e) 4.8 mW, 500 kHz, f) 0.97 mW, 500 kHz. ***Hole numbers: 1160, 1164-1167,1171 – 1174,1178.***

It is evident that higher PRF produces more debris and hole entrance surface deformations. It is noted, however, that higher PRF also produces smother inner walls of the holes and this change is more significant at higher laser powers. Also, a dimple-like formation, Figure 109 (e), occurs at high laser power in all explored PRFs, Figure 109 (a, c, e). The phenomenon is investigated at low PRF, pulse width and trepanning/single-shot drilling in Figure 110. The fixed laser parameters are recorded in

Table 32. The power ranges from 1.9 - 4.8 mW.

Table 32. Fixed drilling parameters for trepanning/single-shot laser drilling, dimple test.

Trepanning diameter (µm)	1
Trepanning speed (mm/s)	0.09
Dwell time (s)	1
No. of trepanning circles	200
PRF (kHz)	1
Pulse width (fs)	300
Spot diameter (µm)	4.1

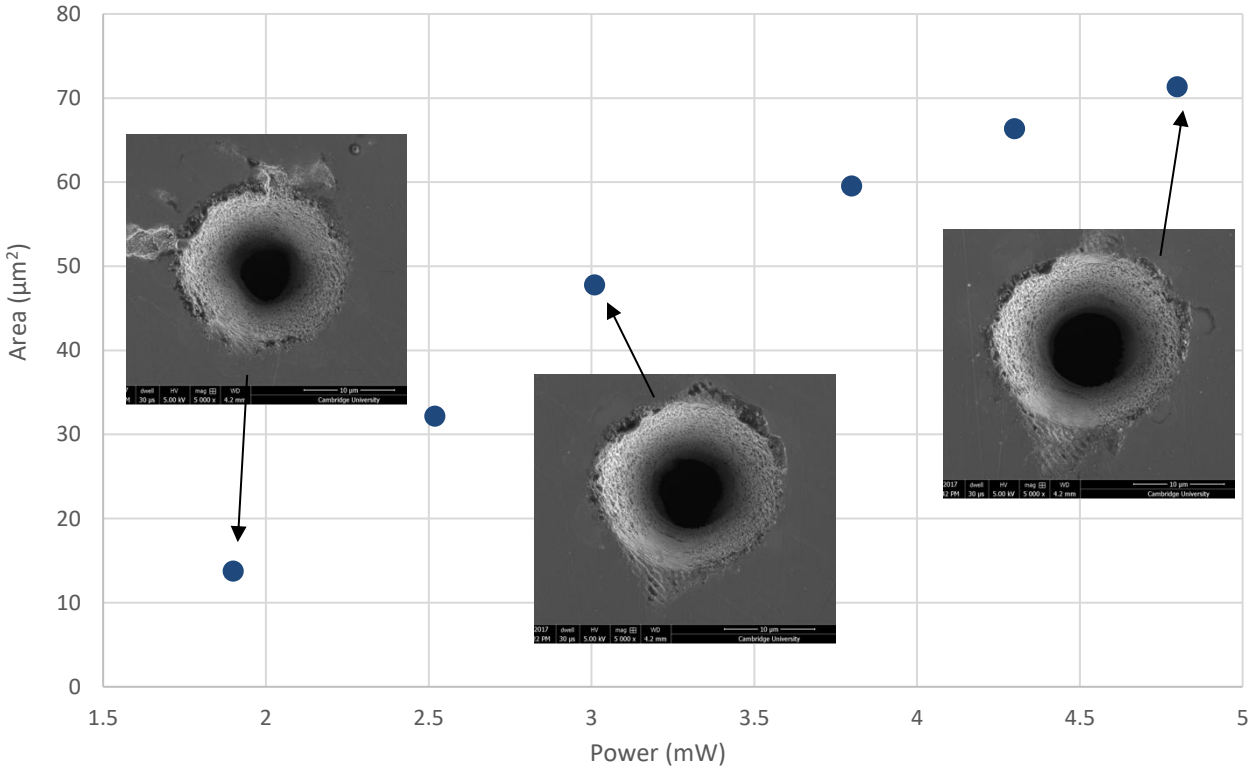

Figure 110. A graph measuring the dimple area vs laser power. SEM images illustrate the visual quality of the holes. Complete SEM images are available in Appendix J.

The dimple reoccurs at high laser power and it is also observed that at > 3.8 mW it appears on the opposite side of the hole. Initially, it was thought to be caused by 1 second of single-shot drilling. After more trials it is suspected to be caused by the mechanical shutter, leakage on shutter closure. Figure 111 shows the hole drilled with trepanning only. The laser parameters are identical to the holes in Figure 110, except 0.01 mm/s trepanning speed, 5 µm diameter and 20 circles. The laser power is set to 4.8 mW.

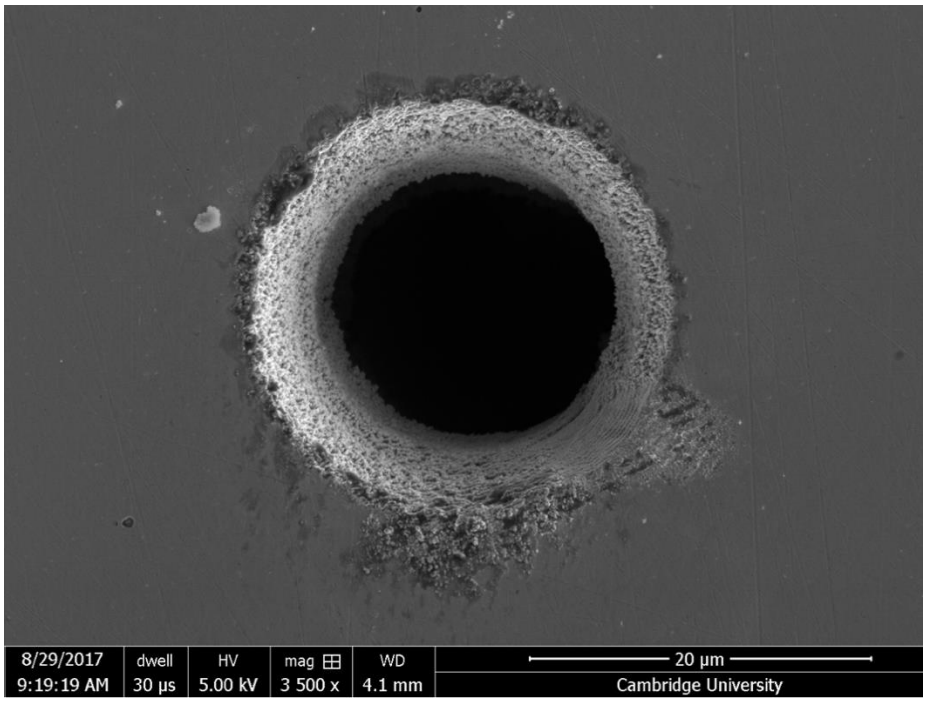

Figure 111. SEM images of hole drilling illustrating the effects of shutter leakage. ***Hole number: 1292.***

The dimple phenomena, possibly caused by the shutter leakage, appears to smooth out the inner walls of the trepanned drilled holes with what appears to be LIPSS formations and this happens on all artefacts regulated only by the laser power parameter, see section 4.11.2.1. It also causes surface deformations at the hole's entrance. It is interesting to note here that in this work trepanning drilling at 700 fs has the least dimple effects on the holes.

In conclusion, higher PRF produces more debris and hole entrance surface deformations. Dimple phenomena is prominent at low pulse durations of 300 fs and > 700 fs.

4.11.2.4. Speed.

The results show that trepanning speeds ≥ 1 mm/s deform the hole entrance, even though the sample is fixed to the XY stage, Figure 112. It is noticed, however, that faster trepanning speeds yield less inner wall deformations. Fixed laser parameters are recorded in Table 33.

Table 33. Fixed drilling parameters for trepanning laser drilling, speed test.

Power (mW)	4.8
Trepanning diameter (µm)	7
No. of trepanning circles	100
PRF (kHz)	1
Pulse width (fs)	700
Spot diameter (µm)	4.1

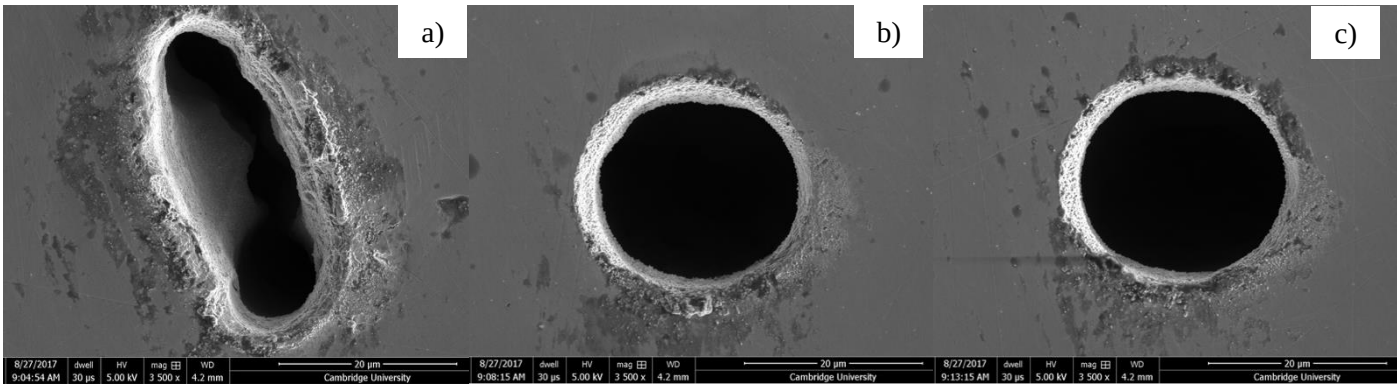

Figure 112. SEM image of a hole in 304SS with a) 1 mm/s, b) 0.06 mm/s and c) 0.04 mm/s trepanning speed. *Hole numbers:* 1228, 1231, 1234.

Conclusion: the trepanning speeds are kept < 1 mm/s and the XY stage has been recalibrated, ± 10 nm repeatability.

4.11.2.5. Number of trepanning circles.

The bar chart in Figure 113 illustrates hole outer diameter and the rim thickness dependency on the speed and number of trepanning circles. The holes were drilled with:

- Power - 4.8 mW.
- PRF – 1 kHz.
- Pulse width – 700 fs.
- Spot diameter – 4.1 µm.

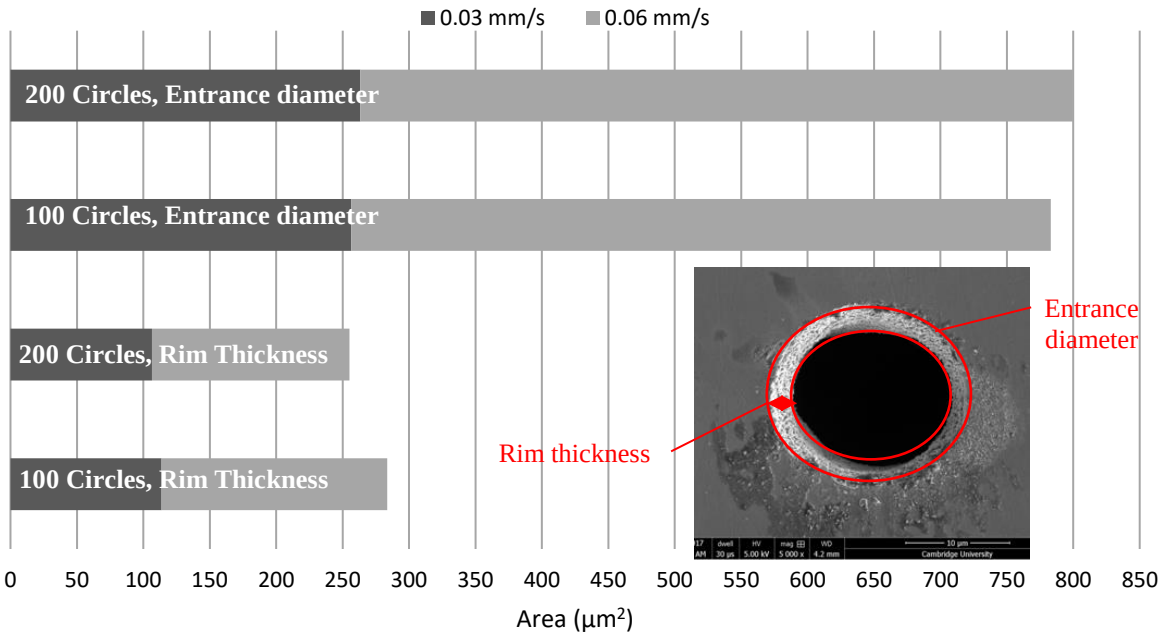

Figure 113. A bar chart recording the rim and outer diameter area of the holes drilled with different trepanning speeds & circle counts. SEM images illustrate the areas of measurements for rim thickness and max diameter. Complete SEM images are available in Appendix K.

The hole rim is thinner and the hole itself is larger with a greater number of trepanning circles, however it is noted that the difference between the results is minimal for a 50% increase in the number of circles. Therefore, the number of circles drilled is negligible for the hole entrance quality.

4.11.2.6. Summary:

The following parameter directions are extrapolated from the results to satisfy the objective:

- Power (W) – decrease.
- Pulse width (fs) – decrease.
- PRF (kHz)- decrease.
- Trepanning speed (mm/s) – increase.

To avoid the dimple effect, the laser output was regulated via the exposure time rather than the mechanical shutter. The XY axes have been re-calibrated to ± 10 nm to compensate for repeatable mechanical errors in the positioning system.

4.11.2.7. Hole Aspect Ratio.

Figure 114 shows SEM images of a hole drilled with trepanning only. The laser parameters are:

- Power – 3.8 mW.
- Trepanning speed - 0.04 mm/s.
- Trepanning diameter – 5 µm.
- Number of trepanning circles - 200.
- PRF – 1 kHz.
- Pulse width – 300 fs.
- Spot diameter – 4.1 µm.
- Manufacturing time – 140 seconds.

FIB was used to section the hole for aspect ratio measurement.

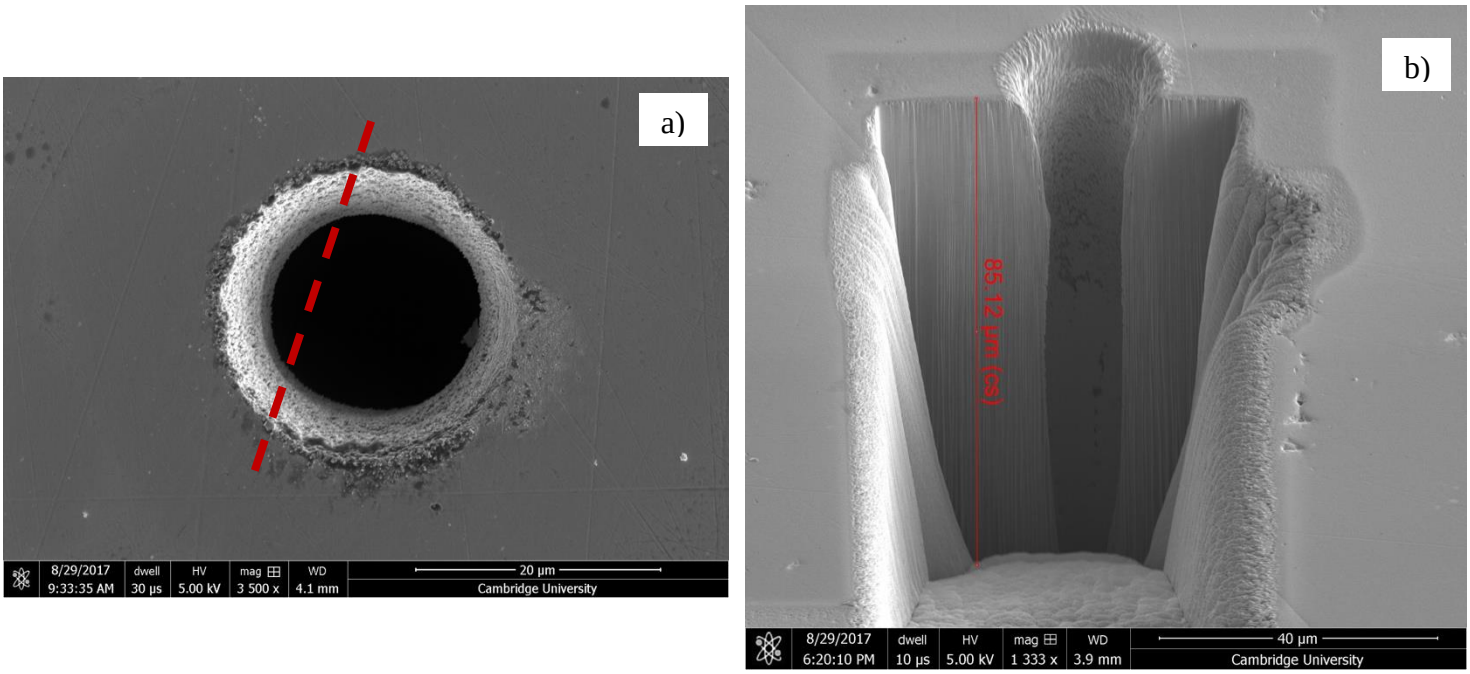

Figure 114. SEM images of a hole drilled on 304SS, a) top view, b) 52-degree tilt view after FIB sectioning. *Hole numbers: 1323, 1323_5.*

The hole appears to be smooth inside the borehole and conically drilled. The depth of the hole is > 85.12 µm for 200 trepanning circles making it a 1/4 aspect ratio hole. This satisfies the objective condition of ½ aspect ratio. The circularity of the hole is calculated by the formula:

$$C = \frac{4\pi A}{P^2} \tag{11}$$

where A is the area and P is the perimeter of the hole measured. For a circle C = 1. The circularity of the hole 1323 is 0.98.

4.11.2.8 Proposed Sample Manufacture.

The proposed hole aspect ratio for manufacture is > 1:2 with hexagonal packing, varying the distance between the holes, illustrated in Figure 115. The hexagonal array offers more packing density than a square one. A square array will be manufactured for comparison.

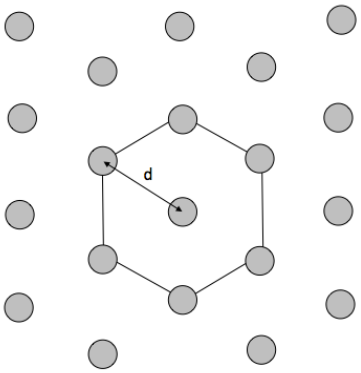

Figure 115. Hexagonal array.

4.11.2.9 Secondary Electron Yield of the Laser Drilled 304SS with High Aspect Ratio Holes.

Figure 116 shows the hole drilling pattern achieved with the XY axis stage motion. The laser beam draws a semicircle, half of the radius of the intended hole, then encircles the starting point for a fixed period of time until the pulse synchronized output of the laser stops the emission. After that the beam comes back to the starting point via another semicircle, half the radius of the intended hole. This pattern minimises acceleration errors in the XY stage motion providing a smooth transition from the centre point to the circumference.

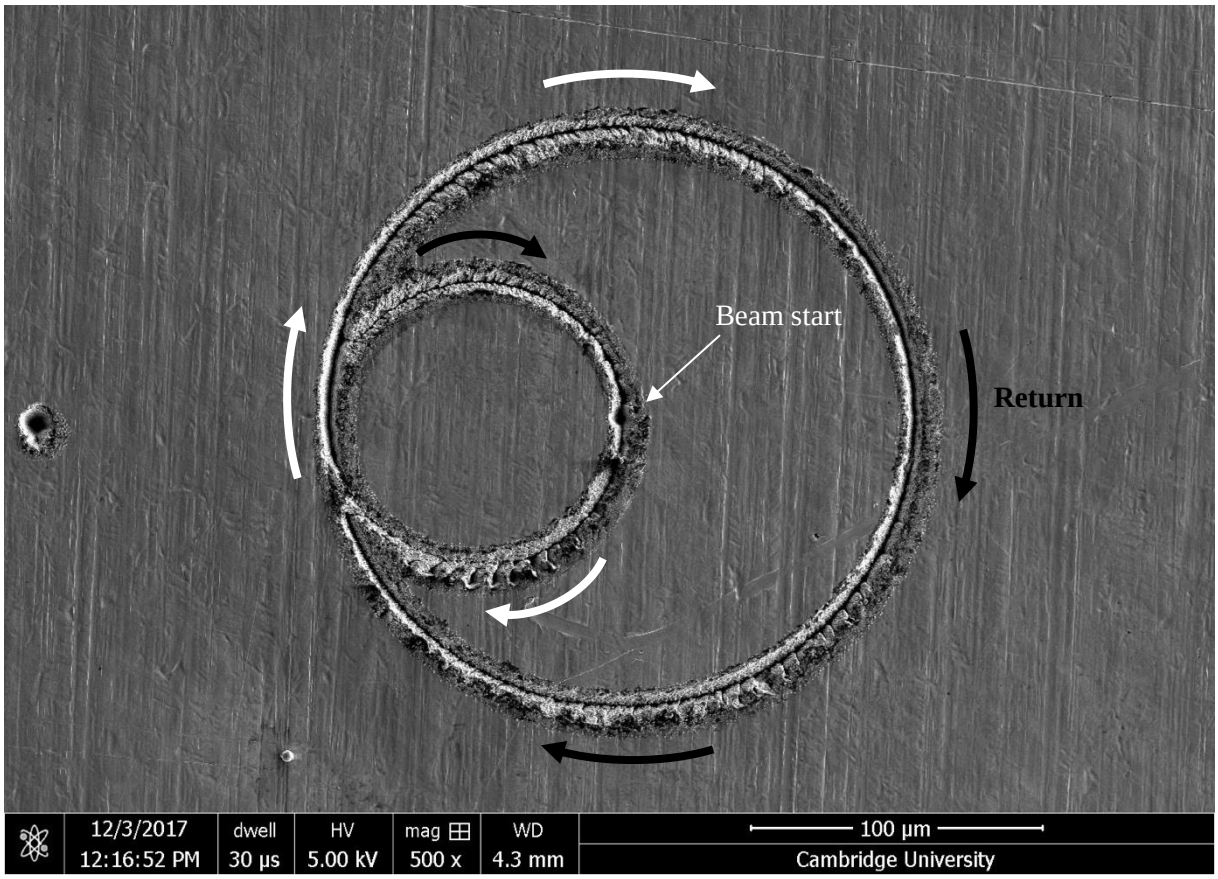

Figure 116. SEM image of laser ablated 304SS using the hole drilling pattern. Trepanning radius 0.1 mm, speed 1 mm/s.

Four samples with a hole array of 4 x 4 mm were produced. Laser parameters are recorded in Table 34.

Table 34. Laser drilling parameters.

Satsuma Ultrafast Fibre Laser	
Wavelength (nm)	1030
PRF (kHz)	1
Pulse duration (fs)	300
Power (mW)	3.8
Trepanning speed (mm/s)	0.4
Spot size (µm)	4.1
Drilling time p/hole (seconds)	2

Figure 117 is a section-view of the laser drilled 304 SS and shows the depth of the high-aspect ratio holes.

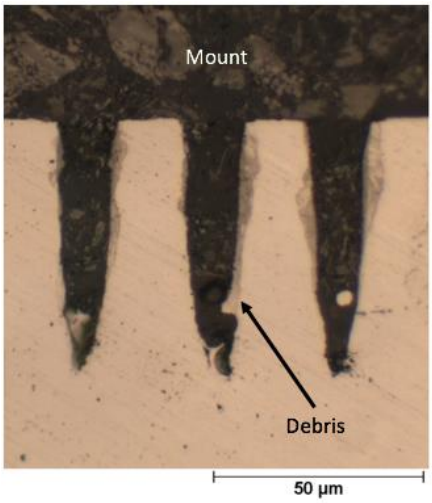

Figure 117. Optical image of cross-sectioned 304 SS. Debris present after mechanical sectioning and polishing.

Table 35 shows the characterisation of the holes. It is noted that samples 3 and 4 have higher aspect ratio due to a smaller manufacturing diameter (possibly an offset during manufacturing). The SEM images are available in Figure 118 - Figure 121.

Table 35. Characterisation of the laser drilled 304SS with high aspect ratio holes.

Sample No.	Array type	Hole distance (µm)	Hole radius (µm)	Aspect Ratio	Porosity	Untreated R_a	Untreated R_t
1	Hexagonal	30	10	3	0.40	14.93 nm	222.71 nm
2	Hexagonal	50	10	3	0.15	22 nm	488.29 nm
3	Square	30	8.6	3.49	0.52	9.22 nm	299.15 nm
4	Square	50	8.6	3.49	0.19	37.74 nm	1.8 µm

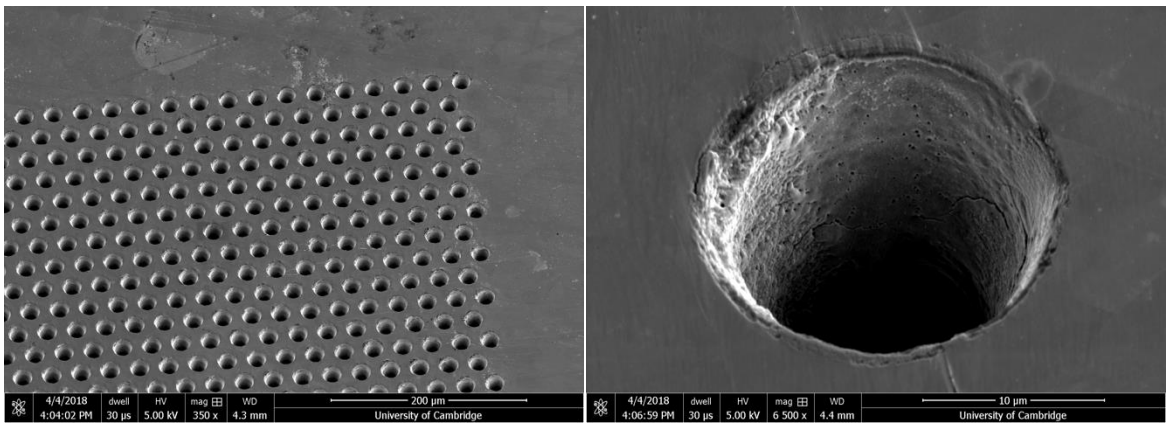

Figure 118. Sample 1. SEM images of the laser drilled holes in 304SS, tilt 30°.

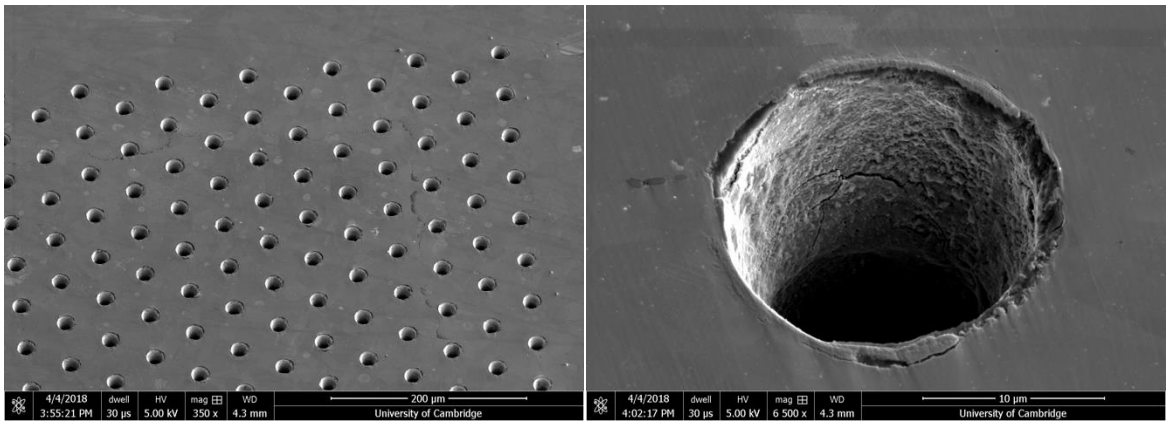

Figure 119. Sample 2. SEM images of the laser drilled holes in 304SS, tilt 30°.

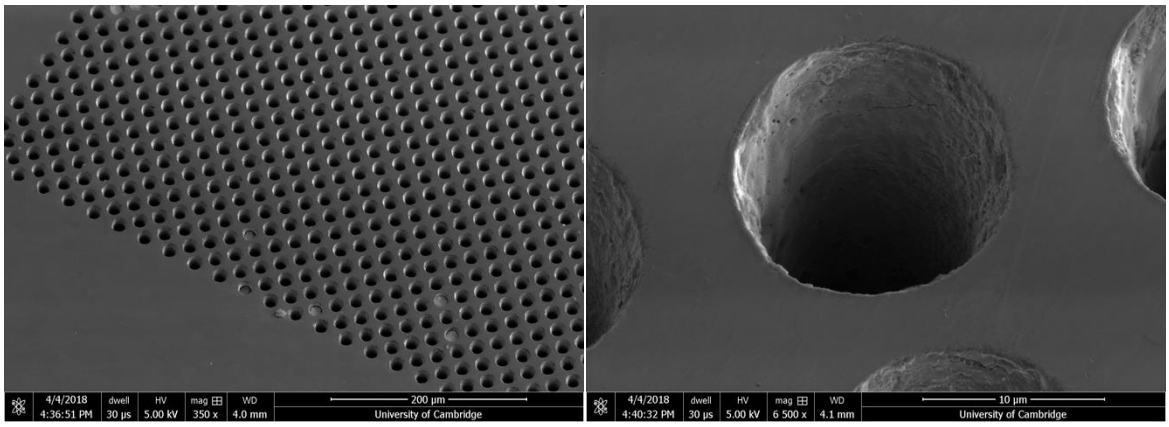

Figure 120. Sample 3. SEM images of the laser drilled holes in 304SS, tilt 30°.

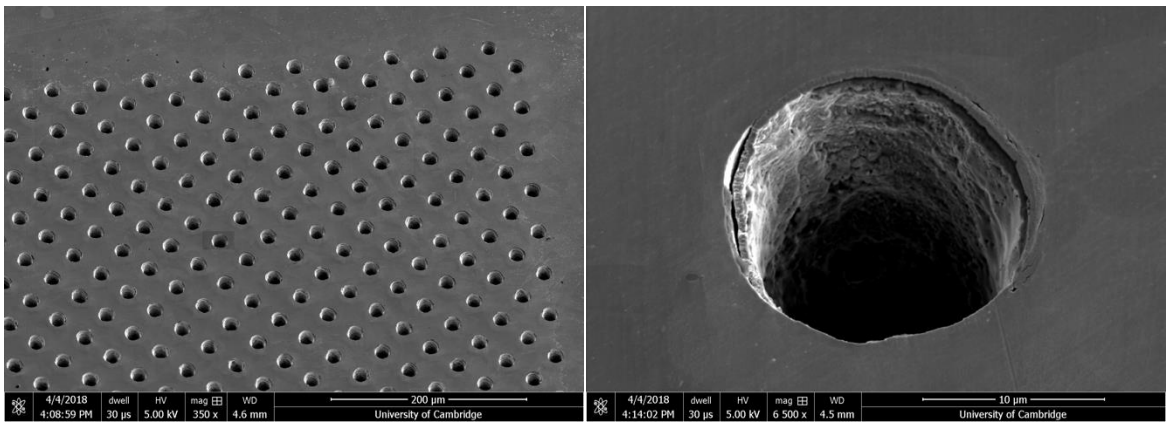

Figure 121. Sample 4. SEM images of the laser drilled holes in 304SS, tilt 30°.

The SEY results are recorded in Figure 122. The samples have been bombarded at normal incidence to the e-beam. The values of the lowest SEY peaks are recorded in Table 36.

Table 36. The lowest recorded SEY peaks for samples 1 to 4.

Sample	Porosity	SEY Peak Reduction	SEY Peak Increase
1	0.40	0.16	1.28
2	0.15	0.13	1.28
3	0.52	0.05	0.98
4	0.19	0.20	1.20

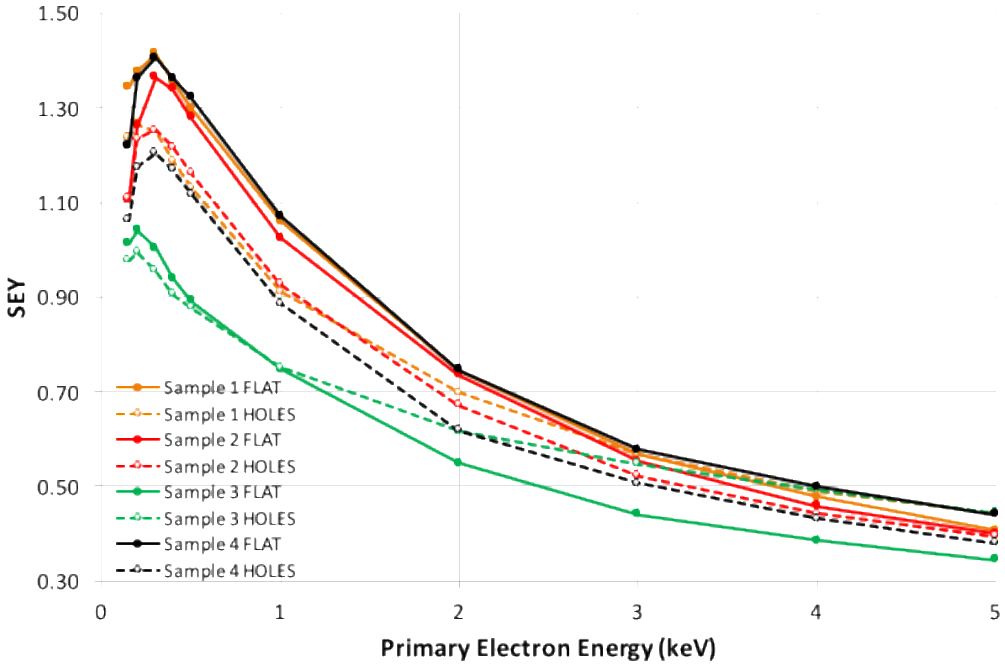

Figure 122. SEY measurements of the laser drilled 304SS samples from Table 35.

Sample 3 showed < 1 SEY which satisfies the Second objective. However, several irregularities are observed in the measured results. Firstly, Sample 1 exhibits similar SEY peak increase compared to Sample 2 despite having higher porosity. Next, Sample 3's untreated or flat region showed similar SEY reduction compared to its treated region. This anomaly is attributed to carbon contamination of the surface. Sample 3 showed almost no iron present on the surface compared to Sample 4, Figure 123.

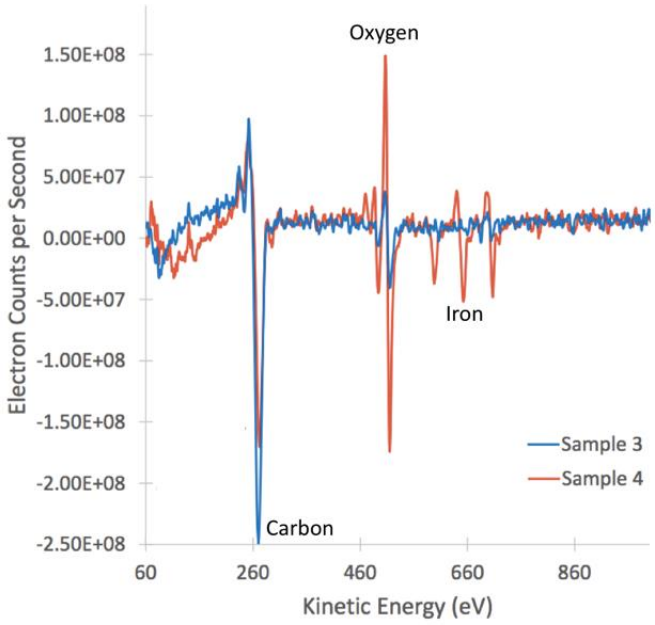

Figure 123. Auger scan of Sample 3 and 4 FLAT regions.

The surface carbon build-up can be attributed to the electron conditioning effect, where continuous electron beam bombardment causes a gradual alteration of surface chemistry that changes the SEY over time. This phenomenon has been reported to occur in stainless steel [162], but seems to have little effect

on gold. Covering the stainless steel samples with a thin (100 nm) Au film (which is known to be a rather inert material) led to reliable SEY measurements over normal incident energy range of 5 keV. It is noted that the hole dimeter changed after the gold was sputtered also changing the porosity of the samples. Table 37 shows the characterisation of the gold-coated samples.

Table 37. Characterisation of the 100 nm gold-coated laser drilled 304SS with high aspect ratio holes.

Sample No.	Hole distance (µm)	Hole radius (µm)	Aspect Ratio	Porosity
1	30	9.9	3.02	0.39
2	50	9.9	3.02	0.14
3	30	8.5	3.52	0.50
4	50	8.5	3.52	0.18

Figure 124 shows the SEY measurements of the gold-coated samples from Table 37. A higher average SEY is expected since gold has a larger number of elections compared to iron. The gold-coated 304SS SEY measurement results which follow the SEY reduction theory in [115], [116], the higher the porosity the lower is the sample's SEY, Table 38.

Table 38. The lowest recorded SEY peaks for Samples 1 to 4 after 100 nm gold-coating.

Sample	Porosity	SEY Peak Reduction	SEY Peak Increase
1	0.39	0.88	1.35
2	0.14	0.94	1.47
3	0.50	0.77	1.26
4	0.18	0.98	1.46

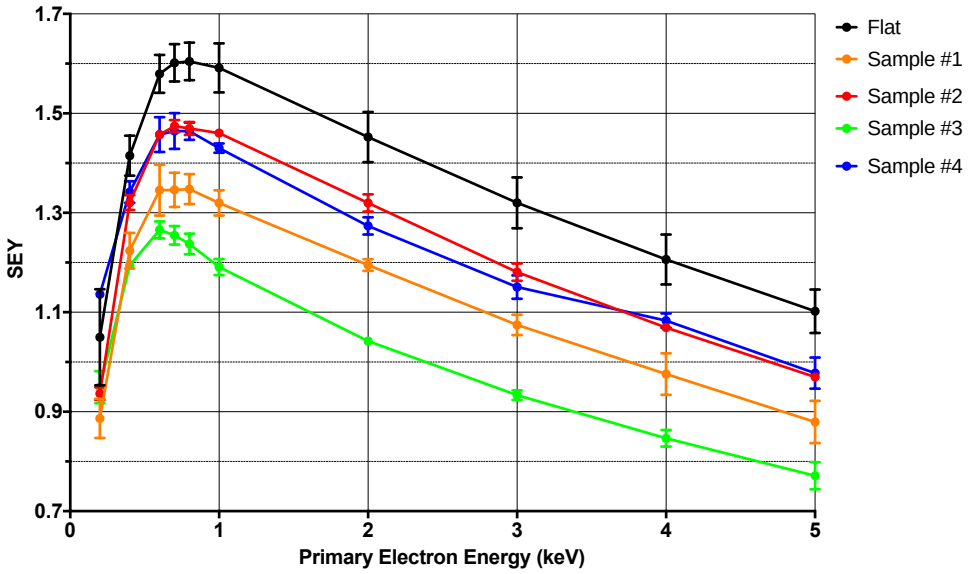

Figure 124. SEY measurements of the 100 nm gold-coated laser drilled 304SS with high aspect ratio holes. The SEM images available in Appendix L.

It is noted that Sample 3 consistently exhibits the lowest SEY in both uncoated and gold-coated SEY measurements. The uncoated Sample's 3 SEY measurement results can be compared to the theoretical model in [116] due to similar porosity of 0.50. The maximum SEY for Sample 3 lines up with the geometrically dependant theoretical 3D model, Figure 125.

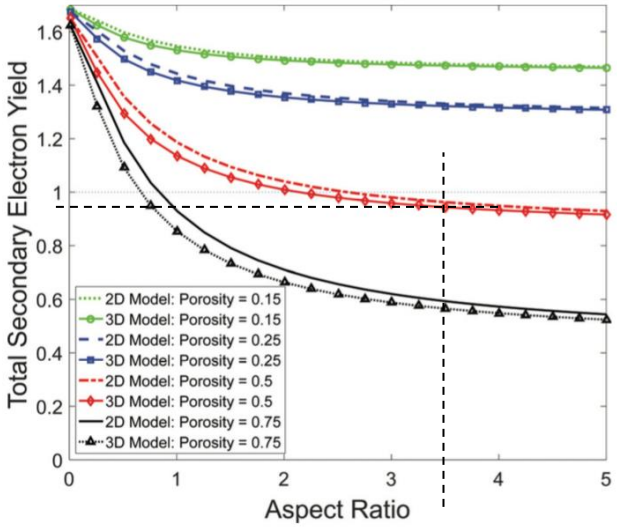

Figure 125. Analytical modelling results showing the total secondary electron yield for 2D and 3D pore models based on an engineered surface with SEY_{max} of 1.7 and 1.6 for untreated/flat and bottom of the hole surfaces, respectively [116].

To avoid the electron conditioning effect, an additional set of samples with matching aspect ratios and porosities to the theoretically simulated values in Figure 125 has been manufactured for angular SEY measurements and further proof of concept from tantalum due to its high purity.

Tantalum has similar electrical conductivity properties to steel, high melting point, is oxidation resistant and readily used in vacuum systems. However, it posed greater challenges for laser processing due to its high reflectivity, 88 % at 1 µm wavelength [163]. To tackle this, firstly, the first experimentation was conducted at a 60 degree angle to normal to avoid the back reflection into the laser. Next, to reduce the reflectivity of Ta further the processing was done on the unpolished original surface, Ra 452.31 nm, Rt 5.56 µm, with the laser fluence above the ablation threshold, laser parameters recorded in Table 39. Fluences above the ablation threshold of the material form plasma at the irradiated zone sharply decreasing the material's reflectivity due to absorption of the laser light by the plasma [164]. Equation 2 and 3 from section 2.5.2.2 for fluence calculation are used below to calculate the ablation threshold:

$$E = \frac{P}{R} = 3.04 * 10^{-6}\ (J) \tag{12}$$

$$F = \frac{E}{A} = 23.89\ \left(\frac{J}{cm^2}\right) \tag{13}$$

Where P is the incident power at 0.0038 * 0.82 W after lens and R is repetition rate at 0.001 Hz, A is the area at π *(0.000205) ^{2} cm^2. Ablation threshold for Ta is 0.95 J/cm^2 [163]. The results yielded holes ~20 µm in deep, Figure 126.

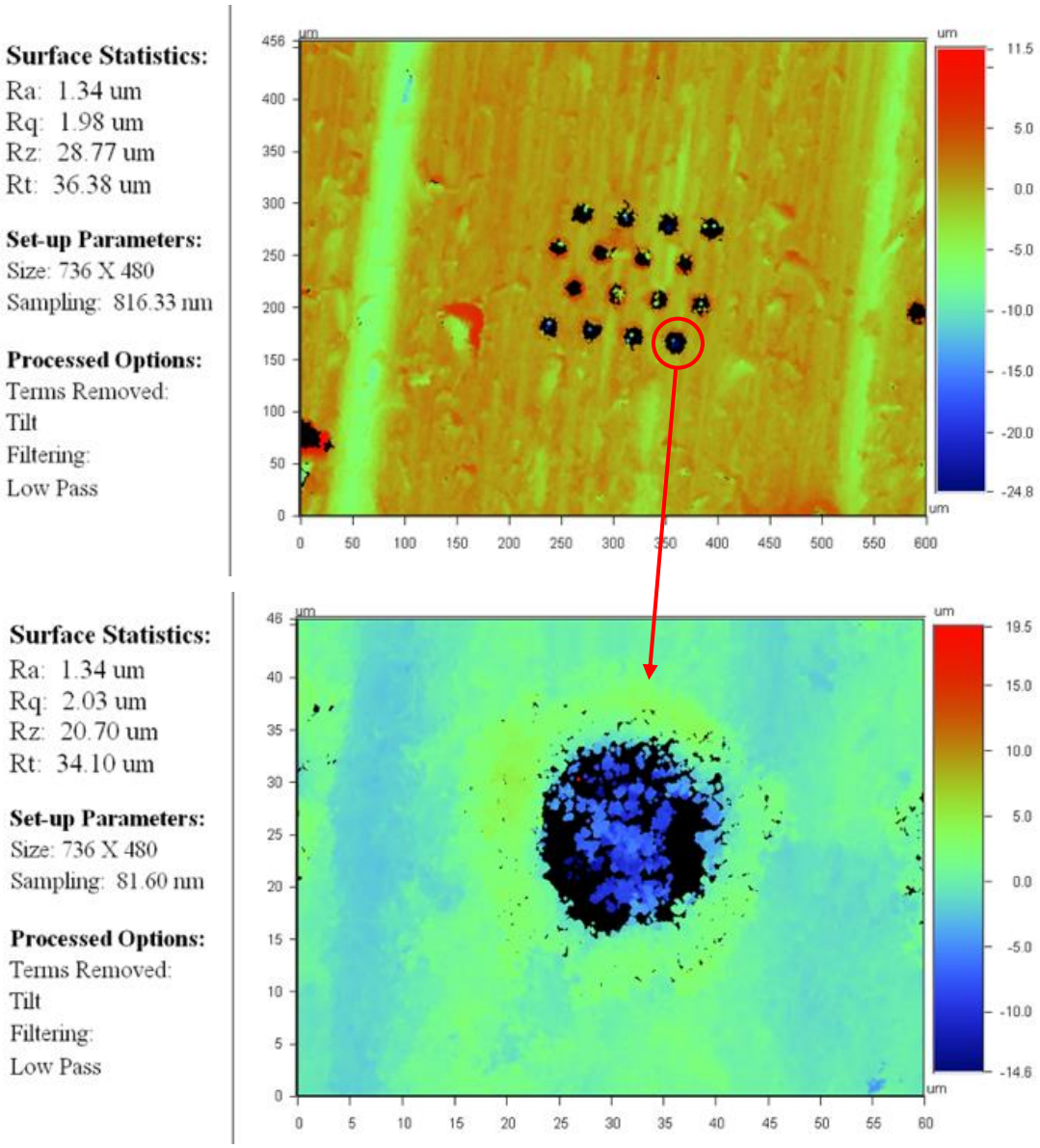

Figure 126. Interferometer measurement of the holes drilled in Ta at 60 degree angle to normal at fluence of 23.89 J/cm^2.

Upon the successful angle trials the Ta samples were mechanically polished to Ra ~26.05 nm and drilled normal to the laser beam incidence with the same above the ablation threshold of Ta fluence of 23.89 J/cm^2. For comparison, 304 SS samples with the same porosities were manufactured. A total of eight samples with a hole array of 4 x 4 mm were produced. Laser parameters are recorded in Table 39.

Table 39. Laser drilling parameters for samples for angular SEY measurement.

Satsuma Ultrafast Fibre Laser	
Wavelength (nm)	1030
PRF (kHz)	1
Pulse duration (fs)	350
Power (mW)	3.8
Trepanning speed (mm/s)	0.4
Spot size (µm)	4.1
Drilling time p/hole (seconds)	2

Mechanical polishing was carried out with colloidal silica 40 nm particle size for 10 seconds to remove the drilling debris from the surface. The samples were cleaned after polishing in acetone using an ultrasonic bath for 15 min. Table 40 records the characterisation of the produced samples. Depth of holes is ~60 µm for 304 SS. Ta was not measured.

Table 40. Characterisation of the samples for angular SEY measurement.

Material	Average R_a before polishing (nm)	Average R_a after polishing (nm)	Circularity	Porosity 1	Porosity 2	Porosity 3	Porosity 4
304 SS	11.84	10.34	0.97	0.08	0.05	0.03	0.02
Ta	26.05	19.68	0.94				

The SEY measurement results have not yet been obtained and are moved to future work of the research. Additionally, the angular measurements will be simulated via Monte-Carlo simulations.

4.11.3. Sample Manufacture With Conical And Reverse Conical Boreholes in 304 SS for SEE Reduction Efficiency Comparison.

According to theory in section 2.4.1, reduced surface area minimises the secondary electron generation on the surface of the sample. A reverse conical design of high aspect ratio hole pattering reduces the surface area for the electron impact. To quantify the efficiency of the SEE reduction with the reverse conical boreholes the packing density and hole entrance diameter must be identical to the conical design boreholes.

The following experiments have been conducted in order to manufacture a reverse conical borehole for SEE reduction in 304SS samples.

The manufacturing strategy included laser drilling through a thin metal foil of > 85 µm thick, according to 4.11.2.7, and flipping it over to obtain reverse conical holes for normal electron beam incidence, Figure 127.

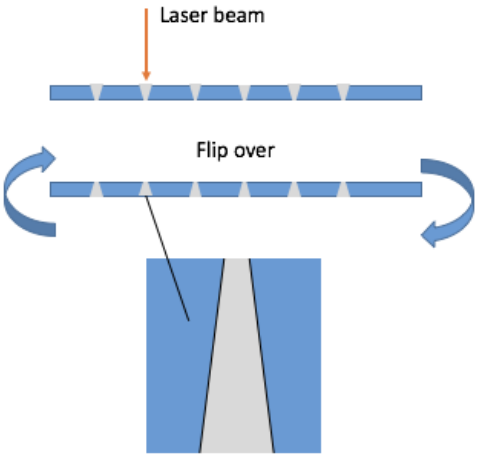

Figure 127. Reverse conical borehole manufacturing strategy.

A hexagonal array of holes has been drilled in 304SS foil with the hole drilling pattern in Figure 116, section 4.11.2.9. Figure 128 shows the hole entrance images of two arrays drilled with 5 µm trepanning radius and trepanning speeds of 0.4 and 1 mm/s. Figure 129 shows the exit images. The drilling parameters are available in Table 43.

Table 41. Laser drilling parameters for reverse conical borehole samples, 5 µm trepanning radius.

Satsuma Ultrafast Fibre Laser	
Wavelength (nm)	1030
PRF (kHz)	1
Pulse duration (fs)	350
Power (mW)	2.52
Spot size (µm)	4.1
Trepanning circles	50

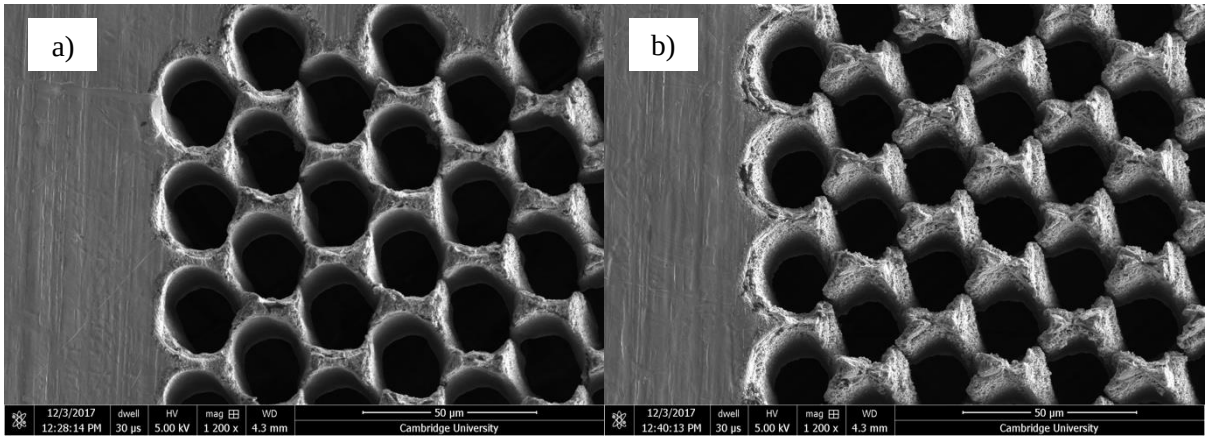

Figure 128. SEM images of the entrance hole arrays drilled in 304SS, a) 0.4 and b) 1 mm/s trepanning speeds. Sample no. a) 1599 and b) 1613. Images of the individual holes are available in Appendix M.

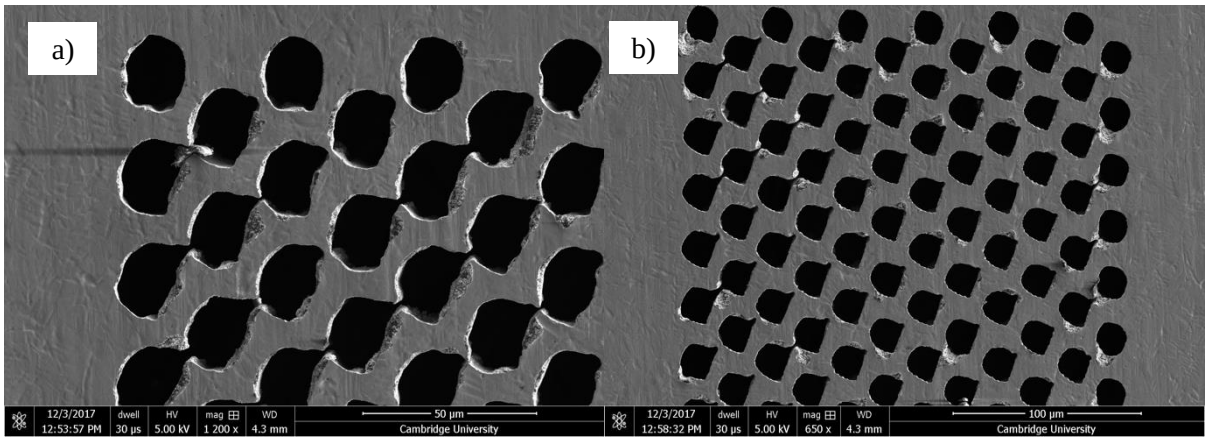

Figure 129. SEM images of the exit hole arrays drilled in 304SS, a) 0.4 and b) 1 mm/s trepanning speeds. Sample no. a) 1599 and b) 1613.

Figure 130 shows the hole entrance images of two arrays drilled with 1 µm trepanning radius and trepanning speeds of 0.4 and 1 mm/s. Figure 131 shows the exit image of the holes drilled with 0.4 mm/s. The hole array drilled with 1 µm trepanning radius and 1 mm/s trepanning speed did not produce a borehole. The drilling parameters are available in Table 42.

Table 42. Laser drilling parameters for reverse conical borehole samples, 1 µm trepanning radius.

Satsuma Ultrafast Fibre Laser	
Wavelength (nm)	1030
PRF (kHz)	1
Pulse duration (fs)	300
Power (mW)	2.52
Spot size (µm)	4.1
Trepanning circles	25

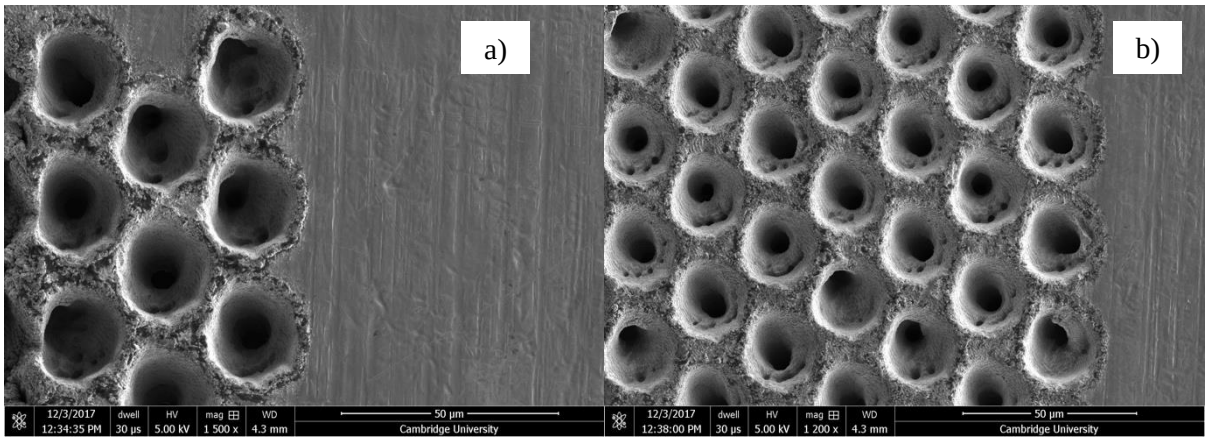

Figure 130. SEM images of the entrance hole arrays drilled in 304SS, a) 0.4 and b) 1 mm/s trepanning speeds. Sample no. a) 1603 and b) 1611. Images of the individual holes are available in Appendix M.

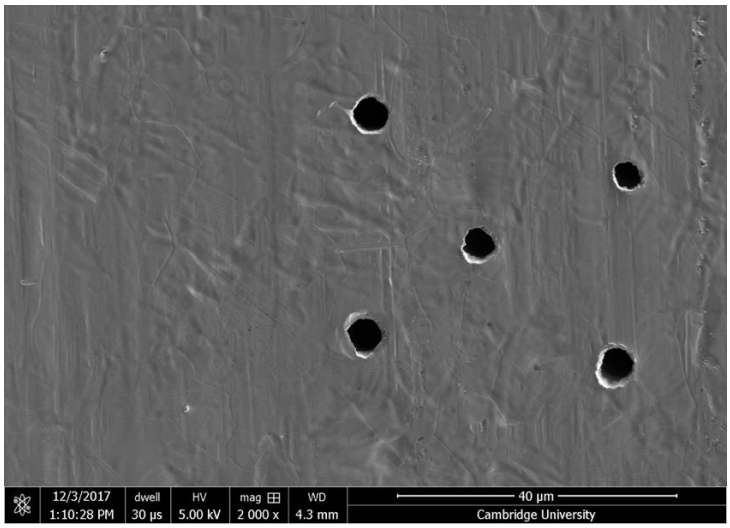

Figure 131. SEM image of the exit hole array drilled in 304 SS. Sample no. 1603.

Figure 132 shows a graph which records entrance/exit radii of the holes produced vs. their initial parameters. The radius is inferred from an area measurement of the holes.

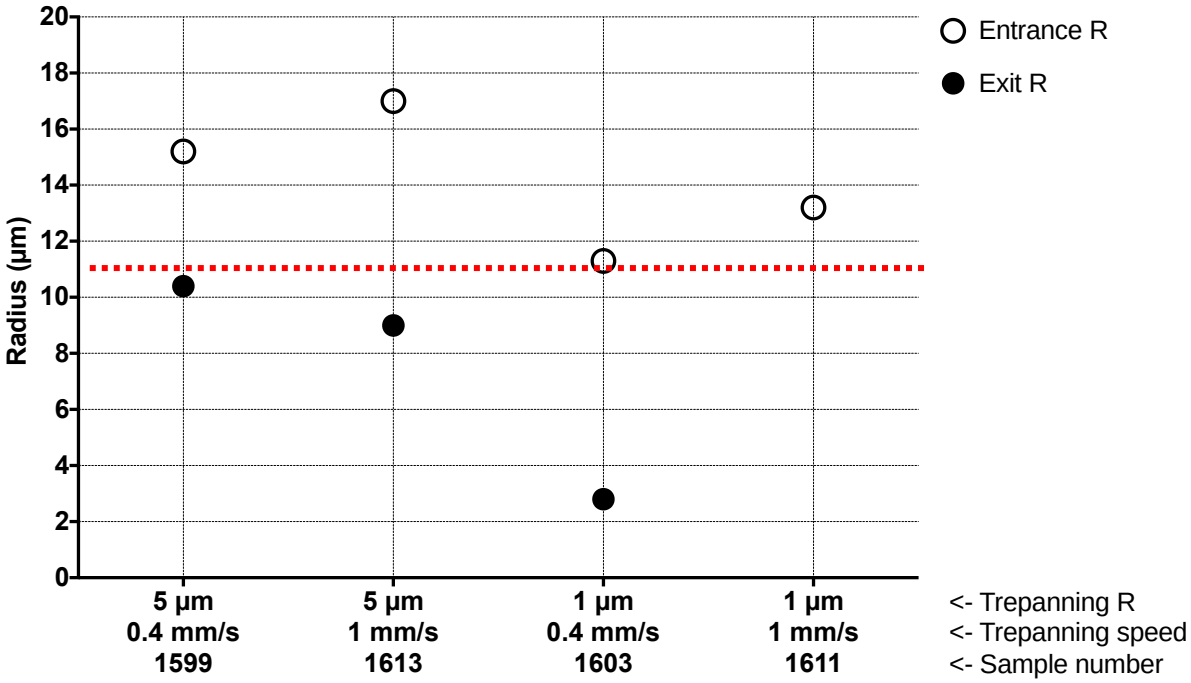

Figure 132. Graph recording the entrance/exit radii of the holes produced vs. their manufacturing parameters.

Samples 1599 and 1603 can be used for SEE reduction sample manufacturing due to their approximately equal radius value of the exit and entrance holes, indicated by the red line in Figure 132.

Figure 133 shows a graph which records the circularity of the holes, calculated using Equation 11, section 4.11.2.7.

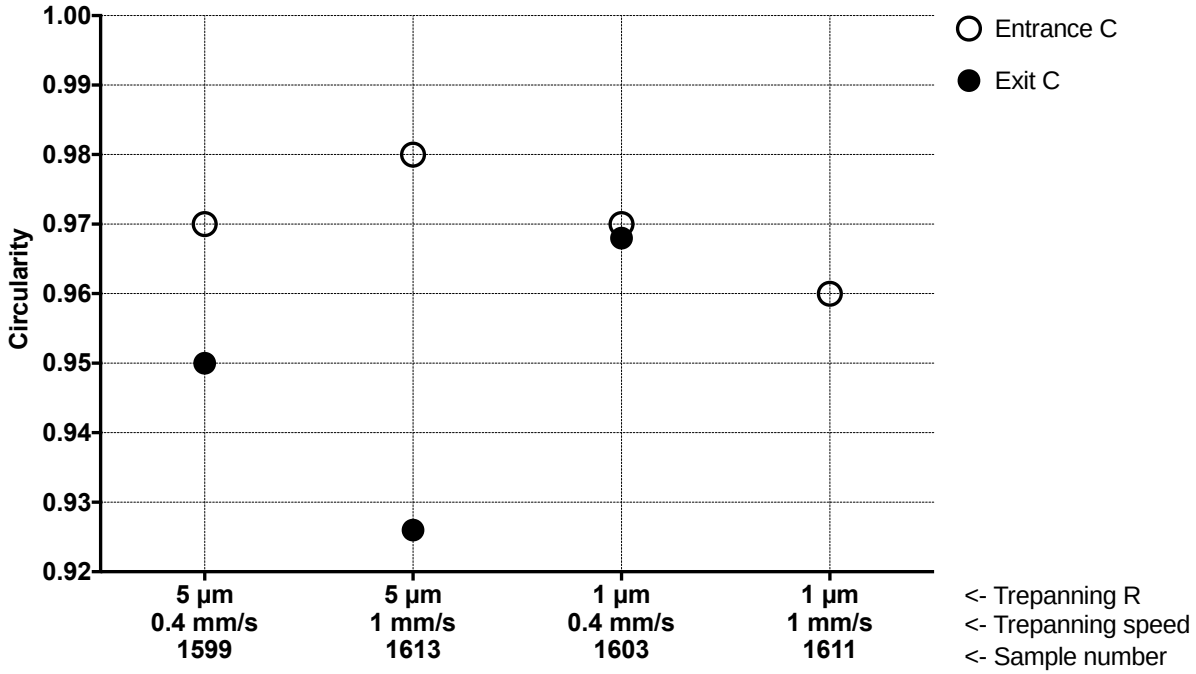

Figure 133. Graph recording the circularity of the entrance/exit holes produced vs. their manufacturing parameters.

The most circular hole measured is the entrance hole of 1613 sample. It, however, has the least circularity for its exit. It is observed that all entrance holes exhibit more circularity then the exit ones.

The circularity of the exit and entrance holes of the samples 1599 and 1603, respectively, varies by 2.06 %.

To conclude the findings of the reverse conical borehole manufacturing strategy explored, Samples 1599 and 1603 can be used for SEE reduction sample manufacturing. The packing density, hole entrance diameter and the circularity margin must be defined for quantifying the SEE reduction efficiency between the conical and reverse conical designs.

4.11.4. LIPSS on Steel.

In this section laser periodic surface structuring is compared to high aspect ratio hole patterning for metal SEE reduction.

The following samples have been produced; the laser parameters are recorded in Table 43:

- Sample 1, 304 SS, 0.6 mm thickness. Surface area pattern 10 x 10 mm. The sample was additionally mechanically polished to R_a of 51.03 nm prior to LIPSS treatment, according to procedures in 3.1.6.4, step 1-2, to eliminate surface defects.

- Sample 2, 316 SS, 1 mm thickness, surface area pattern 10 x 10 mm. The sample was LSM treated prior to LIPSS with ED_{av} 19.17 kJ/cm^2, laser parameters recorded in Table 11, section 4.1.5.

Table 43. LIPSS parameters.

Parameters	Sample 1	Sample 2
Pulse duration (ps)	1.3	1.3
Wavelength (μm)	1.03	1.03
Repetition rate (kHz)	5	5
Energy per pulse (μJ)	1.8	1.8
Speed (mm/s)	11	3
Line spacing (μm)	5	5

Surface morphology difference between samples 1 and 2 is illustrated in Figure 134. Note that the peaks and valleys in the surface morphology of Sample 2 are more prominent.

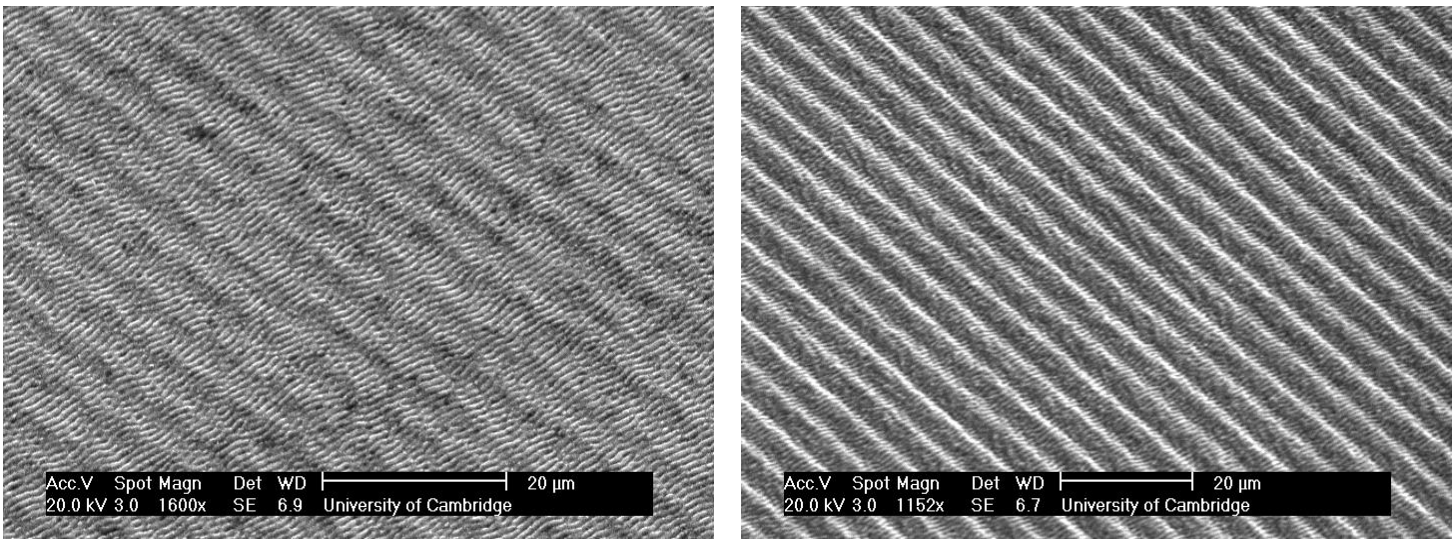

Figure 134. SEM images of Sample 1 on the left and Sample 2 - right. Additional SEM images are available in Appendix N.

LIPSS Samples 1 and 2 were bi-directionally raster scanned. As a result, both samples endure general peaks and ~5 μm wide valley morphology due to a 5 μm line spacing. However, Sample 2 exhibits additional waviness due to the prior LSM treatment, which generated trenches similar to Figure 26, making the ~5 μm wide peak and valley elevations more prominent on its surface. The Λ of the LIPSS is ~1 μm due to lasers wavelength, λ = 1,03 μm, as expected from theory in 2.5.2.7. The LIPSS are parallel and run perpendicular to the laser linear polarisation.

The SEE of three samples has been tested:

- Untreated; 304 SS, 0.6 thickness, mechanically polished to R_a of 51.03 nm, according to procedures in 3.1.6.6 step 1-2.
- LIPSS Sample 1.
- LIPSS Sample 2.

Figure 135 shows SEY for Untreated vs Sample 1 and 2. The testing was done with a break – from 1000 to 50 and 1000 to 5000 eV. Note that Untreated and Sample 1 exhibit a classic SEE pattern for metals, whereas Sample's 2 behaviour is different due to unknown reasons (possibly technical with the AMCS system) and needs further investigation. Untreated and Sample 1 are a direct comparison due to the original surface being of the same surface roughness. Note that the SEE reduction between the two is minimal and needs to be improved (SEY > 1). However, Sample's 2 SEY coefficient is < 1, counting 0.84 at its max SEY, which is lower that C-based materials [165]–[167], hole drilled samples in section 4.11.2.9 and satisfies the research question criteria.

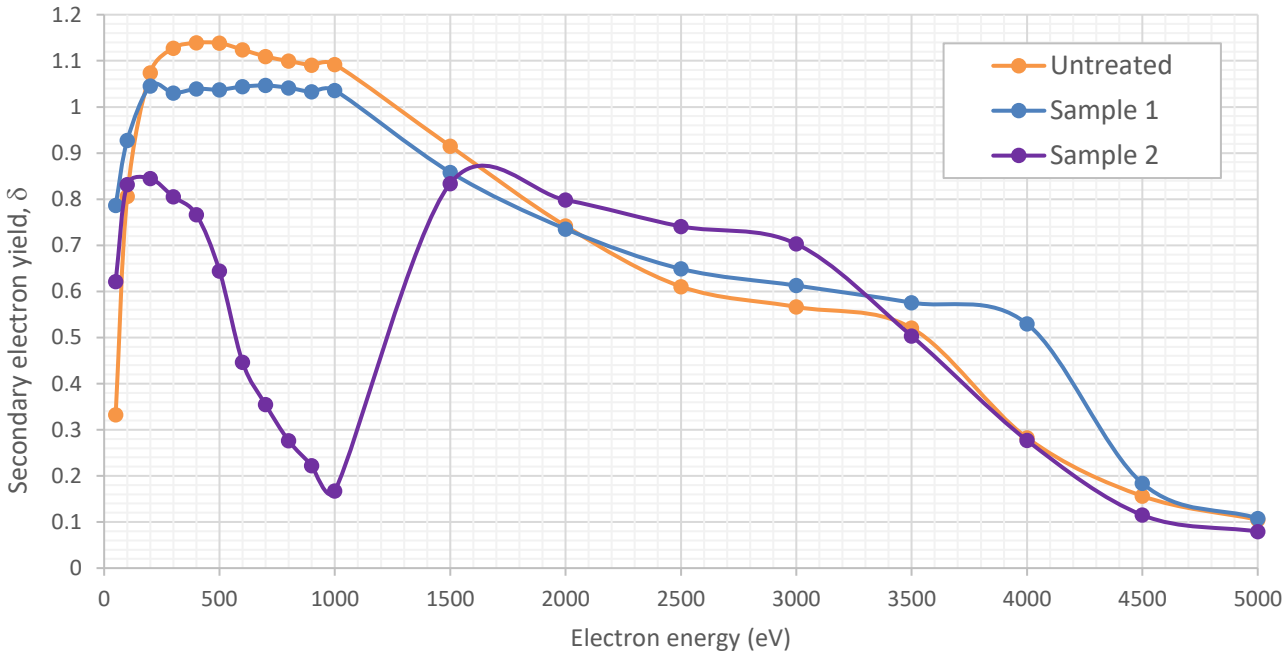

Figure 135. SEY of Untreated vs. Sample 1 and 2. δ is ratio of the number of secondary electrons leaving the surface to the number of incident primaries.

In conclusion, the results obtained for Sample 2 are promising and, thus, the investigation of LIPSS treatment should continue in the direction of its morphology.

For the application of anodes in HPM devices, hole drilling SEE reduction is favoured due to LIPSS affecting the underlying surface microstructure, as was discovered in section 4.5.1.1. It is acknowledged, however, that the material, mode and the laser fluence in the current experiment is different to that of the one in section 4.5.11. A high fluence of 18.50 – 1.85 MJ/cm^2 in CW mode was needed to generate LIPSS on a material with high thermal conductivity, copper. In the current case the peak fluence was significantly lower at 26.44 J/cm^2 in pulsed mode and the material was of low thermal conductivity, 304 SS. The physical phenomenon governing the LIPSS generation in both cases is the same, linear polarisation of the laser [168], therefore, no matter the laser parameters or the thermal conductivity of the material, the surface microstructure of the anode is affected.

Chapter 5

Conclusion and Future Work.

5.1. Conclusions.

This section of the report is divided into two parts, providing answers to the objectives outlined in section 2.6.1. Each part answers the sub-questions of the objectives:

Objective 1: Hydrogen outgassing reduction of metal anodes.

1. By what factor does LSM reduce the hydrogen outgassing of metal samples under HPM conditions?
2. Does LSM generate any abnormal grain growth?
3. How would additional PLM treatment affect the LSM treated microstructure of metals?
4. Can LSM compete with thermal annealing in its efficiency for hydrogen outgassing reduction of metals?

Objective2 : Secondary electron emission reduction of metal anodes with pulsed laser irradiation.

1. What design of LIPSS/micro holes would maximise the SEE reduction?
2. How LIPSS/laser drilling for SE trapping micro holes would affect the microstructure of the sample, consequently its diffusion?
3. What types of groove design reduce the SEY most effectively: laser drilled micro hole array or LIPSS?

5.1.1. Objective 1: Outgassing Reduction of Metal Anodes.

1. By what factor does LSM reduce the hydrogen outgassing of metal samples under HPM conditions?

Laser Surface Melting of SS – raster scanning laser beam (CW Yb fibre laser, 1.064 μm) across the SS surface in a uniform pattern affected its surface morphology and microstructure. The laser treated area showed reduced surface roughness, section 4.10, as a result of surface melting, followed by surface flow and finally re-solidification, as expected from theory in section 2.5.2.2. Microstructural transformation, which is the elongation of the grains in the direction of laser raster, showed a reduction in the number of the grain boundaries by 18.47 % with 13.54 kJ/cm^2 per 0.12 mm^2 and 21.72 % with 19.17 kJ/cm^2 per 0.17 mm^2, which serve as trapping sites for hydrogen in stainless steel. Due to these changes, HPM testing under 50 keV electron bombardment shows a reduction in hydrogen outgassing, by approximately a factor of four compared to that from untreated 304 and 316 SS. The e-beam

bombardment did not distort the microstructure of the SS samples due to the temperature being lower < than the melting temperature of steel, section 4.1.8.

2. Does LSM generate any abnormal grain growth?

The total number of grains in 13.54 kJ/cm^2 ED_{av} laser treated 304 SS was reduced from 1020 to 617 per 0.12 mm^2 surface area with a grain average of 201.59 μm^2, however, some grains measured up to 3500 μm^2 in area. This is attributed to the AGG effect and is regulated by the laser scanning strategy and its energy density. In the current study an increase in average laser ED helped extend the surface cooling temperature, generating much larger grains in the SS microstructure, from 201.59 μm^2 per 0.12 mm^2 to 1756.17 μm^2 per 0.17 mm^2 surface area. The AGG was still observed but amongst fewer grains, 96, with 12040 μm^2 maximum increase in grain size. This is again attributed to the scanning strategy, namely line overlap, as it stayed constant between 13.54 kJ/cm^2 and 19.17 kJ/cm^2 ED_{av} experiments.

Direct Grain Writing in the Microstructure of Metals.

Grain nucleation is not dependent on original grain size but, rather, regulated by the laser power, spot size, speed and line spacing. In this work grain elongation has been observed in 304 and 316 SS, Ni and Ti with CW laser surface melting and in 304 SS with PLM. The grains are pulled in the direction of the laser scan and formed patterns corresponding to the melt on the surface. By controlling the direction and area of laser irradiation it is possible to directly draw with grains in the microstructure of 304 and 316 SS, Ni and Ti. Removing the surface melt via mechanical polishing allowed to establish a metal security marking technique. The patterns are hidden from optical light microscopy and can be viewed with interferometric microscopy due to fine height difference between the untreated and treated areas in sample's microstructure. Three tools were needed in the current work for security marking 316 SS with QR and Bar codes:

1. Laser, SPI G3 20 W to write the QR and Bar codes in the microstructure of 316 SS
2. Grinder, ATM Saphir™ 550 to remove the surface melt.
3. DIC microscope, Olympus™ BX51M.

LSM treatment can be used as technique for controlled electrical conductivity increase of metals.

The results show 34.38 % increase in electrical conductivity after a single bidirectional laser raster scan with a 36 % line overlap at 19.17 kJ/cm^2 average energy density by a continuous wave Yb fibre laser with a wavelength of 1.064 μm.

3. How would additional PLM treatment affect the LSM treated microstructure of metals?

Direct grain writing is not unique to CW LSM. It was observed that the grains, effected by pulsed laser radiation, become elongated once again in the direction of laser scan. PLM and CW LSM treatments, are regulated by the same mechanism. In the current work, additional PLM treatment was not directly explored on LSM treated metals and remains as future work. However, multiple CW LSM laser passes showed that LSM can be used for single grain generation.

Single Crystal Grain Writing in the Microstructure of Steels.

Single crystals have been generated in the microstructure of 304 SS after three consecutive passes with constant laser parameters throughout the length of the laser raster at 19.17 kJ/cm^2 average energy density by a continuous wave non-polarised fibre laser with a wavelength of 1.064 μm at 300 K, 0.1 % oxygen environment. Additionally, bidirectional raster scanning with 19.17 kJ/cm^2 EDs with the line spacing 0.04 mm yielded single crystals in each laser pass min 400 μm. Thus, two scanning strategies have been identified for single crystal generation in steels – multiple passes and bidirectional raster scanning. The exact mechanism for single crystal generation remains to be clarified and is moved to the Future Work section.

4. Can LSM compete with thermal annealing in its efficiency for hydrogen outgassing reduction of metals?

LSM outgassing reduction is due to both evacuated H atoms and reduced number of grain boundaries in the LSMZ of the treated sample but a reduced content of surface H atoms after LSM was not observed. Thus, the LSMZ can serve as a barrier between the bulk and the surface of the material, where the reduced number of GBs slows down the H atom thermal permeation to the surface to recombine into H_2 molecule for outgassing.

To maximise the LSM hydrogen outgassing reduction of metal HPM anodes it is beneficial to increase the LSMZ so that the maximum heating/diffusion under e-beam bombardment takes place in H depleted area.

Commercial applications of the LSM technique for hydrogen outgassing reduction in metals include but are not limited to: LSM of steel chambers for ultra/extreme high vacuum systems (particle accelerators, etc.), analytical techniques (XPS, SIMS, SEM, FIB, etc.). LSM may also be used for the reduction of hydrogen embrittlement for mechanical failures in metals for increased strength of structural metals.

LSM has shown to increase the SEY of metal samples due to surface smoothing effect. The 304SS SEY was increased from 0.9 to 1.2 after LSM with 13.54 kJ/cm^2 ED. Samples treated for H_2 outgassing reduction require a SEE reduction technique.

5.1.2. Objective 2: Secondary Electron Emission Reduction of Metal Anodes.

Second Objective: Secondary electron emission reduction of metal anodes with pulsed laser irradiation.

1. What design of LIPSS/micro holes would maximise the SEE reduction

Two design have been tested in this work on principle of surface structuring for SE trapping:

- High-aspect ratio holes
- Laser-induced periodic surface structuring.

For high-aspect ratio hole SEE reduction, the following parameter directions are extrapolated from the results to satisfy the objective:

- Power (W) – decrease.
- Pulse width (fs) – decrease.
- PRF (kHz)- decrease.
- Trepanning speed (mm/s) – increase.

Maximum SEE reduction with high-aspect ratio holes achieved was 0.98, < 1 SEY and satisfies the research question criteria of eliminating the uncontrollable generation of free electrons in HPM devices. 304 SS was laser drilled via trepanning with a femtosecond laser, 1:3 aspect ratio holes, 0.52 hexagonal packing density. The SEY experimental result was compared to the theoretical model in [116] due to similar porosity and aspect ratio and agrees with the model. Single-shot laser drilling was also explored via picosecond laser in this work. Picosecond laser drilling yielded low circularity holes, thus, proving to be ineffective for the conditions explored here.

For SEE reduction via laser-induced periodic surface structuring, peaks and valley LIPSS treated 316 SS showed < 1 reduction in SEY. Sample's SEY counted 0.84 at its peak, which is lower that C-based materials and high-aspect ratio holes and satisfies the research question criteria. It was discovered that at fluence of 18.50 – 1.85 MJ/cm^2 in CW mode the surface grains were nucleated in OFHC copper, concluding that LIPSS treatment can disrupt the LSM design for reduced hydrogen outgassing in the manufacture of the HPM anode. The results obtained for LIPSS patterning for SEE reduction are

promising and the degree of the microstructural disruption can be user-defined, thus, the investigation of LIPSS treatment should continue in the direction of its morphology.

5.2. Future Work

5.2.1. Outgassing Reduction of Metal Anodes.

Develop a quantified relationship between the grain size and factor of H_2 outgassing.

Adapting this strategy would make possible to identify the size of the grains needed to reduce the 304 SS H outgassing, for example, by a factor of 5 instead of 4 as seen in section 4.1.4. According to discoveries in section 4.1.6, a chart of average laser ED vs penetration depth could be simulated to monitor the depth of the laser-induced microstructural changes in metals to create a quantified relationship between hydrogen outgassing and the grain size in sample's crystal lattice. As well as that, the limits of LSM technique could be tested by monitoring the maximum grain increase achievable (current nucleation in SS goes beyond > ED 19.17 kJ/cm^2). The study could show whether LSM can compete with furnace thermal annealing in its efficiency for of H_2 outgassing reduction in metals. It is suspected that the cost and speed of annealing with LSM would be improved comparing to furnace annealing due to fast localised nucleation rather than increasing the size of the furnaces to accommodate large parts for H outgassing.

LSM of SS anodes for high voltage outgassing testing.

According to the simulation results in section 4.1.9, increased LSMZ ensures that the maximum heating/diffusion during e-beam bombardment takes place in H depleted area. T-shaped discs of 304 SS, diameter of 44.5 mm and 3.2 mm thickness, have been fabricated for both LSM treatments and laser hole drilling, Figure 136. The T shape was chosen to fit the disks in the new AMCS holder. The disks will be subjected to a 240 keV electron bombardment, normal HPM keV, to simulate increased e-beam penetration.

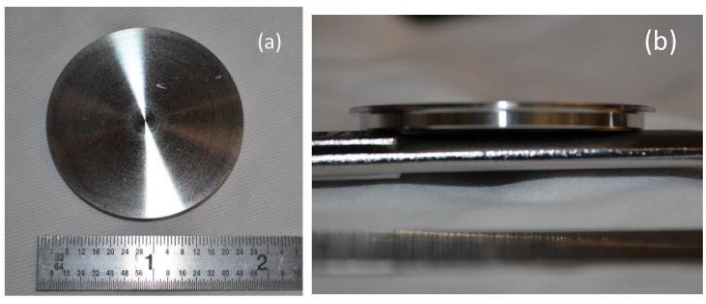

Figure 136. T-shaped discs of 304SS showing (a) top and (b) side view.

Measure the H_2 diffusion speed of LSM treated metals.

Two sides of the sample, front and back, will be LSM treated and measured for H_2 diffusion speed vs e-beam bombardment time. Samples > 3 mm thick showed enough hydrogen content in the sample to not to be mistaken for other gasses or errors in the measurements and, therefore, will be used for this experiment.

LSM of nickel.

A discovery of an impeding mechanism of flow and resolidification of the surface material was made during LSM treatment of Ni samples, section 4.6. A certain mechanism was impeding the laser illumination from affecting the material even at high average EDs. This phenomenon repeated itself throughout the experiments (LSM and single pass irradiations) and requires further investigation. It is proposed to repeat the single pass experiment with EDs ranging from 0.04 to 12.88 kJ/cm^2 at increased and reduced surface roughness of the Ni sample.

Single crystal generation mechanism.

The objective is to find the laser parameters to maximise the grain size as much as possible favouring single crystal growth and explore the possibility of enlarging the grains two-dimensionally, Figure 137.

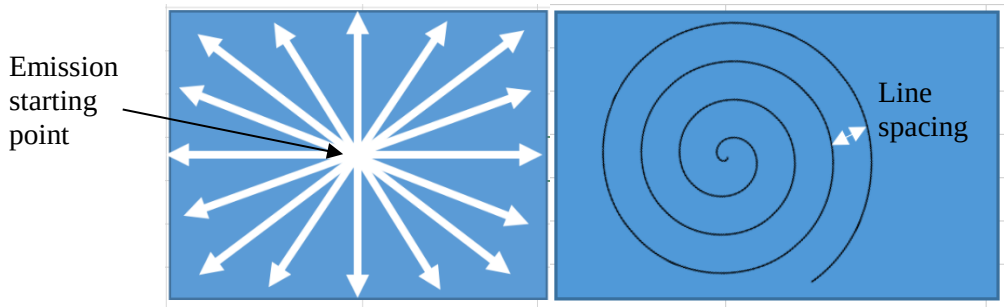

Figure 137. Suggested strategies for 2D grain enlargement, a) star and b) swirl with variable line spacing.

The criteria for direct grain writing in 304 SS, 316 SS, Ni and Ti remains as following:

- The direct grain writing with CW LSM requires the laser spot size to generate surface melt larger or equal to the grain size to be able to nucleate the grains.
- Higher ED generates deeper and wider melt pools, hence, longer cooling time and larger grains.
- Overlapping scan strategy can disrupt the formation of the generated grains. These could be pulled in either direction depending on the scan.

Regarding the experiment in 4.5, the tests with 19.15 kJ/cm^2 and increased spot size of 81.2 µm need to be repeated to see the extend of maximum grain enlargemnt in 304 SS with CW 1064 nm lasers.

For copper, the result in section 4.5.1.1 showed that thermal conductivity of the material effects the grain growth via LSM treatment. To continue copper investigation for direct grain writing, the following steps are outlined.

- Quantify the grain size increase with EBSD testing in OFHC Cu treated with 0.5 and 1 mm/s to relate grain increase to laser power, scan speed and irradiation area.
- Increased laser spot size trials.
- For faster manufacturing of samples, a 532 nm wavelength CW laser system with increased laser power is required.

Further grain dependant metal property changes.

According to discoveries in section 4.9, larger grains show increased microwave reflection, recorded in the form of voltage power, the voltage signal will be converted to the bulk conductivity of stainless steel. This will indicate whether the LSM treatment is significant for conductivity increase in industry. The current experiment shows a 34.38 % increase from the untreated to LSM treated with the largest grain growth, sample 1R.

It is known that metal hardness properties are dependent on the grain size as well [160]. It is proposed to subject the LSM treated samples to different loads for fracture tests.

As the metal electrical conductivity is increased with grain size so grows its thermal conductivity. It is proposed to measure the thermal conductivity of LSM treated samples to quantify that percentage increase.

Collaboration with National Graphene Institute (NGI) in Manchester.

A collaboration with *National Graphene Institute* has been established for producing laser treated steel, nickel and copper samples 12 x 12 x 1 mm for testing the benefit of LSM hydrogen suppression and grain increase technique for substrates used for CVD graphene growth. Laser wavelength of 532 nm in CW is recommended to be used for LSM experiments to maximise copper absorption.

5.2.2. Secondary Electron Emission Reduction of Metal Anodes.

The following sub-questions of the second objective are translated into further work.

1. How LIPSS/laser drilling for SE trapping micro holes would affect the microstructure of the sample, consequently its diffusion?

In order to answer this question, the laser drilled samples in section 4.11.2.9 and LIPSS in 4.11.4 will be subjected to FIB microscopy to identify whether the SEE treatments have affected the microstructure

of the samples. AMCS hydrogen outgassing testing of samples subjected to both treatments, LSMed and laser drilling/LIPSS, would ultimately show the diffusion difference between current and laser manufactured HPM anodes. It is important to mention here that the LSMZ must be larger than the depth of the micro holes for increased H_2 outgassing reduction.

2. What types of groove design reduce the SEY most effectively: laser drilled micro hole array or LIPSS?

From the tests in section 4.11.4, LIPSS have showed 0.84 at its max SEY compared to 0.98 from micro hole laser drilled ones. The limit for hole drilling SEE reduction is the porosity of the surface, whereas for LIPSS smaller periodic structures could be built on top of larger structures, e.g. nano-structures on micro-structures, and is entirely dependent on the capabilities of the laser system used. Nevertheless, both methods follow the theory in section 2.5.2.6 and, therefore, are affected by the angle of incidence of the primary electrons. Angular testing is suggested as the next comparison step for SEE reduction in metals. The Ta and 304 SS samples have been prepared for the angular e-beam bombardment trials in section 4.11.2.9 with Ta to avoid the electron conditioning effect and identical porosity 304 SS to compare the Ta SEY to.

Sample manufacture with conical and reverse conical boreholes in 304 SS for SEE reduction efficiency comparison.

A reverse conical design of a borehole is proposed for further SEE reduction in metals. The drilling strategies used for samples 1599 and 1603 are proposed for the design. The packing density, hole entrance diameter and the circularity margin must remain constant for quantifying the SEE reduction efficiency between the conical and reverse conical designs.

Hybrid anode.

A thin layer of copper (~0.5-1 mm) which undergoes LSM treatment for outgassing reduction can be placed on top of CNT paper which will serve as an SEE reduction material to shield it from harmful high keV of the HPM e-beam, according to investigations in section 2.4.2. For LSM treating copper, < IR wavelength is proposed to avoid surface coatings for reflectivity reduction, section 4.6.1.

LSM and Laser Drilling for Hydrogen outgassing reduction Patent.

USAF is interested in combining the LSM and laser drilling treatments for hydrogen outgassing and SEE reduction, respectively, into one Patent for HPM anode manufacture.

5.3. Research Outcome.

This work led to the following publications and a U.S. patent.

Journals

- D. Gortat, P.T. Murray, S.B. Fairchild, M. Sparkes, T.C. Back, G.J. Gruen, M.M. Cahay, N.P. Lockwood, W. O'Neill. "Laser surface melting of stainless steel anodes for reduced hydrogen outgassing." Materials Letters 2017, 190, 5–8.

Conference papers

- D. Gortat ; M. Sparkes ; S.B. Fairchild ; P.T. Murray ; M. M. Cahay ; T. C. Back ; G. J. Gruen ; N. P. Lockwood ; W. O'Neill. "Laser stimulated grain growth in 304 stainless steel anodes for reduced hydrogen outgassing." Proc. SPIE 10083, Fiber Lasers XIV: Technology and Systems, 100832E, 2017.

- P.T. Murray, S. B. Fairchild, T. C. Back, D. Gortat, M. Sparkes, G. J. Gruen, and N. P. Lockwood. "Laser surface melting of stainless steel anodes for reduced hydrogen outgassing." In 2016 IEEE International Conference on Plasma Science (ICOPS), pp. 1-1. IEEE, 2016.

Patent

- D. Gortat, S.B. Fairchild, M. Sparkes, W. O'Neill. (2017). Laser Surface Melting for Outgassing Reduction. US62/519208.

The following journal papers are in preparation.

- Reliable secondary electron emission measurements from gold covered micro porous stainless steel surfaces.
- High aspect ratio micro hole laser drilling for angular SEE reduction in tantalum and 304 SS.
- Electrical conductivity increase in laser treated 304 SS.

The following conference paper has been accepted for publication in ILAS 2019.

- Direct laser grain writing in steels.

References.

[1] E. Schamiloglu, 'High power microwave sources and applications', in *Microwave Symposium Digest, 2004 IEEE MTT-S International*, 2004, vol. 2, pp. 1001-1004 Vol.2.

[2] K. E. Hackett, 'Directed Energy Applications for High Power Vacuum Electronics', in *Vacuum Electronics Conference, 2006 held Jointly with 2006 IEEE International Vacuum Electron Sources., IEEE International*, 2006, pp. 11–13.

[3] R. J. Barker and E. Schamiloglu, *High-power microwave sources and technologies*. Wiley-IEEE Press, 2001.

[4] J. H. Booske *et al.*, 'Vacuum Electronic High Power Terahertz Sources', *IEEE Trans. Terahertz Sci. Technol.*, vol. 1, no. 1, pp. 54–75, Sep. 2011.

[5] UNITED STATES AIR FORCE, 'HighPower Microwaves.', 2002.

[6] R. J. Barker, N. C. Luhmann, J. H. Booske, and G. S. Nusinovich, 'Modern microwave and millimeter-wave power electronics', *Mod. Microw. Millim.-Wave Power Electron. Robert J Bark. Ed. Neville C Luhmann Ed. John H Booske Ed. Gregory Nusinovich Pp 872 ISBN 0-471-68372-8 Wiley-VCH April 2005*, p. 872, 2005.

[7] D. A. Shiffler Jr and M. D. Haworth, *Carbon nanotube coated anode*. Google Patents, 2003.

[8] X. Zhao, C. Johnston, and P. S. Grant, 'A novel hybrid supercapacitor with a carbon nanotube cathode and an iron oxide/carbon nanotube composite anode', *J. Mater. Chem.*, vol. 19, no. 46, pp. 8755–8760, 2009.

[9] M. Elfsberg, T. Hurtig, A. Larsson, C. Möller, and S. E. Nyholm, 'Experimental studies of anode and cathode materials in a repetitive driven axial vircator', *Plasma Sci. IEEE Trans. On*, vol. 36, no. 3, pp. 688–693, 2008.

[10] D. Shiffler *et al.*, 'Carbon velvet field-emission cathode', *Rev. Sci. Instrum.*, vol. 73, no. 12, pp. 4358–4362, 2002.

[11] J. Vara, 'Anode material testing in a vacuum diode', 2011.

[12] J. Benford, J. A. Swegle, and E. Schamiloglu, *High power microwaves*. CRC Press, 2015.

[13] N. M. Jordan, G. B. Greening, B. W. Hoff, S. S. Maestas, S. C. Exelby, and R. M. Gilgenbach, 'Additively Manufactured High Power Microwave Anodes'.

[14] M. A. Franzi *et al.*, 'Microwave power and phase measurements on a recirculating planar magnetron', *IEEE Trans. Plasma Sci.*, vol. 43, no. 5, pp. 1675–1682, 2015.

[15] S. B. Fairchild, J. Bulmer, M. Sparkes, J. J. Boeckl, and G. Kozlowski, 'Field Emission Cathodes made from Laser Cut CNT Fibers and Films', presented at the 10th International Conference on Diffusion in Solids and Liquids, DSL 2014 - Congress Proceedings, 2014.

[16] S. Avdiaj and B. Erjavec, 'OUTGASSING OF HYDROGEN FROM A STAINLESS STEEL VACUUM CHAMBER', *Mater. Tehnol.*, vol. 46, no. 2, pp. 161–167, 2012.

[17] C. Watts, M. Gilmore, and E. Schamiloglu, ‘Effects of Laser Surface Modification on Secondary Electron Emission of Copper’, *IEEE Trans. Plasma Sci.*, vol. 39, no. 3, pp. 836–841, Mar. 2011.

[18] B. Piosczyk, C. T. Iatrou, G. Dammertz, and M. Thumm, ‘Single-stage depressed collectors for gyrotrons’, *IEEE Trans. Plasma Sci.*, vol. 24, no. 3, pp. 579–585, 1996.

[19] K. Jousten, ‘Thermal outgassing’, CERN, 1999.

[20] M. Bernardini *et al.*, ‘Air bake-out to reduce hydrogen outgassing from stainless steel’, *J. Vac. Sci. Technol. A*, vol. 16, no. 1, pp. 188–193, 1998.

[21] P. A. Redhead, ‘Extreme high vacuum’, Cern, 1999.

[22] M. Leich, ‘Hydrogen outgassing of stainless steel, our present knowledge’, in *Proceedings of the 1st Vacuum Symposium, UK*, 2010.

[23] P. A. Redhead, ‘Hydrogen in vacuum systems: an overview’, in *AIP Conference Proceedings*, 2003, pp. 243–254.

[24] L. Westerberg, B. Hjörvarsson, E. Wallén, and A. Mathewson, ‘Hydrogen content and outgassing of air-baked and vacuum-fired stainless steel’, *Vacuum*, vol. 48, no. 7–9, pp. 771–773, Sep. 1997.

[25] O. B. Malyshev, B. T. Hogan, and M. Pendleton, ‘Effect of surface polishing and vacuum firing on electron stimulated desorption from 316LN stainless steel’, *J. Vac. Sci. Technol. A*, vol. 32, no. 5, p. 051601, Sep. 2014.

[26] M. A. A. Mamun, A. A. Elmustafa, M. L. Stutzman, P. A. Adderley, and M. Poelker, ‘Effect of heat treatments and coatings on the outgassing rate of stainless steel chambers’, *J. Vac. Sci. Technol. A*, vol. 32, no. 2, p. 021604, 2014.

[27] R. F. Berg, ‘Hydrogen traps in the outgassing model of a stainless steel vacuum chamber’, *J. Vac. Sci. Technol. A*, vol. 32, no. 3, p. 031604, 2014.

[28] A. Oudriss *et al.*, ‘Grain size and grain-boundary effects on diffusion and trapping of hydrogen in pure nickel’, *Acta Mater.*, vol. 60, no. 19, pp. 6814–6828, 2012.

[29] S. M. Foiles, ‘Temperature dependence of grain boundary free energy and elastic constants’, *Scr. Mater.*, vol. 62, no. 5, pp. 231–234, 2010.

[30] A. Garbacz, B. Ralph, and K. J. Kurzydl\Lowski, ‘On the possible correlation between grain size distribution and distribution of CSL boundaries in polycrystals’, *Acta Metall. Mater.*, vol. 43, no. 4, pp. 1541–1547, 1995.

[31] N. Yazdipour, D. P. Dunne, and E. V. Pereloma, ‘Effect of grain size on the hydrogen diffusion process in steel using cellular automaton approach’, in *Materials Science Forum*, 2012, vol. 706, pp. 1568–1573.

[32] Y. Pan and B. L. Adams, ‘On the CSL grain boundary distributions in polycrystals’, *Scr. Metall. Mater.*, vol. 30, no. 8, pp. 1055–1060, 1994.

[33] S. Bechtle, M. Kumar, B. P. Somerday, M. E. Launey, and R. O. Ritchie, ‘Grain-boundary engineering markedly reduces susceptibility to intergranular hydrogen embrittlement in metallic materials’, *Acta Mater.*, vol. 57, no. 14, pp. 4148–4157, 2009.

[34] B. O. Hoch, A. Metsue, J. Bouhattate, and X. Feaugas, ‘Effects of grain-boundary networks on the macroscopic diffusivity of hydrogen in polycrystalline materials’, *Comput. Mater. Sci.*, vol. 97, pp. 276–284, 2015.

[35] D. G. Brandon, ‘The structure of high-angle grain boundaries’, *Acta Metall.*, vol. 14, no. 11, pp. 1479–1484, 1966.

[36] D. G. Brandon, B. Ralph, S. t Ranganathan, and M. S. Wald, ‘A field ion microscope study of atomic configuration at grain boundaries’, *Acta Metall.*, vol. 12, no. 7, pp. 813–821, 1964.

[37] A. P. Zakharov, V. M. Sharapov, and E. I. Evko, ‘Hydrogen permeability of polycrystalline and monocrystalline molybdenum and tungsten’, *Mater. Sci.*, vol. 9, no. 2, pp. 149–153, 1975.

[38] K. J. Al-Fadhalah, ‘Texture and grain boundary character distribution in a thermomechanically processed OFHC copper’, *J. Eng. Mater. Technol.*, vol. 134, no. 1, p. 011001, 2012.

[39] S. M. Schlegel, S. Hopkins, and M. Frary, ‘Effect of grain boundary engineering on microstructural stability during annealing’, *Scr. Mater.*, vol. 61, no. 1, pp. 88–91, 2009.

[40] Z. Gu, X. Xu, M. Lei, W. Feng, and S. Yang, ‘Grain Boundary Engineering of SUS304 by Laser Shocking and Annealing’, in *PRICM: 8 Pacific Rim International Congress on Advanced Materials and Processing*, pp. 2199–2204.

[41] U. Köster, ‘Recrystallization involving a second phase’, *Met. Sci.*, vol. 8, no. 1, pp. 151–160, 1974.

[42] J. B. Koo and D. Y. Yoon, ‘Abnormal grain growth in bulk Cu—The dependence on initial grain size and annealing temperature’, *Metall. Mater. Trans. A*, vol. 32, no. 8, pp. 1911–1926, 2001.

[43] P. A. Redhead, ‘Extreme high vacuum’, Cern, 1999.

[44] P. He, H. C. Hseuh, M. Mapes, R. Todd, D. Weiss, and D. Wilson, ‘Hydrogen outgassing and surface properties of TiN-coated stainless steel chambers’, in *AIP Conference Proceedings*, 2003, vol. 671, pp. 292–299.

[45] I. Chun, B. Cho, and S. Chung, ‘Outgassing rate characteristic of a stainless-steel extreme high vacuum system’, *J. Vac. Sci. Technol. A*, vol. 14, no. 4, pp. 2636–2640, 1996.

[46] G. Stupakov and M. Pivi, ‘Suppression of the effective secondary emission yield for a grooved metal surface’, *LCC-0145 SLAC-TN-04-045*, p. 139, 2004.

[47] K. Nishimura, T. Itotani, and K. Ohya, ‘Influence of surface roughness on secondary electron emission and electron backscattering from metal surface’, *Jpn. J. Appl. Phys.*, vol. 33, no. 8R, p. 4727, 1994.

[48] M. Suemitsu *et al.*, ‘Ultrahigh-vacuum compatible mirror-polished aluminum-alloy surface: Observation of surface-roughness-correlated outgassing rates’, *J. Vac. Sci. Technol. A*, vol. 10, no. 3, pp. 570–572, 1992.

[49] P. C. Pinto *et al.*, ‘Carbon coatings with low secondary electron yield’, *Vacuum*, vol. 98, pp. 29–36, 2013.

[50] J. Y. Seto, ‘The electrical properties of polycrystalline silicon films’, *J. Appl. Phys.*, vol. 46, no. 12, pp. 5247–5254, 1975.

[51] K. P. McKenna and A. L. Shluger, ‘Electron-trapping polycrystalline materials with negative electron affinity’, *Nat. Mater.*, vol. 7, no. 11, pp. 859–862, 2008.

[52] J. E. Yater and A. Shih, ‘Secondary electron emission characteristics of single-crystal and polycrystalline diamond’, *J. Appl. Phys.*, vol. 87, no. 11, pp. 8103–8112, 2000.

[53] L. Wang, T. O. Raubenheimer, and G. Stupakov, ‘Suppression of secondary emission in a magnetic field using triangular and rectangular surfaces’, *Nucl. Instrum. Methods Phys. Res. Sect. Accel. Spectrometers Detect. Assoc. Equip.*, vol. 571, no. 3, pp. 588–598, 2007.

[54] L. Wang, T. Raubenheimer, and G. Stupakov, ‘Suppression of Secondary Emission in a magnetic Field using a sawtooth Surface’, in *EPAC Conf. Proceedings, Scotland*, 2006.

[55] M. Ye *et al.*, ‘Suppression of secondary electron yield by micro-porous array structure’, *J. Appl. Phys.*, vol. 113, no. 7, p. 074904, 2013.

[56] R. Valizadeh, O. B. Malyshev, S. Wang, S. A. Zolotovskaya, W. A. Gillespie, and A. Abdolvand, ‘Low secondary electron yield engineered surface for electron cloud mitigation’, *Appl. Phys. Lett.*, vol. 105, no. 23, p. 231605, 2014.

[57] G. Stupakov and M. Pivi, ‘Suppression of the effective secondary emission yield for a grooved metal surface’, CERN, 2004.

[58] A. A. Krasnov, ‘Molecular pumping properties of the LHC arc beam pipe and effective secondary electron emission from Cu surface with artificial roughness’, *Vacuum*, vol. 73, no. 2, pp. 195–199, Mar. 2004.

[59] L. Wang, T. Raubenheimer, and G. Stupakov, ‘Suppression of Secondary Emission in a magnetic Field using a sawtooth Surface’, in *EPAC Conf. Proceedings, Scotland*, 2006.

[60] V. Baglin *et al.*, ‘The secondary electron yield of technical materials and its variation with surface treatments’, 2000.

[61] M. Pivi, F. K. King, R. E. Kirby, T. O. Raubenheimer, G. Stupakov, and F. Le Pimpec, ‘Sharp reduction of the secondary electron emission yield from grooved surfaces’, *J. Appl. Phys.*, vol. 104, no. 10, p. 104904, 2008.

[62] J. Kawata and K. Ohya, ‘Dependence of secondary electron emission on the incident angle and the energy of primary electrons bombarding bowl-structured beryllium surfaces’, 1994.

[63] O. Zhou and S. Washburn, ‘Carbon Nanotube Based Anode for High Power Microwave Systems’, DTIC Document, 2004.

[64] Michael D. Haworth and Donald A. Shiffler, Jr., ‘Carbon nanotube coated anode’, US6645628B2, 13-Nov-2001.

[65] B. W. Smith and D. E. Luzzi, ‘Electron irradiation effects in single wall carbon nanotubes’, *J. Appl. Phys.*, vol. 90, no. 7, pp. 3509–3515, Oct. 2001.

[66] I. Childres *et al.*, ‘Effect of electron-beam irradiation on graphene field effect devices’, *Appl. Phys. Lett.*, vol. 97, no. 17, p. 173109, 2010.

[67] X. Yu, Y. Shen, T. Liu, T. T. Wu, and Q. J. Wang, ‘Photocurrent generation in lateral graphene pn junction created by electron-beam irradiation’, *Sci. Rep.*, vol. 5, 2015.

[68] D. Teweldebrhan and A. A. Balandin, ‘Modification of graphene properties due to electron-beam irradiation’, *Appl. Phys. Lett.*, vol. 94, no. 1, p. 013101, 2009.

[69] I. Childres *et al.*, ‘Effect of energetic electron irradiation on graphene’, in *Aip Conference Proceedings*, 2009, vol. 1194, p. 140.

[70] J. Xie and J. P. Spallas, ‘Different contrast mechanisms in SEM imaging of graphene’, *Tech. Rep. Agil. Technol.*, 2012.

[71] G. Rao, S. Mactaggart, J. U. Lee, and R. Geer, ‘Study of electron beam irradiation induced defectivity in mono and bi layer graphene and the influence on Raman band position and line-width’, *MRS Proc.*, vol. 1184, Jan. 2009.

[72] L. Brown, R. Hovden, P. Huang, M. Wojcik, D. A. Muller, and J. Park, ‘Twinning and twisting of tri-and bilayer graphene’, *Nano Lett.*, vol. 12, no. 3, pp. 1609–1615, 2012.

[73] A. W. Tsen, L. Brown, R. W. Havener, and J. Park, ‘Polycrystallinity and stacking in CVD graphene’, *Acc. Chem. Res.*, vol. 46, no. 10, pp. 2286–2296, 2012.

[74] J. M. Parson *et al.*, ‘A frequency stable vacuum-sealed tube high-power microwave vircator operated at 500 Hz’, *Electron Device Lett. IEEE*, vol. 36, no. 5, pp. 508–510, 2015.

[75] J. Pappis and S. L. Blum, ‘Properties of pyrolytic graphite’, *J. Am. Ceram. Soc.*, vol. 44, no. 12, pp. 592–597, 1961.

[76] W. A. Campbell Jr, R. S. Marriott, and J. J. Park, ‘A Compilation of Outgassing Data for Spacecraft Materials.’, DTIC Document, 1973.

[77] Z. Wang, F. Xu, C. Lu, H. Zhang, Q. Xu, and J. Zhu, ‘Electronic Conductivity Upturn of HOPG Contrast to Transport Properties of Polycrystal Graphite’, *ArXiv Prepr. ArXiv08013298*, 2008.

[78] G. Larkins and Y. Vlasov, ‘Indications of superconductivity in doped highly oriented pyrolytic graphite’, *Supercond. Sci. Technol.*, vol. 24, no. 9, p. 092001, 2011.

[79] G. Jose, T. T. Fernandez, P. Steenson, and A. Jha, ‘Femtosecond laser assisted multi-ion implantation in dielectrics’, in *Transparent Optical Networks (ICTON), 2012 14th International Conference on*, 2012, pp. 1–2.

[80] S. D. Russell and A. D. Ramirez, ‘In situ boron incorporation and activation in silicon carbide using excimer laser recrystallization’, *Appl. Phys. Lett.*, vol. 74, no. 22, pp. 3368–3370, 1999.

[81] S. Stathopoulos, L. Tsetseris, N. Pradhan, B. Colombeau, and D. Tsoukalas, ‘Millisecond non-melt laser annealing of phosphorus implanted germanium: Influence of nitrogen co-doping’, *J. Appl. Phys.*, vol. 118, no. 13, p. 135710, 2015.

[82] M. Takeuchi, S. Muto, T. Tanabe, S. Arai, and T. Kuroyanagi, ‘Damage process in electron-irradiated graphite studied by transmission electron microscopy. II. Analysis of extended energy-loss fine structure of highly oriented pyrolytic graphite’, *Philos. Mag. A*, vol. 76, no. 3, pp. 691–700, Sep. 1997.

[83] S. Yang, Z. Wang, H. Kokawa, and Y. S. Sato, ‘Reassessment of the effects of laser surface melting on IGC of SUS 304’, *Mater. Sci. Eng. A*, vol. 474, no. 1, pp. 112–119, 2008.

[84] A. Temmler, E. Willenborg, and K. Wissenbach, ‘Laser Polishing’, in *SPIE LASE*, 2012, vol. 8243, pp. 82430W-82430W–13.

[85] E. Willenborg and R. Ostholt, ‘Polishing metals with laser radiation’, *Ind. Laser Solut.*, vol. 24, no. 11, 2009.

[86] T. M. Shao, M. Hua, H. Y. Tam, and E. H. Cheung, ‘An approach to modelling of laser polishing of metals’, *Surf. Coat. Technol.*, vol. 197, no. 1, pp. 77–84, 2005.

[87] E. Ukar, A. Lamikiz, L. L. de Lacalle, D. del Pozo, and J. L. Arana, ‘Laser polishing of tool steel with CO 2 laser and high-power diode laser’, *Int. J. Mach. Tools Manuf.*, vol. 50, no. 1, pp. 115–125, 2010.

[88] N. Bidin and S. N. Ab Razak, *ArF excimer laser annealing of polycrystalline silicon thin film*. INTECH Open Access Publisher, 2012.

[89] X. Zhang and A. Atrens, ‘Rapid solidification characteristics in melt spinning’, *Mater. Sci. Eng. A*, vol. 159, no. 2, pp. 243–251, 1992.

[90] J. Armengol, F. Vega, N. Chaoui, J. Solis, and C. N. Afonso, ‘Recalescence after bulk solidification in germanium films melted by ns laser pulses’, *J. Appl. Phys.*, vol. 93, no. 3, pp. 1505–1510, 2003.

[91] L. Mariucci, A. Pecora, G. Fortunato, C. Spinella, and C. Bongiorno, ‘Crystallization mechanisms in laser irradiated thin amorphous silicon films’, *Thin Solid Films*, vol. 427, no. 1, pp. 91–95, 2003.

[92] W. Huang, M. Song, M. Tu, and others, ‘Effects of annealing temperature on the electrical conductivity and mechanical property of Cu-Te alloys’, *J. Wuhan Univ. Technol.-Mater Sci Ed*, vol. 22, no. 1, pp. 88–90, 2007.

[93] W. Huang, M. Song, M. Tu, and others, ‘Effects of annealing temperature on the electrical conductivity and mechanical property of Cu-Te alloys’, *J. Wuhan Univ. Technol.-Mater Sci Ed*, vol. 22, no. 1, pp. 88–90, 2007.

[94] P. G. Klemens, ‘Thermal Conductivity and Lattice Vibrational Modes’, in *Solid State Physics*, vol. 7, F. Seitz and D. Turnbull, Eds. Academic Press, 1958, pp. 1–98.

[95] C. F. Lynn, J. C. Dickens, and A. A. Neuber, ‘Focused cathode design to reduce anode heating during vircator operation’, *Phys. Plasmas*, vol. 20, no. 10, p. 103113, Oct. 2013.

[96] C. Möller, ‘Design and Experiments with High Power Microwave Sources : The Virtual Cathode Oscillator’, PhD Thesis, KTH, Space and Plasma Physics, 2012.

[97] R. J. Reid, ‘Cleaning for vacuum service’, Cern, 1999.

[98] B. E. Wilde, M. Manohar, and C. E. Albright, ‘The influence of laser surface melting on the resistance of AISI 4135 low alloy steel to hydrogen-induced brittle fracture’, *Mater. Sci. Eng. A*, vol. 198, no. 1, pp. 43–49, 1995.

[99] G. Abbas, Z. Liu, and P. Skeldon, ‘Corrosion behaviour of laser-melted magnesium alloys’, *Appl. Surf. Sci.*, vol. 247, no. 1, pp. 347–353, 2005.

[100] K. Pangovski, K. Li, and B. O’Neill, ‘Application of Picosecond Lasers for Surface Modification and Polishing’, *Photonics Lond. Lond. UK*, 2011.

[101] F. E. Pfefferkorn, N. A. Duffie, J. D. Morrow, and Q. Wang, ‘Effect of beam diameter on pulsed laser polishing of S7 tool steel’, *CIRP Ann.-Manuf. Technol.*, vol. 63, no. 1, pp. 237–240, 2014.

[102] F. E. Pfefferkorn, N. A. Duffie, X. Li, M. Vadali, and C. Ma, ‘Improving surface finish in pulsed laser micro polishing using thermocapillary flow’, *CIRP Ann.-Manuf. Technol.*, vol. 62, no. 1, pp. 203–206, 2013.

[103] T. Sarnet *et al.*, ‘Femtosecond laser for black silicon and photovoltaic cells’, in *Lasers and Applications in Science and Engineering*, 2008, pp. 688119–688119.

[104] J. Heitz, B. Reisinger, M. Fahrner, C. Romanin, J. Siegel, and V. Svorcik, ‘Laser-induced periodic surface structures (LIPSS) on polymer surfaces’, in *Transparent Optical Networks (ICTON), 2012 14th International Conference on*, 2012, pp. 1–4.

[105] J. E. Carey III, ‘Femtosecond-laser microstructuring of silicon for novel optoelectronic devices’, Harvard University Cambridge, Massachusetts, 2004.

[106] T. Y. Hwang and C. Guo, ‘Polarization and angular effects of femtosecond laser-induced conical microstructures on Ni’, *J. Appl. Phys.*, vol. 111, no. 8, p. 083518, 2012.

[107] H. Huang, L.-M. Yang, and J. Liu, ‘Micro-hole drilling with femtosecond fiber laser’, in *SPIE LASE*, 2013, pp. 86070K–86070K.

[108] I. Gnilitskyi, T. J.-Y. Derrien, Y. Levy, N. M. Bulgakova, T. Mocek, and L. Orazi, ‘High-speed manufacturing of highly regular femtosecond laser-induced periodic surface structures: physical origin of regularity’, *Sci. Rep.*, vol. 7, no. 1, Dec. 2017.

[109] D. A. Shiffler *et al.*, ‘Effects of anode materials on the performance of explosive field emission diodes’, *Plasma Sci. IEEE Trans. On*, vol. 30, no. 3, pp. 1232–1237, 2002.

[110] Z. Guosheng, P. M. Fauchet, and A. E. Siegman, ‘Growth of spontaneous periodic surface structures on solids during laser illumination’, *Phys. Rev. B*, vol. 26, no. 10, p. 5366, 1982.

[111] T.-Y. Derrien, R. Torres, T. Sarnet, M. Sentis, and T. E. Itina, ‘Formation of femtosecond laser induced surface structures on silicon: Insights from numerical modeling and single pulse experiments’, *Appl. Surf. Sci.*, vol. 258, no. 23, pp. 9487–9490, 2012.

[112] J. E. Sipe, J. F. Young, J. S. Preston, and H. M. Van Driel, ‘Laser-induced periodic surface structure. I. Theory’, *Phys. Rev. B*, vol. 27, no. 2, p. 1141, 1983.

[113] K. Sokolowski-Tinten *et al.,* 'Transient states of matter during short pulse laser ablation', *Phys. Rev. Lett.*, vol. 81, no. 1, p. 224, 1998.

[114] A. Ben-Yakar, A. Harkin, J. Ashmore, R. L. Byer, and H. A. Stone, 'Thermal and fluid processes of a thin melt zone during femtosecond laser ablation of glass: the formation of rims by single laser pulses', *J. Phys. Appl. Phys.*, vol. 40, no. 5, p. 1447, 2007.

[115] M. Ye *et al.*, 'Suppression of secondary electron yield by micro-porous array structure', *J. Appl. Phys.*, vol. 113, no. 7, p. 074904, 2013.

[116] J. M. Sattler, R. A. Coutu Jr, R. Lake, T. Laurvick, T. Back, and S. Fairchild, 'Modeling micro-porous surfaces for secondary electron emission control to suppress multipactor', *J. Appl. Phys.*, vol. 122, no. 5, p. 055304, 2017.

[117] M. Kraus, M. A. Ahmed, A. Michalowski, A. Voss, R. Weber, and T. Graf, 'Microdrilling in steel using ultrashort pulsed laser beams with radial and azimuthal polarization', *Opt. Express*, vol. 18, no. 21, pp. 22305–22313, 2010.

[118] R. Weber *et al.*, 'Effects of radial and tangential polarization in laser material processing', *Phys. Procedia*, vol. 12, pp. 21–30, 2011.

[119] C. Föhl and F. Dausinger, 'High precision deep drilling with ultrashort pulses', in *Fourth International Symposium on laser Precision Microfabrication*, 2003, pp. 346–351.

[120] J. J. Chang, B. E. Warner, E. P. Dragon, and M. W. Martinez, 'Precision micromachining with pulsed green lasers', *J. Laser Appl.*, vol. 10, no. 6, pp. 285–291, 1998.

[121] F. Dausinger, 'Precise drilling with short-pulsed lasers', in *Proc. SPIE*, 2000, vol. 3888, pp. 180–187.

[122] M. Advent, 'Advent Research Materials Nickel Sheet', 2016.

[123] W. Hanlein and K. G. Gunther, 'Advances in vacuum science and technology', *Lond. Per*, 1960.

[124] I. Guide, 'User Manual for G3. 0 Pulsed Fibre Laser, 2007–2008', *SPI Photonics*.

[125] M. W. Phaneuf, 'Applications of focused ion beam microscopy to materials science specimens', *Micron*, vol. 30, no. 3, pp. 277–288, 1999.

[126] F. J. Humphreys, 'Review grain and subgrain characterisation by electron backscatter diffraction', *J. Mater. Sci.*, vol. 36, no. 16, pp. 3833–3854, 2001.

[127] H. Grimmer, W. t Bollmann, and D. H. Warrington, 'Coincidence-site lattices and complete pattern-shift in cubic crystals', *Acta Crystallogr. A*, vol. 30, no. 2, pp. 197–207, 1974.

[128] A. H. King and S. Shekhar, 'What does it mean to be special? The significance and application of the Brandon criterion', *J. Mater. Sci.*, vol. 41, no. 23, pp. 7675–7682, 2006.

[129] D. H. Warrington and M. Boon, 'Ordered structures in random grain boundaries; some geometrical probabilities', *Acta Metall.*, vol. 23, no. 5, pp. 599–607, 1975.

[130] G. Palumbo, K. T. Aust, E. M. Lehockey, U. Erb, and P. Lin, 'On a more restrictive geometric criterion for "special" CSL grain boundaries', *Scr. Mater.*, vol. 38, no. 11, pp. 1685–1690, 1998.

[131] D. Gerth and R. A. Schwarzer, ‘Graphical Representation of Grain and Hillock Orientations in Annealed Al–1%Si Films’, *Textures Microstruct.*, vol. 21, no. 2–3, pp. 177–193, 1993.

[132] C. A. Schuh, M. Kumar, and W. E. King, ‘Analysis of grain boundary networks and their evolution during grain boundary engineering’, *Acta Mater.*, vol. 51, no. 3, pp. 687–700, 2003.

[133] J. Friel, S. Wright, and S. Sitzman, ‘ASTM Grain Size by EBSD-A New Standard’, *Microsc. Microanal.*, vol. 17, no. S2, pp. 838–839, 2011.

[134] R. A. Schwarzer, ‘Automated crystal lattice orientation mapping using a computer-controlled SEM’, *Micron*, vol. 28, no. 3, pp. 249–265, Jun. 1997.

[135] S. Nishikawa and S. Kikuchi, ‘The diffraction of cathode rays by calcite’, *Proc. Imp. Acad.*, vol. 4, no. 8, pp. 475–477, 1928.

[136] K. Geels, D. B. Fowler, W.-U. Kopp, and M. Rückert, *Metallographic and materialographic specimen preparation, light microscopy, image analysis, and hardness testing*. ASTM International West Conshohocken, PA, 2007.

[137] G. F. Vander Voort, *Metallography, principles and practice*. ASM International, 1984.

[138] R. Patel, J. Bovatsek, and H. Chui, ‘Nano to pico to femto: Pulse widths for optimal laser micromachining outcomes’, *Ind. Laser Solut.*, vol. 32, no. 3, pp. 21–24, May 2017.

[139] D. Ashkenasi, T. Kaszemeikat, N. Mueller, R. Dietrich, H. J. Eichler, and G. Illing, ‘Laser trepanning for industrial applications’, *Phys. Procedia*, vol. 12, pp. 323–331, 2011.

[140] B. Klimt, ‘Micromachining with industrial picosecond lasers’, *Laser Tech. J.*, vol. 4, no. 1, pp. 40–43, 2007.

[141] H. Huang, L.-M. Yang, and J. Liu, ‘Micro-hole drilling and cutting using femtosecond fiber laser’, *Opt. Eng.*, vol. 53, no. 5, p. 051513, Feb. 2014.

[142] E. J. Sternglass, ‘Theory of secondary electron emission by high-speed ions’, *Phys. Rev.*, vol. 108, no. 1, p. 1, 1957.

[143] W. M. Steen and J. Mazumder, *Laser Material Processing*. London: Springer London, 2010.

[144] A. Pauli, ‘Faster and Smoother Thanks to Laser Polishing: Ultra-short pulse lasers allow for improved surface finishing capabilities’, *Laser Tech. J.*, vol. 11, no. 5, pp. 46–48, Nov. 2014.

[145] T. A. Mai and G. C. Lim, ‘Micromelting and its effects on surface topography and properties in laser polishing of stainless steel’, *J. Laser Appl.*, vol. 16, no. 4, pp. 221–228, Nov. 2004.

[146] D. Gortat *et al.*, ‘Laser surface melting of stainless steel anodes for reduced hydrogen outgassing’, *Mater. Lett.*, vol. 190, pp. 5–8, Mar. 2017.

[147] A. Temmler, E. Willenborg, and K. Wissenbach, ‘Design surfaces by laser remelting’, *Phys. Procedia*, vol. 12, pp. 419–430, 2011.

[148] J. K. Gorman and W. R. Nardella, ‘Hydrogen permeation through metals’, *Vacuum*, vol. 12, no. 1, pp. 19–24, 1962.

[149] R. W. Powell, R. P. Tye, and M. J. Hickman, ‘The thermal conductivity of nickel’, *Int. J. Heat Mass Transf.*, vol. 8, no. 5, pp. 679–688, May 1965.

[150] W. F. Gale and T. C. Totemeier, *Smithells metals reference book*. Butterworth-Heinemann, 2003.

[151] H. de Amorim Almeida *et al.*, ‘Innovative developments in virtual and physical prototyping’, 2012.

[152] S. Kou, C. Limmaneevichitr, and P. S. Wei, ‘Oscillatory Marangoni flow: a fundamental study by conduction-mode laser spot welding’, *Weld J*, vol. 90, no. 12, pp. 229–240, 2011.

[153] C. L. Giles and W. J. Wild, ‘Fresnel reflection and transmission at a planar boundary from media of equal refractive indices’, *Appl. Phys. Lett.*, vol. 40, no. 3, pp. 210–212, 1982.

[154] H. D. Young, *University physics*, 7th ed. Addison-Wesley Pub. Co., 1992.

[155] C. A. Howsare, X. Weng, V. Bojan, D. Snyder, and J. A. Robinson, ‘Substrate considerations for graphene synthesis on thin copper films’, *Nanotechnology*, vol. 23, no. 13, p. 135601, 2012.

[156] S. Thiele *et al.*, ‘Engineering polycrystalline Ni films to improve thickness uniformity of the chemical-vapor-deposition-grown graphene films’, *Nanotechnology*, vol. 21, no. 1, p. 015601, 2009.

[157] K. M. Al-Shurman and H. Naseem, ‘CVD Graphene Growth Mechanism on Nickel Thin Films’, in *Excerpt from the Proc. 2014 COMSOL Conf.*, 2014.

[158] N. F. Mott, ‘The resistance of liquid metals’, *Proc. R. Soc. Lond. Ser. Contain. Pap. Math. Phys. Character*, vol. 146, no. 857, pp. 465–472, 1934.

[159] G. Reiss, J. Vancea, and H. Hoffmann, ‘Grain-boundary resistance in polycrystalline metals’, *Phys. Rev. Lett.*, vol. 56, no. 19, p. 2100, 1986.

[160] V. Rudnev, D. Loveless, R. L. Cook, and M. Black, *Handbook of induction heating*. CRC Press, 2002.

[161] J. R. Davis and others, *Copper and copper alloys*. ASM international, 2001.

[162] R. Valizadeh, O. B. Malyshev, S. Wang, S. A. Zolotovskaya, W. Allan Gillespie, and A. Abdolvand, ‘Low secondary electron yield engineered surface for electron cloud mitigation’, *Appl. Phys. Lett.*, vol. 105, no. 23, p. 231605, 2014.

[163] L. Torrisi, ‘Radiation effects induced by pulsed laser ablation in tantalum surfaces’, *Appl. Surf. Sci.*, vol. 195, no. 1, pp. 8–15, Jul. 2002.

[164] O. Benavides, O. Lebedeva, and V. Golikov, ‘Reflection of nanosecond Nd: YAG laser pulses in ablation of metals’, *Opt. Express*, vol. 19, no. 22, pp. 21842–21848, 2011.

[165] P. C. Pinto *et al.*, ‘Carbon coatings with low secondary electron yield’, *Vacuum*, vol. 98, pp. 29–36, 2013.

[166] J. Wang *et al.*, ‘Research on Low Secondary Electron Yield Materials for Future Accelerators’, in *7th International Particle Accelerator Conference (IPAC’16), Busan, Korea, May 8-13, 2016*, 2016, pp. 3284–3286.

[167] C. Y. Vallgren and others, *Low secondary electron yield carbon coatings for electron cloud mitigation in modern particle accelerators*. Chalmers University of Technology Göteborg, 2011.

[168] J. Bonse, S. Höhm, S. V. Kirner, A. Rosenfeld, and J. Krüger, 'Laser-Induced Periodic Surface Structures— A Scientific Evergreen', *IEEE J. Sel. Top. Quantum Electron.*, vol. 23, no. 3, May 2017.

Appendix A

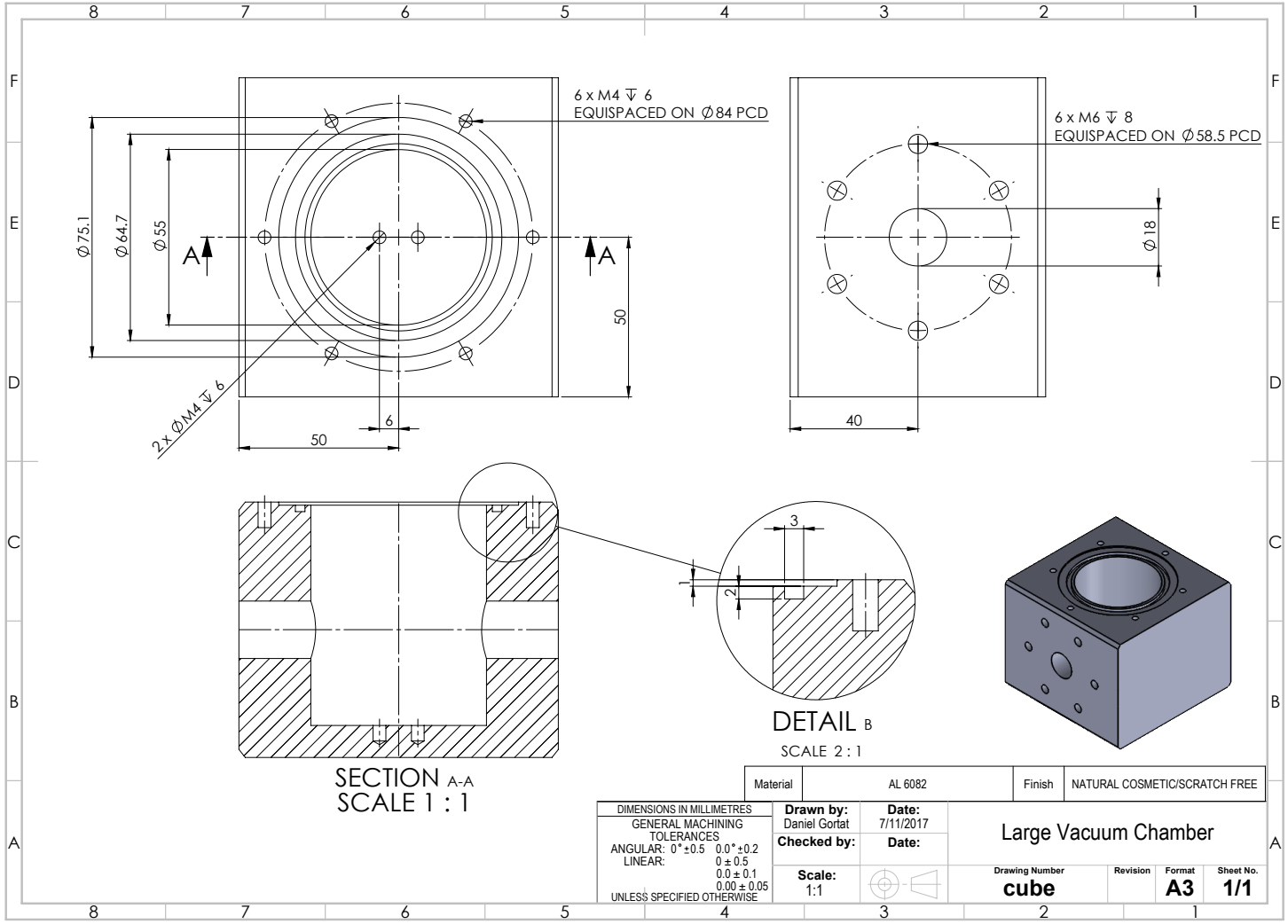

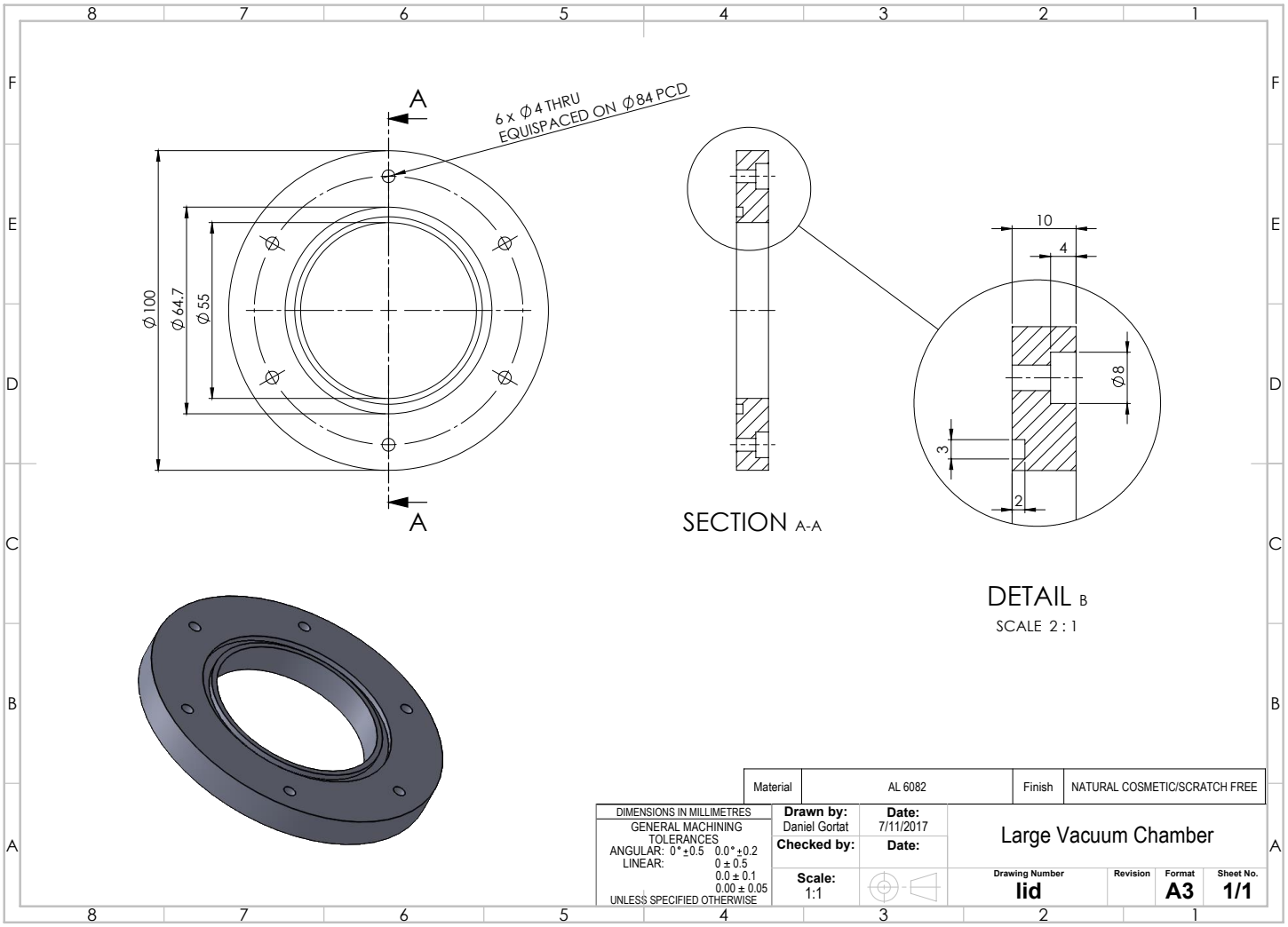

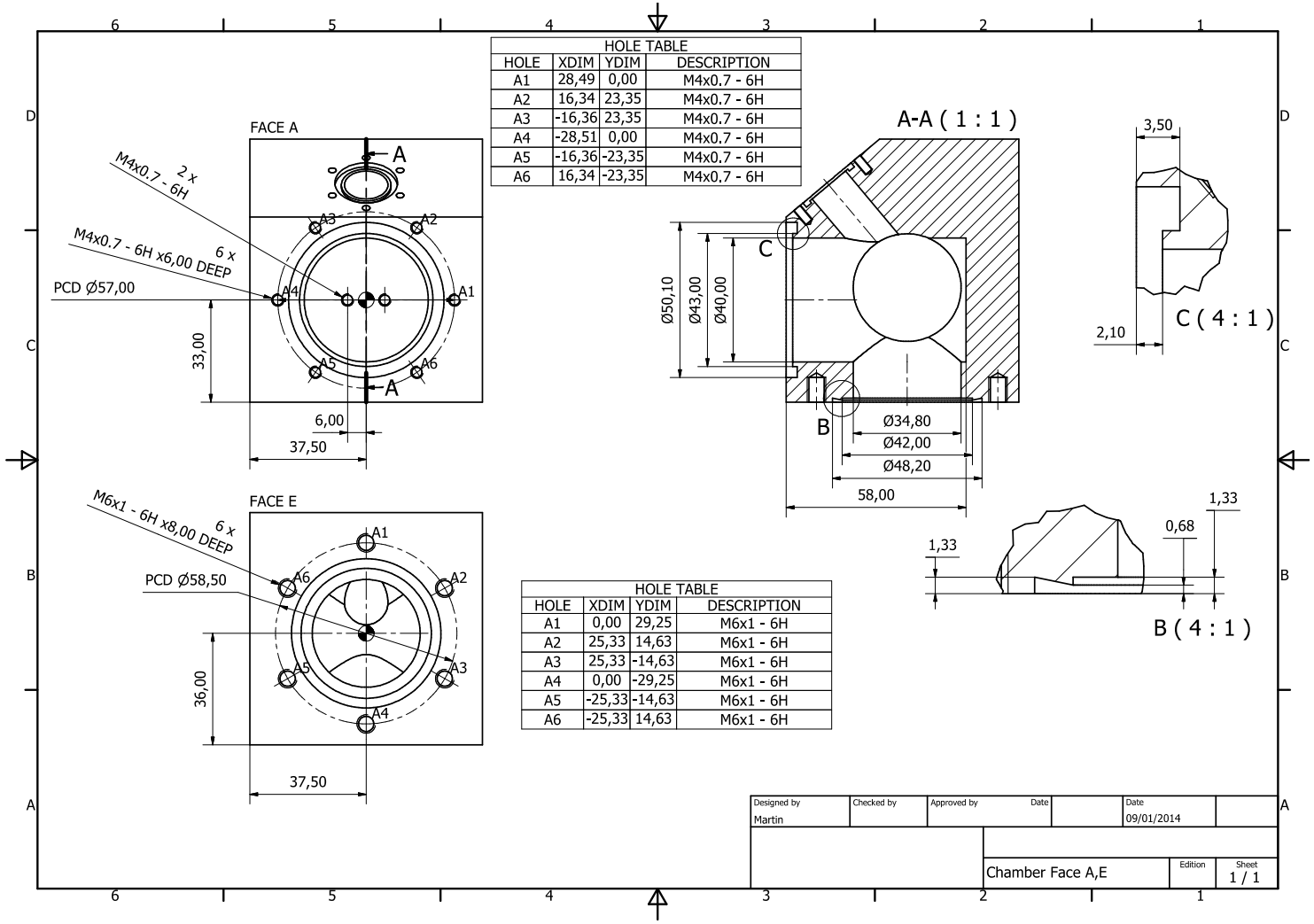

Stainless steel vacuum chamber.

Appendix B

```
DVAR $XDistance          //  X processed distance
DVAR $YDistance          //  Y processed distance
DVAR $Samples            //  Total number of samples away from the start point
DVAR $Samples2
DVAR $Counter
DVAR $Counter2
G91                              //  Incremental
G71                              //  Metric
G109                     //  Turn off look ahead

//  PARAMETERS
$XDistance          = 0.015 //Length of the track
$YDistance          = 0.015 //Separation of the tracks
$Samples            = 10     //  Must be greater than 2 and EVEN

$Counter      = 1
$Samples2           = 5      //  Must be greater than 2 and EVEN
$Counter2     = 1

//START
FOR $Counter2 = 1 to $Samples2
  FOR $Counter = 1 to $Samples

  DWELL 5

  G01 X-$XDistance F5

  NEXT $Counter

  G01 Y-$YDistance F10

  FOR $Counter = 1 to $Samples

  DWELL 5

  G01 X$XDistance F5

  NEXT $Counter

  G01 Y-$YDistance F10

 NEXT $Counter2

    G90
    G91
M02
```

Appendix C

TREPPANING LASER DRILLING

```
DVAR $XDistance                 //  X processed distance
DVAR $XDistance2
DVAR $YDistance2
DVAR $YDistance//  Y processed distance
DVAR $YDistanceA//  Y processed distance
DVAR $Samples                   //  Total number of samples away from the start point
DVAR $ProcessSpeed
DVAR $Samples2
DVAR $Counter
DVAR $Counter2
DVAR $Counter3
DVAR $Samples3
DVAR $Counter4
DVAR $Samples4
DVAR $Radius
DVAR $RadiusA

DVAR $OffsetX          // offset from Dino to machining point
DVAR $OffsetY   //
DVAR $OffsetZ
DVAR $InterchangeSpeed // speed to and back from camera to machining point
DVAR $safetyZ // height to retreat Z axis as safety
DVAR $InterchangeSpeedZ // speed to move Z turret
//DVAR $flag
G91                                     //  Incremental
G71                                     //  Metric
G108                            //

//DINO
$OffsetX                = -9.5   // mm
$OffsetY                = -87.1  //mm
$OffsetZ                = -6.21 //mm
$safetyZ                = 6 //mm

$InterchangeSpeed = 8  //mm/s
$InterchangeSpeedZ = 8          //mm/s


$Radius                 = 0.005
$RadiusA        = 0.0025
$ProcessSpeed           = 0.4    //  mm/s
$YDistance              = $Radius/2
$YDistanceA             = 0.091
$XDistance2             = 0.0788 //R
$YDistance2             = 0.0455 //A/2
$Samples                = 40     //  number of trepanning circles

$Counter        = 1
$Counter4       = 1
$Samples4               = 44 //row
$Samples2               = 24     // column
```

```
$Counter2       = 1

$Counter3       = 1

//start//loop

$DO2.X =1//
G01 Z+ (-$safetyZ) F$InterchangeSpeedZ
G01 X+ $OffsetX F$InterchangeSpeed
G01 Y+ $OffsetY F$InterchangeSpeed
G01 Z+ ($OffsetZ+$safetyZ) F$InterchangeSpeedZ
DWELL 3

PSOCONTROL X RESET
PSOPULSE X TIME 2000010, 2000000 CYCLES 1
PSOOUTPUT X PULSE

//loop
FOR $Counter2 = 1 to $Samples2

  FOR $Counter4 = 1 to $Samples4

 PSOCONTROL X FIRE

 G02 Y$RadiusA*2 R$RadiusA F$ProcessSpeed

  FOR $Counter = 1 to $Samples

G02 Y-$Radius*2 R$Radius F$ProcessSpeed
G02 Y$Radius*2 R$Radius F$ProcessSpeed

NEXT $Counter

G02 Y-$RadiusA*2 R$RadiusA F$ProcessSpeed

    G01 Y$YDistanceA F0.5

  NEXT $Counter4

    G01 X$XDistance2 F0.5
  G01 Y-$YDistance2 F0.5

  FOR $Counter4 = 1 to $Samples4

 PSOCONTROL X FIRE

 G02 Y$RadiusA*2 R$RadiusA F$ProcessSpeed
  FOR $Counter = 1 to $Samples

G02 Y-$Radius*2 R$Radius F$ProcessSpeed
G02 Y$Radius*2 R$Radius F$ProcessSpeed


NEXT $Counter
```

```
G02 Y-$RadiusA*2 R$RadiusA F$ProcessSpeed


 G01 Y-$YDistanceA F0.5

  NEXT $Counter4


G01 X$XDistance2 F0.5
G01 Y$YDistance2 F0.5

 NEXT $Counter2

  DWELL 2

G01 Z+ (-$safetyZ) F$InterchangeSpeedZ
G01 X+ (-$OffsetX) F$InterchangeSpeed
G01 Y+ (-$OffsetY) F$InterchangeSpeed
G01 Z+ (+$safetyZ-$OffsetZ) F$InterchangeSpeedZ
 $DO2.X =0//
M02



LIPSS LASER PATTERNING

DVAR $XDistance              //  X processed distance
DVAR $YDistance              //  Y processed distance
DVAR $Samples                //  Total number of samples away from the start point
DVAR $ProcessSpeed[10]       //  Processing movement speed
DVAR $SquareProcessSpeed //square speed
DVAR $Counter
DVAR $Counter_2
DVAR $Counter_3              //
DVAR $flag
G91                                  //  Incremental
G71                                  //  Metric
G109                         //  Turn off look ahead

//  EDIT HERE
$XDistance              = 12     //Length of the track
$YDistance              = 0.005 //Separation of the tracks
$Samples                = 1300  //  Must be greater than 2 and EVEN

$Counter       = 1

$SquareProcessSpeed = 3
$flag=0

//start//
  FOR $Counter = 1 to $Samples

  ;Shutter_open//
```

```
  $DO2.X =1 //
        //X$XDistance F$ProcessSpeed[$flag]
  G01 X$XDistance F$SquareProcessSpeed

  $DO2.X =0//Laser off
  G01 Y-$YDistance F10
  $DO2.X =1
  G01 X-$XDistance F$SquareProcessSpeed
  $DO2.X =0
  G01 Y-$YDistance F10
  $flag=$flag+1

  NEXT $Counter

     G90
     G91

M02
```

Appendix D

Table 44. LSM parameters for SPI™ G3 laser.

304 stainless steel/Nickel					
Line no	Power (W)	Speed (mm /min)	Beam diameter (mm)	Energy Density (J/cm^2)	Speed (mm/s)
23	17	120	0.0394	21573.6	2
22	17	180	0.0394	14382.4	3
21	17	240	0.0394	10786.8	4
20	17	300	0.0394	8629.442	5
19	17	420	0.0394	6163.887	7
18	17	480	0.0394	5393.401	8
17	17	600	0.0394	4314.721	10
16	17	720	0.0394	3595.601	12
15	17	900	0.0394	2876.481	15
14	17	1200	0.0394	2157.36	20
13	17	1500	0.0394	1725.888	25
12	17	1800	0.0394	1438.24	30
11	17	2100	0.0394	1232.777	35
10	17	2400	0.0394	1078.68	40
9	17	2700	0.0394	958.8268	45
8	17	3000	0.0394	862.9442	50
7	17	3300	0.0394	784.4947	55
6	17	6000	0.0394	431.4721	100
5	17	12000	0.0394	215.736	200
4	17	18000	0.0394	143.824	300
3	17	24000	0.0394	107.868	400
2	12	6000	0.0394	304.5685	100
1	17	60000	0.0394	43.14721	1000

Table 45. Complete laser parameters for AMCS sample generation in section 4.1.2. Laser power is constant at 17 W.

Sample	ED (kJ/cm^2)	Scanning velocity (mm/s)	Line spacing (mm)
1	13.54	2.25	0.03
2	7.55	4.035	0.03
3	5.80	5.25	0.02
4	3.60	12	0.05
5	3.02[a]	10	0.02
6	2.03	15	0.02
7	0.40	76	0.027
8	0.30	100	0.02
9	3.60[b]	12	0.05

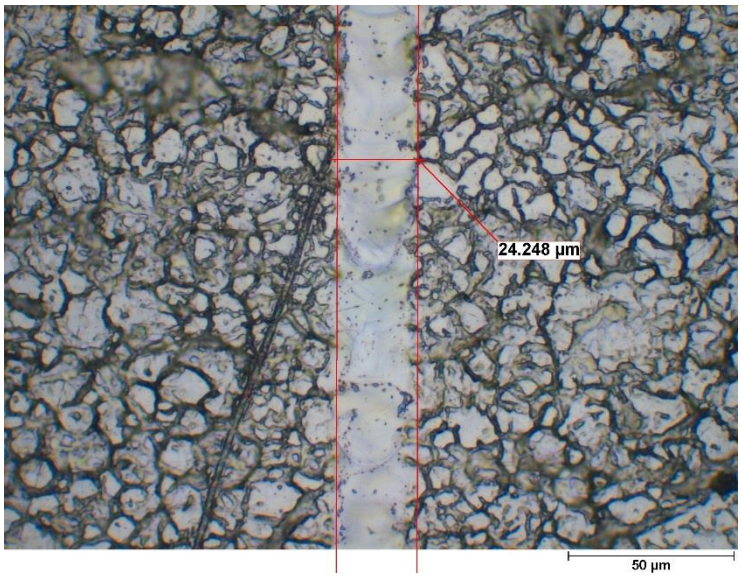

Line 1

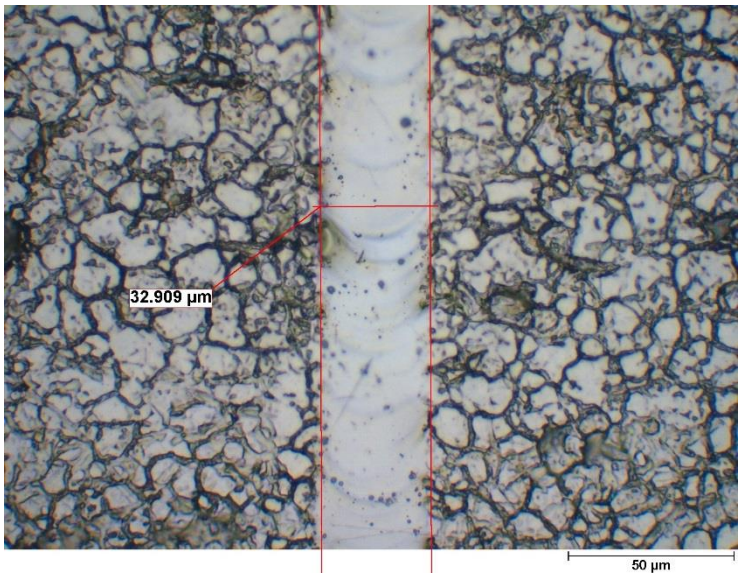

Line 2

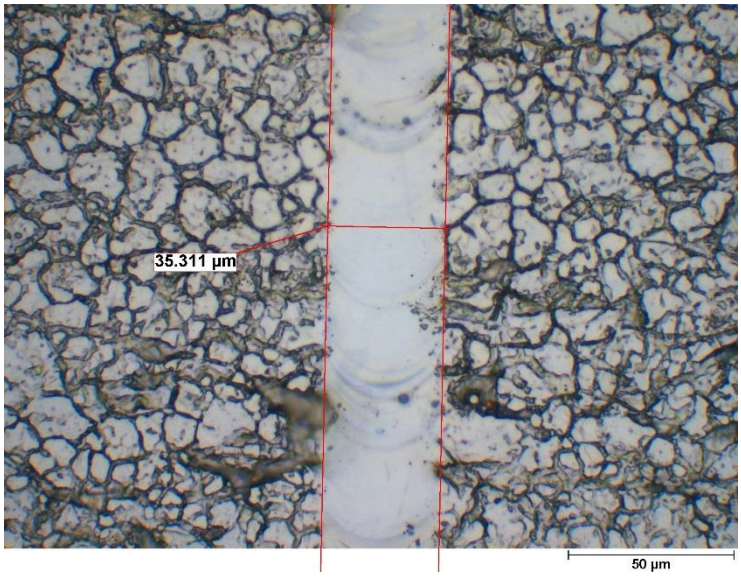

Line 3

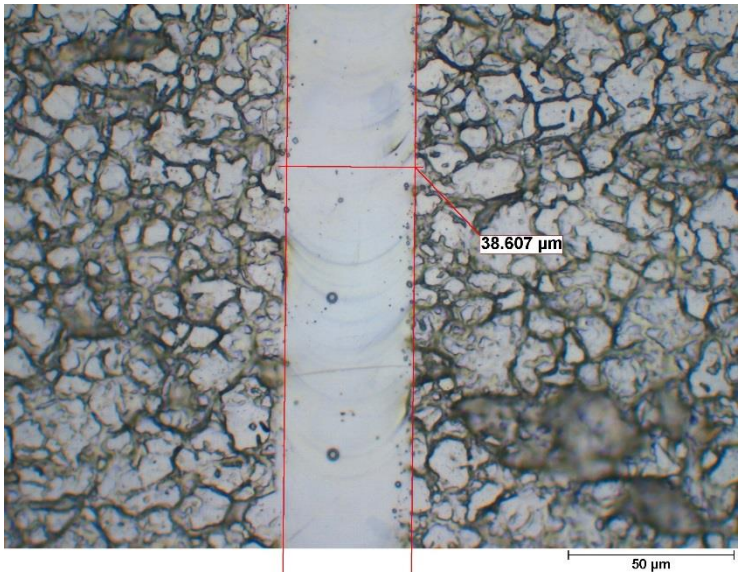

Line 4

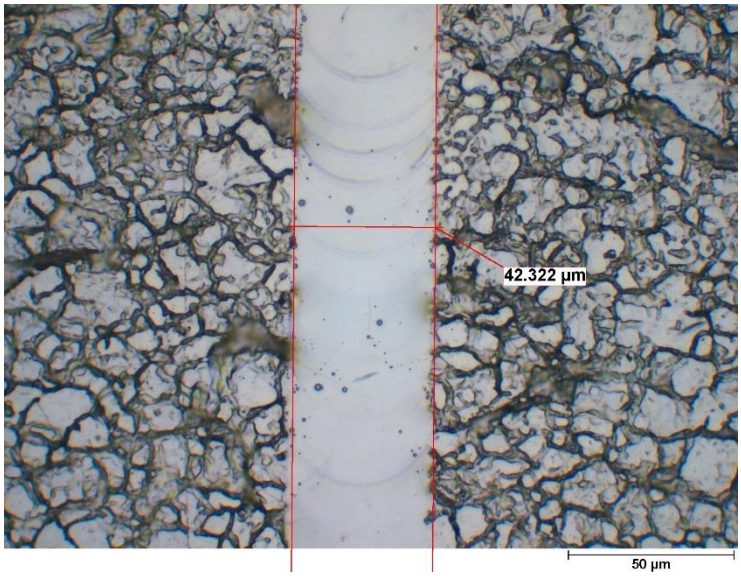

Line 5

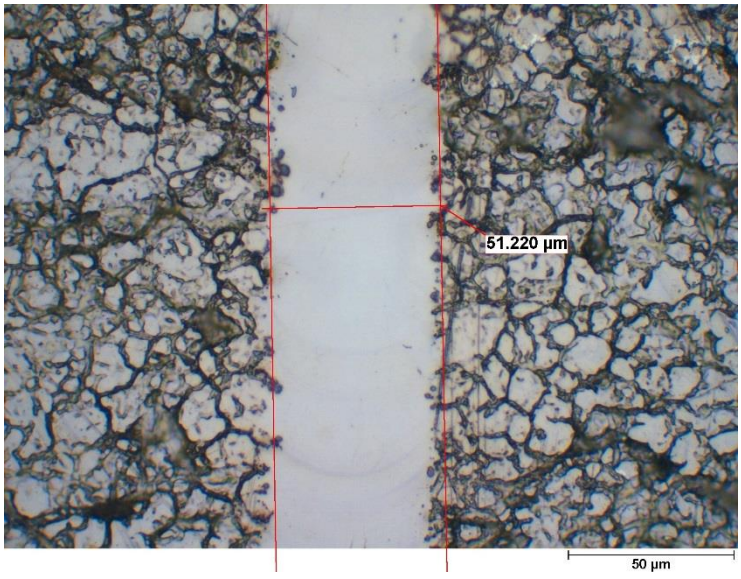

Line 6

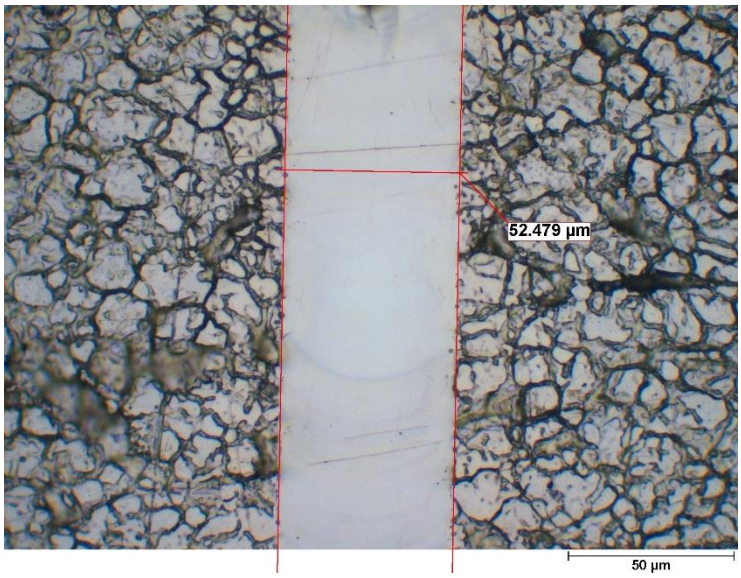

Line 7

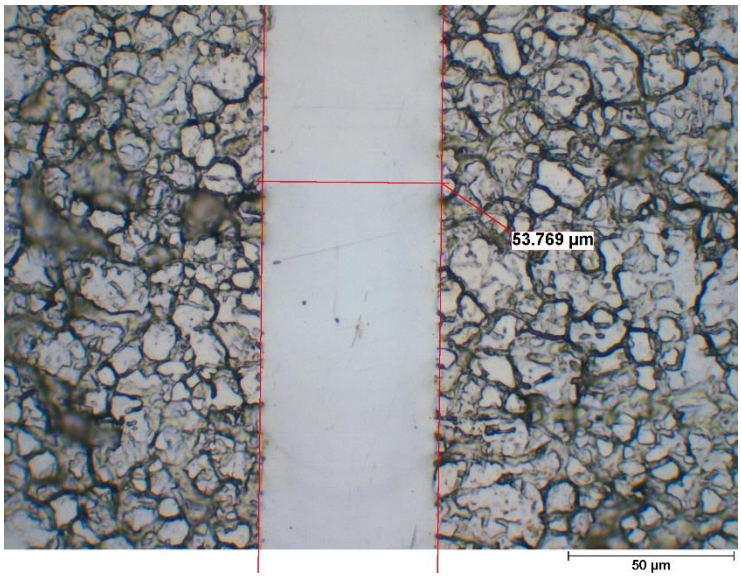

Line 8

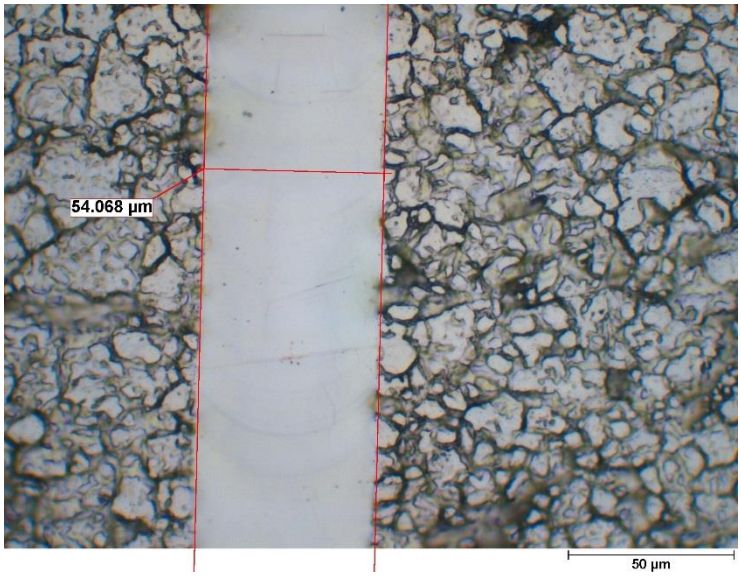

Line 9

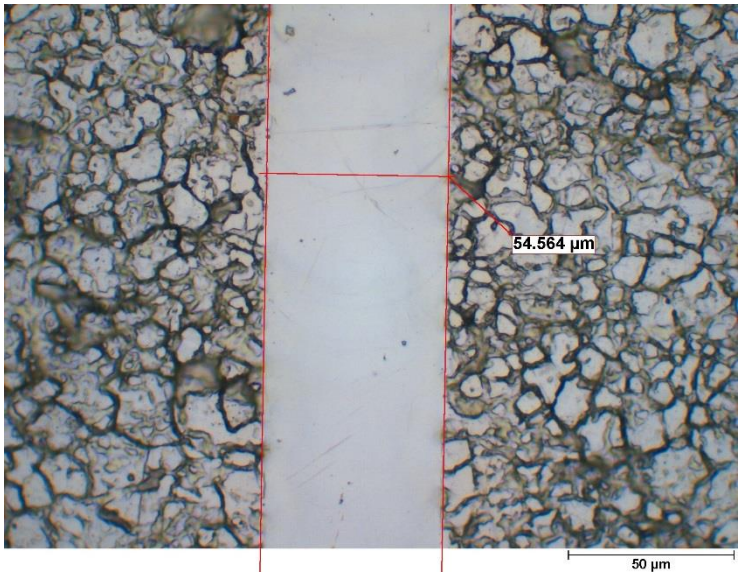

Line 10

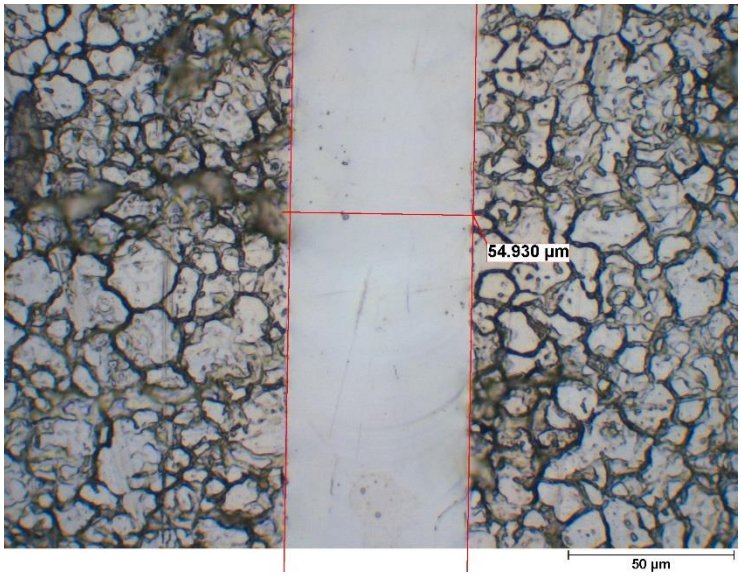

Line 11

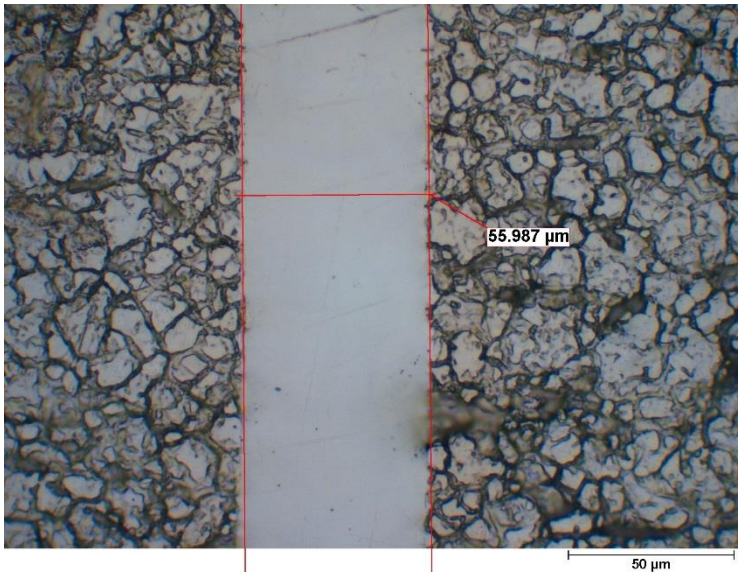

Line 12

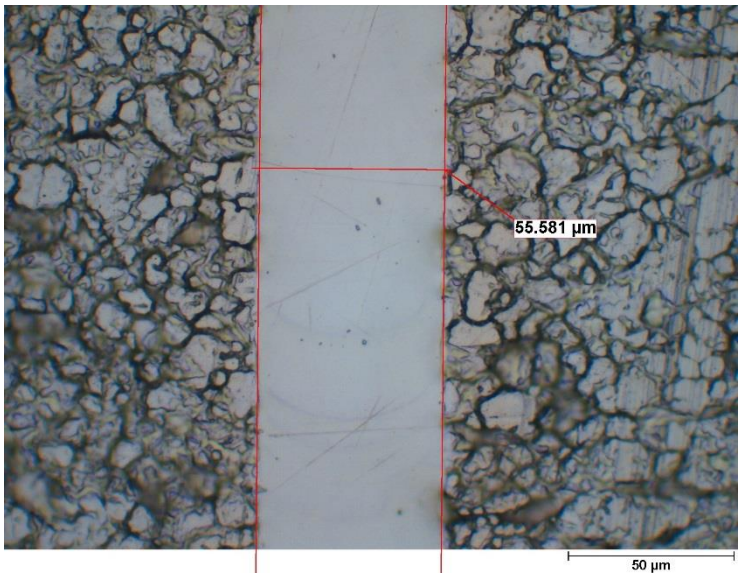

Line 13

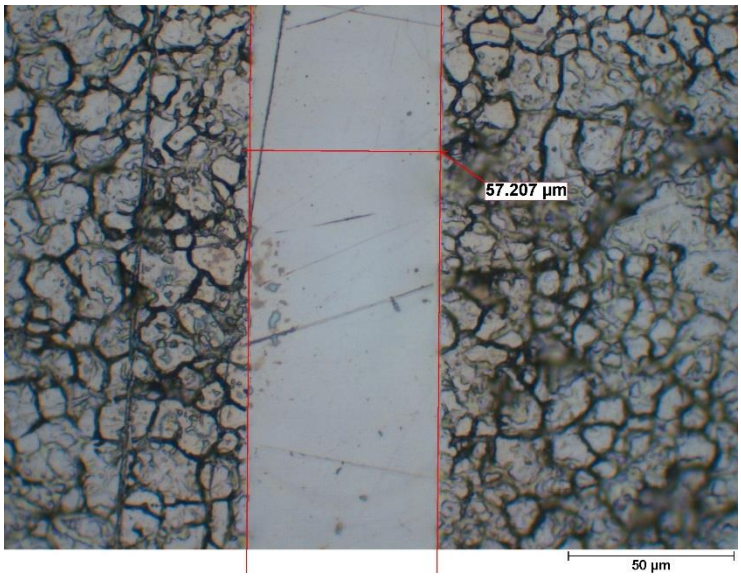

Line 14

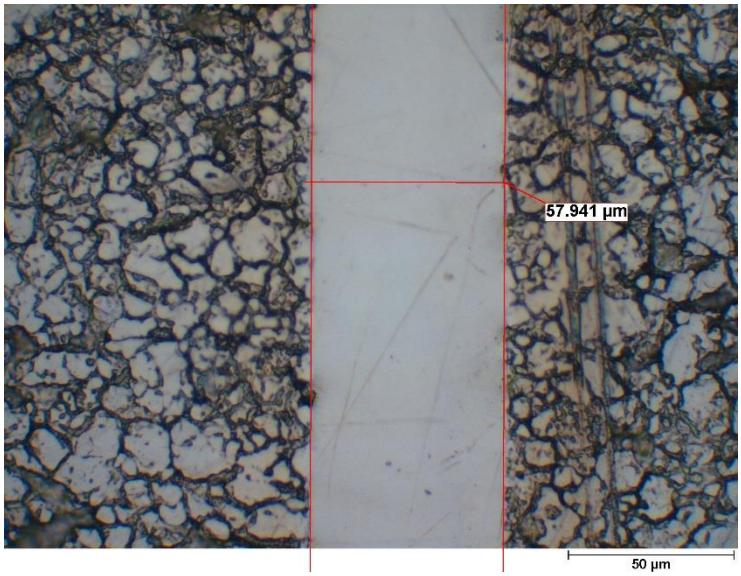

Line 15

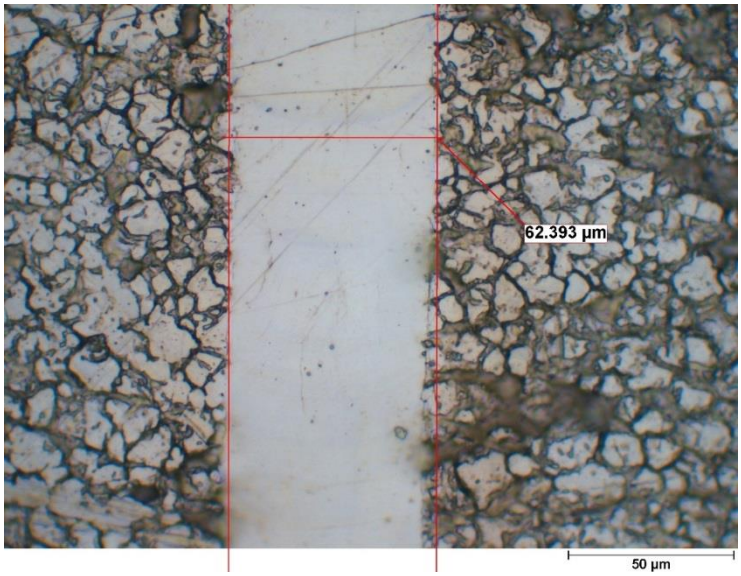

Line 16

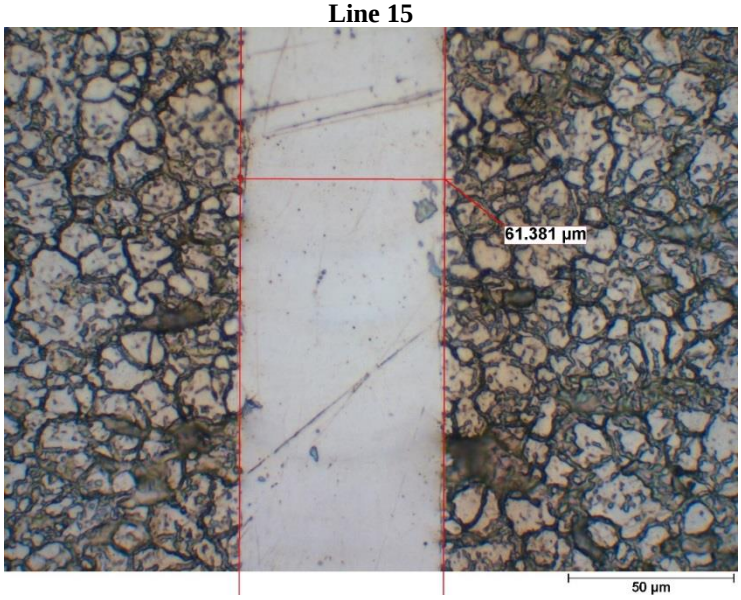

Line 17

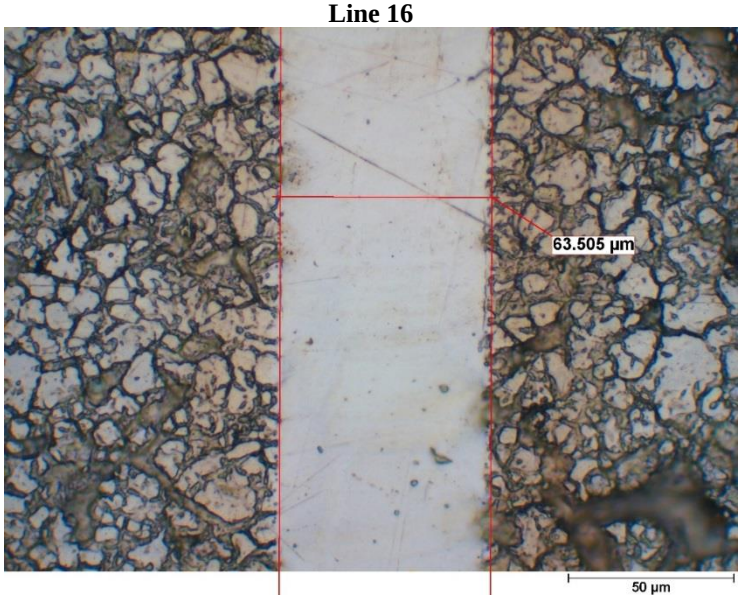

Line 18

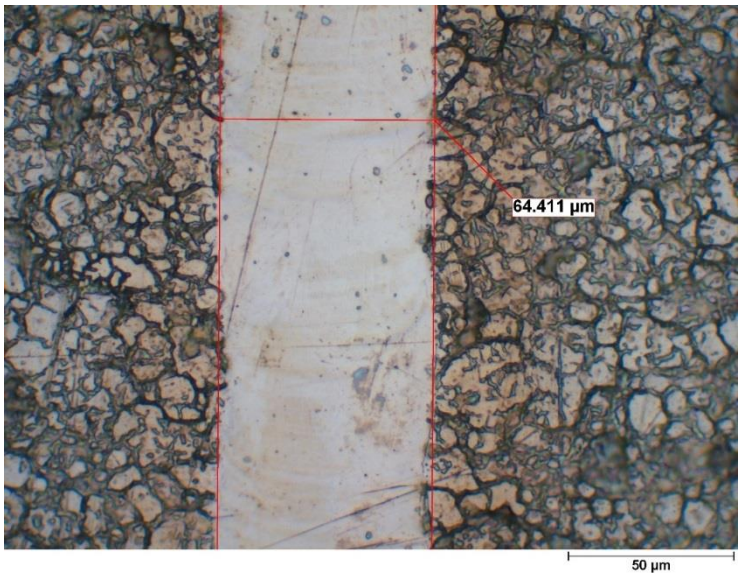

Line 19

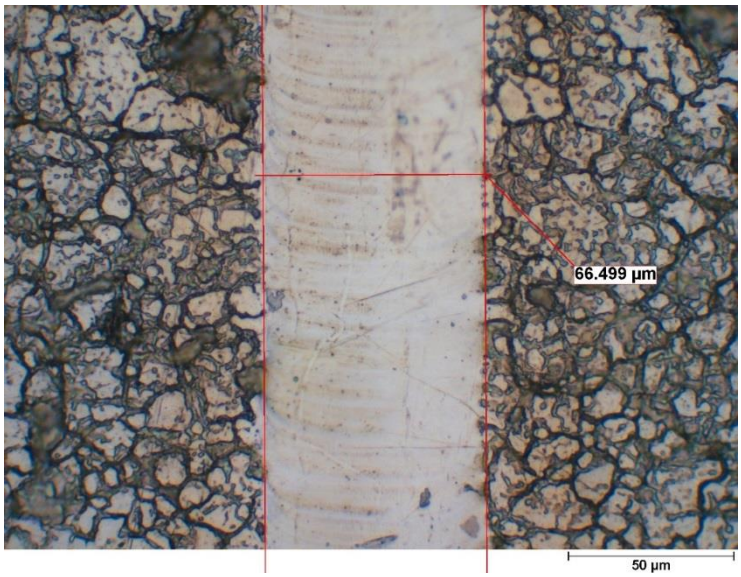

Line 20

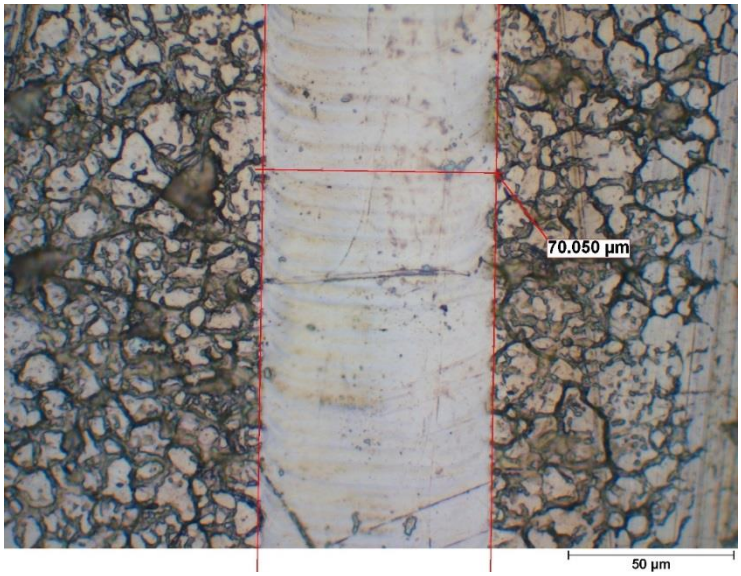

Line 21

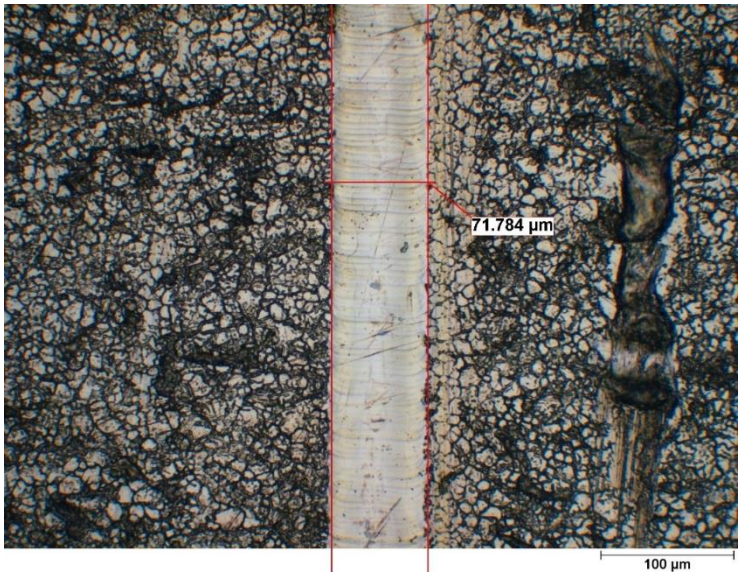

Line 22

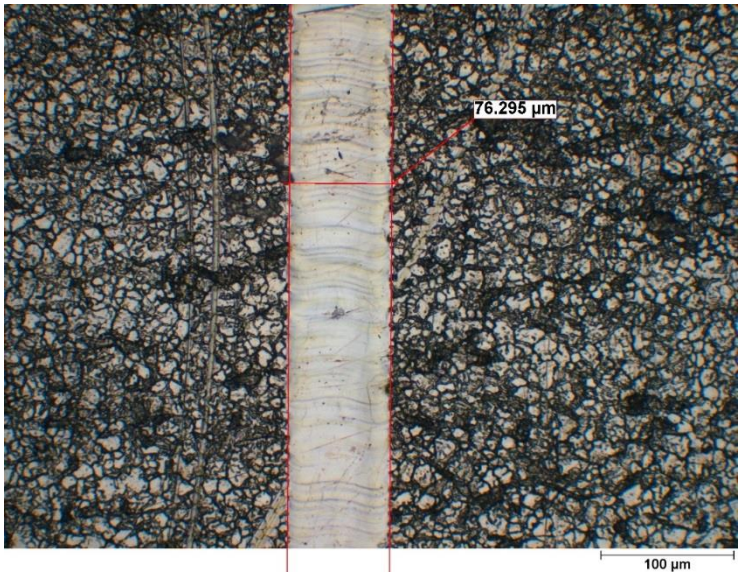

Line 23

Figure 138. Stainless steel, Olympus BX51 images. 23 Lines. Width measurements.

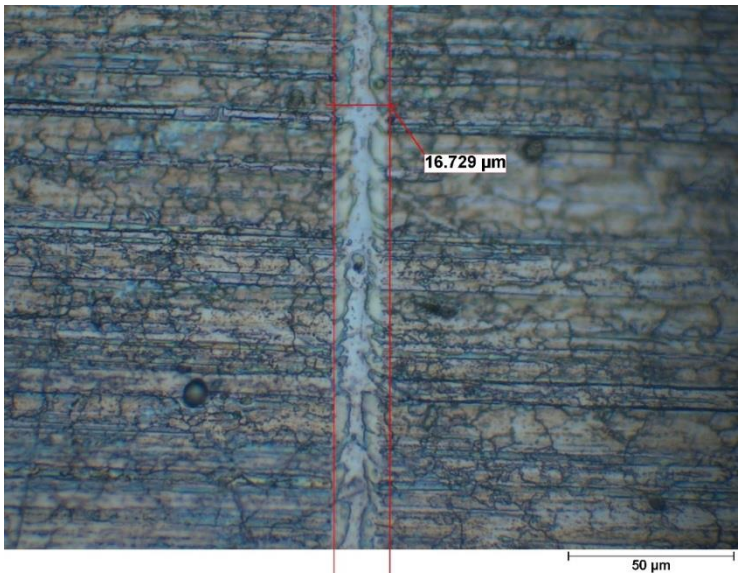

Line 2

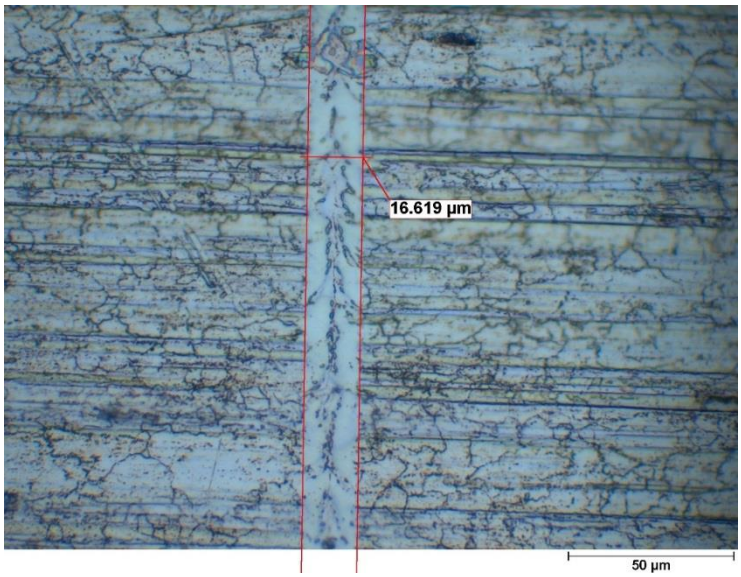

Line 3

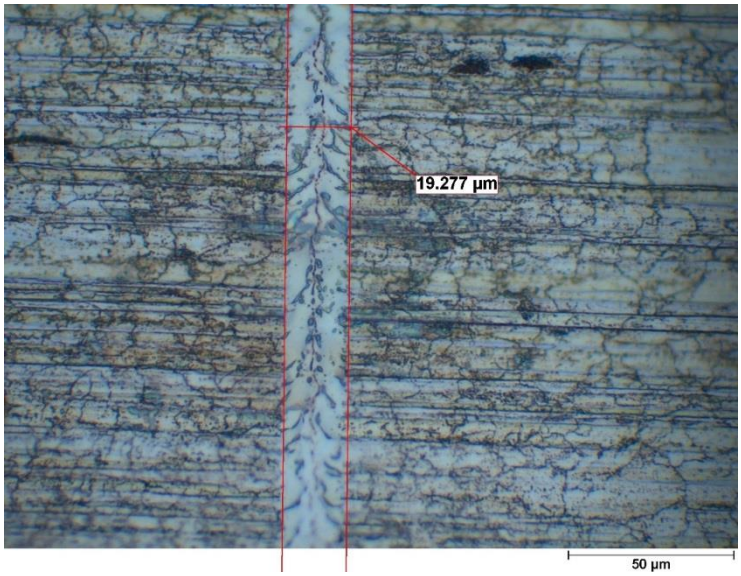

Line 4

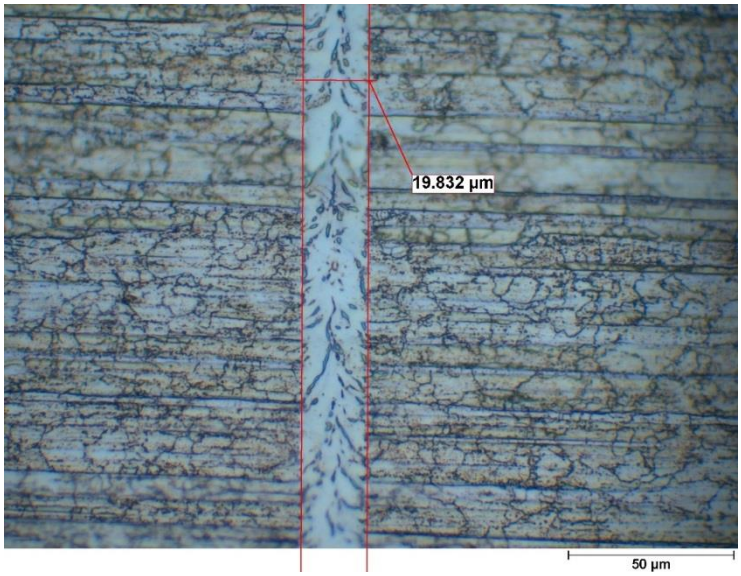

Line 5

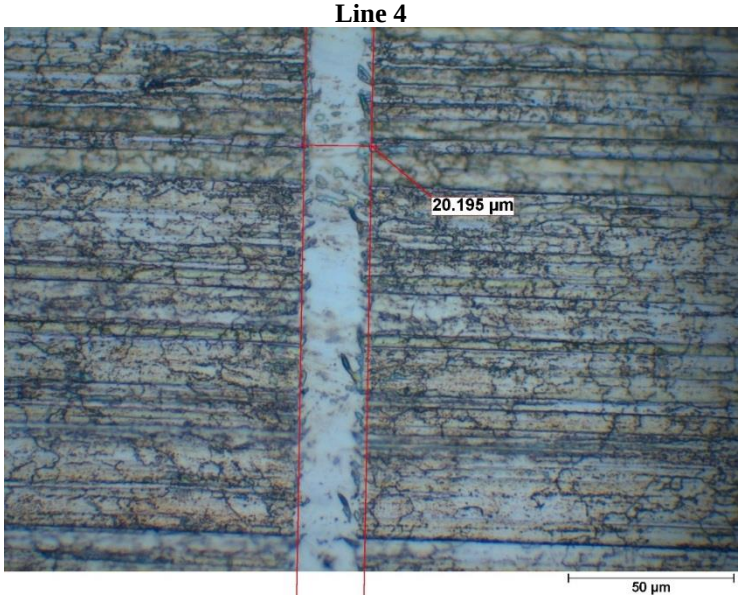

Line 6

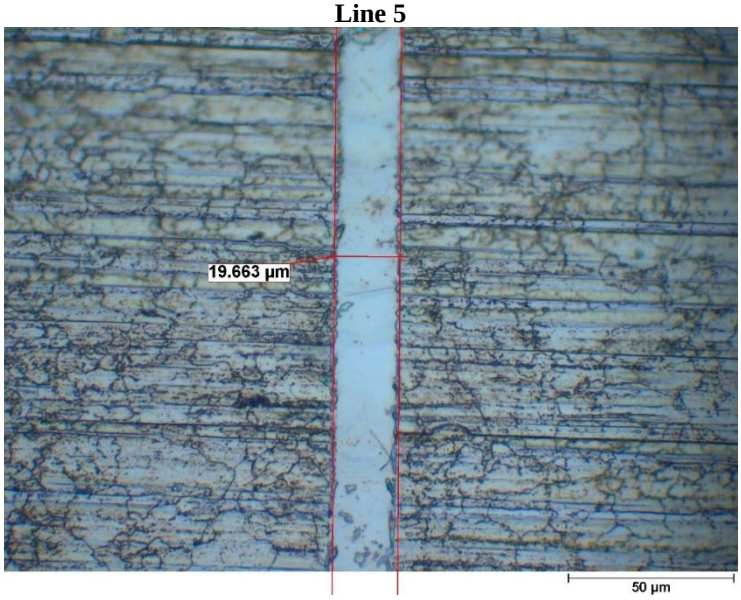

Line 7

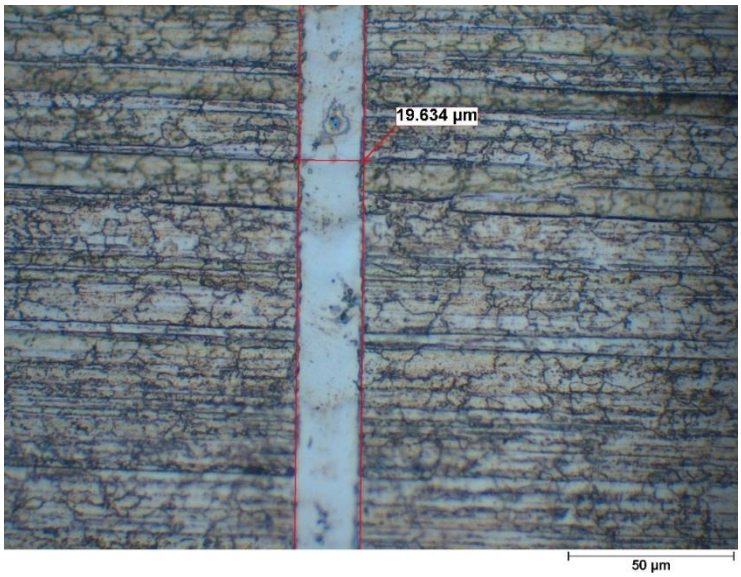

Line 8

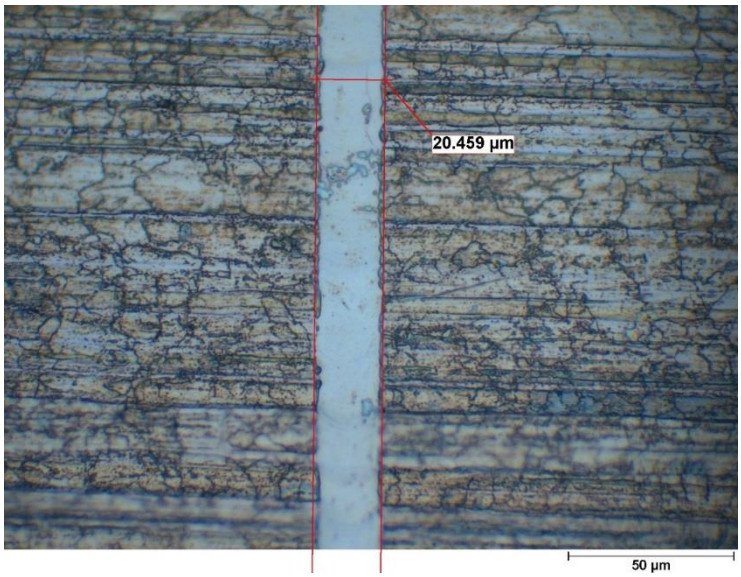

Line 9

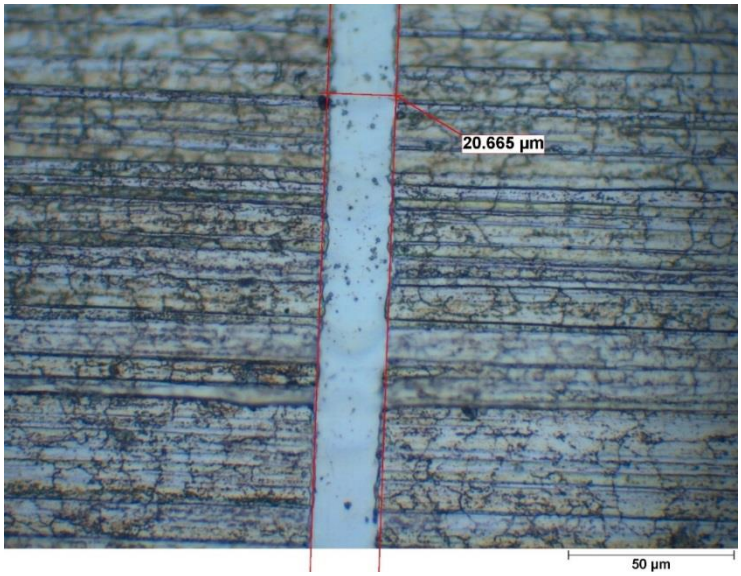

Line 10

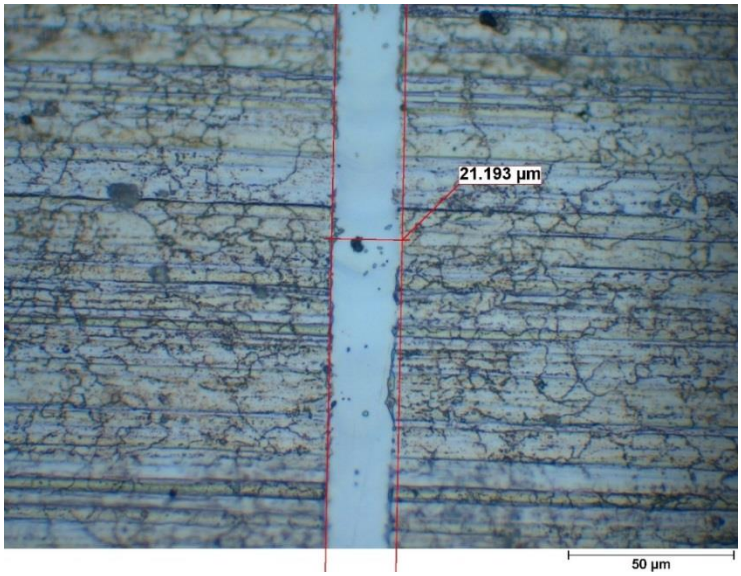

Line 11

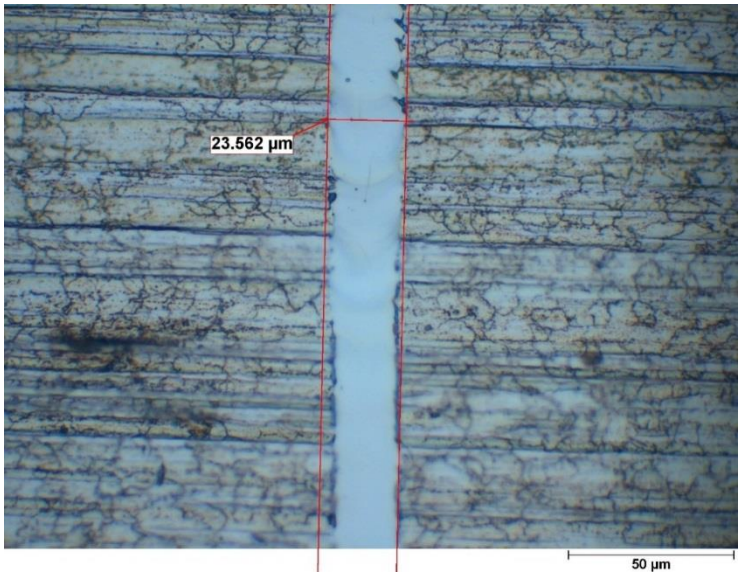

Line 12

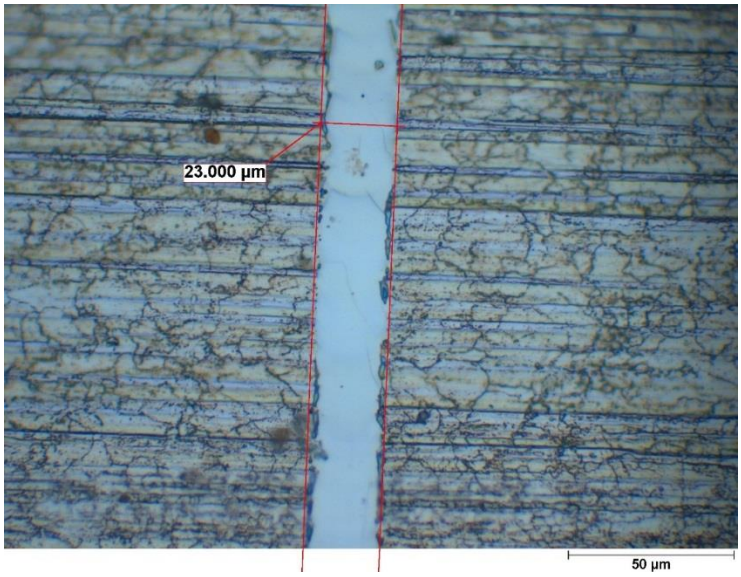

Line 13

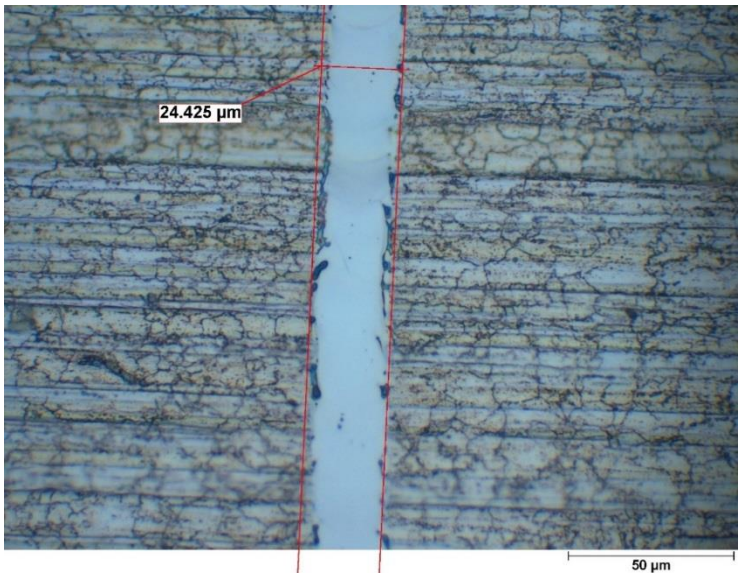

Line 14

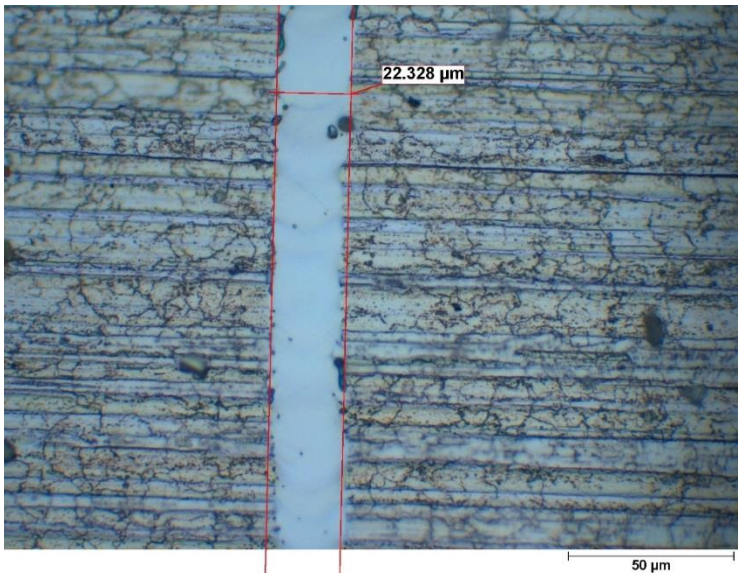

Line 15

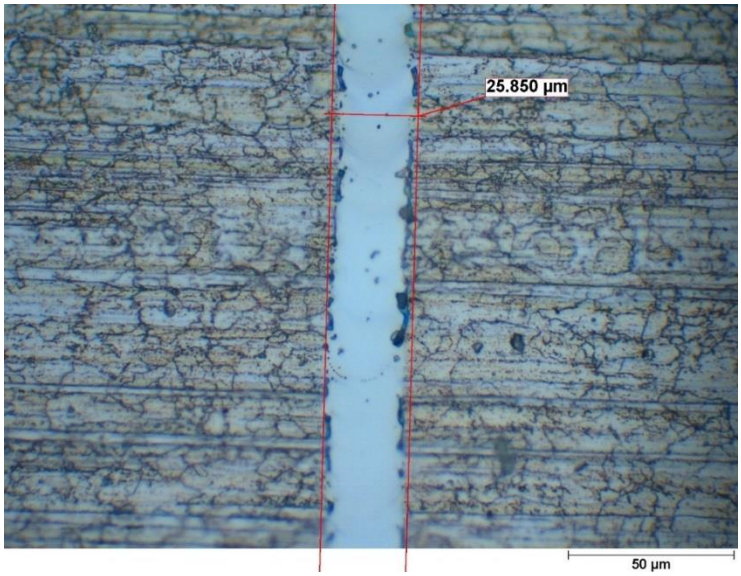

Line 16

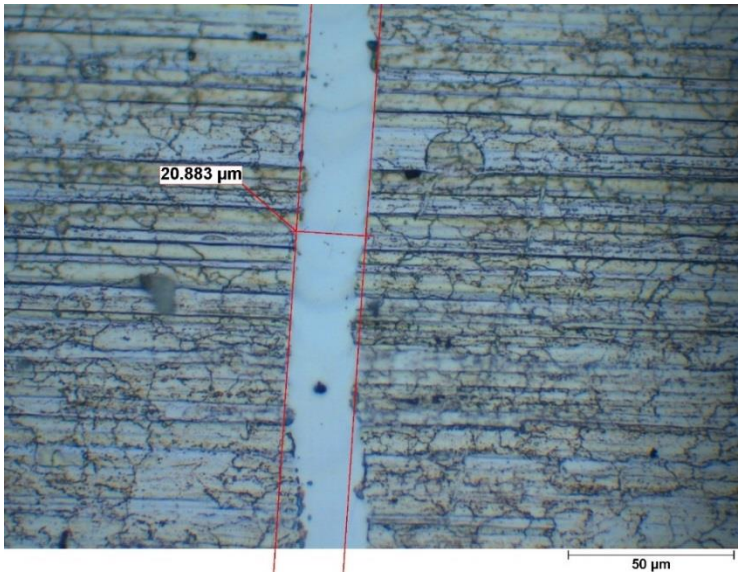

Line 17

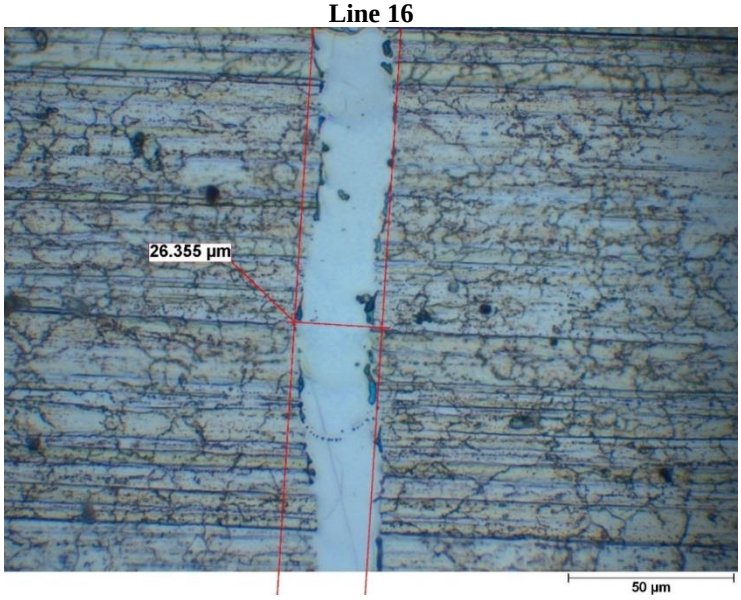

Line 18

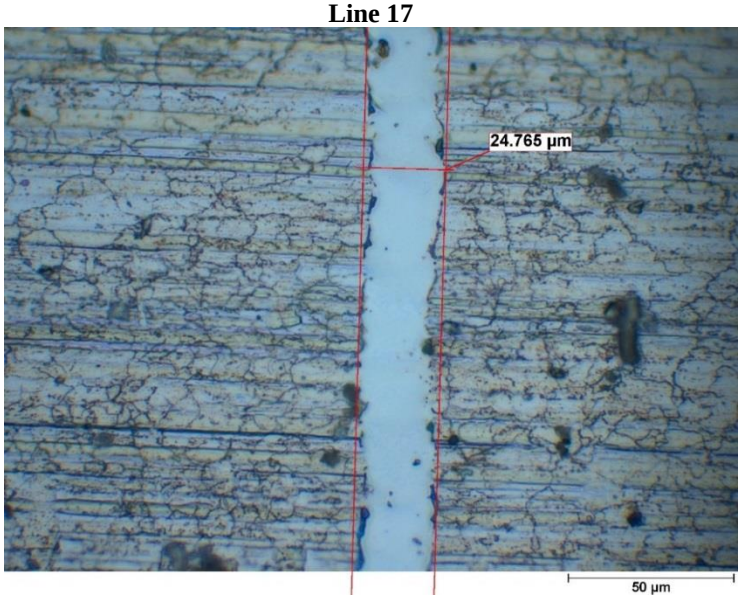

Line 19

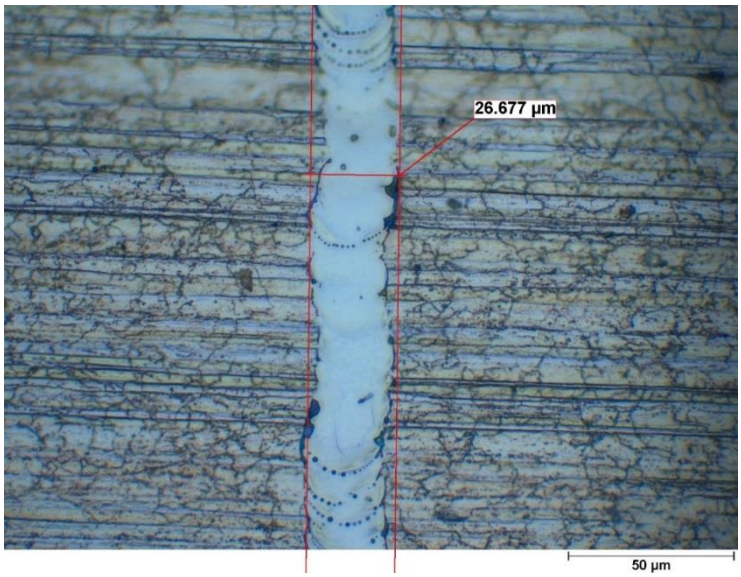

Line 20

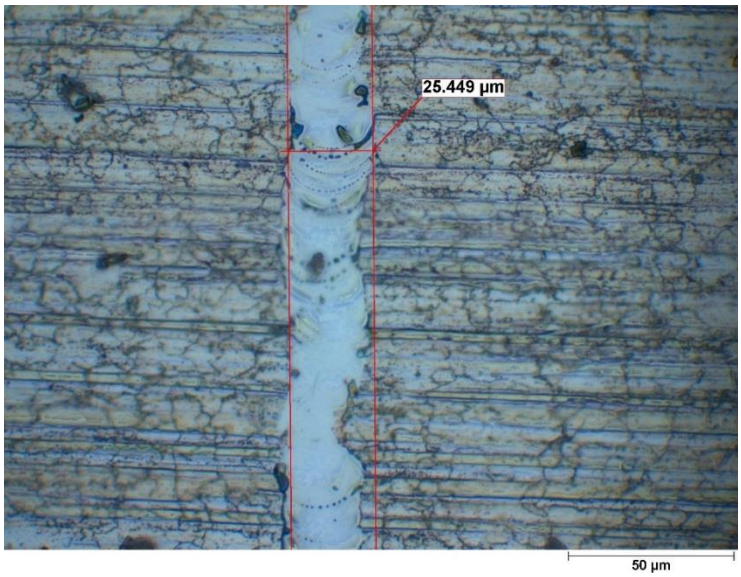

Line 21

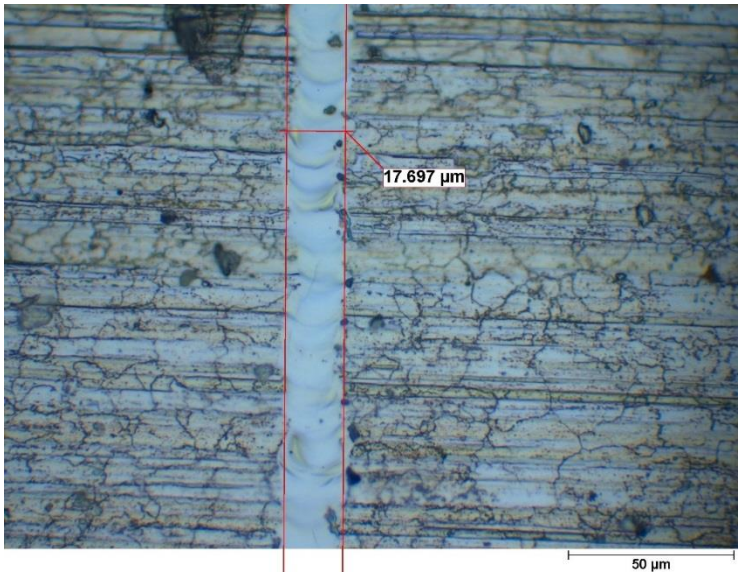

Line 22

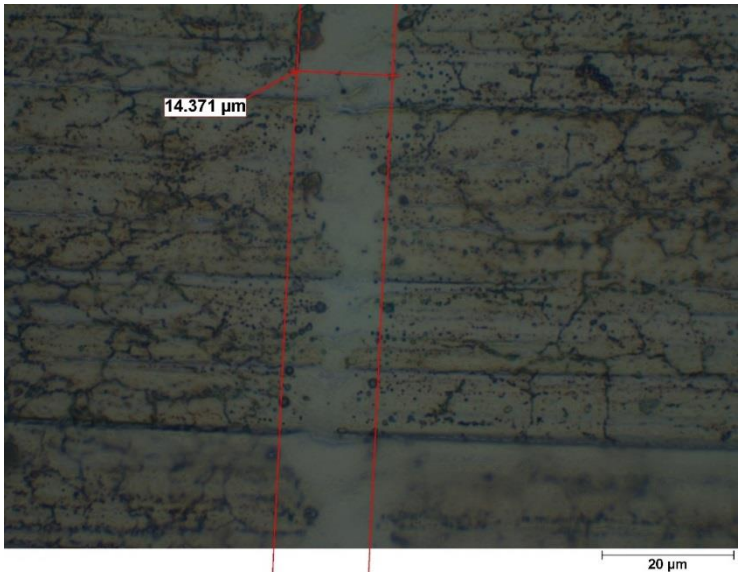

Line 23

Figure 139. Nickel, Olympus BX51 images. 23 Lines. Width measurements.

Appendix E

Figure 140 shows how lack of the nitrogen gas and consequently increased oxidation in the setup effects the end result.

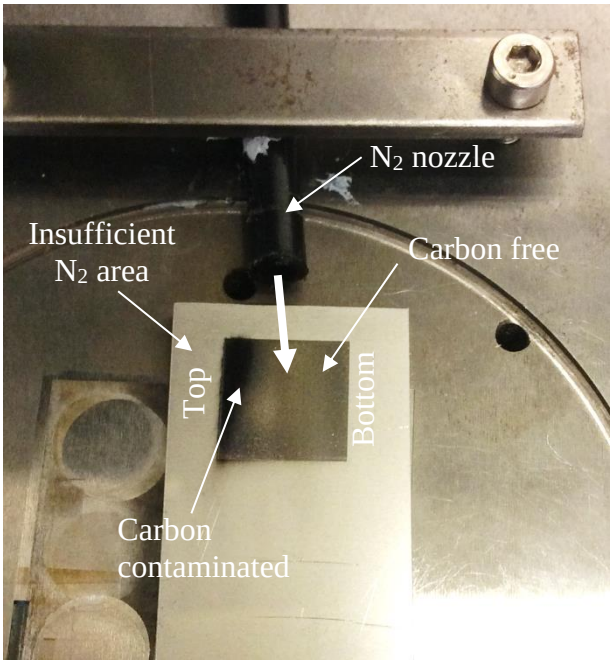

Figure 140. Lack of nitrogen during LSM.

Appendix F

The laser pattern is chosen to mimic a circuit grid with 45º angle lines, Figure 141. A total of 8 laser passes was used.

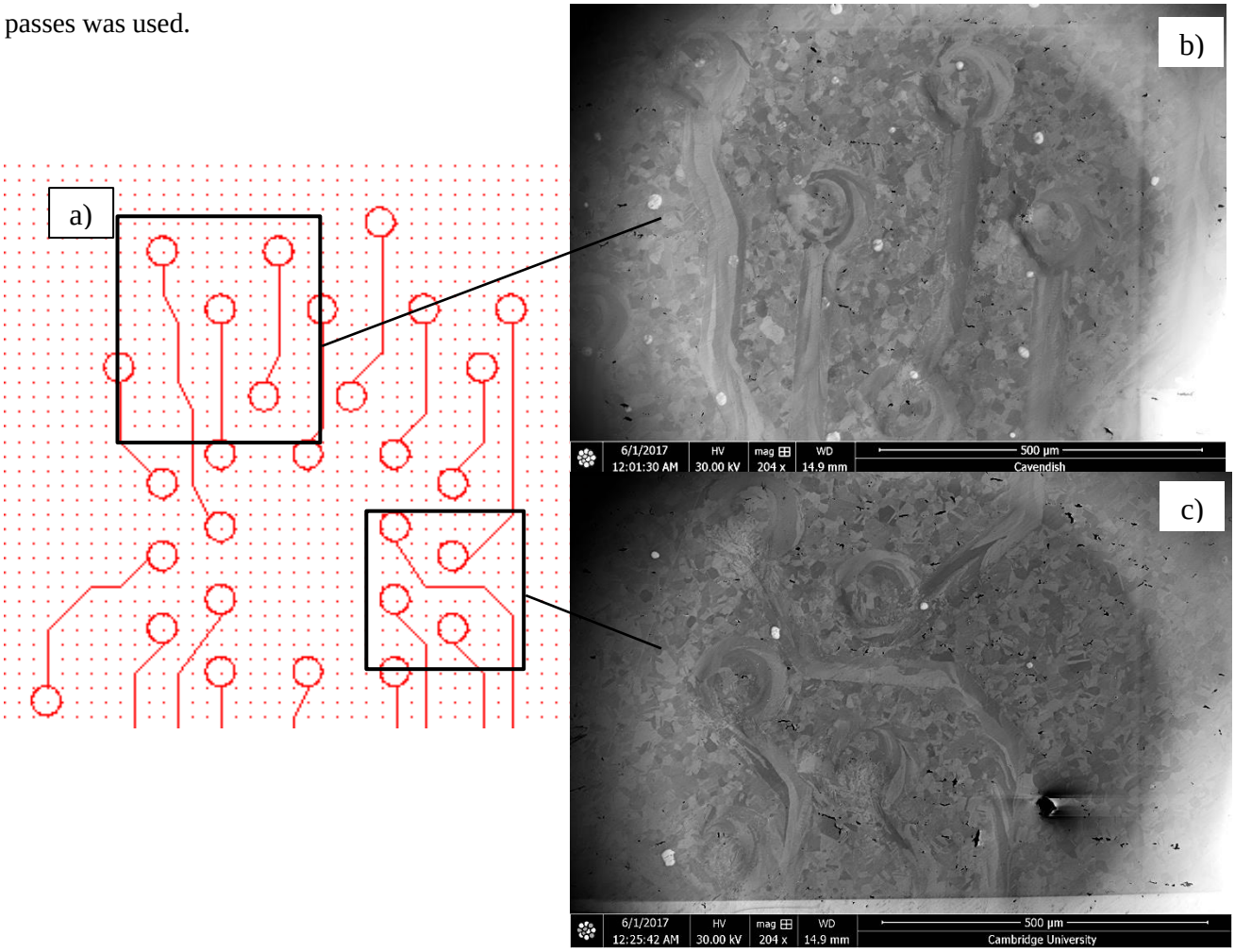

Figure 141. a) Laser pattern in the software. The b) and c) are FIB images of the microstructure generated by eight laser passes with 19.17 kJ/cm^2.

Single crystal lines are once again observed in the surface microstructure of 304 SS.

Appendix G

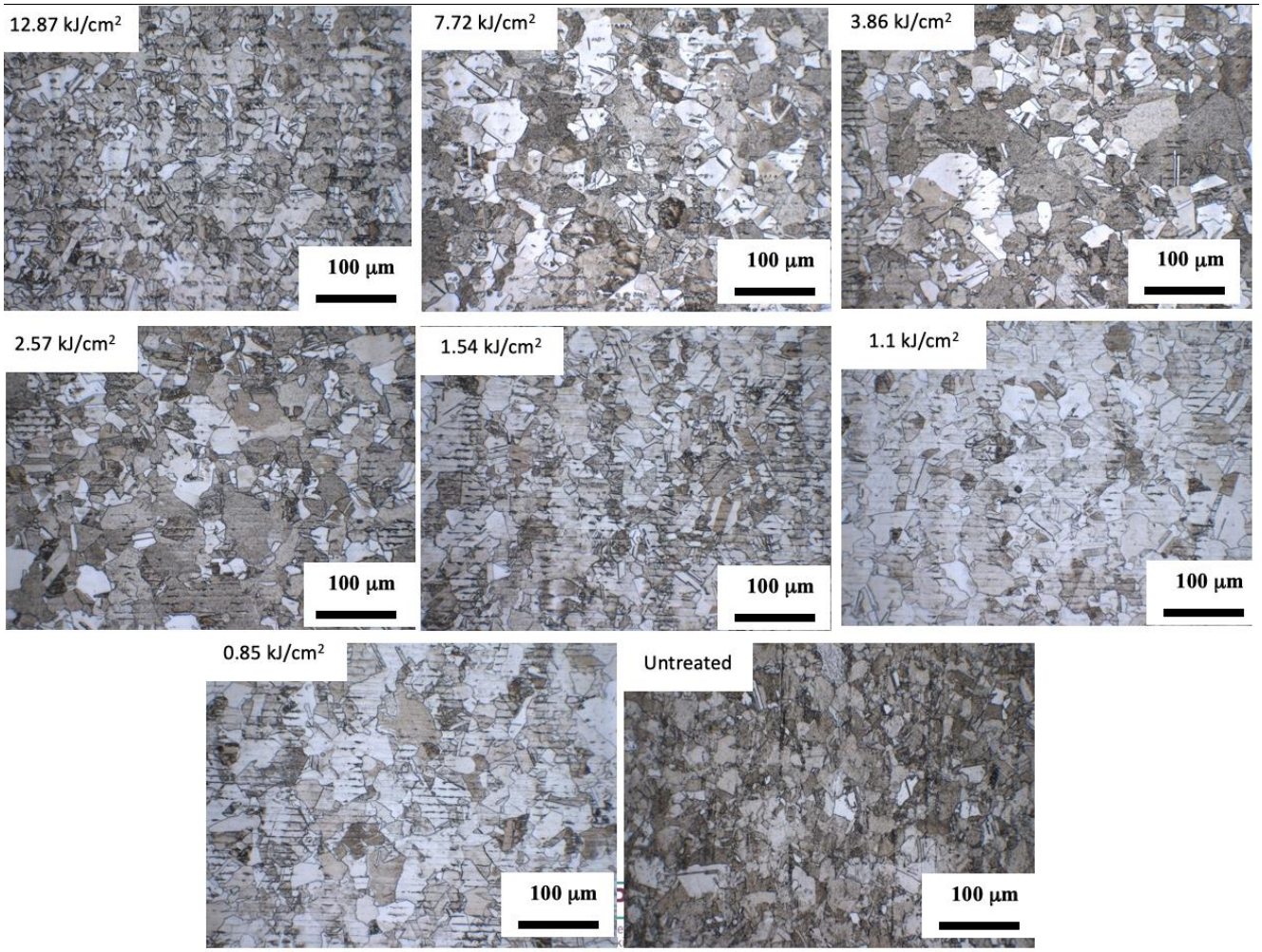

Figure 142. Optical microscope images LSM treated Ni with various average EDs. The laser raster is visible on the sample's surface as black parallel lines.

Appendix H

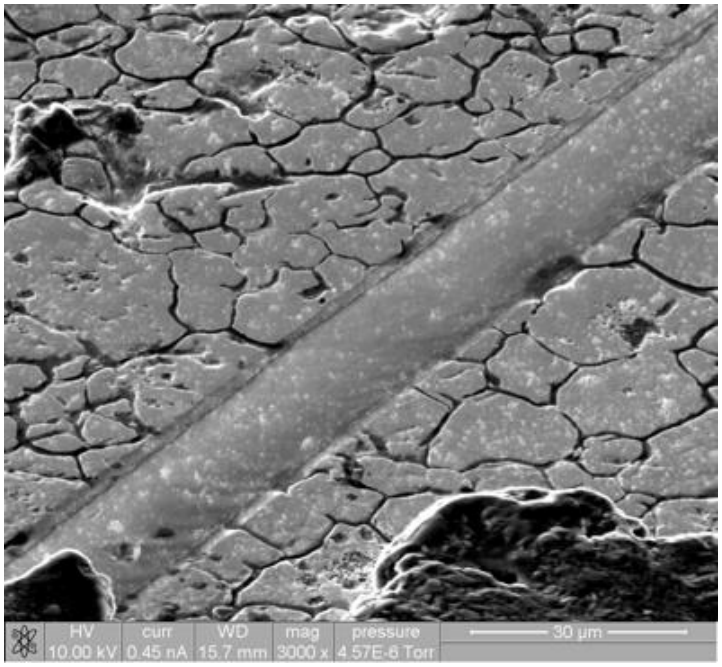

SEM image of PLM 304 SS using 100 ps pulses.

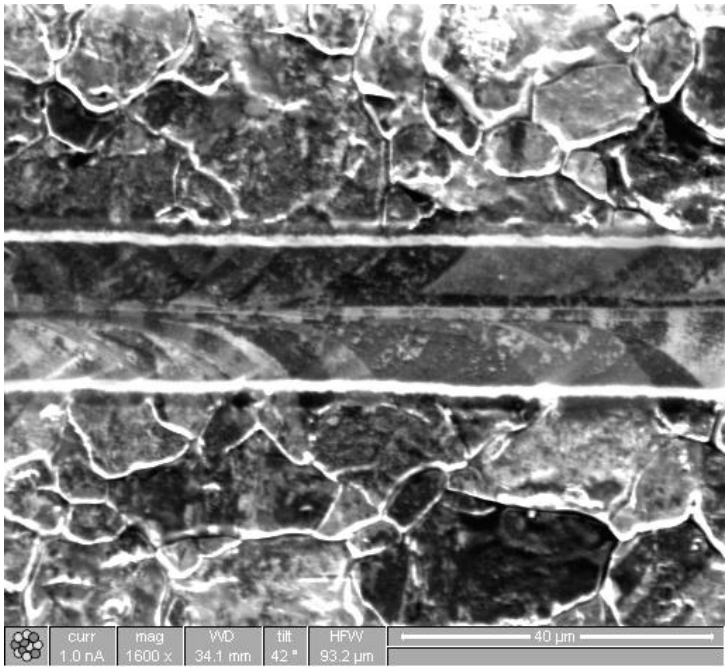

SEM image of PLM 304 SS using 100 ps pulses. Elongated grains are once again observed in the irradiated region following the laser scan direction.

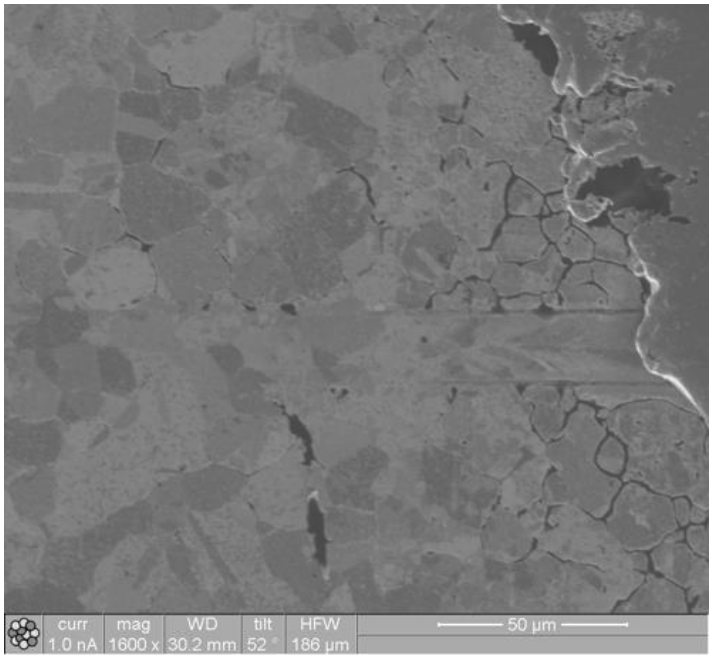

FIB image of PLM 304 SS using 100 ps pulses. The track is partially mechanically polished away.

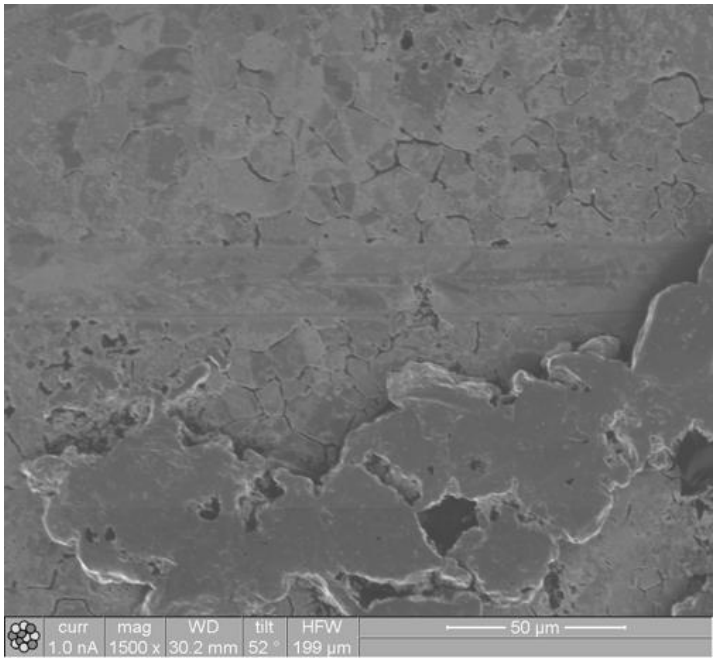

Another section of the FIB image of PLM 304 SS using 100 ps pulses.

Figure 143. Additional laser track images of PLM 304 SS, 100 ps pulses.

Appendix I

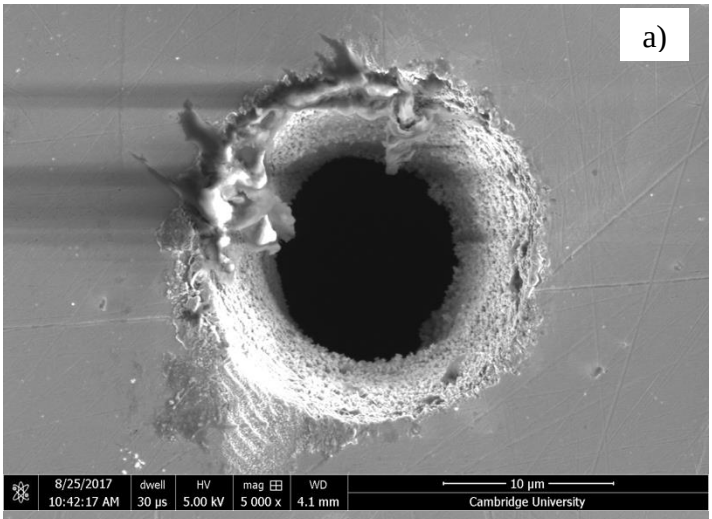

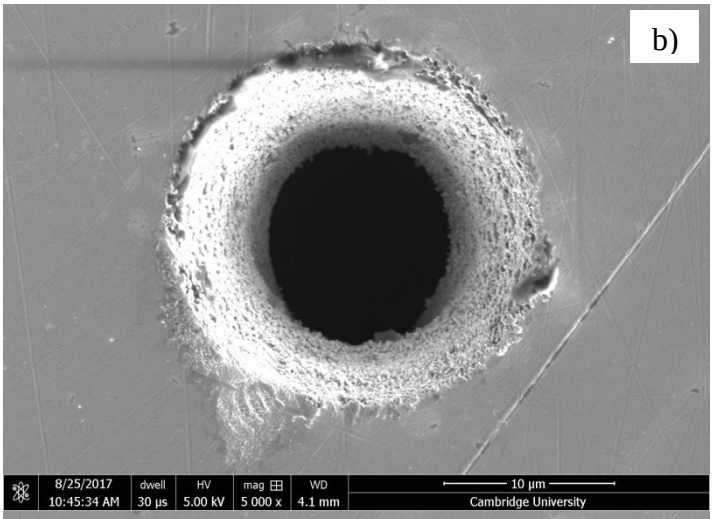

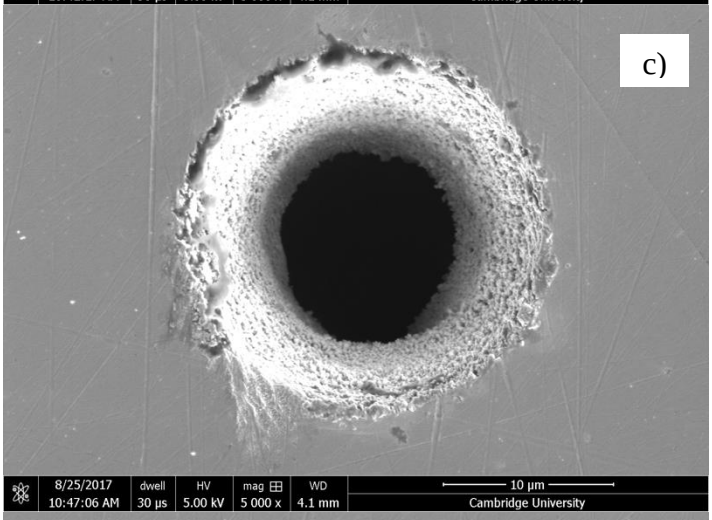

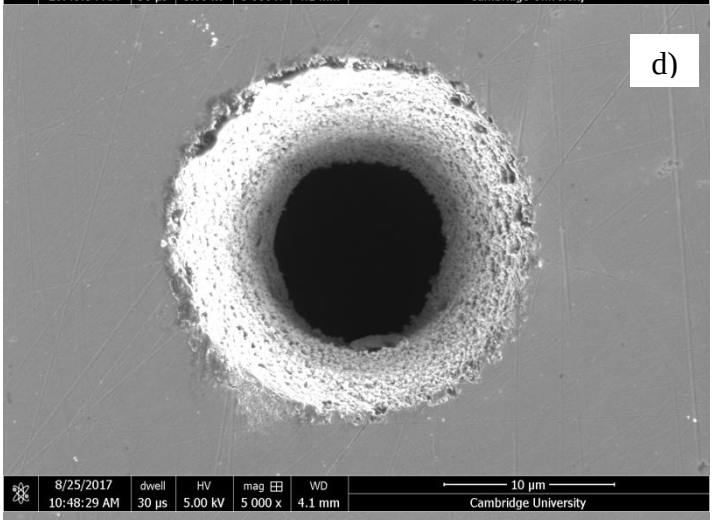

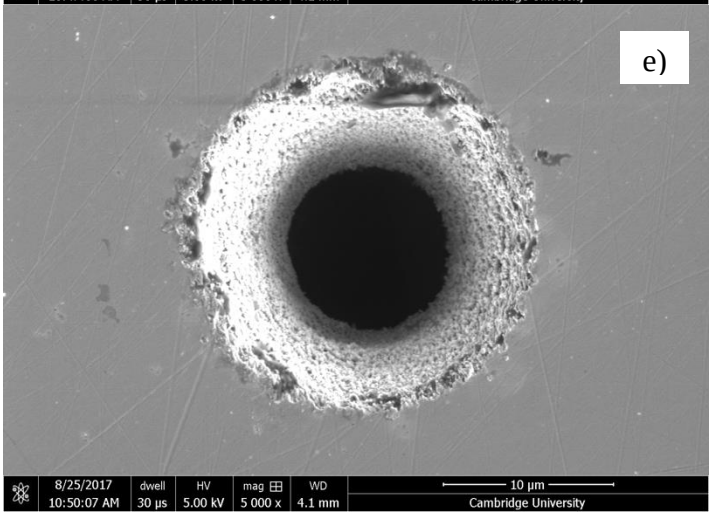

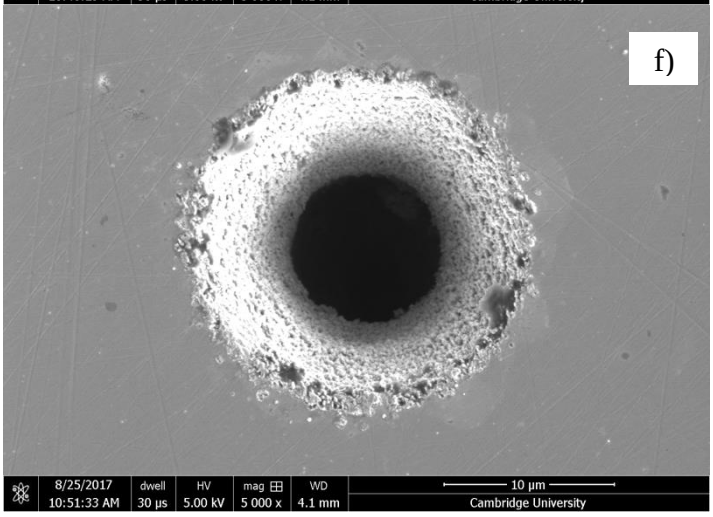

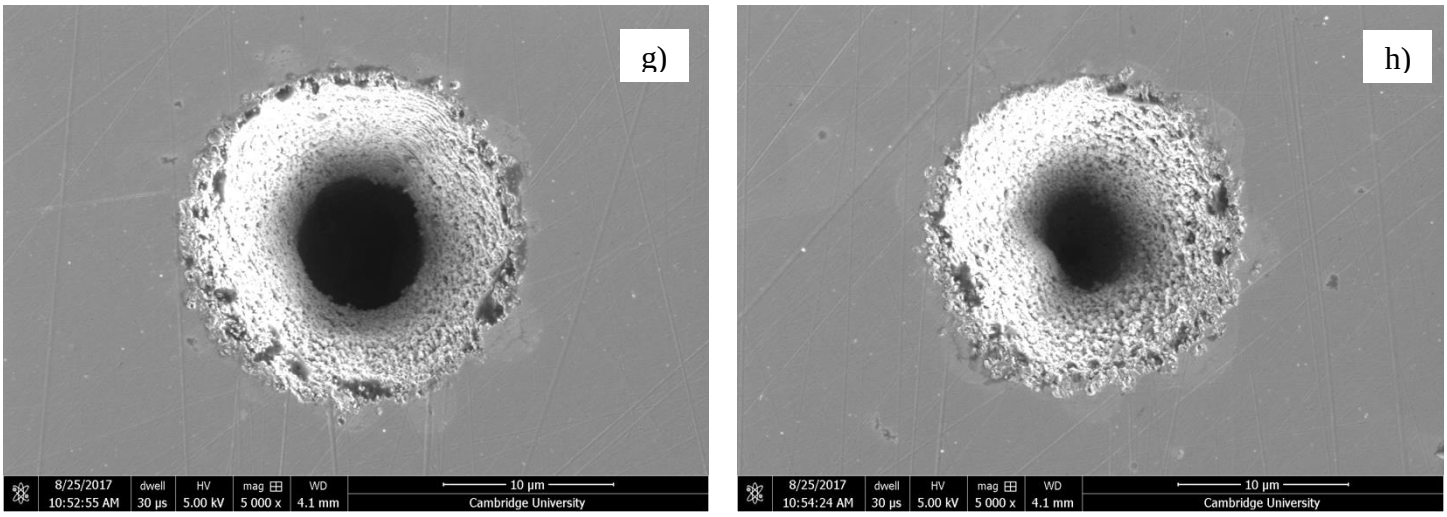

Figure 144. SEM images of hole drilling on 304SS surface, a) 4.8 mW, b) 3.8 mW, c) 3.01 mW, d) 2.52 mW, e) 1.9 mW, f) 1.54 mW, g) 1.2 mW, h) 0.97 mW. Hole numbers: 974, 976 – 982.

Appendix J

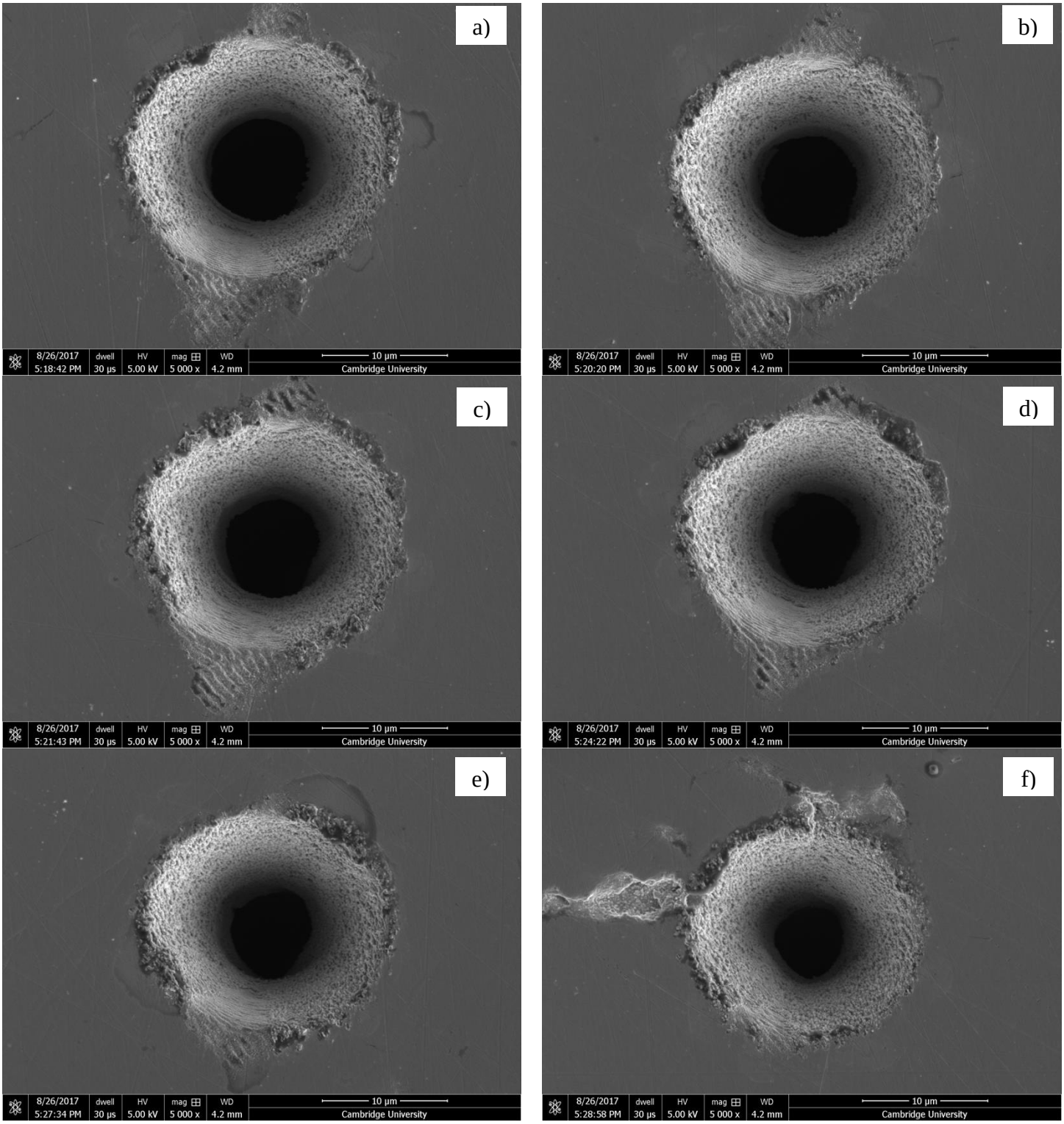

Figure 145. SEM images of hole drilling on 304SS surface, a) 4.8 mW, b) 4.3 mW, c) 3.8 mW, d) 3.01 mW, e) 2.52 mW, f) 1.9 mW. Hole numbers: 1205 – 1210.

Appendix K

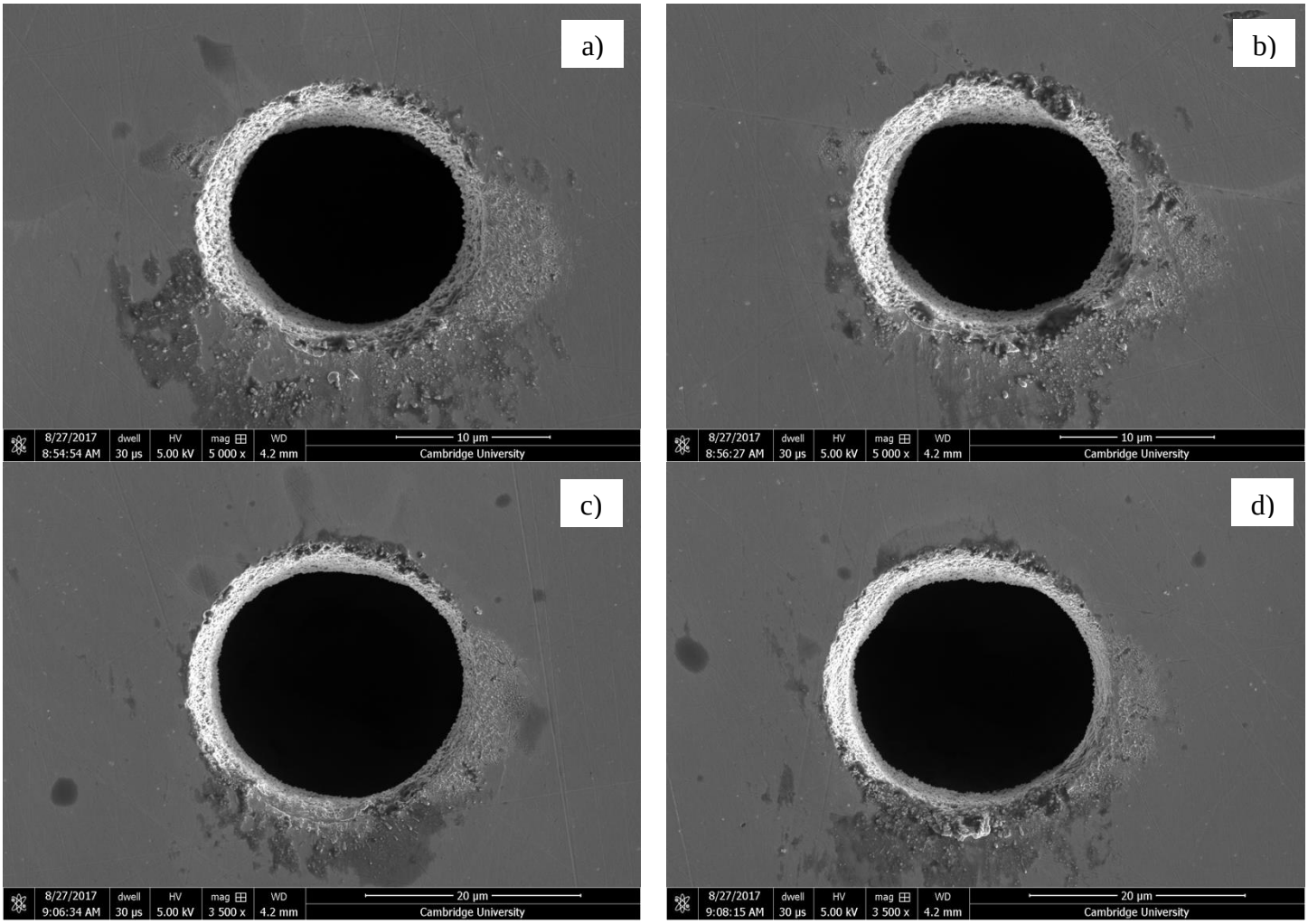

Figure 146. SEM images of holes with a) 200 circles, 3 µm diameter, 0.03 mm/s trepanning speed, b) 100 circles, 3 µm diameter, 0.03 mm/s trepanning speed, c) 200 circles, 7 µm diameter, 0.06 mm/s trepanning speed, d) 100 circles, 7 µm diameter, 0.06 mm/s trepanning speed. Hole numbers: 1221,1222; 1230,1231.

Appendix L

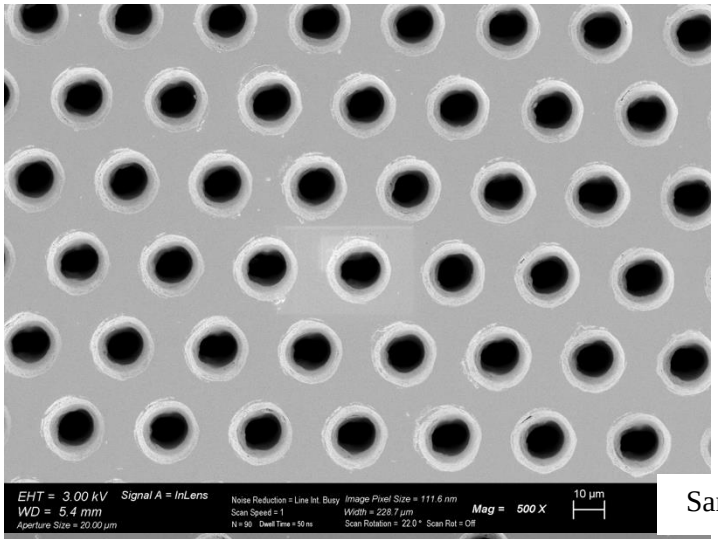

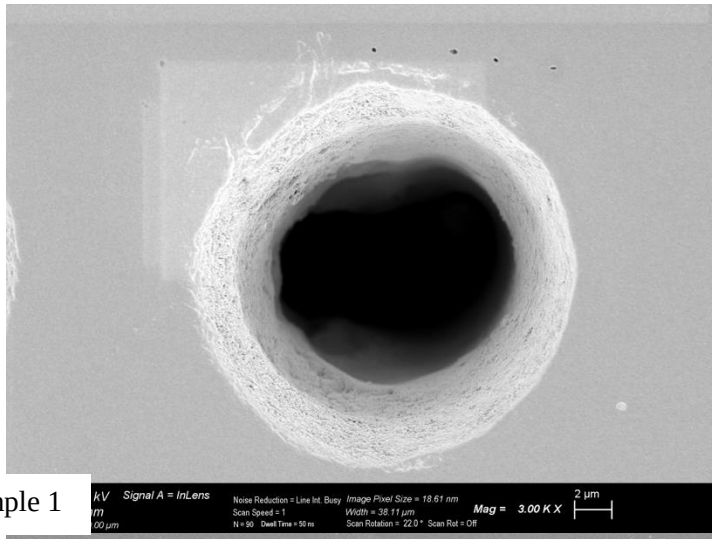

Sample 1

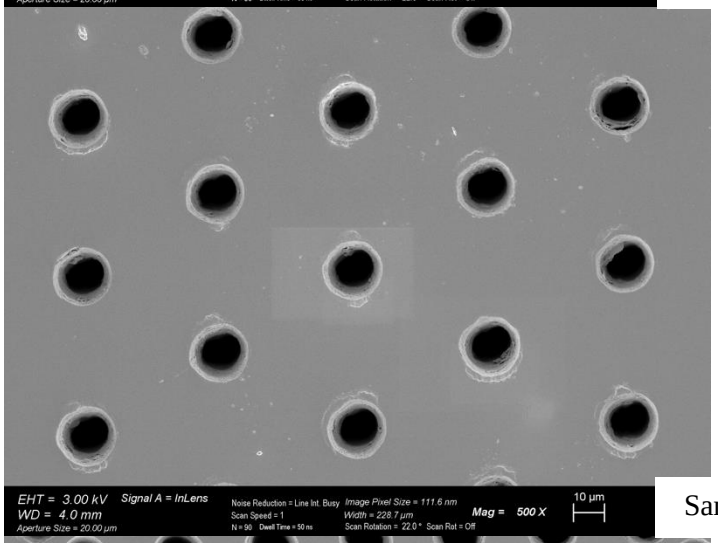

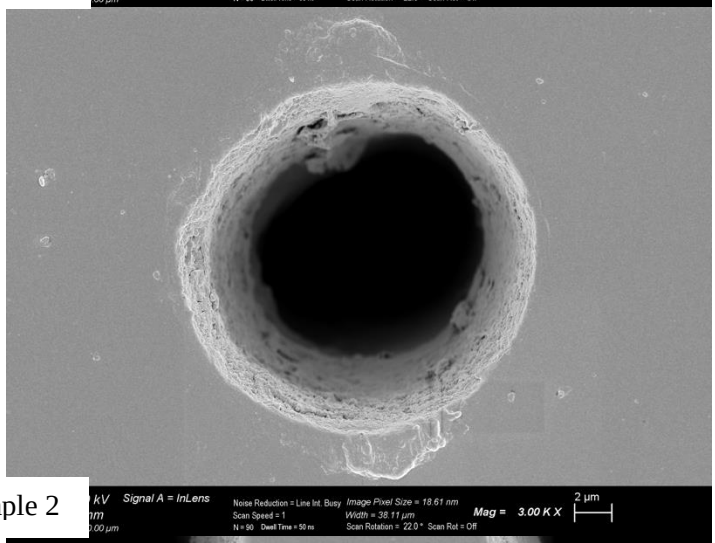

Sample 2

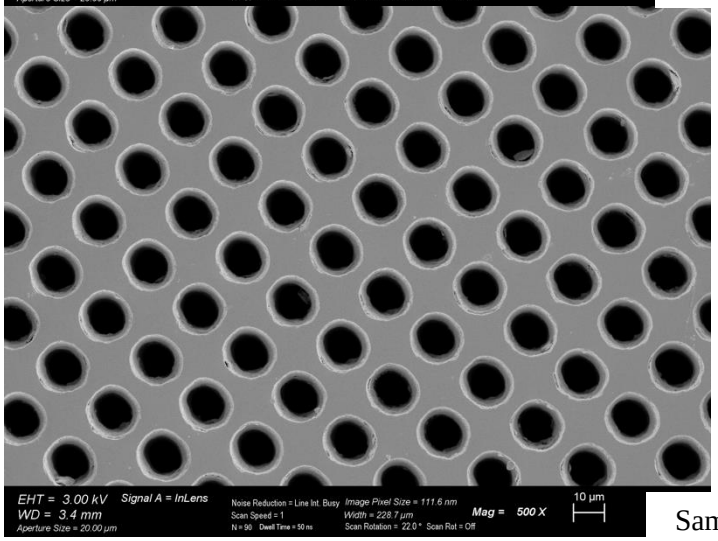

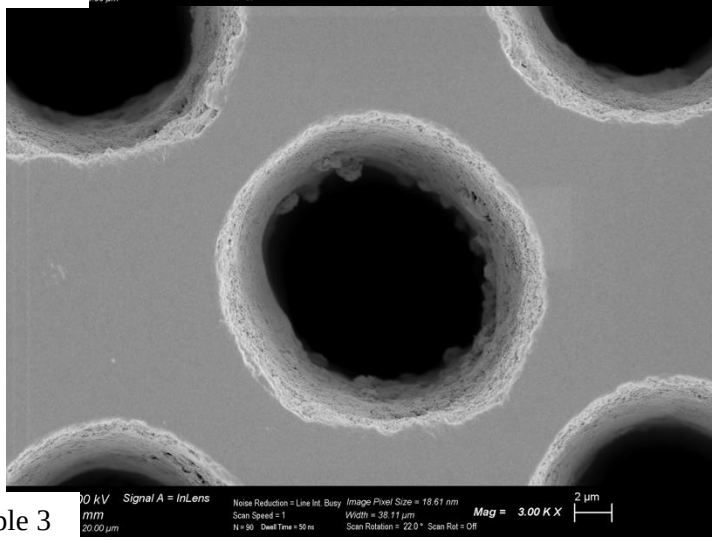

Sample 3

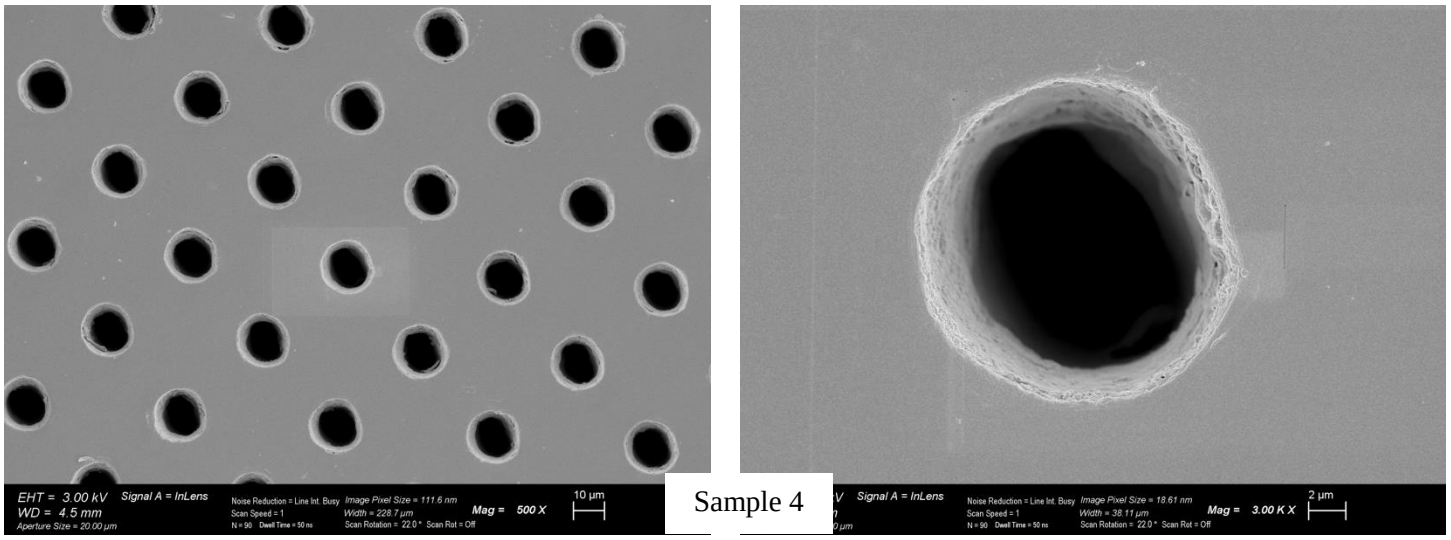

Figure 147. SEM images of gold-coated laser drilled 304 SS.

Appendix M.

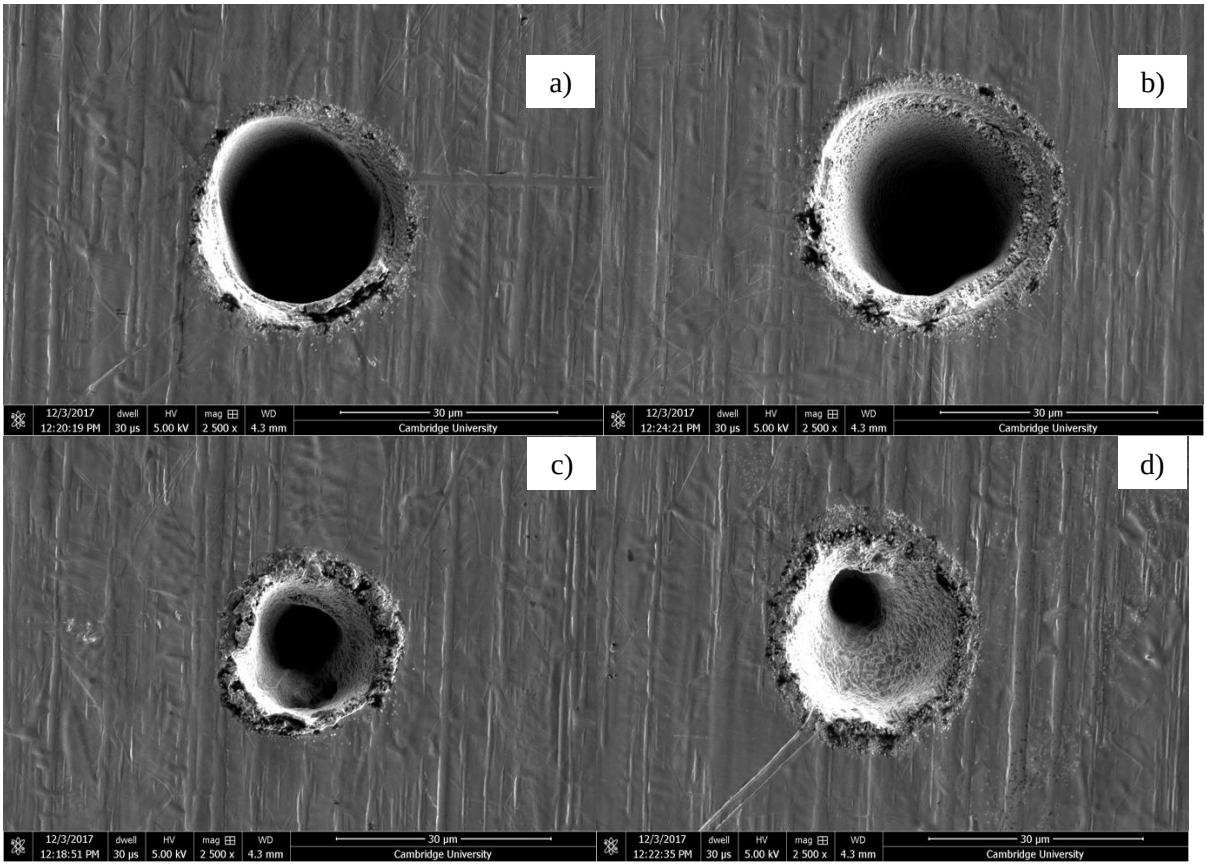

Figure 148. SEM images of the entrance holes drilled in 304SS, a), c) 0.4 and b), d) 1 mm/s trepanning speeds. Sample no. a) 1596 and b) 1608, c) 1595 and d) 1607.

Appendix N

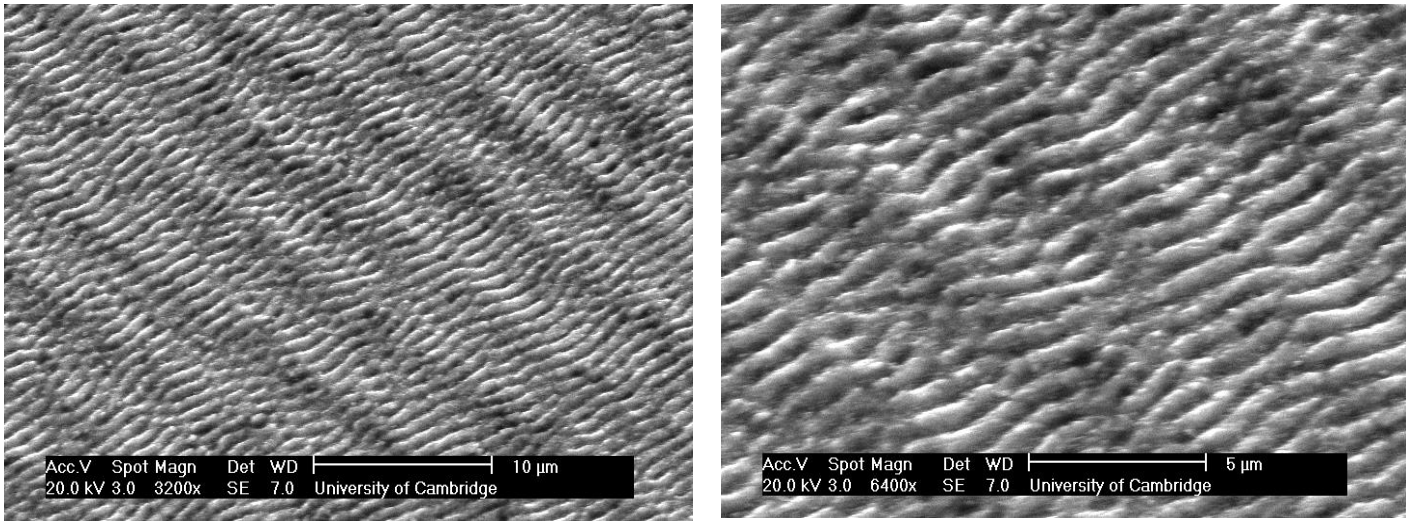

Figure 149. SEM images of Sample 1, surface close-up.

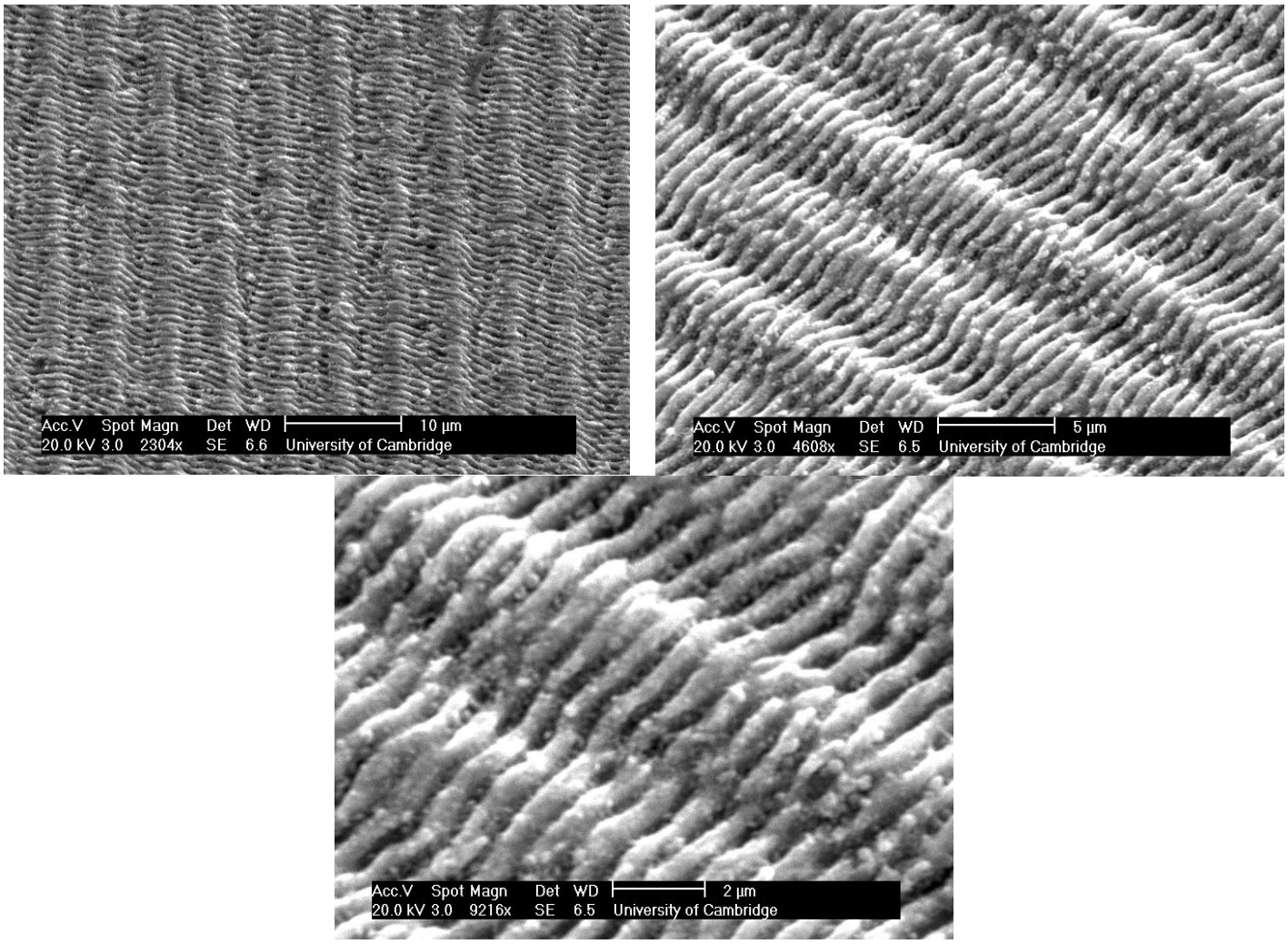

Figure 150. SEM images of Sample 2, surface close-up.